A versatile setup for experiments with Rubidium Bose Einstein condensates: From optical lattices to Rydberg matter

Von der Fakultät Mathematik und Physik der Universität Stuttgart
zur Erlangung der Würde eines Doktors der
Naturwissenschaften (Dr. rer. nat.) genehmigte Abhandlung

vorgelegt von

Robert Löw

aus München

Hauptberichter:	Prof. Dr. Tilman Pfau
Mitberichter:	Prof. Dr. Ulrich Stroth
Tag der mündlichen Prüfung:	13. Dezember 2006

Physikalisches Institut der Universität Stuttgart

2006

D93

In memoriam Josef Löw

Contents

Zusammenfassung

In dieser Arbeit präsentiere ich einen neuartigen Aufbau für Experimente mit Bose-Einstein Kondensaten bestehend aus ^{87}Rb Atomen und die ersten experimentellen Ergebnisse, die an dieser Apparatur erbracht wurden. Der Fokus liegt dabei in der Untersuchung von Fragestellungen aus der Festkörperphysik sowie der Eigenschaften von Rydberg Materie bei sehr hohen Dichten und Temperaturen nahe des absoluten Nullpunktes.

Als im Jahr 2002 Eric Cornell, Carl Wieman and Wolfgang Ketterle den Nobelpreis für die Erzeugung eines Bose-Einstein Kondensates (BEK) und für erste fundamentale Untersuchungen daran überreicht bekamen, war dies nicht nur eine Auszeichnung für eine nun historische wissenschaftliche Leistung, sondern auch der Startschuss für ein überaus lebendiges Forschungsgebiet. Diese Aussage wird durch die Entwicklung der wissenschaftlichen Veröffentlichungen im Forschungsgebiet der quantenentarteten Gase gestützt, die der Abbildung 1.1 entnommen werden kann. Dabei wurden nur Fachartikel gewertet, die auf experimentellen Daten basieren. Zu diesen Artikeln kommen dreißig mal soviele theoretische Veröffentlichungen hinzu, sodass nun seit der ersten Erzeugung eines BEKs in 1995 bis heute mehr als 20.000 wissenschaftliche Abhandlungen entstanden sind. Dabei zeigt die Steigung der Veröffentlichungskurve bislang keine Abflachung, was auf eine lebendige Zukunft der Quantengase hindeutet. Diese Zukunft wird von inzwischen weltweit über fünfzig Arbeitsgruppen mit circa achtzig funktionstüchtigen BEK-Aufbauten gestaltet werden. In diesen Gruppen konnten bislang die Elemente ^{1}H [1], ^{4}He [2], ^{52}Cr [3], ^{133}Cs [4], ^{41}K [5], ^{7}Li [6], ^{23}Na [7], ^{85}Rb [8], ^{87}Rb [9], and ^{174}Yb [10] erfolgreich kondensiert werden. Seit kurzem wurden die BEKs basierend auf atomaren Gasen noch um zwei festkörperartige Systeme erweitert. So konnte nun auch die Existenz einer quantenentarteten Phase mit Polaritonen [11] und Magnonen [12] nachgewiesen werden.

Die Forschung an Quantengasen erstreckt sich heute über fast alle klassischen Gebiete der Physik und hat so eine Vielfalt angenommen, dass es unmöglich ist, sie in ein einfaches Struktogramm zu pressen. Darum sei im Folgenden eine subjektive Übersicht über die verschiedenen Aktivitäten gegeben.

In fast allen bislang durchgeführten Experimenten ist die Wechselwirkung zwischen den Atomen von entscheidender Bedeutung, welche hier als kleinster gemeinsamer Nenner herangezogen werden soll. Typischerweise ist die Wechelwirkungsenergie von magnetisch oder optisch gefangenen BEKs eine Größenordnung größer als der entsprechende Quantendruck durch den Falleneinschluss. Diese Energie drückt die BEKs auseinander und macht sie damit für optische Abbildungssysteme wesentlich leichter zugänglich. Die dadurch entstandenen detailierten Aufnahmen von BEKs waren sicherlich maßgeblich für den großen Erfolg dieses Gebietes verantwortlich.

In den ersten Jahren nach der ersten erfolgreichen Kondensation in 1995 wurden alle möglichen Arten von elementaren hydrodynamischen Anregungen untersucht, wie z.B. Dipoloszillationen, Quadrupolanregungen, Formoszillationen, Atmungsmoden und Scherenmoden [13, 14, 15, 16, 17] sowie deren korrespondierenden Dämpfungsmechanismen. Eine ganz andere Art von kollektiver Anregung, die erst durch die Präsenz einer Wechselwirkung möglich ist, sind Phononen, die auf verschiedene Arten [18, 19, 20] untersucht wurden. Die Kombination von makroskopischer Quantenkohärenz und einer phononenartige Dispersionsrelation verbietet die Anregung von Quasiteilchen

unterhalb einer kritischen Geschwindigkeit[21, 22], was gemeinhin als Superfluidität bezeichnet wird. Der Nachweis einer superfluiden Phase in einem BEK wurde auf verschiedene Arten erbracht [23, 24, 25], manifestiert sich aber am schönsten durch die Existenz von quantisierten Wirbeln [26, 27, 28]. Durch interferometrische Methoden konnte auch gezeigt werden, dass die beobachteten Wirbel tatsächlich quantisiert sind [29]. Interferometrie ist überhaupt eines der wichtigsten Werkzeuge, um BEKs zu untersuchen, und wurde erstmals zum Nachweis der makroskopischen Kohärenz der Materiewellen verwendet [30]. Bald wurde sie aber auch benutzt, um z.B. die Phase eines Kondensats zu bestimmen [30] oder um Beschleunigungen [31, 32] und fundamentale Konstanten [33] zu messen.

Wie schon gesagt wurde, sind Wechselwirkungen von fundamentaler Bedeutung und machen sich vor allem in Experimenten bemerkbar, in denen sie als Nichtlinearität auftauchen. Hier sei zum Beispiel die Erzeugung von Solitonen [34, 35, 36] oder der Nachweis von Vierwellenmischung [37] genannt. Mit Hilfe von Feshbachresonanzen ist es möglich, die Stärke der Wechselwirkung durch Magnetfelder annähernd beliebig zu verändern [38, 39, 40, 41, 42], was viele neue experimentelle Möglichkeiten eröffnet. Dieser Effekt wurde zum Beispiel ausgenutzt, um BEKs, bestehend aus Molekülen, herzustellen [43, 44]. Dazu werden zwei Atome eines BEKs mittles einer Feshbachresonanz adiabatisch in ein Molekül umgewandelt. Diese Moleküle müssen aber nicht zwangsläufig aus zwei Bosonen bestehen, sondern können auch Fermionen enthalten [45, 46, 47].

Diese knappe Übersicht soll noch um einige wichtige Ergebnisse von fundamentaler Bedeutung erweitert werden. Die Verwirklichung von verschiedenen Atomlasertypen [48, 49, 50] zeigte eindrucksvoll die nahe Verwandschaft zwischen den Kohärenzeigenschaften eines normalen Lasers zu dem eines Strahls von kohärenten Materiewellen. Weiterhin wurde ein kohärenter Verstärker für Materiewellen entwickelt [51, 52], Licht auf wenige Meter pro Sekunde abgebremst [53, 54] oder die Physik der Spinorkondensate eingehend untersucht [55, 56, 57]. Zuletzt sei noch auf die Herstellung eines Gases im Tonks-Girardeau Regime [58, 59], der Nachweis von Efimov Zuständen [60] und die Erzeugung von Verschränkung [61] verwiesen.

Nachdem ich die Forschung der letzten zehn Jahre grob umrissen habe, stellt sich nun die Frage, was die Zukunft bringen wird. Aktuell ist ein Hauptgebiet die Untersuchung von quantenentarteten Gasen in optischen Gittern, die auch ein Ziel des hier vorgestellten experimentellen Aufbaus ist und darum in einem eigenen untenstehenden Abschnitt behandelt wird. Mit der erfolgreichen Kondensation von Chromatomen [3] steht nun erstmalig ein System mit einer spürbaren dipolaren Wechselwirkung zur Verfügung, was innerhalb kürzester Zeit zu einer überaus großen Anzahl von theoretischen Arbeiten führte und viel erwarten lässt. BEKs wurden aber auch intensiv als ein System für Präzisionsmessungen von Naturkonstanten [62], als Sensor für Beschleunigungen und Rotationen [63] oder zum Nachweis eines permanenten Dipolmoments des Elektrons [64] diskutiert. Weitere Anwendungen ergeben sich in der Atomlithographie [65] oder dem Aufbau von Hybridsystemen, die Kondensate mit makroskopischen Festkörperelementen kombinieren [66].

Festkörperphysik mit ultrakalten Atomen

Die experimentelle und theoretische Festkörperphysik behandelt fast ausschließlich die Eigenschaften von Elektronen in kristalliner Materie und deren Struktur. Ultrakalte Gase befinden sich dagegen normalerweise in einem ungeordneten Zustand, können aber mit Hilfe von optischen Gittern periodisch angeordnet werden. Nun übernehmen die Atome die Rolle der Elektronen und das optische Gitter stellt das tight-binding Potential der remanenten Ionen dar. Die schwache Wechselwirkung zwischen den Atomen, die vielfältigen Einstellmöglichkeiten der Potentiallandschaft und

die Kontrolle über den Quantenzustand der Atome macht dies zu einem idealen Modellsystem, um festkörperphysikalische Fragestellungen zu untersuchen.

Der erste Versuch optische Gitter mit einem BEK zu kombinieren wurde im Jahre 1998 vorgenommen und lieferte sogleich den Nachweis von Blochoszillationen [67], was gerade mal fünf Jahre zuvor in einem Festkörpersystem erreicht wurde [68]. Die Untersuchung der Dynamik von Atomen in optischen Gittern erbrachte auch den Nachweis von Wannier-Stark Leitern [69] und Landau-Zener Tunneln [70].

Der größte Erfolg der optischen Gitter ist sicherlich die Erzeugung eines Mott-Isolator Zustands eines BEKs in einem dreidimensionalen optischen Gitter [71, 72], was bis heute nicht in Festkörpern erreicht wurde. Die theoretische Beschreibung dieses stark korrelierten Zustands erfolgt mit Hilfe des Bose-Hubbard Modells [73]. Dieses Modell ist aufgrund seiner großen Komplexität schwierig handzuhaben und weitere Experimente werden sicher zum Verständnis dieses Systems beitragen [74].

Ein weiteres festkörpertheoretisches Modellsystem ist das Spin-Boson Modell [75], welches die Kopplung eines Pseudo-Spins an ein bosonisches Bad beschreibt. Die Kopplung induziert Dissipation des Spinzustands abhängig von den Eigenschaften des thermischen Bades. Wie auch das Bose-Hubbard Modell kann das Spin-Boson Modell auf BEKs übersetzt werden [76, 77]. Die Untersuchung dieses Quanten-Dissipation Modells ist ein Hauptziel des hier vorgestellten Aufbaus. Die experimentelle Umsetzung erfordert im Prinzip nicht die Periodizität eines optischen Gitters, welches aber als Hilfsmittel zur Erzeugung des thermischen Bades eingesetzt genutzt werden kann. Solch ein Gitter wurde im Rahmen dieser Arbeit schon erfolgreich implementiert.

Rydberg Materie

Neben der Untersuchung des Spin-Boson Modells ist die Erforschung von ultrakalten Rydberggasen die zweite Hauptrichtung dieses Projektes. Rydbergatome sind hoch angeregte Atome mit einem oder mehreren Elektronen in Zuständen mit hohen Hauptquantenzahlen [78]. Erste Untersuchungen zu den Eigenschaften von Rydbergzuständen waren nur in hochangeregten Plasmen oder durch astronomische Beobachtungen möglich [79], wo sie durch Rekombination von Ionen und Elektronen entstehen. Die Erfindung des Lasers ermöglichte es schließlich, Atome in wohldefinierte Zustände anzuregen, was hinreichend ausgenutzt wurde [80]. Als Quellen dienten dabei meist Dampfzellen oder thermische Atomstrahlen. Mit der Entdeckung der Laserkühlung [81, 82, 83] waren nun atomare Wolken im μK Bereich verfügbar, was das Forschungsgebiet der gefrorenen Rydberggase initiierte [84, 85]. Der Name spiegelt dabei die Tatsache wieder, dass auf der Zeitskala der durchgeführten Experimente oder der Lebensdauer der angeregten Zustände die Atome sich nicht merklich bewegen und somit eingefroren sind. Damit ist es nun möglich, die Wechselwirkungen zwischen den Atomen weitaus genauer zu untersuchen als je zuvor. Rydbergatome haben eine große Polarisierbarkeit, was eine starke van-der-Waals Wechselwirkung nach sich zieht [86, 87, 88, 89, 90]. Legt man zusätzlich noch ein elektrisches Feld an, ergibt sich für die meisten Zustände ein großes elektrisches Dipolmoment. Die Dipol-Dipol Wechselwirkung führt für zwei nahe beieinanderliegende Atome zu einem Blockadeeffekt der Anregung, welche als Grundlage eines c-NOT Gatters für die Quanteninformationsverarbeitung dienen könnte [91].

Die Erweiterung der Rydbergforschung auf lasergekühlte Atomwolken erweiterte den Parameterraum um mehrere Größenordnungen und eröffnete damit neue physikalische Situationen. Eine logische Konsequenz ist es nun, BEKs für Experimente heranzuziehen, da sie eine wesentlich höhere Dichte bei extrem kleinen Temperaturen aufzeigen. Weiterhin hat man nun auch die Möglichkeit,

die internen und externen Freiheitsgrade kohärent zu kontrollieren, wie die obige Auflistung der Experimente deutlich gezeigt hat. Auf der Agenda steht zunächst die Untersuchung der dipolaren Wechselwirkung und der Nachweis des Blockadeeffekts. Hiermit läßt sich nun in Kombination mit einem kohärenten Anregungsschema ein c-NOT Gatter bewerkstelligen. Weiterhin wird die Möglichkeit untersucht, inwiefern sich Rydbergatome in elektrostatischen Fallen einfangen lassen oder die ob die Erzeugung von Molekülen bestehend aus einem Rydbergatom und einem Grundzustandsatom machbar ist [92].

Experimenteller Aufbau

Bose-Einstein Kondensate werden unter Einsatz verschiedener Kühlmechanismen und Fallentypen erzeugt. Hierzu wurde zunächst eine Ultrahochvakuum-Kammer aufgebaut, die bei 10^{-11} mbar betrieben wird. Das Kammerdesign beinhaltet, unüblich zu sonstigen Aufbauten, zusätzlich acht Feldplatten zur Erzeugung komplexer elektrischer Feldgeometrien, sowie zwei Multikanalplatten zur Detektion von Ionen und Elektronen. Dies wurde in Hinblick auf die geplanten Experimente mit Rydbergatomen vorgenommen. Dabei war es wichtig, dass die Komponenten zur Erzeugung eines BEK nicht beeinträchtigt werden. Das wäre zum einen ein guter optischer Zugang zur Laserkühlung aus drei Raumrichtungen sowie eine Möglichkeit, eine spezielle Magnetfalle zur Speicherung der Atome möglichst nah an die Atome heranzubringen. Weiterhin muss noch ein Atomstrahl zum Laden der magneto-optischen Falle (MOT) hinzugefügt werden, eine Antenne innerhalb der Kammer, um radiofrequenzinduzierte Verdampfungskühlung vornehmen zu können und zwei Achsen zur optischen Abbildung der kalten Atomwolke. All dies wurde bewerkstelligt, und es können Kondensate mit mehreren hunderttausend Atomen erzeugt werden. Hierzu wird zunächst ein Atomstrahl mit einem effusiven Ofen erzeugt, der mittels eines Zeeman-Abbremsers vorgekühlt wird und eine MOT lädt. Die Funktionsweise einer MOT basiert auf einer geschickten Kombination von sechs Laserstrahlen und einem magnetischen Quadrupolfeld, das es erlaubt, die Atome nicht nur zu kühlen, sondern auch räumlich einzufangen. Mit dieser Methode werden typischerweise 10^{10} Atome in der MOT gefangen und anschließend mittels Molassenkühlung auf wenige 10 μK heruntergekühlt. Als nächstes wird diese so vorgekühlte Wolke in eine rein magnetische Falle transferiert. In unserem Fall handelt es sich dabei um eine Ioffe-Pritchard artige Kleeblattfalle. Eine weitere Verringerung der Temperatur wird durch evaporatives Kühlen erreicht. Bei dieser Methode werden Atome mit hoher kinetischer Energie aus der Falle durch das Einstrahlen einer passender Radiofrequenz entfernt. Über elastische Stöße rethermalisieren sie zu einer tieferen Temperatur und erreichen schließlich bei wenigen 100 nK die kritische Temperatur, bei der der Grundzustand der Falle makroskopisch besetzt wird und das BEK entsteht. Dabei wurden alle wichtigen Kenngrößen der einzelnen Kühlschritte sowie des Kondensats ausführlich untersucht, sodass es nun möglich ist, im täglichen Betrieb zuverlässig Kondensate im Minutentakt herzustellen.

Experimentelle Ergebnisse

Nachdem der Aufbau charakterisiert wurde, konnten erste Experimente durchgeführt werden, die für die beiden angestrebten Projekte (Rydberg-Materie und Spin-Boson Modell) entscheidende Grundlagen darstellen.

Die Rydberganregung in einen definierten Zustand erfolgt mittels eines schmalbandigen Lasersystems durch eine zwei-Photonen Anregung. Um die Rydbergatome selektiv detektieren zu können, wurden zwei Multikanalplatten (MCP) eingebaut. Durch Anlegen eines starken elektrischen

Feldes, das durch die Feldplatten erzeugt wird, werden die Rydberatome feldionisiert und mit einem geeigneten Feldgradienten in die MCP gelenkt und dort detektiert. Mit dieser Anordnung wurde eine Auflösung von ca. 100 Rydbergatomen erreicht. Um die Felder die durch die acht Feldplatten erzeugt werden zu testen, wurde die Starkverschiebung des 43S Zustandes für verschiedene Feldkonfigurationen ausgemessen und mit theoretischen Modellen verglichen, was zu einer sehr guten Übereinstimmung führte. Weiterhin wurde die Lebensdauer des 43S Zustandes gemessen, und auch diese Resultate stimmen gut mit den theoretischen Modellen überein.

Für das zweite Projekt, der experimentellen Untersuchung des Spin-Boson Modells, wurde ein eindimensionales Gitter aufgebaut und charakterisiert. Dieses Gitter wird in einem nächsten Schritt auf zwei Dimensionen erweitert um eindimensionale Quantengase erzeugen zu können, die später mal das bosonische Bad darstellen sollen. Um die Gittertiefe bestimmen zu können, wurde ein BEK an dem Gitterpotential gebeugt und die Beugungsordnung als Funktion der Wechselwirkungszeit detektiert. Durch Vergleich mit einem theoretischen Modell konnte die Gittertiefe auf 5% Genauigkeit bestimmt werden.

Als drittes Resultat wurde ein Mikrowellensystem bei 6.8 GHz aufgebaut, was gerade der Hyperfeinaufspaltung von ^{87}Rb entspricht. Mit einer speziellen Helixantenne wurde die Mikrowellenstrahlung auf eine lasergekühlte Atomwolke gerichtet, und es wurden kohärente Rabioszillationen beobachtet. In Kombination mit dem Radiofrequenzsystem der Verdampfungskühlung ist es nun möglich, die Atome in jeden beliebigen magnetischen Grundzustand kohärent zu transferieren.

Theoretische Ergebnisse

Schließlich wird noch ein Vorschlag zur experimentellen Untersuchung der lichtinduzierten Dipol-Dipolwechselwirkung vorgestellt. Wenn Atome einer elektromagnetischen Welle ausgesetzt sind, verhalten sie sich wie ein gedämpfter harmonischer Oszillator und weisen ein oszillierendes Dipolmoment auf. Die Atome erfahren eine Kraft über die Potentiale, die durch die Dipolmomente aller Atome in einer atomaren Wolke erzeugt werden und werden darin beschleunigt. Jedoch weisen die Dipolpotentiale eine Retardierung auf der Längenskala der Wellenlänge des eingestrahlten Lichts auf. Damit sich die einzelnen Potentiale nicht zu Null mitteln, ist es nötig, die Dichteverteilung der Atome auf wenige Wellenlängen einzuschränken, was mit Hilfe von optischen Gittern möglich ist. Der resultierende Impulsgewinn durch die Wechselwirkung sowie der Beitrag durch spontane Streuung wird im Detail diskutiert.

1 Introduction

When in 2002 the Nobel prize was given to Eric Cornell, Carl Wieman and Wolfgang Ketterle *for the achievement of Bose-Einstein condensation in dilute gases of alkali atoms, and for early fundamental studies of the properties of the condensates* [93, 94, 95], did this not denote the end of a well settled research field but rather a beginning. This notion is propped by figure 1.1. It shows the annual amount of published articles in the field of quantum degenerate gases, which must include some experimental results to be counted. The annual number of publications with only theoretical content is roughly thirty times as large [96] and reached in the year 2005 a value of more than 3500 articles. All in all more than 20.000 articles have been written on this topic since the first experimental observation of Bose-Einstein condensation in 1995 until the end of 2006. The relative increase of publications is more or less constant over the last ten years and seems not to level off in the near future. This ascent is also owed to the number of experimental groups working worldwide on degenerate quantum gases, which reached by now roughly eighty running individual experimental setups distributed among fifty research groups worldwide.

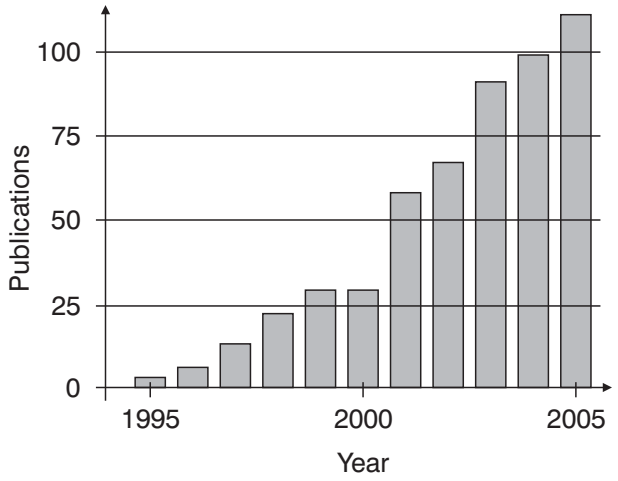

Figure 1.1: Publications per year in refereed journals with an experimental content regarding quantum degenerate gases. This includes Bose-Einstein condensates as well Fermi-gases below the Fermi temperature. The bar chart was compiled with the help of the homepages of the individual experimental groups, the ISI web of knowledge, google scholar and the journals themselves. The error of the annual count is at most underestimated by 10%.

The year 1924 was decisive for nowadays cold atom physicists in three manners. Satyendra Nath Bose and Albert Einstein established theoretically the existence of a Bose-Einstein condensate [97, 98, 99] by using statistical physics. In the same year published Louis-Victor de Broglie his PhD-thesis on quantum theory in which he proposed the wave-particle duality [100]. The matter-wave character of a Bose-Einstein condensate is a direct implementation of this idea. Finally received Karl Manne Georg Siegbahn the nobel prize *for his discoveries and research in the field of X-ray spectroscopy* [101], which led in combination with the advancements in quantum theory to

a full understanding of the internal structure of atoms.

It took another 14 years until the idea of the Bose-Einstein statistic received a broader attention, when Fritz London and Laszlo Tisza revived it to explain superfluidity in liquid ^{4}He in 1938 [21, 102]. Although the properties of superfluid liquids or superconductors are closely related to the Bose-statistics, is the description as an ideal gas not sufficient to describe this systems. A loophole from this strongly interacting systems is the changeover to weakly interacting gases. The first notion of gases of Hydrogen atoms as a system for Bose-Einstein condensation was given by C.E. Hecht in 1959 [103] and emphasized by a more quantitative analysis by W.C. Stwalley and L.H. Nosanow in 1976 [104].

But it needed the *development of methods to cool and trap atoms with laser light* [105], also honored with a Nobel prize in 1997 [81, 82, 83], which pioneered the breakthrough of the the first observations of a Bose-Einstein condensate in a dilute gas of ^{87}Rb [9], ^{23}Na [7] and ^{7}Li [6] in 1995. In the following years researchers also managed to condense ^{1}H [1], ^{4}He [2], ^{41}K [5], ^{52}Cr [3], ^{85}Rb [8], ^{133}Cs [4] and ^{174}Yb [10].

The research on quantum degenerate gases has evolved in such a diversity and is by now connected to almost any field of physics, that it is impossible to reduce it to a simple flip chart. In the following I want to give a small overview over the different research activities without aiming for completeness.

As a superior topos may act the interaction among the atoms, which is a key ingredient in almost all conducted experiments. The interaction energy in magnetically or optically trapped condensates is about an order of magnitude larger than the quantum pressure, which pushes the atoms apart and makes condensed clouds by this much better accessible to optical imaging techniques. By this researchers could produce detailed pictures of BECs and was probably crucial for the tremendous success of the whole research field. In the beginning researchers investigated all kind of collective (hydrodynamic) excitations of trapped condensates as dipole modes, quadrupolar modes, shape oscillations, breathing modes or scissor modes [13, 14, 15, 16, 17] and their corresponding damping mechanisms. Another kind of collective excitation are phonon modes [18, 19, 20] with their corresponding structure factor [106]. A phonon-like energy-momentum dispersion relation in combination with a macroscopic quantum coherence does not allow the generation of elementary excitations below a critical velocity [21, 22], which is commonly known as superfluidity. The existence of a superfluid phase has been shown with several methods [23, 24, 25], but has its most intriguing proof by the generation of quantized vortices [26, 27, 28]. The evidence that the produced vortices are really quantized ones, has been provided by an interference experiment [29], which clearly showed the azimuthal phase twist by 2π. Interferometric techniques have been used in the first place to show the macroscopic coherence of Bose-Einstein condensates [30], but were soon expanded to measure the phase of condensates [31, 32], accelerations [67] or fundamental constants [33].

As claimed before interactions are the heart of Bose-Einstein condensate physics. This is most noticeable in a set of diverse experiments based on a nonlinearity imparted by the interactions among the atoms. This arises for example in four wave mixing of matter waves [37] or in the existence of solitons [34, 35, 36]. Nature delivered by chance a knob to adjust the scattering length of the atoms by applying a certain magnetic field, the Feshbach resonances [38, 39, 40, 41, 42]. This effect made the first production of a molecular Bose-Einstein condensate possible [43, 44]. But molecular condensates do not have to consist only of bosonic atoms but can also be created with two fermionic atoms [45, 46, 47].

This racy overview omitted some major achievements which shall not be forgotten. This are the

demonstration of several atom lasers [48, 49, 50], matter wave amplifiers [51, 52], slow light propagation [53, 54], spinor condensates [55, 56, 57], the generation of a Tonks-Girardeau gas [58, 59], the detection of an Efimov state [60], the generation of entanglement [61] and finally all the effort put into the miniaturization of the experimental setups for generating Bose-Einstein condensates [107, 108]. A major domain of current research are solid state related topics, which will be presented in the following chapter separately, because of its special connection to this thesis.

After recapitulating the research of the last ten years remains the question on the future of cold atom physics. A survey of recent theoretical publications allows one to distill future research tendencies but one has to be aware that experimental research often discover new effects which were on no ones mind.

With the successful condensation of Chromium [3], one has the first BEC with a noticeable dipolar interaction [109] at hand, which has triggered already a large amount of theoretical work. Bose-Einstein condensates have also been widely discussed as a source for precision experiments for e.g. measuring accelerations and rotations [63] or fundamental constants [62]. But the major fraction of theoretical publications deals with solid state related topics, which are partly discussed in the next section. Other directions may be the measurement of the permanent dipole moment of the electron [64], the usage of condensates as a coherent source for atom lithography [65] or building hybrid systems made of condensates and some solid state device [66]. Finally it should be mentioned that there is condensate physics beyond cold atoms, as was shown just recently by reaching quantum degeneracy with exciton polaritons at room temperature [11] and also with magnons [12].

1.1 Cold atoms meet solid state physics

Experimental and theoretical solid state physics mostly focuses on the electronic properties and the structure of crystal matter. Ultra-cold atomic gases are usually in an unordered state, but they can be structured by transferring them into a periodic potential, for instance into one produced by the interference pattern of two laser beams. Now the atoms adopt the role of the electrons in a solid and the optical lattice potential the tight-binding potential of the remanent ions. The weak interactions among the cold atoms, the variability of the optical lattices (depth, geometry, lattice constant) and the control over the internal and external quantum state of the atoms makes this an ideal construction kit for many fundamental questions.

The conjunction of a Bose-Einstein condensate with an optical lattices was achieved for the first time in 1998 [67]. Bloch oscillations [110, 111] were observed, when a condensate was falling downwards in a vertical lattice potential [67]. The corresponding confirmation of Bloch oscillations in a solid state system happened only five years earlier in a semiconductor superlattice [68]. Further experiments with one-dimensional lattices also established Wannier-Stark ladders [69] and Landau Zener tunneling [70]. Of large interest in solid state physics are Josephson junctions [112] which are widely discussed as qubits for quantum information processing. Also this can be imprinted on cold atom physics with the help of optical lattices [113].

A major breakthrough constitutes the experimental realization of a Mott-Insulator [71, 72] with a Bose-Einstein condensate confined in a three-dimensional optical lattice. Up to now there exists no analogous finding in a solid state system. The theoretical description of bosonic atoms in optical lattices is usually done with the Bose-Hubbard model [73]. The investigation of strongly correlated atomic systems is just at a start and much insight into theoretical intractable problems can be expected [74]. Another famous model in solid state physics is the Spin-Boson model [75], which describes the coupling of a pseudo-spin to a bosonic bath. This coupling induces a dissipation on

the spin depending on the properties of the bath. Also this model can be translated, as in the case of the Bose-Hubbard model, into cold atom physics [76, 77]. Such an implementation requires in principle not the periodicity of an optical lattice, but systems of lower dimensionality, which are best doable with them. The investigation of such quantum dissipative systems is a major goal of the experimental setup described in this thesis and will be discussed in more detail in chapter 6.2.1.

There exists also another way to do solid state physics with ultracold atoms. Quantum degenerate Fermi gases [114, 115, 116] are an ideal system to study high temperature superconductivity. The superfluidity of a Bardeen-Cooper-Schrieffer state of strongly interacting Fermions at only a tenth of the Fermi temperature has been shown by monitoring quantized vortices [117].

1.2 Rydberg matter

Joseph von Fraunhofer discovered in 1814 in the spectrum of the sun light distinct dark lines, which was the first indication for a discretization of the energy levels in atoms [118]. About half a century later Gustav Kirchhoff and Robert Bunsen noticed that all elements exhibit characteristic spectral properties [119]. They actually also discovered the element Rubidium by doing spectroscopy on mineral water from Bad Dürkheim (Rheinland Pfalz). Johannes Rydberg established then in 1888 an empirical equation, which described the wavelengths of the spectral lines of a Hydrogen atom [120]. But it was not until the discovery of quantum mechanics, that a full understanding of the spectral properties were possible [121].

Rydberg atoms are excited atoms with one or more electrons that have a very high principal quantum number [78]. First experimental investigations of Rydberg atoms were only possible in plasmas or by astronomical observations, where they arise from ion-electron recombination [79]. The invention of lasers made it eventually possible to excite atoms into a specific state. The properties of Rydberg atoms where examined in the following years in a broad manner [80], but until a decade ago only in room temperature vapor cells or atomic beams. The development of laser cooling [81, 82, 83] provided at once atomic samples in the μK regime. The combination of both techniques founded the research field of frozen Rydberg gases [84, 85]. The name reflects the fact, that during the time-scales of the conducted experiments or the excited state lifetime of the Rydberg states, the atoms are only minimally displaced by thermal motion. This allows a much more sensitive investigation of the interactions among the atoms. This can be the dipole-dipole interaction or the van-der-Waals interaction, which can be quite large due to the large polarizability of Rydberg states. Such an interaction can induce a blockade effect for excitation of close by atoms, which has been studied by several groups [86, 87, 88, 89, 90]. This nonlinearity of the dipole blockade effect was proposed to be used as a c-NOT gate for quantum information processing [91].

The advancement of Rydberg research to ultra-cold and also much denser samples of gases expanded the parameter range for researchers by several orders of magnitude and opened by this many new opportunities. A logical consequence is the next step towards even colder and denser samples, the Bose-Einstein condensates. The control over the internal and external states of Bose condensed samples expands the possibilities to a large variety of novel experiments. This is the other main route of the experimental setup described in this thesis and more details on planned experiments can be found in chapter 6.2.2.

1.3 This thesis

In this thesis I present the realization of an experimental setup for up-to-date research on degenerate quantum gases. The performance of the assembly with all its components was tested carefully and first experimental results on Bose-Einstein condensates were achieved. The presetting for this project was to create a setup, which is as versatile as possible, but avoids any disturbance for an efficient performance of BEC production. By including components for electric field generation and specialized charged particle detectors is this vacuum chamber in combination with degenerate quantum gases a unique tool for the experimental investigation of ultra-cold Rydberg matter. Just as well innovative is the effort to explore the physics of the Spin-Boson model, which will be a major advancement for a better understanding of decoherence in many systems.

In chapter 1 I recapitulate the research field of quantum degenerate gases and show in which manner this project will contribute. The required theoretical tools for laser cooling, Bose-Einstein condensation, manipulation of matter waves and and the basic properties of Rydberg atoms are reviewed in chapter 2. Chapter 3 deals then with the whole experimental setup and characterizes the system performance starting from the thermal gas in the oven step by step till the generation of Bose-Einstein condensates. With this chapter is the basic operation of the system demonstrated and I present in chapter 5 three experiments, which are important foundations for both planned projects. Chapter 4 presents a proposal to measure the effects of light induced dipole potentials in momentum space. The thesis closes with chapter 6, which summarizes the work done and gives an detailed description and working plan for the intended experiments on Rydberg matter and the Spin-Boson model.

2 Theoretical foundations

The production of Bose-Einstein condensates (BEC) consists of many different experimental steps [122]. The interactions of the atoms with light fields, magnetic fields, radio-frequency fields or among themselves is used in each step in different combinations to cool down an atomic sample to quantum degeneracy. This chapter gives an outline of the required theoretical background for each type of interaction and its physical implementation. Almost all experimental steps exploit the interaction of atoms with electromagnetic fields. The basic theoretical description of atom light interaction and its extension to laser cooling methods is given in chapter 2.1. Magnetic fields are used to design conservative potentials, especially trap configurations as shown in chapter 2.2. The inherent limitations of laser cooling are bypassed by the evaporative cooling method (see chapter 2.3) which leads finally to quantum degeneracy. The basic properties of BECs and the influence of interactions among the atoms is discussed in chapter 2.4. Another way to generate conservative potentials besides magnetic fields is given by far off resonant dipole potentials (see chapter 2.5), which finds an applications in the generation of an optical lattice. Finally is an outline on the properties of Rydberg atoms given in chapter 2.6.

2.1 Atom-light interaction

For a simplified description of the the atom-light interaction we assume a two level system with a ground state $|g\rangle$ and an excited state $|e\rangle$ which are separated by an energy $\hbar\omega_0$. This two level system is exposed to a single mode light field with energy $\hbar\omega_L$. Furthermore is the atom coupled to all modes of the vacuum, which can be modeled by a damping Γ [123]. The following abbreviated treatment follows the articles [124, 125, 126]. The full Hamiltonian of this system is given by

$$H_{\text{ges}} = H_A + H_L + H_{AL} + H_{AV}. \tag{2.1}$$

The kinetic energy part of the atomic Hamiltonian $H_A = p^2/2m + \hbar\omega_0|e\rangle\langle e|$ is from now on treated classically. The Hamiltonian of the light field $H_L = \hbar\omega_L(a^\dagger a + 1/2)$ can be omitted by assuming a general classical light field $\vec{E} = \vec{\varepsilon}(\vec{r})E(\vec{r})\cos(\omega_L t - \phi(\vec{r}))$. The electric field component $\vec{E}$ of the light field is defined by the amplitude E, the polarization $\vec{\varepsilon}$ and the phase ϕ. The coupling between the atom and the light field is given then by $H_{AL} = -\vec{d}\cdot\vec{E} = -\frac{\hbar\omega_R}{2}(e^{i\omega_L t} + e^{-i\omega_L t})(|e\rangle\langle g| + |g\rangle\langle e|)$ where the Rabi-frequency $\omega_R = |\langle g|\vec{d}\cdot\vec{\varepsilon}|e\rangle|E_0/\hbar$ was introduced. The dipole matrix element $\vec{d}_{ge} = \langle g|\vec{r}|e\rangle$ is the overlap integral between the ground stated and the excited state and is proportional to the transition strength. The dipole moment is given by $\vec{d} = e\vec{r}$ and $\vec{\varepsilon}$ is the unit polarization vector. The damping Γ, given by the coupling H_{AV} of the atom to all modes of the vacuum, is inserted into the Liouville equation in the $|g\rangle = (0,1)$ and $|e\rangle = (1,0)$ basis

$$\dot{\rho} = \frac{i}{\hbar}[H,\rho] + \Gamma\hat{D}\rho \tag{2.2}$$

by the Lindblad superoperator $\hat{D}$ [127], also known as the decoherence superoperator or Dee-operator. The application of $\hat{D}$ on the density matrix ρ gives

$$\hat{D}\rho = \sigma_-\rho\sigma_+ - \frac{1}{2}(\sigma_+\sigma_-\rho + \rho\sigma_+\sigma_-) = \begin{pmatrix} -\rho_{ee} & -\frac{\rho_{eg}}{2} \\ -\frac{\rho_{ge}}{2} & +\rho_{gg} \end{pmatrix}, \tag{2.3}$$

where we used the raising and lowering matrices σ_+ and σ_- defined as

$$\sigma_+ = \begin{pmatrix} 0 & 1 \\ 0 & 0 \end{pmatrix} \quad \text{and} \quad \sigma_- = \begin{pmatrix} 0 & 0 \\ 1 & 0 \end{pmatrix}. \tag{2.4}$$

To eliminate the terms oscillating with ω_L the equations are transformed into a new basis as $\sigma_{ge} = \rho_{ge}e^{i\omega_L t}$, $\sigma_{eg} = \rho_{eg}e^{-i\omega_L t}$, $\sigma_{gg} = \rho_{gg}$ and $\sigma_{ee} = \rho_{ee}$. Further all terms with $2\omega_L$ are eliminated (rotating wave approximation) and one obtains as a result four coupled equations:

$$\begin{aligned} \dot{\sigma}_{ee} &= \frac{i\omega_R}{2}(\sigma_{eg} - \sigma_{ge}) - \Gamma\sigma_{ee} \\ \dot{\sigma}_{gg} &= -\frac{i\omega_R}{2}(\sigma_{eg} - \sigma_{ge}) + \Gamma\sigma_{ee} \\ \dot{\sigma}_{ge} &= -\frac{i\omega_R}{2}(\sigma_{ee} - \sigma_{gg}) - i\delta_L\sigma_{ge} - \frac{\Gamma}{2}\sigma_{ge} \\ \dot{\sigma}_{eg} &= \frac{i\omega_R}{2}(\sigma_{ee} - \sigma_{gg}) + i\delta_L\sigma_{eg} - \frac{\Gamma}{2}\sigma_{eg}. \end{aligned} \tag{2.5}$$

The time evolution of this equations are now dominated by the coupling ω_R and the laser detuning $\delta_L = \omega_L - \omega_0$. As a final step this system of differential equation can be reduced to three equations without loss of information by setting $u = (\sigma_{ge} - \sigma_{eg})/2$, $v = (\sigma_{ge} - \sigma_{eg})/2i$ and $w = (\sigma_{ee} + \sigma_{gg})/2$. These are the three components of a so called Bloch-vector $\vec{\beta} = (u, v, w)$ and the equations of motion are finally

$$\begin{aligned} \dot{u} &= \delta_L v - \frac{\Gamma}{2}u \\ \dot{v} &= -\delta_L u - \omega_R w - \frac{\Gamma}{2}v \\ \dot{w} &= \omega_R - \Gamma w - \frac{\Gamma}{2}. \end{aligned} \tag{2.6}$$

By setting $\vec{\Omega} = (\omega_R, 0, \delta_L)$ equations (2.6) can be rewritten as $\dot{\vec{\beta}} = \vec{\Omega} \times \vec{\beta}$ which is analogous to the motion of a spin in a magnetic field or a classical spinning top on which acts a torque. The Bloch-vector precesses around $\vec{\Omega}$ with the effective Rabi frequency

$$\Omega_{\text{eff}} = \sqrt{\omega_R^2 + \delta_L^2}. \tag{2.7}$$

Of interest is the steady state solution $\dot{\vec{\beta}}_{st} = 0$ since most experimental steps happen on a time scale long compared to the damping Γ.

$$\begin{aligned} u_{st} &= \frac{\delta_L}{\omega_R}\frac{s}{s+1} \\ v_{st} &= \frac{\Gamma}{\omega_R}\frac{s}{s+1} \\ w_{st} &= -\frac{1}{2}\frac{1}{s+1}. \end{aligned} \tag{2.8}$$

Here we introduced the saturation parameter s

$$s = \frac{\omega_R^2/2}{\delta_L^2 + \Gamma^2/4} = \frac{I/I_{\text{sat}}}{1 + 4\delta_l^2/\Gamma^2}, \tag{2.9}$$

where $I \sim E^2$ is the intensity of the applied light field and the saturation intensity is

$$I_{\text{sat}} = \frac{\hbar\omega_0^3\Gamma}{12\pi c^2} = \frac{\pi h c \Gamma}{3\lambda_0^3}. \tag{2.10}$$

The saturation intensity depends on the wavelength λ_0, respectively the frequency ω_0 of the transition and the lifetime Γ of the excited state. In steady state the most relevant result is the spontaneous scattering rate of photons $\Gamma_{\text{scatt}} = \frac{\Gamma}{2}\frac{s}{s+1}$ which is determined by the spontaneous decay rate Γ of the steady state excited state fraction. This inelastic scattering rate is directly connected to cooling or heating rates of atomic samples.

To extract the forces an atom experiences in the generalized light field $\vec{E} = \vec{\varepsilon}E(\vec{r})\cos(\omega_L t - \phi(\vec{r}))$ it is advantageous to use the Ehrenfest theorem $\vec{F} = m\langle\ddot{\vec{r}}\rangle = \langle\nabla(\vec{d}\cdot\vec{E})\rangle$. In steady state the time averaged force consists of two parts:

$$\vec{F} = \underbrace{-\hbar u_{st}\nabla\omega_R}_{\vec{F}_{\text{dip}}} \quad \underbrace{-\hbar\omega_R v_{st}\nabla\phi}_{\vec{F}_{\text{spont}}}. \tag{2.11}$$

The first term $\vec{F}_{\text{dip}}$ is the dipolar force, which is a conservative force and allows coherent manipulation of matter waves like e.g. diffraction in optical lattices [128]. The second term $\vec{F}_{\text{spont}}$ is the spontaneous force which is dissipative and can be used to heat or cool atomic samples [125].

2.1.1 Doppler-cooling

The second term in equation (2.11) can be used to slow down and therefore cool atoms. Let us assume an atom located within one laser beam which is set to be a plane wave with wave vector $\vec{k}_L$. The phase of the light field is then $\phi = \vec{k}_L \cdot \vec{r}$. The spontaneous force calculates to $\vec{F}_{\text{spont}} = \omega_R v_{st}\hbar\vec{k}_L = \frac{\Gamma}{2}\frac{s}{s+1}\hbar\vec{k}_L$ where the steady state values of equation (2.8) have been inserted. The atom absorbs photons from the laser beam and receives with each scattering process one photon recoil in the direction of the wave vector. After excitation the atom decays within in the lifetime Γ back into the ground state and receives a nondirectional momentum due to the emitted photon. The spatial symmetry of the radiation pattern of the spontaneous emission (see appendix D) entails that the center of mass of multiple recoils add up to zero. But there remains a random walk in momentum space which is equivalent to a heating process that only scales with the square

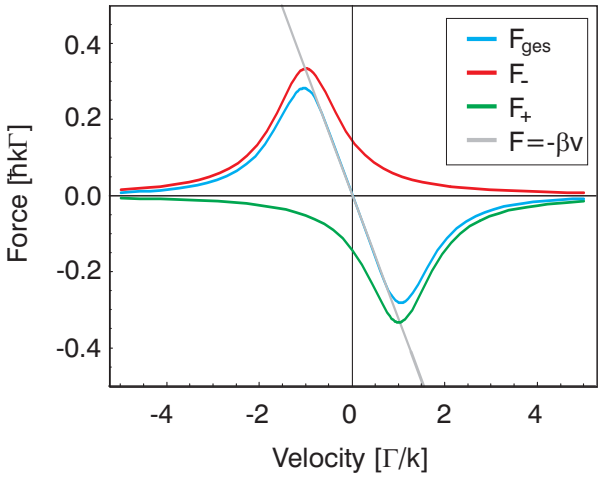

Figure 2.1: Spontaneous force on an atom in an one dimensional Doppler-cooling setup. The atom is irradiated by two counter-propagating laser beams denoted with +, respectively -. The red and green line represent the forces induced by each individual laser beam. The sum (blue line) of both forces can be approximated linearly (grey line) for small velocities.

root of scattered photons [125]. This heating can be modeled by a Brownian motion in momentum space.

In a next step one has to include the Doppler-shift of the atoms, which move with a certain velocity $\vec{v}$ relative to the propagation of the laser beam. The Doppler-shift $\vec{k}_L \cdot \vec{v}$ alters the resonance frequency of the atomic transition and with this the scattering rate. The first proposal to use the Doppler effect of the atoms and laser radiation for cooling dilute gases was already released in 1975 [129]. The idea consists of two parallel, but counter-propagating laser beams. The so called Doppler-cooling technique requires, that both laser frequencies are detuned to the red relative to the atomic resonance frequency. In one dimension the entire force on the atoms is then

$$\vec{F} = \hbar k_L \left(\frac{I/I_{\text{sat}}}{1 + I/I_{\text{sat}} + 4\left(\delta_L - \vec{k}_L \cdot \vec{v}\right)^2/\Gamma^2} - \frac{I/I_{\text{sat}}}{1 + I/I_{\text{sat}} + 4\left(\delta_L + \vec{k}_L \cdot \vec{v}\right)^2/\Gamma^2} \right). \tag{2.12}$$

For small velocities, namely $|kv| \ll \Gamma$, this force can be linearized and is equivalent to an ordinary friction term.

$$\vec{F} \approx \frac{-8\hbar k_L^2 \delta_L I/I_{\text{sat}}\, \vec{v}}{\Gamma(1 + I/I_{\text{sat}} + (2\delta_L/\Gamma)^2)^2} = -\beta \vec{v}. \tag{2.13}$$

The atoms motion is damped in this frictional environment which is commonly known as optical molasses [130].

The heating rate of the cloud by the momentum diffusion combined with the cooling rate results in an optimum steady state temperature at $\delta_L = -\Gamma/2$ [130]. The obtained temperature is the so called Doppler-temperature T_D. In one dimension it is given by

$$T_D = \frac{\hbar\Gamma}{2k_B} \tag{2.14}$$

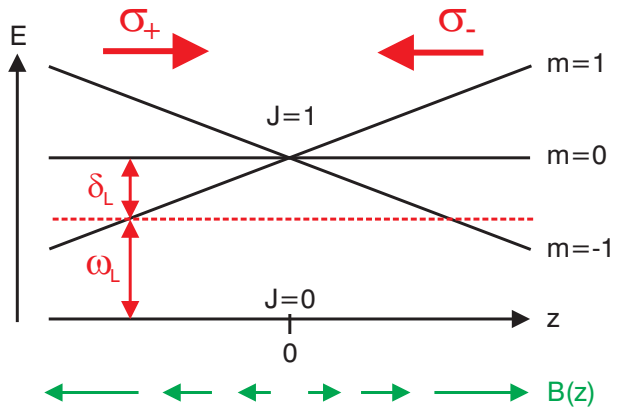

Figure 2.2: Principle of magneto-optical trapping of atomic clouds. Depicted are the Zeeman shifted energy levels (black lines) for a J=0→J=1 system. The strength and the direction of the magnetic field is indicated by the green arrows. If an atom is located to the left, with respect to zero magnetic field at z=0, it is shifted into resonance with respect to the laser beam coming in from the left and is pushed back to the center.

and is e.g. for Rubidium 146 μK [131].

2.1.2 Magneto-optical trapping

The Doppler-cooling mechanism described in the section before is unfortunately space invariant and can not be used to trap a sample of cold atoms in space. But by combining the spontaneous force with a spatial dependent magnetic field this becomes possible. Such a magneto-optical trap (MOT), consisting of three orthogonal pairs of counter propagating laser beams and a magnetic quadrupole field, was first demonstrated in 1987 [132]. The magnetic field shifts the atomic transition frequencies as $(g'_F m'_F - g_F m_F)\mu_B B$ where the primes denote the excited state, μ_B the Bohr magneton and B the magnetic field. It is the magnetic sublevels of the atoms and their differing Zeeman shifts, which make spatial dependent forces possible. The magnetic field is chosen to be a three dimensional quadrupole with a zero magnetic field at the center, which coincides with the center of the trap. The detuning δ_L is again negative and the polarizations have to be circular as shown in figure 2.2

To calculate the forces in a MOT equation (2.12) has to be expanded by the Zeeman term $\mu_{\text{eff}} B' z/\hbar$ where B' is the magnetic field gradient. The effective magnetic moment μ_{eff} is the median of the magnetic moment of all possible transitions and is $5/6\mu_B$ for the F=2 →F=3 transition in ^{87}Rb. The total force in one dimension is then

$$\vec{F} = \hbar k_L \left(\frac{I/I_{\text{sat}}}{1 + I/I_{\text{sat}} + 4\left(\frac{\delta_L - \vec{k}_L \cdot \vec{v} - \mu_{\text{eff}} B' z/\hbar}{\Gamma}\right)^2} - \frac{I/I_{\text{sat}}}{1 + I/I_{\text{sat}} + 4\left(\frac{\delta_L + \vec{k}_L \cdot \vec{v} + \mu_{\text{eff}} B' z/\hbar}{\Gamma}\right)^2} \right). \quad (2.15)$$

This force can also be linearized for small velocities and small distances and yields

$$\vec{F} \approx -\beta \vec{v} - \kappa \vec{r}. \quad (2.16)$$

The friction coefficient β is identical to the coefficient calculated for pure Doppler-cooling in section 2.1.1. The second term $\kappa\vec{r}$ adopts the form of a restoring force in a harmonic oscillator. Both forces together are equivalent to a damped harmonic oscillator. The spring constant calculates to $\kappa = \mu_{\text{eff}} B'\beta/\hbar k_L$. Starting from this equations several properties of the MOT can be calculated analytical as e.g. the density distribution, size, capture range and so on [132, 133]. These solutions are valid for noninteracting samples, hence samples with small atom numbers up to one million atoms. There exist several semi-empirical results on larger clouds up to 10^7 atoms [134, 135, 136, 137, 138, 139] but this is still a small atom number compared to our MOTs with well more than 10^{10} atoms. In this regime the properties of the cold cloud are dominated by the high optical density and radiation trapping effects which make a theoretical description up to now impossible.

2.1.3 Polarization gradient cooling

In experiments with small magneto-optical traps the measured temperatures are up to ten times smaller than the expected Doppler-temperature. The reason for this is the magnetic substructure of the atoms and optical pumping between these levels. This method is called polarization gradient cooling, optical molasses or Sysiphus cooling depending on the polarization properties of the laser beams and is discussed to quite some extend in [140, 130].

The physical situation in our experimental setup consists of three pairs of counter propagating laser beams with σ^+ and σ^- polarization respectively. The light creates a periodic potential which differs for the different magnetic substates. The atoms are preferentially pumped from one magnetic sublevel of one hyperfine state at a potential maximum into another magnetic sublevel within the same hyperfine state into a minimum of the potential. By this the atom climbs repeatedly uphill in the optical potential and looses by this kinetic energy.

We use the grey molasses scheme, where the detuning of the cycling laser is negative by some line widths with respect to resonance [141]. This limits multiple scattering effects by the reduced optical thickness. To ensure that all atoms within the cloud see the same potential, all magnetic fields have to be switched off. Furthermore additional coils are used to compensate the earth magnetic field, which already causes a disturbance for this cooling scheme. The temperature of an atomic cloud cooled in such a manner scales as $T \approx I/\delta_L$ [140, 130] and is ultimately limited by a single photon recoil, which corresponds for Rubidium to a temperature of 392 nK [131].

2.2 Magnetic trapping

The interaction of atoms with magnetic fields can be used to create conservative potentials, particulary traps, for cold atom clouds. The advantage of such traps is the absence of heating processes as found in MOTs (see chapter 2.1.2). To actually trap neutral particles one has to generate a local field minimum or a local field maximum. But the latter is forbidden by the Maxwell equations [142]. The magnetic dipoles interact with the field by the Zeeman-effect. For not too large magnetic fields, the energy shift of the atoms is linear with the magnetic field strength as

$$E = g_f m_F \mu_B |\vec{B}|. \tag{2.17}$$

If now the Zeeman energy for a magnetic sub-level of an atom increases with increasing magnetic field, they will feel a force towards the field minimum. Such states are commonly referred to as weak field seekers. At larger fields the hyperfine coupling is lifted and the energy shift can be

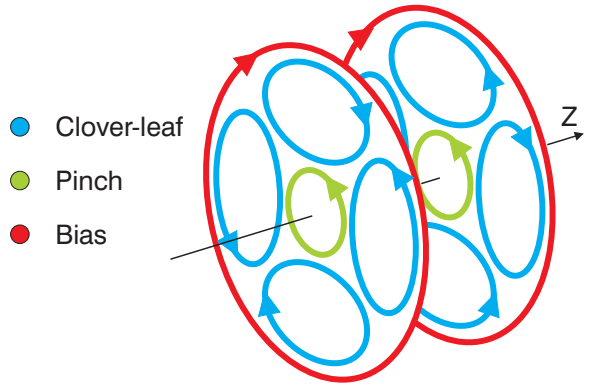

Figure 2.3: The cloverleaf magnetic trap. Two identical units are mounted on the opposite sides of the vacuum chamber to trap atoms in the geometric center of the setup. In each unit four gradient coils (blue) are aligned in one plane with two circular coils (green). By increasing the distance between the small pinch coils (green) along z, compared to a Helmholtz configuration, one achieves a curvature of the magnetic field in the center. To compensate the offset field, produced by the pinch coils one has to add two bias coils (red) in Helmholtz configuration. The arrows indicate the direction of the applied currents.

described with the Breit-Rabi equation [143] (see also Appendix B). In conventional experimental setups, the magnetic fields are generated by current carrying loops, which has the advantage that the trapping geometry can easily be changed in time.

As long the magnetic field varies slowly compared to the energy splitting between different magnetic sub-states, the orientation of the magnetic moment will follow the magnetic field adiabatically. A change in the magnetic field can be caused either by the motion of the atoms within the inhomogeneous field or by temporal change of the applied fields. This limitation can be expressed as

$$\omega_{\text{Larmor}} \gg \left| \frac{d}{dt} \left(\frac{\vec{B}(t)}{|\vec{B}(t)|} \right) \right|, \tag{2.18}$$

with the Larmor-frequency $\omega_{\text{Larmor}} = \mu B/\hbar$. If this constrain is violated the atoms can change their spin in a so called Majorana spin flip process [144, 145] and get transferred into other magnetic sublevels, likely non-trapped states.

2.2.1 Cloverleaf trap

There exist several methods to generate a minimum in a magnetic field distribution by current carrying coils. The simplest realization is an arrangement of two coils in anti-Helmholtz configuration which gives a three dimensional quadrupolar field [146]. This is also the field configuration needed for magneto-optical trapping. The spherical quadrupole trap can be used to store atoms, but is disadvantageous due to a point of zero magnetic field in the center. At this point the atoms can easily undergo Majorana spin flips and leave the trap. There are different designs for static magnetic traps with a non-zero magnetic field at its minimum. These are Ioffe-Pritchard type traps [147, 148], optically plugged Ioffe-Pritchard traps [7], top traps [149], baseball traps [150], quic traps [151], circular waveguides [152] and micro-structured planar z-traps [153].

A special version of a Ioffe Pritchard trap is a so called cloverleaf trap [154, 155]. The principal geometry of a cloverleaf trap is shown in figure 2.3 and the actual design as used in our experimental setup is shown in figure 3.9. The magnetic field generated by this configuration of coils can be approximated in second order to

$$\vec{B}(\vec{r}) = \begin{pmatrix} 0 \\ 0 \\ 1 \end{pmatrix} B_0 + \begin{pmatrix} x \\ -y \\ 0 \end{pmatrix} B' \begin{pmatrix} -xz \\ -yz \\ z^2 - \frac{1}{2}(x^2+y^2) \end{pmatrix} \frac{B''}{2}. \tag{2.19}$$

B_0 is the magnetic field offset, B' the field gradient and B'' the curvature. The potential seen by the atoms is given by $U = g_F m_F \mu_B |\vec{B}(\vec{r})|$, with

$$|\vec{B}(\vec{r})| = \sqrt{\left(B_0 + \frac{B''}{4}(2z^2 - x^2 - y^2)\right)^2 + \left(B'y + \frac{B''}{2}yz\right)^2 + \left(B'x + \frac{B''}{2}xz\right)^2}. \tag{2.20}$$

For small distances this potential can be expanded to second order

$$U_{\text{harm}} = g_F m_F \mu_B \left(B_0 + \frac{1}{2}\left(\frac{B'^2}{B_0} - \frac{B''}{2}\right)(x^2+y^2) + \frac{1}{2}B''z^2\right), \tag{2.21}$$

which represents a harmonic oscillator potential $U = \frac{1}{2}m\omega_\rho^2\rho^2 + \frac{1}{2}m\omega_z^2 z^2$. The oscillation frequencies exhibited by particles in such a potential are commonly referred to as trapping frequencies:

$$\begin{aligned} \omega_\rho &= \sqrt{\frac{g_F m_F \mu_B}{m}\left(\frac{B'^2}{B_0} - \frac{B''}{2}\right)} \\ \omega_z &= \sqrt{\frac{g_F m_F \mu_B}{m} B''}, \end{aligned} \tag{2.22}$$

where $\rho = \sqrt{x^2+y^2}$.

For larger temperatures or small offset fields the atomic cloud extends radially far into regions beyond the harmonic oscillator approximation and the trapping potential can be approximated linearly as

$$U_{\text{lin}} = g_F m_F \mu_B \left(B'\rho + \frac{1}{2}B''z^2\right). \tag{2.23}$$

The axial harmonic oscillator approximation is retained.

From interest are the density distributions and the peak densities in the different regimes. Generally the density distribution is given by $n(\vec{r}) = n_0 \exp(-U(\vec{r})/k_B T)$ with the peak density $n_0 = N/\int \exp(-U(\vec{r})/k_B T) d^3r$. Explicit expressions are given in the table 2.2.1.

The linear regime is separated by the harmonic one, when the cold cloud extends in the linear regime into a magnetic field comparable with the offset field as $\xi_\rho B' \approx B_0$, where ξ_ρ was defined in table 2.2.1. To calculate reliable peak densities in this intermediate regime one has to use a numerical integration algorithm. [1]

[1] Reliable results were produced with the Monte-Carlo Method from Mathematica (Wolfram Research).

	Harmonic regime	Linear regime
Radial width	$\sigma_\rho = \sqrt{\frac{k_B T}{g_F m_F \mu_B \left(\frac{B'^2}{B_0} - \frac{B''}{2}\right)}} = \frac{1}{\omega_\rho}\sqrt{\frac{k_B T}{m}}$	$\xi_\rho = \frac{k_B T}{g_F m_F \mu_B B'}$
Axial width	$\sigma_z = \sqrt{\frac{k_B T}{g_F m_F \mu_B B''}} = \frac{1}{\omega_z}\sqrt{\frac{k_B T}{m}}$	$\sigma_z = \sqrt{\frac{k_B T}{g_F m_F \mu_B B''}} = \frac{1}{\omega_z}\sqrt{\frac{k_B T}{m}}$
Density distribution	$n(\vec{r}) = n_0 \exp\left(-\frac{\rho^2}{2\sigma_\rho^2} - \frac{z^2}{2\sigma_z^2}\right)$	$n(\vec{r}) = n_0 \exp\left(-\frac{\rho}{\xi_\rho} - \frac{z^2}{2\sigma_z^2}\right)$
Peak density	$n_0 = \frac{N}{(2\pi)^{3/2}\sigma_\rho^2 \sigma_z}$	$n_0 = \frac{N}{\sqrt{8\pi}\xi_\rho^2 \sigma_z}$
Mean density	$\overline{n} = \frac{n_0}{2^{3/2}}$	$\overline{n} = \frac{n_0}{2^{5/2}}$

Table 2.1: *Properties of an atomic cloud confined in a magnetic trapping potential. The harmonic regime is described by an three-dimensional harmonic oscillator potential as given in equation (2.21). In the linear regime the axial potential remains harmonic, but is radially changed to a constant gradient potential $B'\rho$ as indicated by equation (2.23).*

The axial curvature B'' has also a contribution into the radial direction as can be seen in equation (2.20). At some point this part cancels out the curvature of the radial confinement and the atoms can get lost at these so called instability points. These points are given by solving $|\dot{B}(x,0,z)|/dx = 0$ and are located at

$$z_{inst} = \pm\left(\frac{B'}{B''} - \frac{B_0}{2B'}\right). \tag{2.24}$$

Another aspect of magnetic trapping is the influence of gravity. The atoms get dragged down in a harmonic trap by the gravitational force as $\rho_{sag} = 2g/\omega_\rho^2$, with $g = 9.81\mathrm{m/s}^2$ being the acceleration due to gravity. In a purely linear trap, the field gradient has to be larger than $\frac{mg}{m_F g_f \mu_B}$ to keep the atoms trapped.

In the experimental procedure of BEC-production different trapping field geometries are needed. The cold atomic cloud, which was prepared by laser-cooling methods as described above, has to be transferred into a suitable magnetic trap. This means during transfer the loss in temperature, density and atom-number should be minimized. The density distribution of the cold cloud after molasses cooling is in a good approximation Gaussian in all three directions. The parameters B_0, B' and B'' have to be adjusted such, that for the given temperature the widths σ_i of the trapped cloud match. With an increasing size of the molasses cooled cloud the curvatures of the magnetic field potential have to be reduced more and more. This can be done axially only by reducing the currents in the Pinch-coils. Radially one can either reduce the currents in the clover-leaf coils or increase the offset field via the current in the Bias coils. This procedure causes several problems. A reduction of the currents comes along with a reduced trap depth and hotter atoms will be lost from the trap. Another problem is the nearly isotropic shape of the laser-cooled cloud. If the radial and axial curvature converge to the same value, then the instability points migrate towards the trapping center and even less atoms can be trapped. It is even impossible to generate an isotropic trapping potential with Ioffe-Pritchard type traps [155]. The last complicacy is the increased gravitational sag. This can be handled either by shifting the magneto-optical trap downwards with an additional gradient field along the direction of gravity to the new minimum position of the catching potential or by shifting the magnetic trap minimum upwards by an constant magnetic field along gravity. The latter is harder to do, since the fields in the catching trap are larger than in a magneto-optical trap.

After the atoms were successfully transferred into a mode-matched trap, the density of the cloud has to be increased. This increases the elastic collision rate, which is necessary for efficient evaporative cooling. The confinement of the trap is done adiabatically, which causes also a rise of the temperature as

$$T_{\mathrm{lin}} = \left(\frac{\pi}{e} \frac{g_F m_F \mu_B}{k_B} B_{0,\mathrm{harm}} \frac{B'^2_{\mathrm{lin}} \sqrt{B''_{\mathrm{lin}}}}{B'^2_{\mathrm{harm}} \sqrt{B''_{\mathrm{harm}}}} \right)^{1/4} T^{3/4}_{\mathrm{harm}}. \tag{2.25}$$

The trap geometry changes during compression from a three dimensional harmonic (harm) oscillator to a radially linear (lin) trap. Although this compression is done adiabatically the phase space density is increased by Euler's constant e, which is caused by the different geometries of the traps.

The increased density allows now for efficient evaporative cooling. The peak density in the linear case scales as $n_0 \sim T^{-5/2}$ whereas in the harmonic trap only as $n_0 \sim T^{-3/2}$. But sometimes it is advantageous to reduce the confinement during evaporation, to avoid density dependent inelastic three body collisions as described in chapter 2.4.

2.3 Evaporative cooling

Laser cooling has its limits in temperature and density as discussed in chapter 2.1.3. There exists up to day no concept to reach quantum degeneracy by pure optical cooling techniques, therefore a different kind of cooling method is needed[2]. The principle of the forced evaporative cooling method is to remove above average hot atoms from the atomic cloud and let the remaining atoms rethermalize [157]. By the truncation of the hottest atoms of a Maxwell-Boltzmann distribution, the remaining atoms reside in a non-equilibrium situation. If the energy of the remaining atoms is redistributed along all atoms according to a Maxwell-Boltzmann distribution, is the temperature reduced. Essential for this thermalization process are collisions between the atoms. It takes only about five collisions per atom to find the cold cloud again in thermal equilibrium, after the hot atoms were removed [158]. The elastic scattering rate is given by $\Gamma_{\mathrm{scatt}} = n\sigma v$. Although the velocity drops with falling temperature, does the scattering rate increase with proceeding evaporation, due to the larger gain in density. This regime is called runaway evaporation. The time needed to reach quantum degeneracy is limited by the losses of atoms due to background collisions, namely the trap lifetime.

To quantify the performance of an experimentally conducted evaporative cooling step it is common to express it as the gain in temperature or phase space density with respect to the lost atoms. The efficiency α of the evaporative process is expressed in temperature gain per atom loss

$$\alpha = \frac{d(\ln T)}{d(\ln N)} = \frac{\dot{T}/T}{\dot{N}/N} \tag{2.26}$$

and the efficiency ξ is the gain in phase space density (psd) per atom loss

$$\xi = \frac{d(\ln \mathrm{psd})}{d(\ln N)} = \frac{\dot{\mathrm{psd}}/\mathrm{psd}}{\dot{N}/N} \ . \tag{2.27}$$

[2] The evaporation to quantum degeneracy in a purely optical dipole trap [156] is sometimes referred to as an all optical method.

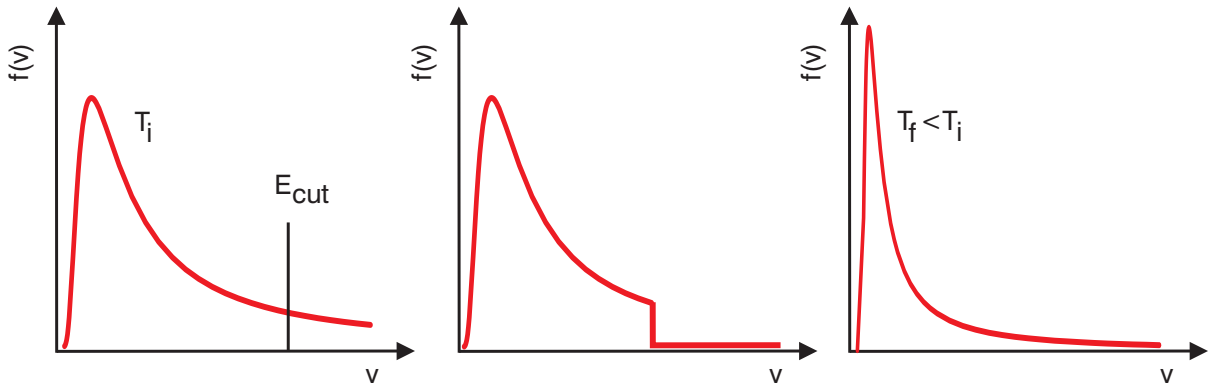

Figure 2.4: Schematic sequence of the evaporative cooling technique. From an sample with a Maxwell-Boltzmann distribution $f(v) = \sqrt{\frac{2}{\pi}}\left(\frac{m}{k_B T}\right)^{3/2} v^2 \exp\left(\frac{-mv^2}{2k_B T}\right)$ and a temperature T_i the hottest atoms ($T > E_{\mathrm{cut}}/k_B$) are removed. The remaining atoms are not anymore in thermal equilibrium. After some collisions the cloud follows again a Maxwell-Boltzmann distribution, but at lower temperature T_f.

The truncation parameter η gives the ratio of the temperature of the cold cloud and the cutoff energy.

$$\eta = \frac{E_{\mathrm{cut}}}{k_B T} \,. \tag{2.28}$$

The removal of the hottest atoms can be either done by lowering the trap depth, as it is done in dipole traps [156], or by addressing them with radio-frequency fields. The first method has the disadvantage that with the reduction of the trap depth, usually also the confinement is reduced and by this the elastic scattering rate. This is for magnetically trapped particles not the method of choice, since evaporation can be accomplished at full confinement. In a magnetic trap the atoms are located in the minimum of a magnetic field. The hotter atoms extend in regions with higher magnetic fields and experience a larger Zeemann-shift which allows a spatial dependent resonance condition for the radio-frequency field. The rf-field transfers by a magnetic dipole transition the atoms into a non-trapped state and they get lost. This is only possible if the two states coupled by the rf-field have different Zeeman-shifts. In ^{87}Rb exist two different transitions to do so. The most common one is the transfer of the atoms within one hyperfine manifold into non-trapped magnetic sub-states by high-frequency-fields (HF). The other one is the transfer of the trapped atoms into an other non-trapped hyperfine state by microwave radiation (MW). The resonance condition for both methods is

$$(g_F' m_F' - g_F m_F)\mu_b |B(\vec{r})| = \hbar\omega_{rf} \,, \tag{2.29}$$

where g_F is the Landé factor and m_F the projection of the magnetic moment.

For a constant frequency ω_{rf} the atoms move through the region of resonance with a velocity v. The transition probability into a non-trapped state can be derived by using the Landau-Zener picture. The probability depends on the Landau-Zener parameter [159] which is valid for transitions within one hyperfine manifold

$$\Gamma_{\mathrm{LZ}} = \frac{\hbar\omega_R^2}{g_F \mu_B 2v(dB/dr)}. \tag{2.30}$$

with the Rabi frequency $\omega_R = g_F \mu_B B_{rf}/2\hbar$. B_{rf} is the amplitude of the magnetic field produced by the rf-field and dB/dr the gradient of the magnetic field at the position where the atoms are in resonance. A numerical calculation for Rubidium atoms [160] showed that for a Landau-Zener parameter more than 1 almost all atoms are transferred into non-trapped states.

2.4 Bose-Einstein condensation

As the forced evaporation cooling proceeds, the phase space density increases until the cold atomic cloud undergoes at a critical temperature a phase transition to a Bose-Einstein condensate. The existence of such a phase transition was already postulated in 1925 by Albert Einstein [98] based on an article of Satyendra Nath Bose [97]. A more extended derivation of the phase transition for a non interacting bosonic gas is given in [161]. The physics of Bose-Einstein condensates of dilute atomic gases is reviewed in [22, 162].

2.4.1 The non-interacting Bose gas

For a theoretical description of the phase transition from a thermal gas with Bose-statistics to a Bose-Einstein condensate we assume a non interacting Bose gas confined in a potential $U(\vec{r})$. To model its thermodynamic properties we assume a grand canonical ensemble, which allows the exchange of energy and particles with a reservoir [161]. The occupation number n_k of a state k at a given temperature T is given by the Bose-distribution

$$\langle n_k \rangle = \frac{1}{e^{(\epsilon_k - \mu)/k_B T} - 1}, \tag{2.31}$$

ϵ_k is the energy of a state k and μ the chemical potential. For high temperatures this distribution is equivalent to a Boltzmann-distribution of a classical gas. A given total atom number N fixes the chemical potential.

$$N = \sum_k \langle n_k \rangle. \tag{2.32}$$

As the temperature is reduced, the chemical potential approaches the ground state energy ϵ_0 of the potential and the ground state population $\langle n_0 \rangle$ becomes a macroscopic number N_0.

As a next step we want to calculate the number of atoms $N - N_0$ not occupying the ground state

$$N - N_0 = \sum_{k=1}^{\infty} \frac{1}{e^{(\epsilon_k - \mu)/k_B T} - 1} \approx \int_0^{\infty} \rho(\epsilon) \frac{1}{e^{(\epsilon - \mu)/k_B T} - 1} d\epsilon. \tag{2.33}$$

The sum over all states (except the ground state) can be approximated by an integral with a continuous density of states function $\rho(\epsilon)$. This is allowed as long the temperature is large compared to the level spacings. Since the density of states goes to zero for $\epsilon \to 0$ the error made by starting the integral from zero is negligible. The density of states is given by

$$\begin{aligned}\rho(\epsilon) &= \frac{1}{(2\pi\hbar)^3}\int_{-\infty}^{\infty}\int_{-\infty}^{\infty}\delta\left(\epsilon - U(\vec{r}) - \frac{p^2}{2m}\right)d^3r\,d^3p \\ &= \frac{2\pi(2m)^{3/2}}{(2\pi\hbar)^3}\int_{U<\epsilon}\sqrt{\epsilon - U(\vec{r})}\,d^3r.\end{aligned} \tag{2.34}$$

For temperatures above the phase transition, the density distribution $n(\vec{r})$ can be calculated with the help of the normalization $N = \int n(\vec{r})d^3r$

$$n(\vec{r})d^3r = \frac{1}{\lambda_{dB}^3}g_{3/2}\left(e^{(\mu - U(\vec{r}))/k_BT}\right), \tag{2.35}$$

where the thermal deBroglie wavelength

$$\lambda_{dB} = \sqrt{\frac{2\pi\hbar^2}{mk_BT}} \tag{2.36}$$

was introduced. The poly-logarithmic function is defined as $g_\alpha(x) = \sum_{j=1}^{\infty} x^j/j^\alpha$ [163]. For any trapping potential reaches the poly-logarithmic function a critical value, if $x \to 1$, which is equivalent with a chemical potential that approaches 0. If the phase space density (psd) reaches this point the phase transition to the Bose-Einstein condensate occurs:

$$\text{psd} = \max\left(n(\vec{r})\right)\lambda_{dB}^3 = g_{3/2}(1) = 2.612... \tag{2.37}$$

In a three dimensional harmonic oscillator potential $U(\vec{r}) = \frac{m}{2}(\omega_x^2x^2 + \omega_y^2y^2 + \omega_z^2z^2)$ the density of states is given by $\rho(\epsilon) = \frac{1}{2(\hbar\overline{\omega})^3}\epsilon^2$. The mean trapping frequency is given by $\overline{\omega} = (\omega_x\omega_y\omega_z)^{1/3}$. The fraction of atoms $N - N_0$ remaining in an arbitrary excited state evaluates to

$$N - N_0 = g_3(1)\left(\frac{k_BT}{\hbar\overline{\omega}}\right)^3. \tag{2.38}$$

At the phase transition the ground state fraction can be set to zero ($N_0 = 0$) and the critical temperature in an harmonic oscillator is

$$T_c = \frac{\hbar\overline{\omega}}{k_B}\left(\frac{N}{g_3(1)}\right)^{1/3}. \tag{2.39}$$

With this we can give an expression for the fraction of atoms in the condensed state

$$\frac{N_0}{N} = 1 - \left(\frac{T}{T_c}\right)^3. \tag{2.40}$$

The above treatment of the phase transition is only valid for large atom numbers $N \to \infty$. For a finite atom number one can not assign a definite critical temperature to the system. The initial transition point is softened in a region around T_c. Theoretical and experimental studies of the finite size effects can be found in [22, 164, 165].

2.4.2 The interacting Bose gas

Until now the interaction among the atoms was omitted, which shall now be included. It is sufficient for dilute Bose gases at very low temperatures to model the interaction by pairwise elastic scattering events. The scattering potential can be described by a pseudo potential [22]

$$V(\vec{r}-\vec{r}') = g\delta(\vec{r}-\vec{r}'), \tag{2.41}$$

with the interaction parameter $g = 4\pi\hbar^2 a/m$ and the s-wave scattering length a. The temperature in Bose condensed gases is typically so low, that higher partial waves of the scattering amplitude can be neglected [166]. The atoms in a Bose-Einstein condensate happen to be all in the same internal as well external quantum state and the condensate fraction can be described with a macroscopic wave-function $\phi(\vec{r})$. This mean field approach results finally the so called Gross-Pitaevskii equation which is a nonlinear Schroedinger equation.

$$\left(-\frac{\hbar^2\nabla^2}{2m} + U(\vec{r}) + g|\phi(\vec{r})|^2\right)\phi(\vec{r}) = \mu\phi(\vec{r}). \tag{2.42}$$

At very low temperatures or high densities the kinetic term in equation (2.42) can be neglected. With this so called Thomas-Fermi approximation the solution is algebraic and the density distribution calculates to

$$n(\vec{r}) = |\phi(\vec{r})|^2 = \frac{1}{g}\left(\mu - U(\vec{r})\right). \tag{2.43}$$

In a harmonic oscillator potential the density distribution adopts a parabolic shape. The extension of the condensate is given in this case by the Thomas-Fermi radius r_{TF}, which can be calculated by setting $\mu - U(\vec{r}) = 0$:

$$r_{\mathrm{TF},i}^2 = \frac{2\mu}{m\omega_i^2}. \tag{2.44}$$

By using the normalization $N = \int n(\vec{r})d^3r$ for the given atom number N one can also calculate the chemical potential as [162]

$$\mu = \frac{15^{2/5}}{2}\left(\frac{Na}{\bar{a}_{ho}}\right)^{2/5}\hbar\overline{\omega} = \frac{15^{2/5}}{2}(\overline{\omega}^3\sqrt{m}\hbar^2 aN)^{2/5}, \tag{2.45}$$

where we used the width a_{ho} of the harmonic oscillator ground state eigen-function, given by

$$a_{ho,i} = \sqrt{\hbar/(m\omega_i)}. \tag{2.46}$$

The bars indicate the geometric mean for the trapping frequencies defined as $\overline{\omega} = (\omega_x \cdot \omega_y \cdot \omega_z)^{1/3}$ and is analogous given for the harmonic oscillator ground state. Finally one can calculate the peak density of the interacting condensate wave function

$$n_0 = \frac{\overline{\omega}m}{8\pi\hbar a}\left(\frac{15Na}{\bar{a}_{ho}}\right)^{2/5}. \tag{2.47}$$

With the equations given in this chapter it is now possible to characterize quantitativly all physical properties of the condensate fraction and will find their usage in chapter 3.11.

2.4.3 Collisional processes

We have seen that the dominant collisional process in a Bose-Einstein condensate is elastic the s-wave scattering and the corresponding scattering rate is given by

$$\Gamma_{elastic} = n\langle v\rangle\sigma_0, \tag{2.48}$$

where $\langle v\rangle$ is the mean velocity in the center of mass frame of the two colliding particles and n is the mean density. For identical bosons is the total scattering cross section given by $8\pi a^2$ with a being the s-wave scattering length. For distinguishable particles is the total scattering cross section reduced by a factor two to $4\pi a^2$.At such cold temperatures as found in Bose-Einstein condensates it is fair to omit the corrections to the scattering cross section for higher temperatures.

Beyond this elastic scattering events, there exist also inelastic two body processes, by which the internal state of the atoms is changed and they may be lost from the trap. The first one is a spin exchange collision between two atoms. In this process the total magnetic moment of the two particles $m_{tot} = m_1 + m_2$ is redistributed within the the two particles. However the total magnetic moment has to be conserved. The spin exchange collisions rate scales with the third power of the total magnetic moment [167]. But if all the trapped atoms are in the same stretched state as e.g. $F = 2, m_F = 2$, which is the case for our trapped sample of atoms, this collision will not occur since there exists no other combination of magnetic moments which conserves the total moment.

The second inelastic two body scattering process is the dipolar relaxation. In this case the atoms transfer during the scatterung event angular momentum, given by the kinetic energy, into the internal state. This process scales with the velocity of the atoms and can also be neglected for very small temperatures.

One inelastic process, which can not be neglected is the inelastic three body decay. Here are three particles involved, where two of them create a molecular state and the third atom takes away the excess energy of the bound state. This process determines the lifetime of Bose-Einstein condensates, if other heating processes are absent. The decay rate can be calculated by

$$\frac{dN}{dt} = -L\int Nn^2(\vec{r})d^3r, \tag{2.49}$$

where L is the rate constant for inelastic three body collisions [168, 169].

2.5 Dipole potentials

Atoms can not only be stored in magnetic traps but also in dipole potentials made of light [170, 171, 172, 173]. The dipole force arises from the dispersive part of the atom light interaction (see chapter 2.1) in a light field with an intensity gradient. The resultant conservative potential U_{dip} is given by the shifted energy levels of a two-state atom dressed with the light field $I(\vec{r})$ and can be approximated for large detunings and small saturation parameters as

$$U_{\text{dip}}(\vec{r}) = -\frac{3\pi c^2}{2\omega_0^3}\left(\frac{\Gamma}{\omega_0-\omega_L}+\frac{\Gamma}{\omega_0+\omega_L}\right)I(\vec{r}). \tag{2.50}$$

The frequency of the light field is ω_L, and the resonance frequency of the atom is ω_0. Γ is the natural linewidth of the transition. Although the dispersive part of the atom light interaction

is conservative remains in the presence of a light field always a contribution of the spontaneous scattering rate Γ_{sc} which is given by

$$\Gamma_{sc} = \frac{3\pi c^2}{2\hbar\omega_0^3}\left(\frac{\omega_L}{\omega_0}\right)^3\left(\frac{\Gamma}{\omega_0-\omega_L}+\frac{\Gamma}{\omega_0+\omega_L}\right)^2 I(\vec{r}). \tag{2.51}$$

Advantageous is that the scattering rate drops quadratically with the detuning $\delta = \omega_0 - \omega_L$ where as the potential depth only drops linearly. This allows one to generate potentials at a large enough detuning which can trap atoms without suffering heating or optical pumping by spontaneous scattering events. For detunings relatively close to resonance equations (2.50) and (2.51) can be simplified in a rotating wave approximation by dropping the counter-rotating (second) term. A detailed treatment for multi-level atoms is given in Appendix E.

If the detuning δ is negative (red detuned) the atoms experience a force towards higher intensity. For $\delta > 0$ (blue detuned) the situation is vice versa and the atoms move to regions of lower intensity. Let us assume a focused Gaussian beam, which has a maximum intensity at its geometric center. In the case of red detuning the atoms are attracted towards the focus of the beam and can by this be trapped. The intensity distribution of Gaussian beam propagating along z is given by

$$I(\vec{r}) = \frac{2P_0}{\pi w_x(z) w_y(z)}\exp\left(-\frac{2x^2}{w_x(z)}\right)\exp\left(-\frac{2y^2}{w_y(z)}\right). \tag{2.52}$$

The total light power in the laser beam is given by P_0. The functions $w_x(z)$ and $w_y(z)$ describe the radial extension of the beam while it propagates along z and are given by

$$w_{x,y}(z) = w_{x,y}^0\sqrt{1+\left(\frac{\lambda_L z}{\pi w_{x,y}^0}\right)^2}. \tag{2.53}$$

The radius of a Gaussian beam is defined by the length at which the intensity drops to $1/e^2$. The radii $w_{x,y}^0$ are the extensions of the beam at the position of the focus and λ_L is the wavelength of the laser. The distance from the focus to the point at which the beam waist expands by a factor of $\sqrt{2}$ is called the Rayleigh-range

$$z_R = \frac{\pi {w_{x,y}^0}^2}{\lambda_L}. \tag{2.54}$$

If the trapped cloud is small compared to the radii, the intensity distribution can be expanded quadratically by

$$I_{\text{harm}}(\vec{r}) = \frac{2P_0}{\pi w_\rho^{0^2}}\left(1-\frac{\lambda^2}{\pi^2 w_\rho^{0^4}}z^2-\frac{4}{w_\rho^{0^2}}\rho^2\right), \tag{2.55}$$

where we assumed a spherical beam with $w_x(z) = w_y(z) = w_\rho(z)$.

One can easily extract from this intensity distribution the trapping frequencies in rotating wave approximation as

$$\begin{aligned} \omega_z &= \sqrt{\frac{6c^2\Gamma P_0\lambda_L^2}{\omega_0^3\delta\pi^2 w_\rho^{0^6} m}} \\ \omega_\rho &= \sqrt{\frac{24c^2\Gamma P_0}{\omega_0^3\delta w_\rho^{0^4} m}} \end{aligned} . \tag{2.56}$$

With these trapping frequencies all properties of a trapped cold cloud or a Bose-Einstein condensate [174] can be extracted with the methods described in chapter 2.2 and 2.4.

2.5.1 Optical lattices

An optical lattice is a periodic potential that is formed due to interference of two or more laser beams [175, 74]. Depending on their polarizations, directions and intensity distributions a large variety of optical potentials can be generated. The simplest case emerges if a linear polarized laser beam is retro-reflected into itself. By this a cosine shaped intensity distribution arises along the direction of the k-vector of the laser beams. The intensity distribution of such an optical lattice is radially still Gaussian in shape as in the case of an ordinary single beam dipole trap. The associated potential for a constant intensity distribution of both beams is

$$U_{\text{lat}} = 4U_{\text{dip}}\cos^2(kz). \tag{2.57}$$

The potential U_{dip} is the potential of a single laser beam and can be calculated with the methods presented in the section before. The factor 4 in the lattice potential U_{lat} arises from the interference of the electric field components. $k = 2\pi/\lambda$ is the wave-number of the laser and z is the axis of propagation.

To explore the dynamics of an atom in such an optical lattice potential it is beneficial to calculate first the eigen-energies. This is done by solving the time independent Schroedinger equation

$$\left(\frac{\hbar^2}{2m}\frac{d^2}{dz^2} + U_0\cos^2(kz)\right)\psi = E\psi, \tag{2.58}$$

with $U_0 = 4U_{dip}$. This Schrödinger equation is now rescaled with $\zeta = kz$, $q = U_0/4E_r$ and $a = \frac{E}{E_r} - \frac{U_0}{2E_r}$, where E_r is the recoil energy of one photon, to obtain the form of the well known Mathieu differential equation [163]:

$$\frac{d^2}{d\zeta^2} + (a - 2q\cos(2\zeta))\psi = 0 \tag{2.59}$$

The solutions to the Mathieu differential equation are given by the Mathieu functions which can be looked up in [163]. As consequence the eigen-energies of the optical lattice system appear only in bands separated by band gaps as commonly found in solid-state systems [176].

With the knowledge of the time independent solution of the Schrödinger equation it is straightforward to calculate the dynamics of a particle in an optical lattice as long the quantum state is known at a certain time. Let us assume an atom with an external state wave-function ψ which is suddenly superimposed by an optical lattice with a depth U_0. At time $t = 0$ the optical lattice is switched on and the wave function of the formerly free particle has to be projected in the new basis set of Bloch-states $|n, \wp\rangle$, the eigen-states of the optical lattice as

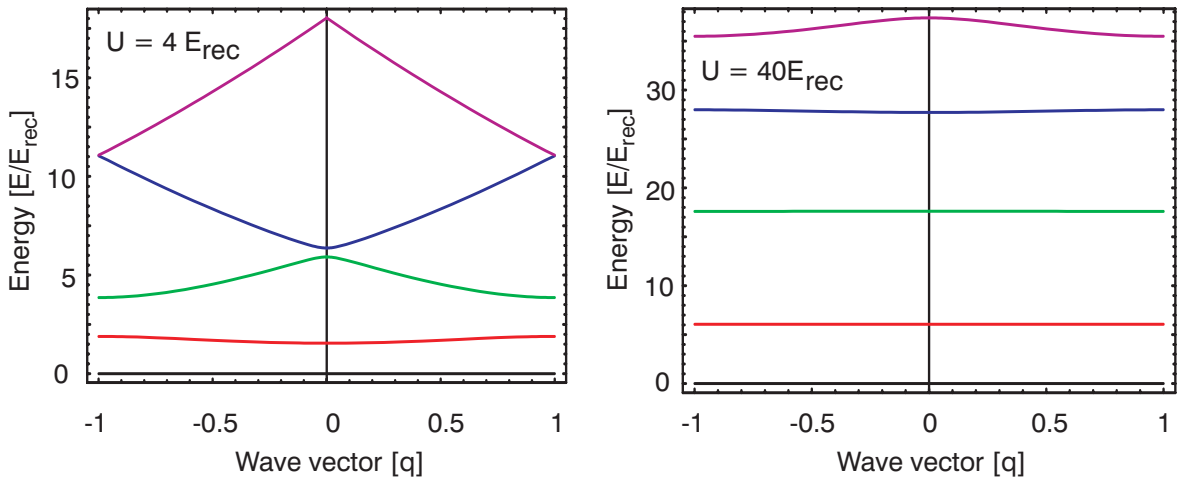

Figure 2.5: Dispersion relation of a particle in an optical lattice. Depicted are the allowed Eigen-energies for a given quasi-momentum q. The left figure is calculated for a lattice depth of $U = 4E_{\mathrm{rec}}$ and the right for $U = 40E_{\mathrm{rec}}$. The left figure resembles still the unperturbed parabolic dispersion relation for a free particle. On the right the bands are nearly flat for small band indices. For very deep potentials the band structure approaches that of a harmonic oscillator.

$$|\psi(t=0)\rangle = \sum_{n=0}^{\infty} |n, \wp\rangle\langle n, \wp|\psi(t=0)\rangle. \tag{2.60}$$

The Bloch states are characterized by a band index n and the quasi-momentum in the lattice $\wp$. With the eigen-energies $E_n(\wp)$ the evolution of the wave function is given by

$$|\psi(t)\rangle = \sum_{n=0}^{\infty} \langle n, \wp|\psi(t=0)\rangle e^{-iE_n(\wp)t/\hbar}|n, \wp\rangle. \tag{2.61}$$

After a certain time τ the lattice is switched off again. The wave function $|\psi(t)\rangle$ has now to be projected into the basis set of plane waves, since the detection of the atoms happens in momentum space (see chapter 3.3). The resulting wave function is then

$$|\psi(\tau) = \sum_{-\infty}^{\infty} b_{\wp}(n)|2n\hbar k_{\mathrm{latt}}\rangle, \tag{2.62}$$

with the coefficients

$$b_{\wp}(m) = \sum_{n=0}^{\infty} \langle n, \wp|\psi(t=0)\rangle\langle 2m\hbar k_{latt}|n, \wp\rangle e^{-iE_n(\wp)\tau/\hbar}. \tag{2.63}$$

The coefficients $b_{\wp}(n)$ are the probability amplitudes to find a population in the m-th diffraction order. If the particle was initially at rest it is sufficient to use a reduced momentum spectrum with $2n\hbar k_{\mathrm{latt}}$ for integer n, since by symmetry only this momenta occur.

For very small interaction times the whole problem reduces to the diffraction of a plane wave at a thin phase-grating [177, 178]. In this so called Raman-Nath regime does the density distribution not change during the interaction time but the particle wave function accumulates a space dependent phase. The Raman-Nath approximation is valid, as long the interaction time is well shorter than the oscillation period T of the harmonically approximated optical lattice potential and is given by

$$T = \frac{1}{2\pi}\sqrt{\frac{m}{U_0 k_{latt}^2}}. \tag{2.64}$$

The acquired phase is proportional to the applied intensity times the interaction time and with this the wave function evolves like

$$|\psi(t)\rangle = |\psi(0)\rangle e^{iU_{latt}(\vec{r})t/\hbar}. \tag{2.65}$$

The free evolution after the interaction time τ during the time of flight phase is the determined by the gradients of the accumulated phase. The probability to find a population in the n-th momentum state is then easily obtained by a Fourier transformation of equation 2.65 and yields

$$p(n) = \left| J_n\left(\frac{U_0}{4E_{\mathrm{rec}}}\tau\right)\right|^2, \tag{2.66}$$

where the J_n are Bessel functions of the first kind.

The results derived above are not only valid for a single particle but to some extend also for Bose-Einstein condensates. The spatial extension of a BEC is typically well larger than the lattice constant and can therefore be assumed to be a planar wave. On the other hand is the interaction energy among the atoms in most cases much smaller than the depth of the optical lattice and by this is the dynamics determined by the lattice potential. An exception are very shallow optical lattices, where a modification of the dynamics due to interactions are expected [179, 180].

2.6 Rydberg atoms

This sections reviews the basic properties of Rydberg atoms. If one or several electrons in an atom are excited to a large quantum number n one speaks of a Rydberg atom. The electron is now far separated from the core which leads to a reduced interaction with the nucleus and the remaining electrons. The energy level of the excited electron is very close to the vacuum level and therefore only weakly bound. Such an almost free electron reacts very sensitive to electric fields. The electron orbital can be easily deformed if an external electric field is applied and leads to an enhanced polarizibility of Rydberg states. The large polarizability entails a strong van der Waals interaction among the Rydberg atoms, as well large dipole moments. A strong dipole-dipole interaction, which is in its nature long range and anisotropic, is from special interest for further investigations. The interactions of ultracold atomic samples are typically dominated by the short range, isotropic and much weaker s-wave scattering length. The dipole-dipole interaction among Rydbgerg atoms is even discussed as a tool for quantum computing [91]. One further aspect of Rydberg atoms, among many others [78], is the long excited state lifetime. For Rydberg states with a principle quantum number of n=40 is the lifetime already three orders of magnitude larger compared to the excited states used for laser cooling.

State	n $^2S_{1/2}$	n $^2P_{1/2}$	n $^2P_{3/2}$	n $^2D_{3/2}$	n $^2D_{5/2}$	n ^2F_J
δ_0	3.131 180 4(10)	2.654 884 9(10)	2.641 673 7(10)	1.348 0917 1(40)	1.346 4657 2(30)	0.016 312
δ_2	0.178 4(6)	0.290 0(6)	0.295 0(7)	-0.602 86(26)	-0.596 00(18)	-0.064 007
δ_4	-1.8	-7.904 0	-0.974 95	-1.505 17	-1.505 17	-0.360 05
δ_6	-	116.437 3	14.600 1	-2.420 6	-2.420 6	3.239 0
δ_8	-	-405.907	-44.726 5	19.736	19.736	-
valid for n>	14	11	13	4	4	4
ΔE (mK)	± 0.5	± 3	±3	±3	±3	±10
E_i,cm^{-1}	33 690.798 9(5)	33 690.799(3)	33 690.797(3)	33 690.797 8(30)	33 690.797 8(30)	33 690.799 (10)
Source	[183, 183, 184]	[183, 183, 185, 185, 185]	[183, 183, 185, 185, 185]	[183, 183, 186, 186, 186]	[183, 183, 186, 186, 186]	[187]

Table 2.2: *Rydberg-Ritz-Parameter for ^{85}Rb. All data are relative to the center of mass values of the hyperfine splits. The errors of the calculated energies are given in the column ΔE. The ionization energies E_i and the errors are taken from [185], the sources of the Rydberg-Ritz parameters are given at the bottom of each column.*

There exist many different ways to generate Rydberg atoms. The simplest method is given by the recombination of ions and free electrons [80] as it occurs in all kinds of plasmas. Another method is the excitation of ground state atoms by inelastic collisions with an energetic charged particle beam. However, this are random processes and are useless if one wants to populate selectively one and only one excited state. Such a controlled way of excitation into a definite quantum state is possible with the help of narrow band lasers, which is also the approach in our setup (see chapter 5.3).

2.6.1 General properties of Rydberg atoms

If only one electron of an alkali atom is excited to a large quantum number n the system is very similar to the Hydrogen atom. The other electrons remain close to the core in a noble gas configuration and interact by this only minor with the excited electron. The large distance of the excited electron orbit to the core lifts also the coupling to the angular momentum to that of the nuclear spin. The quantum numbers F and m_F of the total angular momentum are now not suitable anymore. Nevertheless remains the LS-coupling and J and m_J are now the quantum numbers of choice. The effective charge seen by the excited electron is $+e$, since the N protons of the nucleus are shielded by the $N-1$ core electrons. By this Rydberg states of alkali atoms are very similar to that of a Hydrogen atom.

This simplest possible description of the energy levels in atomic Hydrogen was already given in the late 19th century by W. Hartley [181] as

$$\overline{\nu} = R_\infty \left(\frac{1}{4} - \frac{1}{n^2} \right). \tag{2.67}$$

This equation describes the position of the fluorescence line of the Balmer series in wave numbers $\overline{\nu}$ with positive integers n and the Rydberg constant $R_\infty = 1.097 \times 10^7$ 1/m. Johannes Rydberg extended the research on the atomic structure to highly excited states of alkalis and their appendant fluorescence lines [182]. This endeavor resulted in a modified version of equation (2.67), which now also describes the level structure of alkali atoms

$$\overline{\nu}_l = \overline{\nu}_{\infty l} - \frac{R_\infty}{(n - \delta_l)^2}. \tag{2.68}$$

The position of the fluorescence lines (given in wavenumbers) are now characterized with the help of an index l which includes the different angular momentum states s, p, d (l=0,1,2). Further is the

Property	Expression	$(n^*)^x$	Rb(41d)	Rb(43s)
Binding energy	$W_n = -\frac{R'_\infty}{(n^*)^2}$	$(n^*)^{-2}$	8.65 meV	8,56 meV
Level spacing	$W_n - W_{n-1}$	$(n^*)^{-3}$	107.8 GHz	109.66 GHz
Orbit-radius <r>	$\simeq \frac{1}{2}\left(3(n^*)^2 - l(l+1)\right)$	$(n^*)^2$	2355.46 a_0	2384.2 a_0
Geom. size	π<r>^{2}	$(n^*)^4$	$1.74 \cdot 10^7 a_0^2$	$1.78 \cdot 10^7 a_0^2$
Lifetime (spontaneous decay)	$\tau = \tau' \cdot (n - \delta_{n,j,l})^\gamma$	$(n^*)^3$	78 μs	99 μs
Lifetime (black body radiation)	$\tau_{bb} = \frac{3\hbar(n^*)^2}{4\alpha^3 k_B T}$	$(n^*)^{-2}$	82 μs	90 μs
Fine-structure splitting (for d)	10.8 $(n^*)^{-3}$ THz	$(n^*)^{-3}$	172 MHz	no fss

Table 2.3: *properties of Rydberg atoms calculated for Rb(41d)- and Rb(43s)-states following the calculation in [78].*

element specific quantum defect δ_l and the series limit $\overline{\nu}_{\infty l}$ introduced. They have their nature in the altered electrostatic potential seen by the excited electron due to the remaining electrons close to the nucleus. The dependence on the angular momentum l is caused by the different shapes of the orbitals. The electron in the excited state has a differing probability to be found within the cloud of the core electrons depending on l. The Coulomb interaction with the core electrons and the exchange interaction leads then to corrections, embedded in the quantum defect and the series limits.

The absolute binding energy of an electron in a Hydrogen atom can be calculated with the atom model by Niels Bohr. The binding energy W decreases quadratically with increasing quantum number as

$$W = -\frac{e^2 m_e}{32\pi^2 \varepsilon_0^2 \hbar^2}\frac{1}{n^2} = -R_\infty \frac{1}{n^2}. \tag{2.69}$$

The size r of the hydrogen atom scales as n^2

$$r = \frac{4\pi\varepsilon_0\hbar^2}{e^2 m_e} n^2 = a_0 n^2, \tag{2.70}$$

where the Bohr radius $a_0 = 5.29 \cdot 10^{-11}$ m is given by the width of the Gaussian ground state electron distribution of a Hydrogen atom. The extension of this theory to alkali atoms, particulary Rubidium is given in the next section.

2.6.2 General properties of Rubidium Rydberg atoms

Throughout all experiments presented in this thesis ^{87}Rb was used. The excited electron sees for high lying Rydberg states a nucleus with 37 protons shielded by 36 nearby electrons. This leads to an alternation of the level structure as explained in the chapter before. The altered energy levels of non-hydrogenic atoms can be calculated by introducing an effective quantum number

$$n^* = n - \delta_{n,j,l} \tag{2.71}$$

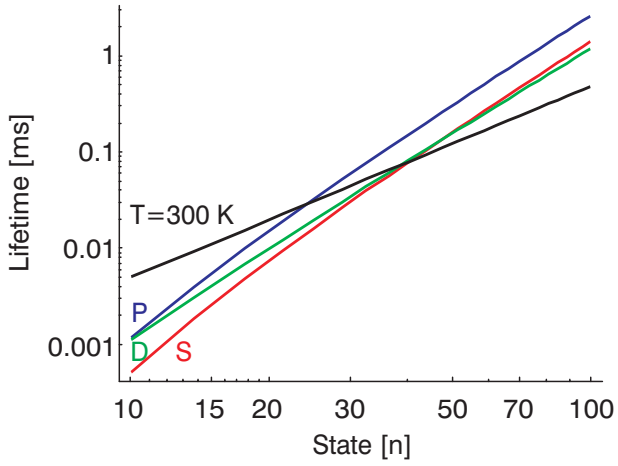

Figure 2.6: Lifetime of Rubidium-Rydberg states following equation (2.75). The calculated lifetimes for S, P and D states are given at 0 K. The black line is the lifetime τ_{bb} due to black-body radiation at 300 K.

where $\delta_{n,j,l}$ is the quantum defect [188] which depends on the main quantum number n, the coupled angular momentum j and the orbital angular momentum l. The quantum defects can be calculated with the Rydberg-Ritz equation [185] as

$$\delta_{n,j,i} = \sum_{i=0,2,4,\ldots} \frac{\delta_i}{(n-\delta_i)^i} \tag{2.72}$$

The coefficients $\delta_{n,j,i}$ have been determined experimentally and are summarized in the table 2.2. The energies W of the Rydberg states can now be calculated with

$$W = -\frac{R'_\infty}{n^{*2}} \tag{2.73}$$

where R'_∞ is an element specific Rydberg constant. The ionization energy for the two Rubidium isotopes differs only by $\hbar \cdot 174$ MHz [184] and are in wave-numbers $E_i^{85} = 33690.7989(2)$ cm^{-1} and $E_i^{87} = 33690.8048(2)$ cm^{-1}.

Further physical properties of Rubidium Rydberg states are given in table 2.3. This scaling laws are important for many aspects when doing experiments with Rydberg atoms. As an example a Rubidium atom in the 43S state has a diameter of about 250 nm, which is larger than the inter-particle distance in a typical Bose-Einstein condensate, but well below the distances in a magneto optical trap. On the other hand is the lifetime of the 43S state about 100 μs and the corresponding line width is about 10 kHz. This narrow line width in combination with a comparable narrow excitation scheme results in a very sensitive spectroscopy tool of external fields or interaction energies. Another feature is the small gapping between different Rydberg states which can be addressed by simple micro-wave techniques. This opens manifold options for manipulating the internal quantum state of Rydberg atoms. Chapter 6.2.2 gives an outlook on several possible experiments, which can be done with the available system.

State	τ'_{th}(ns)	γ_{th}	τ'_{exp}(ns)	γ_{exp}
S	1.43	2.94	1.45 ± 0.03	3.02 ± 0.02
P	2.76	3.02	2.80 ± 0.03	3.01 ± 0.03
D	2.09	2.85	2.10 ± 0.03	2.89 ± 0.02

Table 2.4: *Parameters to calculate the lifetimes of Rydberg states according to equation (2.75). The values are either experimental (exp) or theoretical (th) results [191, 190].*

2.6.3 Lifetime of Rubidium Rydberg atoms

The lifetime of any excited state $|n', l'\rangle$ is determined by the Einstein-coefficients $\tau = 1/A_{n',l',n,l}$. If there exist several possible decay channels to lower lying states $|n, l\rangle$ the lifetime contains all allowed transition by summation of the individual Einstein coefficients $1/\tau = \sum_{n,l} A_{n',l',n,l}$. With the knowledge of the eigenfunctions $|n, l\rangle$ and the corresponding eigen-energies of the Rydberg states [189] it is straightforward to calculate the Einstein coefficients by integration of the dipole matrix elements

$$A_{n',l',n,l} \frac{2}{3} \frac{e^2 \omega^3_{n',l',n,l}}{\varepsilon_0 c^3 h} \left| \langle n', l' | \vec{r} | n, l \rangle \right|^2 \tag{2.74}$$

The lifetimes for S, P and D states have been measured up to n=44 [190] and the acquired data can be condensed in an empirical equation for the lifetime:

$$\tau = \tau'(n - \delta_{n,j,l})^\gamma. \tag{2.75}$$

The quantum defects $\delta_{n,j,l}$ can be found in table 2.3 and the state dependent parameters τ' and γ in table 2.4.

The lifetimes calculated above are only valid at T=0. For temperatures above zero the black-body radiation induces transitions into other states. This is caused by the enlarged number of allowed transitions at low frequencies. The corrected lifetime is then [78]

$$\frac{1}{\tau} = \frac{1}{\tau_{T=0K}} + \frac{1}{\tau_{bb}} \quad \text{with} \quad \tau_{bb} = \frac{3\hbar n^{*2}}{4\alpha^3 k_B T}. \tag{2.76}$$

A further correction of the lifetime arises, if one includes the altered black body spectrum of electromagnetic modes in a finite size cavity. This corrections are carried out in appendix I.

3 Experimental setup and performance of Bose-Einstein production

This chapter reviews the experimental setup and the techniques used to achieve Bose-Einstein condensation (BEC). Figure 3.1 illustrates the main steps starting from an ordinary thermal gas in an effusive oven towards the quantum degenerate regime. To reach quantum degeneracy, the temperature has to be reduced by nine orders of magnitude and the phase space density has to be increased by almost 14 orders of magnitude starting from a saturated Rubidium gas at 160 °C. The phase space density is given by $n\lambda_{dB}^3$ with the density n and the deBroglie wavelength λ_{dB}. If the phase space density approaches unity, the trapped atoms undergo a phase transition as described in chapter 2.4. Below a critical temperature the ground state of the system is macroscopically occupied by the BEC. The immense gain in phase space density is realized by several cooling techniques which will be presented in the following.

As a starting point an ultra-high vacuum chamber is needed to isolate the ultracold atomic ensemble from its thermal environment. Its geometrical layout and its features are addressed in section 3.1. The element of choice is ^{87}Rb, which is by now the most common atom used in cold atom experiments and therefore also the best characterized element. Since it is an alkali atom with only one electron in the outer shell the complexity of the electronic level scheme is not too branched out. The required transitions for laser cooling can be addressed by standard, well developed, laser systems. A further advantage of ^{87}Rb is its well behaved scattering properties which allow for efficient evaporative cooling. The basic optical and physical properties of ^{87}Rb are given in appendix A.

The description of the laser system and the methods for data acquisition are given in chapter 3.2 and 3.4. The chapters 3.5 to 3.11 follow the atoms on their way from the effusive oven, through the Zeeman-slower, laser cooling steps, pure magnetic trapping, evaporative cooling and finally to the phase transition to a Bose-Einstein condensate. Some aspects of the setup can be found in more detail in [192].

The time table below gives an idea of the time-scales needed to setup up and debug such an experiment.

- January 2004 - Starting point of designing the vacuum chamber
- August 2004 - First bake-out of the main chamber. Some leaks made some re-welding necessary.
- September 2004 - Bake-out of the full vacuum assembly. A leaky ion gauge and a leaky high voltage feedthrough had to be exchanged.
- November 2004 - Observation of the first magneto-optical trap.
- December 2004 - First transfer of atoms in the magnetic trap. Due to a problem with the cloverleaf trap we had to exchange some of the magnetic coils.

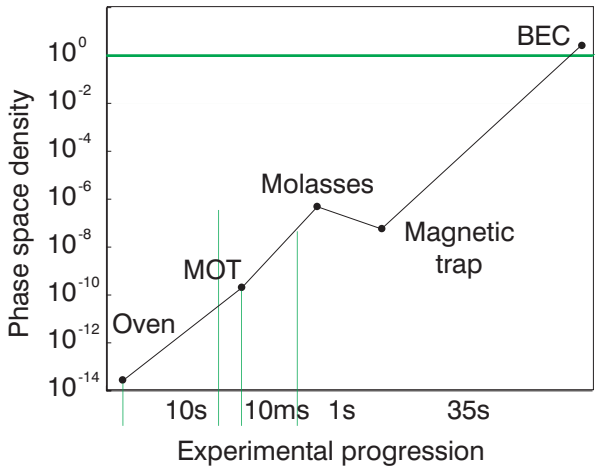

Figure 3.1: The graph depicts the different experimental steps from the effusive oven to a Bose-Einstein condensate in phase space density. First a magneto-optical trap (MOT) is loaded for ten seconds by atoms decelerated with a Zeeman-slower. The temperature of the fully loaded MOT is then reduced by molasses cooling. Directly after this the atoms are transferred into a mode matched purely magnetic trap which is subsequently compressed within one second to the full confinement. Finally evaporative cooling for about half a minute delivers the desired Bose-Einstein condensate (BEC).

- April 2005 - The refurbished cloverleaf trap is running. First observation of radio-frequency evaporation in the magnetic trap
- June 2005 - One of the power supplies for the magnetic trap exhibits too much current noise and has to be exchanged.
- June 2005 - First Bose-Einstein condensate
- August 2005 - First diffraction of a BEC in an optical lattice
- August 2005 - A defective high voltage feedthrough for the multi-channel plate had to be exchanged, for which the vacuum had to be opened.
- November 2005 - Ultra-high vacuum is restored, the laser optics in place and the MOT is running again.
- December 2005 - A short circuit in the magnetic trap has to be fixed
- February 2006 - The BEC and the optical lattice is working again and the apparatus is ready for new physics.
- March 2006 - First excitation of Rydberg atoms in a MOT and detection of field ionized atoms on the multi-channel plates.
- April 2006 - First Rydberg excitation in a Bose-Einstein condensate.

3.1 The vacuum system

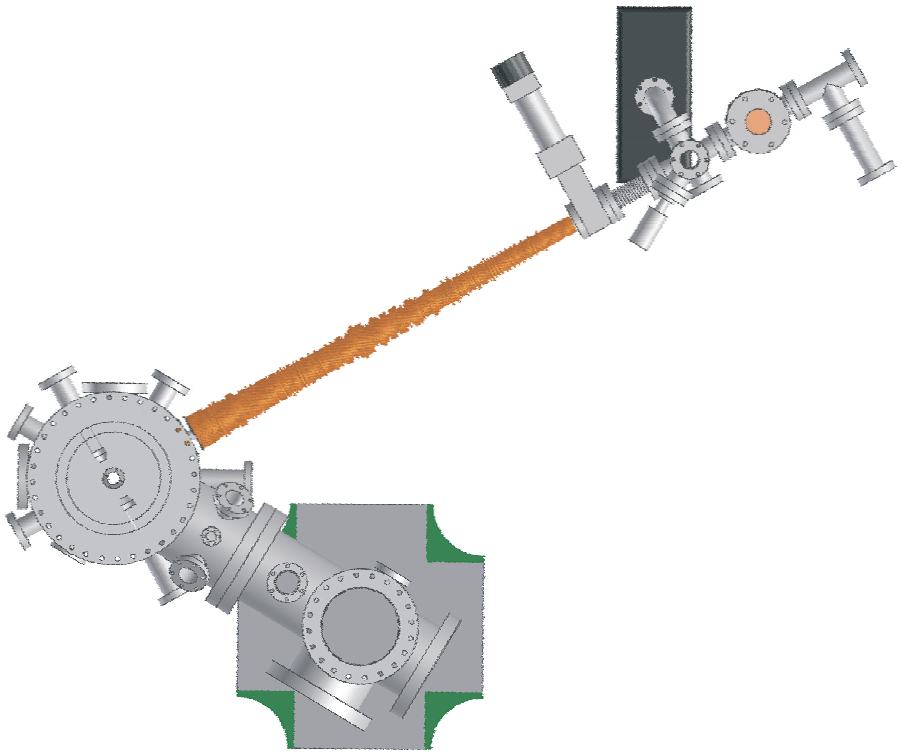

Figure 3.2: Schematic view of the whole vacuum setup. The construction can be divided into four segments. On the upper right is the oven assembly depicted, which provides an intense beam of Rubidium atoms. The hot atoms enter the Zeeman-slower, which connects the oven part with the main chamber. In the center of the main chamber the slowed down atoms are caught in a magneto-optical trap, transferred into a purely magnetic trap and cooled down to a Bose-Einstein condensate. The main chamber combines very good optical access, nonetheless nearby strong magnetic field coils, high voltage field plates, two multi-channel plates for charged particle detection and an antenna to expose the atoms to radio frequencies. On the lower right of the main chamber the pumping cross is attached, which consists of an 200 l/s ion pump (green edges) and an Titan sublimation pump, opposite of the ion pump.

The vacuum chamber consists mainly of two parts as depicted in figure 3.2. The oven assembly is operated at high vacuum (10^{-7} mbar) and delivers a thermal beam of gaseous Rubidium into the ultra high vacuum part of the chamber ($< 2 \cdot 10^{-11}$ mbar) for further processing. The BEC-setup located at Wolfgang Ketterles group in MIT [193] acted as a template for our design. Its elementary concept can be found in several groups worldwide [2, 194, 195, 196]. In addition to the usual requests for cold atom experiments, we expanded our system by two components. First we inserted several field plates inside the vacuum chamber to apply well controlled electric fields across the atoms and second we installed two multi-channel plates for ion and electron detection. This combination of techniques is to this day unique in the world, but several groups are planning to set up similar experiments.

There are many constraints, which have to be accomplished simultaneously, but are most likely to hinder one another.

- Good optical access to the atoms from all directions for laser cooling, imaging, optical lattices

and etc. This demands large windows close to the atoms.

- A small volume of the vacuum chamber to allow for high pumping rates. This particulary forbids narrow apertures.
- The ultra-high vacuum restricts the materials, which can be used, to steel, better stainless steel, Titanium, noble metals, glass, ceramics, oxygen free copper and special purpose glue.
- High flux of cold atoms into the ultra-high vacuum part of the chamber without polluting the vacuum.
- Close by coils to apply strong enough magnetic fields with moderate currents to trap the atoms.
- Field plates, which can be set very fast to high voltages. This demands spacious high voltage feedthroughs into the vacuum chamber.
- Two multi-channel plates close to the atoms and electrically well shielded to avoid stray fields.
- A radio-frequency antenna inside the vacuum chamber close to the atoms for evaporative cooling.

All this requirements are fulfilled by the experimental setup presented in this theses and their implementations are presented in the following chapters in detail.

3.1.1 Effusive oven

The starting point for the Rubidium atoms is an effusive cell which contains a Rubidium vapor. A vial with 5 g of a natural mixture of ^{85}Rb and ^{87}Rb (ratio 72:28) is heated to typically 160 °C. This results in a vapor pressure of about $8 \cdot 10^{-3}$ mbar [131]. The oven assembly contains several units to divide the high pressure part from the ultra high vacuum side and to produce a well collimated atomic beam.

In figure 3.3 a schematic view of the oven is depicted and figure 3.4 shows a photo of the real setup. All elements are based on standard ConFlat flanges. The temperature of the effusive cell ① is heated up with a strip heater and controlled by a two step control. The oven can be brought up to 160 °C within 2 hours. A faster heating would result in a temperature gradient within the oven part and by this in mechanical stress on the vacuum fittings, which has to be avoided. The atoms leave the cell through the nozzle ②, which is just a hole with 3 mm in diameter. Right behind the nozzle the atoms pass a cooling shield made of copper ③. The copper tube is thermally contacted by a copper rod to a peltier element outside the vacuum. The peltier element cools the copper tube to about 5 °C and all atoms, which do not follow the straight trajectory get adsorbed. The vapor pressure of Rubidium at a temperature of 5 °C is a few times 10^{-8} mbar. To switch on and off the atomic beam a motorized shutter ④ can be moved into the beam within several milliseconds. An ion pump[1] is mounted with a right angle to the six-way cross ④ to avoid direct deposition of Rubidium into the pump. An ion gauge[2] also connected to the cross ④ measures a pressure below 10^{-7} mbar. At position ⑤ a differential pumping tube of 120 mm length and 3 mm diameter separates the oven part from the ultra-high vacuum side. A flexible coupling ⑦ is necessary to

[1] Vaclon, 40 l/s, Varian
[2] Bayard-Alpert ion gauge UHV-24, Varian

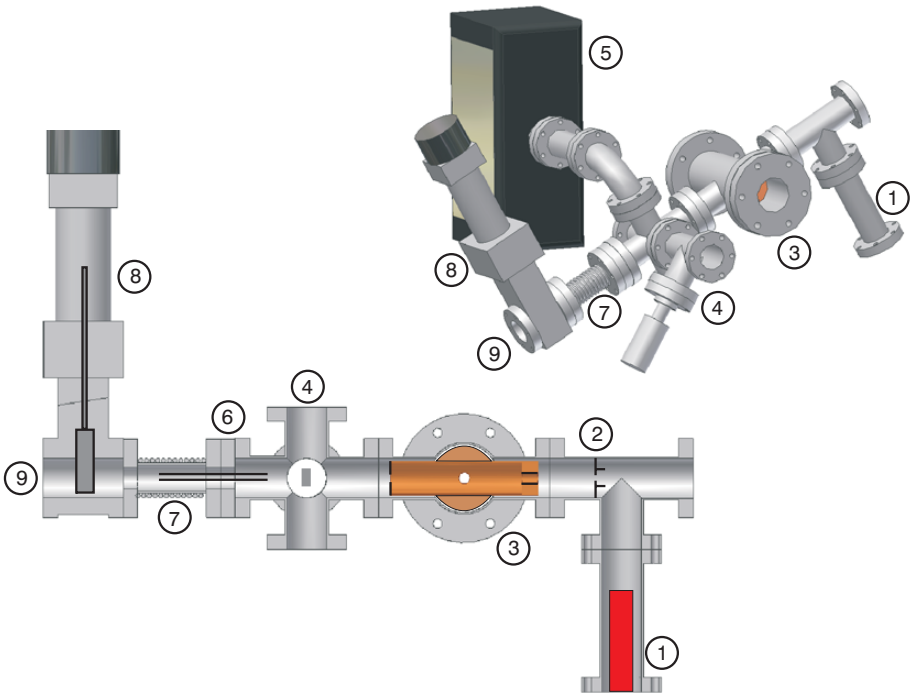

Figure 3.3: Schematic view of the oven. ① effusive cell ② nozzle ③ cooled copper shield ④ motorized shutter ⑤ ion pump ⑥ differential pumping tube ⑦ flexible bellow coupling ⑧ manual valve ⑨ CF-flange to Zeeman-slower

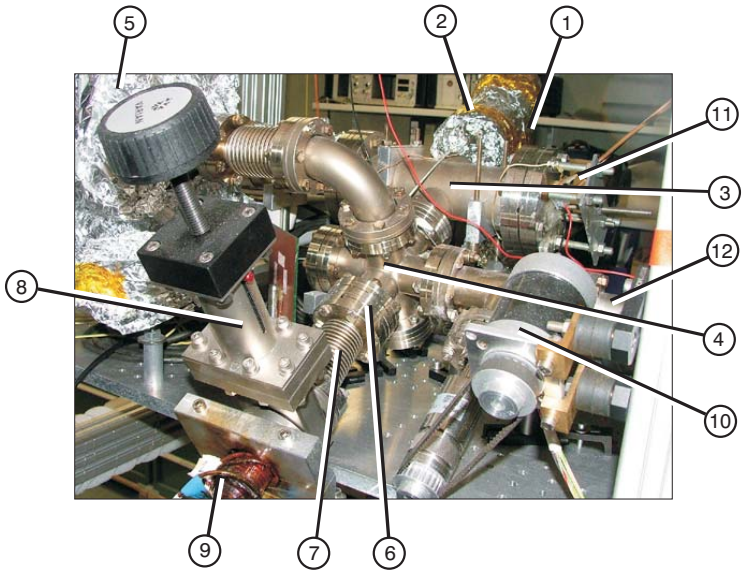

Figure 3.4: Picture of the oven. ① effusive cell ② nozzle ③ cooled copper shield ④ motorized shutter ⑤ ion pump ⑥ differential pumping ⑦ flexible bellow ⑧ valve ⑨ CF-flange to Zeeman-slower ⑩ motor for mechanical shutter ⑪ Peltier element for cooling shield ⑫ ion gauge

align the whole rigid oven assembly parallel to the Zeeman-slower. Finally a gate valve ⑧ allows to disconnect the ultra-high vacuum of the main chamber completely form the oven, which is only done for exchanging the Rubidium vial in ① and other maintaining work. Behind the valve follows the Zeeman-slower, which will be discussed in chapter 3.6.

3.1.2 Main chamber

The main vacuum chamber depicted in figure 3.5 and figure 3.2 is the heart of the whole setup. It was built completely in the machine shop of the University of Stuttgart. All elements are made of stainless steel and welded together from the vacuum side. The principle of the design is a tube on which radially all the ports (①-⑫) point towards the center. The angle between each port is 30°. Into this tube extend two buckets, which give space for the magnetic trap. To get also optical access in the third dimension a one inch glass-metal view-port is welded centered onto each bucket. They are made of a one inch steel tubing, on which a window is directly fused. By this the radial extension is minimized and allows a better insertion of the magnetic trapping coils. The buckets are connected to the main chamber with CF250 flanges (outer diameter 304.8 mm), the distance between the two fittings is 249.2 mm. A more detailed description of the physical dimensions of the main vacuum chamber is given in appendix F. This rather large layout was chosen to minimize eddy-currents when switching off the magnetic trap suddenly, since the high conductive copper gaskets are by this further away from the atoms. The main tubing, which holds the radial ports (①-⑫) has an inner diameter of 200 mm and an outer diameter of 205 mm. The buckets have an inner diameter of 155 mm and an outer diameter of 159 mm. The inner diameter of the bucket is important for the design of the magnetic trap, which will be set into the bucket. There is enough space between the bucket and the main tube, such that good pumping speed is ensured. Between the two buckets is an open area with a distance between of 28 mm. We used for the inner surface steel with 2 mm thickness, which limits the minimum distance of the magnetic trapping coils to 32 mm.

Optical access to the atoms is possible through one of the 11 radial viewports ② to ⑫, except the ports ④ and ⑩ (see figure F.1), which are occupied by the high voltage feedthroughs[3] for the two multi-channel plates. Port ① is used to connect the Zeeman-slower to the main vacuum chamber. For laser cooling and trapping an optical access in the third dimension is indispensable. This is accomplished by two viewports ⑱ inside the buckets as mentioned above. The magneto-optical trap is then operated with the ports ②, ⑤, ⑧, ⑪ and the two ports ⑱. There are two larger ports ③ and ⑥ for the imaging system to improve the numerical aperture and with this the optical resolution. When using light with a wavelength of 780 nm for imaging the maximum spatial resolution is limited to 2.8 μm. All ports can be used manifold as e.g. for optical lattices. The table 3.1 gives an overview of all optical ports and their usage.

The large flange ⑪ connects the pumping cross to the main chamber. The main chamber is kept at ultra-high vacuum with a 200 l/s ion-getter pump[4] and a titan sublimation pump. A liquid nitrogen container is connected to the titan sublimation pump to increase the pumping efficiency. After a bake-out of the whole vacuum setup at about 200 °C for one week the pressure in the UHV region is measured with an ion gauge ⑳ to be below $2 \cdot 10^{-11}$ mbar. The lifetime of the magnetic trap, which is a direct measure of the background pressure, is 163 s as can be seen from figure 3.6.

Uncommon to standard Bose-Einstein condensation setups, we included two multi-channel plates and field plates, which are used for experiments with Rydberg atoms and their detection. The

[3] 4 pin HV feedthrough, 3 kV, Hositrad
[4] Meca 2000, Meca

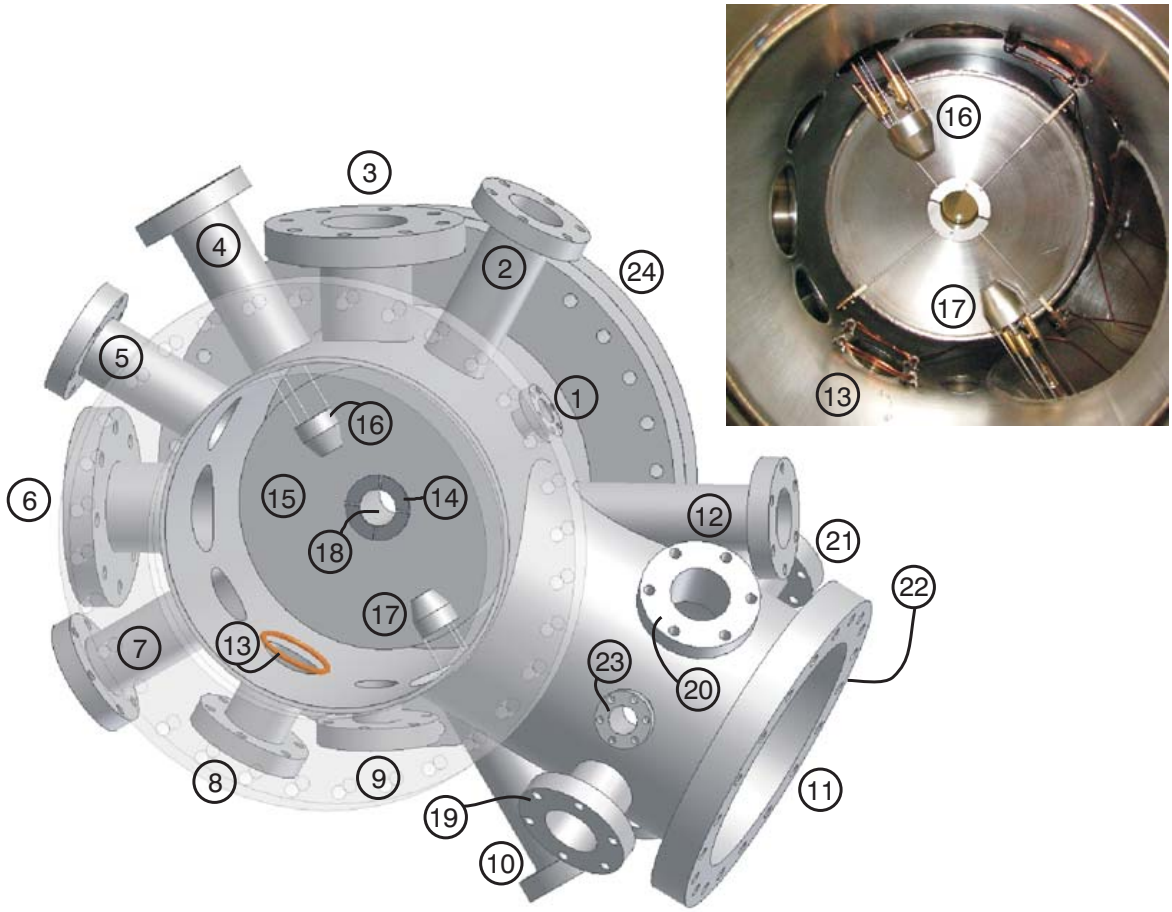

Figure 3.5: Schematic view of the main vacuum chamber and a picture into the chamber, both with one bucket removed.
① CF16 flange for Zeeman-slower
② CF35 optical port for the magneto-optical trap (MOT)
③ CF63 optical port for absorption imaging, alternative optical lattice
④ CF35 Multi-channel plate attached to a fourfold high voltage feedthrough (ion detection)
⑤ CF35 optical port for the MOT
⑥ CF63 optical port for fluorescence imaging, alternative absorption imaging or optical lattice.
⑦ CF35 optical port for the Zeeman-slowing light
⑧ CF35 optical port for the MOT
⑨ CF35 optical port for absorption imaging, alternative optical lattice
⑩ CF35 Multi-channel plate attached to a fourfold high voltage feedthrough (electron detection)
⑪ CF150 flange towards pumping cross and optical port for the MOT
⑫ CF35 optical port for optical lattice, alternative absorption imaging
⑬ Radiofrequency antenna, the second antenna is symmetrically attached to 2)
⑭ High voltage field plates, isolated by a ceramic spacers
⑮ Recessed bucket containing the magnetic coils
⑯ and ⑰ Multi-channel plates deployed in a Faraday cage
⑱ One inch optical viewport for the MOT and optical lattice
⑲,㉑ and ㉒ High voltage feedthroughs, e.g. for connection to field plates
⑳ Ion gauge
㉓ Dual electric feedthrough for the radiofrequency antenna
㉔ CF250 main flange, on which the buckets are mounted

Flange ♯	CF-size	usage	distance to window	NA
1	16	Zeeman-slower	-	-
2	35	MOT	215.4 mm	0.09
3	63	Imaging	184.7 mm	0.17
4	35	MCP	-	-
5	35	MOT	220.4 mm	0.09
6	63	Imaging	184.7 mm	0.17
7	35	Zeeman-slowing light	220.7	0.09
8	35	MOT	170.4 mm	0.11
9	35	Imaging	145.5 mm	0.13
10	35	MCP	-	-
11	150	MOT	652.4 mm	0.10
12	35	Imaging	255.4 mm	0.07
18 front	1 inch	MOT/lattice/Rydberg/pumping	46 mm	0.28
18 back	1 inch	MOT/lattice	46 mm	0.28

Table 3.1: *Characteristics of all flanges and their usage. The right column gives the numerical apertures (NA) including the optical viewports. The optical resolution is then given by the Rayleigh criterion* $\Delta x = 0.61\lambda/NA$*, where* Δx *is the smallest resolvable structure and* λ *the wavelength of the light.*

materials used in multi channel plates[5] are stainless steel, glass and chromium and suitable for our extreme ultra-high vacuum condition. The eight field plates are electrically isolated to the chamber walls with ceramic spacers and are glued onto them with a special vacuum glue[6]. The outgassing rate of this glue is low enough, to maintain the low pressure. The plates are connected to Kapton-isolated copper wires with special vacuum copper-beryllium clamps.

3.2 The laser system

In our experiments laser light is used to slow, cool, pump, polarize and detect the atoms. For this we set up two laser-systems to generate all necessary frequencies. For all transitions ascending from the $F = 2$ ground state, we use an Titanium:Sapphire laser[7] pumped by an 10 W solid state laser[8]. About one Watt of resonant light is now available for further processing. Most of the laser power is taken for the cooling light of the magneto-optical trap (MOT) and the Zeeman-slower. The cooling cycle is tuned to the $F = 2, m_F = 2 \rightarrow F' = 3, m'_F = 3$ transition, which behaves nearly as a two level system. For more details on the optical properties of ^{87}Rb see appendix A.

Two further beams are detached for resonant absorption imaging and polarizing the atoms. Polarizing stands for transferring all atoms after the last laser cooling step into the $F = 2, m_F = 2$ state, which can be caught by a purely magnetic trap. The polarizing light is tuned to the $F = 2 \rightarrow F' = 2$

[5] Type B012VA, El-Mul
[6] High temperature epoxy EpoTek 377, Epoxy Technology
[7] MBR 110, Coherent
[8] Verdi V10, Coherent

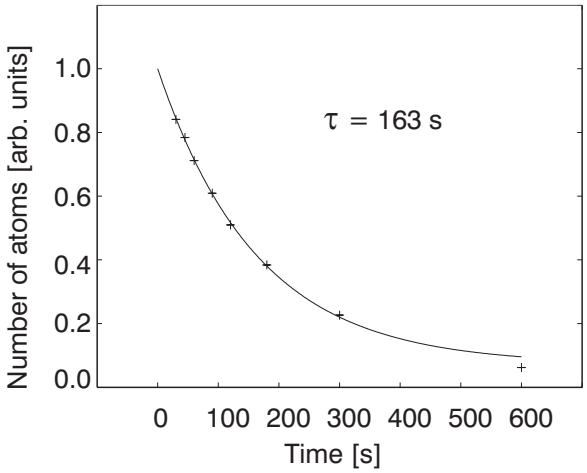

Figure 3.6: Measured lifetime in the magnetic trap. Atoms were stored in a pure conservative trapping potential. After 163 s the initial atom number dropped due to background gas collisions to 1/e in an exponential (solid line) decay.

transition and is σ^+ polarized. By this the atoms are shuffled from any m_F state in the $m_F = 2$ state which is a dark state with respect to the light, which is on resonance with the $F = 2 \rightarrow F' = 2$ transition. The imaging beam is tuned resonantly to the $F = 2, m_F = 2 \rightarrow F' = 3, m'_F = 3$ transition, and is also σ polarized. Details of our imaging system will be discussed in chapter 3.3.

The second laser system used for trapping and cooling, is the repumping system tuned to the $F = 1 \rightarrow F = 2$ transition. This is inevitable, since the light of the cooling laser is still transferring atoms into the $F' = 2$ state although it is 267 MHz detuned from the $F' = 3$ state. From there the atoms decay with a 50 % probability into the $F = 1$ state and do not participate anymore in the cooling cycle. Since high laser power is not required here, we use a standard laser diode[9] in an Littrow setup [198], which was developed in our group. With this setup we obtain about 80 mW of laser power after the optical diode.

To stabilize the laser frequencies within 1 MHz we use a polarization spectroscopy method [197]. The Titanium:Sapphire laser is stabilized to the $F = 2 \rightarrow F' = 3$ transition line and the diode laser to the $F = 1 \rightarrow F' = 0$ transition. To shift the light to the desired frequencies, we use accusto-optical modulators[10] (mostly) in a double pass configuration. These modulators are also used for fast switching the laser power within typically 30 nano-seconds. Since there remains always some leakage of light through the modulators, every laser beam is equipped additionally with a mechanical shutter[11] to switch the light entirely off.

All driving unit assemblies for the accusto-optical modulators are homebuild with a similar design. The radio-frequency is generated by voltage controlled oscillators (VCO)[12] and its frequency can be tuned with an external control voltage. The signal level of the VCO is subsequently adjusted with either a frequency mixer[13] controlled by an emitter follower or a bi-phase attenuator[14]. The

[9] LD-07800-P250-1, Toptica
[10] 3200-121, 3110-120 and 3080-120, Crystal Technology
[11] LS2, Uniblitz, Vincent Associates
[12] ZOS 300, ZOS 200 and ZOS 150, Mini Circuits
[13] ZAD 1.1, Mini Circuits
[14] ZMAS-1, Mini Circuits

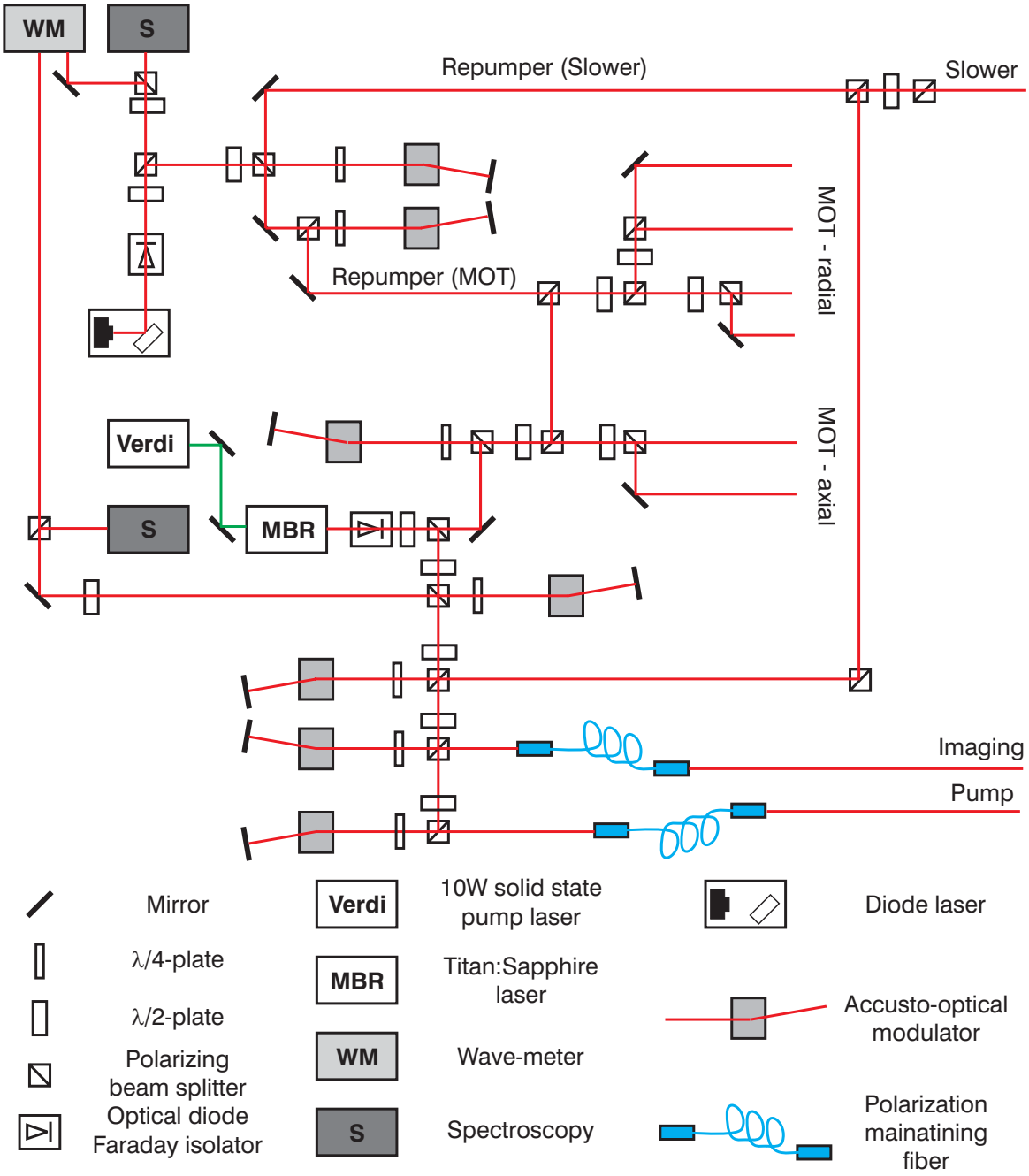

Figure 3.7: Schematic view of the laser system for trapping and cooling. All necessary beams are extracted from two lasers, a pumped Titanium:Sapphire laser and an external cavity diode laser. In the figure all lenses, apertures, shutters, motorized mirrors are omitted for clarity. A detailed description of the spectroscopy setup and its functionality can be found in [197].

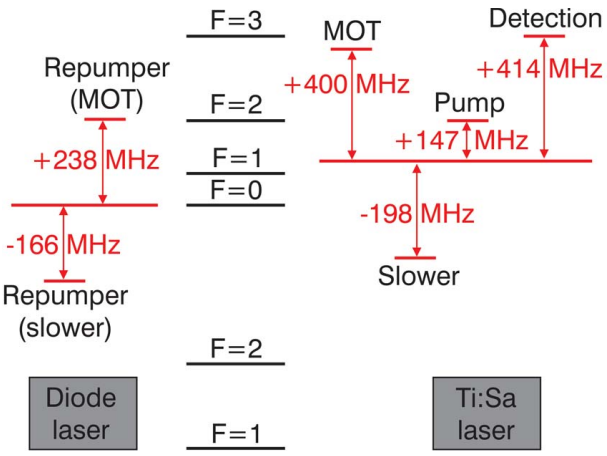

Figure 3.8: Locking scheme of the laser system. Shown are the lock-points for the Titanium:Sapphire laser (right) and the diode laser system (right). The arrows indicate the shift of the laser frequencies to the desired transitions by accusto-optical modulators.

rf-switch[15] which follows next is used to attenuate the rf-power in the off-state by at leasr 40 dB. Finally the radio-frequency is amplified to a maximum power of 33 dBm (2 W) by a high power amplifier[16] and delivered with an ordinary SMA cable to the transducer of the accusto-optical modulator. The suppression of the laser light in the first order beam in the off-state is typically better than 1:1000.

3.3 Imaging system

To obtain quantitative information about the atomic ensemble it is sufficient to measure the spatial density distribution of the atomic cloud for example with a CCD camera. If this measurement is repeated for different times, after the cloud was released from its trapping potential, one can derive from this pictures the temperature, the atom number and with the knowledge of the shape of the confining potential the density inside the trap. In most imaging techniques resonant, or near resonant light, is used and the atoms are imaged by suited optics onto a CCD-chip. The pictures taken by the CCD-chip contain only two-dimensional information about the cloud since the signal along the imaging axis is integrated. Typically one assumes radial symmetric samples for computation. But it is also possible to take pictures simultaneously in two directions and extract from this the real three dimensional situation.

If the atoms are not Bose condensed, but establish a classical thermal gas, they adopt a Gaussian density distribution $n(\vec{r}, t)$ after they are released from any trapping potential for a certain time of flight. This is valid as long as the expanded cloud is well larger than in the initial trapped situation and the velocities in the trap follow a Maxwell-Boltzmann distribution [137]. The density distribution of a sufficient expandend cloud is then given by

$$n(\vec{r}) = n_0 \exp\left(-\frac{x^2}{2\sigma_x^2} - \frac{y^2}{2\sigma_y^2} - \frac{z^2}{2\sigma_z^2}\right). \tag{3.1}$$

[15] ZYSWA-2-50 DR, Mini Circuits
[16] ZHL-1-2W, Mini Circuits

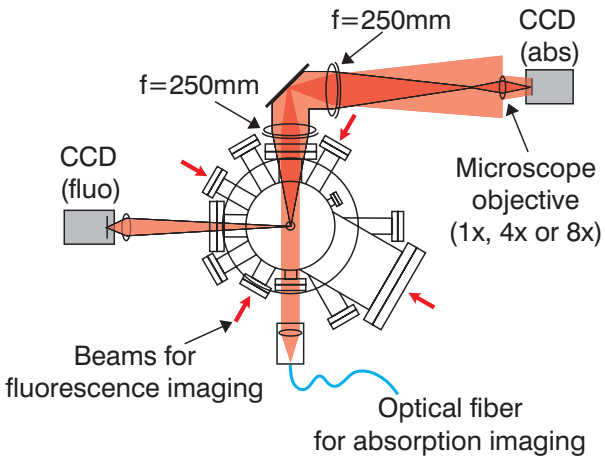

Figure 3.9: Schematic setup of the absorption (abs) and fluorescence (fluo) imaging system.

The σ_i's are the $1/\sqrt{e}$ radii of the cloud. The peak density is determined by $n_0 = \frac{N}{(2\pi)^{3/2}\sigma_x\sigma_y\sigma_z}$ with N being the total atom number. Integrating the Gaussian curve over one axis, e.g. the x-axis, gives the corresponding signal on the CCD-camera.

$$\tilde{n}(y,z) = n_0\sqrt{2\pi}\sigma_x exp\left(-\frac{y^2}{2\sigma_y^2} - \frac{z^2}{2\sigma_z^2}\right). \tag{3.2}$$

After a certain time of flight the size of the cloud increases as

$$\sigma(t) = \sqrt{\sigma_0^2 + \frac{k_B T}{m}t^2}. \tag{3.3}$$

This is valid as long the initial density distribution at $t = 0$ is also Gaussian with a width σ_0. This is true for atomic clouds in harmonic trapping potentials or to some extent for magneto-optical traps with a Gaussian shape. For large time of flights dominates the second term in (3.3) and the temperature is simply given by

$$T = \frac{m\sigma^2(t)}{k_B t^2}. \tag{3.4}$$

The analysis of Bose-Einstein condensed samples in time of flight will be discussed in chapter 3.3.3.

3.3.1 Fluorescence imaging

In fluorescence imaging the spontaneous emitted light of an atomic sample is detected. This is usually done by irradiating the atomic cloud resonantly with the six beams for magneto-optical trapping (MOT). The glowing cloud is imaged with a diminution optic onto a CCD-chip[17], because the magneto-optically trapped cloud is usually larger than the chip size. The signal level is proportional to the collected light, which is constrained by the numerical aperture of the imaging

[17] Slow Scan Imaging System SIS 9, ThetaSystems

system. In our case this is the first lens (see figure 3.9) of our objective. Although the distance to the atoms is larger than necessary and the entrance aperture of the objective relatively small, is the signal level sufficient down to 10^6 atoms.

For a quantitative analysis of the CCD-pictures it is necessary to estimate the scattering rate of the atoms and the radiation pattern of the emitted light. The atoms are exposed in six directions with circular polarized light, thus it is fair to assume that the directions of the spontaneous emitted photons are isotropic. The light is tuned into resonance with the $F = 2 \rightarrow F' = 3$ transition. It remains the scattering rate of the atoms on resonance

$$\Gamma_{sc} = \frac{\Gamma}{2} \frac{\eta_{cg} s}{1 + \eta_{cg} s}. \tag{3.5}$$

The saturation parameter was defined in chapter 2.1. I introduced here an effective Clebsch-Gordan coefficient η_{cg} which takes the differing transition strengths, given in appendix A, into account. By assuming that the atomic sample is uniformly distributed among the magnetic sublevels of the $F = 2$ ground state and every atom is irradiated in equal shares circular polarized light (by the six MOT-beams), one obtains η_{cg}=7/15. The intensity in each beam is about 18 I_{sat} which gives an saturation parameter of $s = 6 \cdot 18$ on resonance. With such a high intensity the scattering rate is within 1 % accuracy $\Gamma/2$.

Although the detuning in respect to the next possible transition $F = 2 \rightarrow F' = 2$ is quite large, the high intensity provokes every 75 cycles an off-resonant excitation into the $F' = 2$ state and every 200 cycles into the $F' = 1$ state. The probability for a decay from the $F' = 2$ state into the $F = 1$ ground state is 50 % and for a decay from $F' = 1$ 80 %. To return the atoms into the cycling transition $F = 2 \rightarrow F' = 3$ the repumping laser has also to be present.

There are several effects, which can alter the actual physical situation by the presence of the imaging light. The major deviation is due to the optical density of the cloud, which causes the intensity of the resonant laser beam to be reduced while it intrudes into the cloud. The atoms in the center of the cloud scatter less photons due to the reduced intensity. These are lacking on the CCD-camera and pretend a smaller atom number. On the other hand is the light emitted by the atoms inside the cloud also hindered to propagate outwards by multiple scattering events. This effect is commonly known as radiation trapping. This deviations can be avoided by detuning the laser away from resonance to obtain a more transparent cloud by reducing the effects of multiple scattering events.

Finally it should be mentioned, that the cold cloud is heated by the spontaneous scattered photons. The heating scales with the square root of scattered photons, which gives in our case of 100 μs irradiation time at full saturation a temperature gain of about 22 μK.

3.3.2 Absorption imaging

The spontaneous scattering events in fluorescence imaging alter the velocity distribution of the atomic cloud. For very cold and small samples this leads already to an alternation of the density distribution within the exposure time (typically 100 μs) of the resonant imaging light. To avoid this, one uses the absorption imaging technique, where the applied intensity is reduced well below the saturation intensity and by this the number of spontaneous scattered photons. In spite to fluorescence imaging the absorption imaging method detects the photons not being absorbed by

the sample. One laser beam is shone onto the atoms and a shadow picture is recorded on the CCD-chip[18]. The absorption of photons in the atomic cloud follows simply Beer's law

$$I(x) = I_0 e^{-\mathrm{OD}\cdot x}. \tag{3.6}$$

The cross section $\sigma(\delta)$ for light scattering at a two level atom with detuning δ is given by

$$\sigma(\delta) = \frac{3\lambda^2/2\pi}{1 + 4\frac{\delta^2}{\Gamma^2}}. \tag{3.7}$$

For small intensities ($I \ll I_{\mathrm{sat}}$) the amount of scattered power is linear to the incident laser intensity $P_{\mathrm{scattered}} = \sigma(\delta)I$. The attenuation dI of the intensity I of the laser intruding a cloud with a density distribution $n(\vec{r})$ is given by

$$dI = -\sigma(\delta)n(\vec{r})I\,dx. \tag{3.8}$$

Integration along x gives

$$\overline{\mathrm{OD}}(y,z) = \sigma(\delta)\int_{-\infty}^{\infty} n(x',y,z)\,dx'. \tag{3.9}$$

The intensity at the position (y,z) is then $I(y,z) = I_0 e^{-\overline{\mathrm{OD}}}$. By recording the unperturbed intensity distribution $I_0(y,z)$ and the diminished distribution $I(y,z)$ one can reconstruct the two-dimensional density distribution of the cloud with

$$n(y,z) = \frac{1}{\sigma(\delta)}\ln\frac{I_0(y,z)}{I(y,z)}. \tag{3.10}$$

The spontaneous emitted light does not contribute to the image since it is scattered into the complete solid angle and only a very small fraction reaches the chip. The integration of $n(y,z)$ along y and z yields the total atom number N. To recover the the full three-dimensional density distribution one has to use the knowledge of the existing symmetries of the atomic samples.

For large column densities is the incident light almost blackened out. At an optical density of three already 95 % of the initial intensity is lacking. It depends on the dynamic range of the camera and the noise level in the pictures if this information is still valuable. In our experiments the limit of resolution is reached at an optical density of about 3.5, which is due to the remanent noise level. To circumvent this problem, the imaging frequency can be shifted away from resonance and the sample becomes more transparent. However, the density distribution is not uniform and the the refractive index of the cloud acts as a lens on the imaging light and leads to distorted images [199]. A secure way to reduce the optical density is a large expansion time of the cold cloud, which is usually the procedure in our experiment. Another way to image very dense clouds is the phase contrast imaging method, which also makes use of the refractive index of the atoms [200] and is planned to be implemented in our setup.

The depth of focus of the absorption imaging system is given by the Rayleigh range (see equation 2.54) and is in our case 55 μm. Since the imaging axis is parallel to gravity the atomic sample falls

[18] NTE/CCD Detector, Princeton Instruments

downwards during the free expansion and the imaging system has to be adjusted for each time of flight. For example the cloud drops by 4.4 mm for a time of flight of 30 ms.

Usually we apply absorption imaging only to atomic clouds, which were already evaporatively cooled down in a magnetic trap (see chapter 3.10). The atoms are captured in the $F = 2, m_F = 2$ ground state. To imaging the atoms they are released from the trap and a magnetic field of a few Gauss is applied parallel to the resonant beam to define a quantization axos. One has to assure that the atoms follow adiabatically the magnetic field, so we switch on the quantization field already before they are released from the magnetic trap. The σ^+ polarization of the beam only couples the ground state atoms to the $F' = 3, m'_F = 3$, which always decays back into the initial state $F = 2, m_F = 2$. An admixture of π polarization would pump the atoms away from the closed cycle, and the scattering rate would drop according to the Clebsch-Gordan coefficients. The evaluated atom number is then underestimated.

In absorption imaging it is not necessary to have any repumping light present. First of all the polarization hinders an excitation into the $F' = 2$ state. But a finite contribution of π light is likely to be present. At small intensities every 8000 cycles an atoms enters the $F' = 2$ state from which it decays with 50 % probability into the $F = 1$ state. With an exposure time of typically 100 μs about 200 Photons are scattered on the cycling transition and only a negligible fraction of atoms gets pumped away.

3.3.3 Time of flight expansion of a Bose-Einstein condensate

The time of flight method is mostly applied to the analysis of Bose-Einstein condensed samples. In spite to thermal clouds is the dominant effect on the expansion no longer the thermal motion of the atoms but the chemical potential μ, given by the interaction among the atoms (see chapter 2.4.2). This is valid as long the chemical potential is larger than the energy of the lowest eigenstate in the trap and larger than the temperature of the sample. The following treatment follows [201]. The force on a particle inside the condensate is

$$\vec{F}(\vec{r}, t) = -\nabla \left(g\, n(\vec{r}, t) \right), \tag{3.11}$$

where the interaction parameter $g = 4\pi\hbar^2 a/m$ was defined in chapter 2.4. The simplest ansatz is a scaling law for the Thomas-Fermi radii $r_{\mathrm{TF},i}(t)$:

$$r_{\mathrm{TF},i}(t) = \lambda_i(t) r_{\mathrm{TF},i}(t = 0). \tag{3.12}$$

This takes already into account, that the parabolic density distribution of the trapped condensate is conserved. The condensates produced in a cloverleaf trap are cigar-shaped with an aspect ratio $\epsilon = \omega_z/\omega_\rho$. With re-scaling the time as $\tau = \omega_\rho t$ and using that usually $\epsilon \ll 1$ one gets in lowest order in ϵ for the two scaling factors

$$\begin{aligned} \lambda_\rho(\tau) &= \sqrt{1+\tau^2} \\ \lambda_z(\tau) &= 1 + \epsilon^2 \left(\tau \arctan\tau - \ln\sqrt{1+\tau^2} \right). \end{aligned} \tag{3.13}$$

The expansion of the condensate can be expressed with the aspect ratio $\aleph$ of the Thomas-Fermi radii which is independent of the atom number.

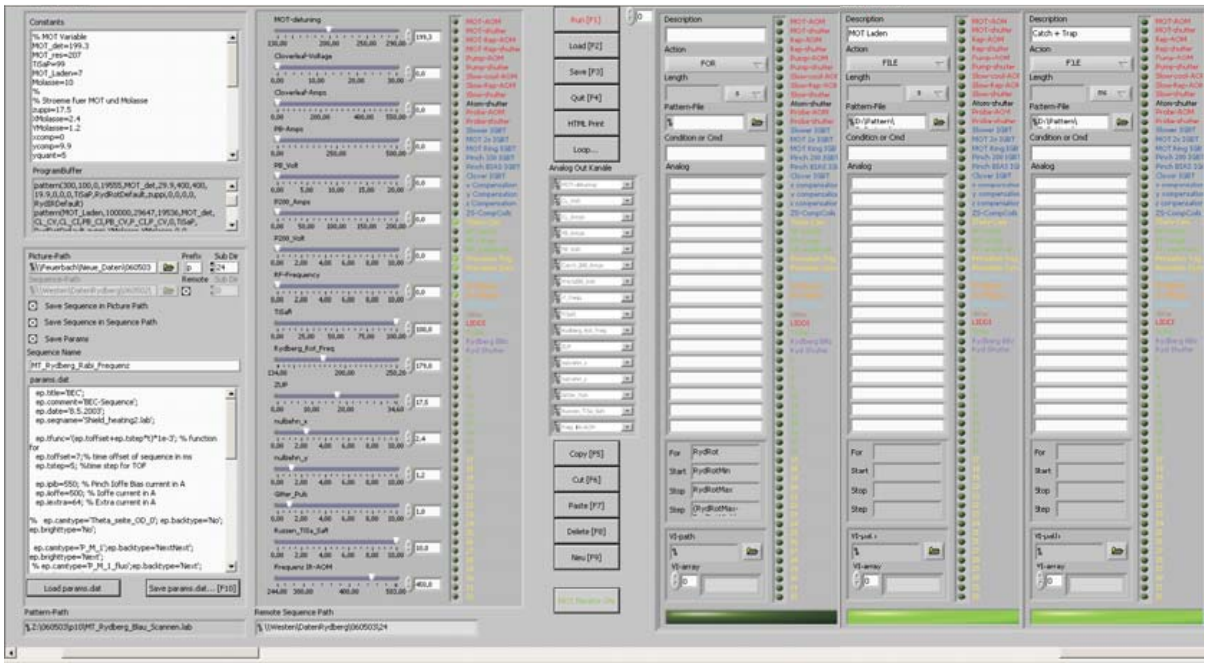

Figure 3.10: Snapshot of the computer control software. More details are given in the text.

$$\aleph = \frac{\lambda_z(t)}{\lambda_\rho(t)} \frac{\omega_\rho}{\omega_z} \tag{3.14}$$

It is also possible to solve the three coupled differential equations (3.11) numerically.

The distinct expansion behavior of a BEC compared to a thermal cloud can be used as evidence for the successful production of a quantum degenerate Bose gas.

3.4 Computer control

The creation of a Bose-Einstein condensate and experiments with them is a procedure consisting of many single steps. About fifty devices have to be controlled time sensitive. This are namely actions like opening and closing mechanical shutters, altering frequencies and intensities of the lasers, triggering cameras, controlling the magnetic fields and many more actions which cannot be treated here entirely. A Bose-Einstein condensate is typically produced within 45 seconds and requires a sequence of more than thirty steps. In principle one must be able to vary every parameter, which forbids mostly hard-wired solutions. In our experiment the sequences are programmed in an graphical interface[19] based on LabView 7 (National Instruments). Each word in the sequence defines the state of the experiment for a certain time, until it proceeds to the next word. It is possible to use many basic programming tools, as loops, subroutines, state dependent functions and similar

[19] The programming of the interface was done by Rolf Heidemann and Jörg Werner. More details about the coding can be found in [202]

elements. With this it is possible to implement experimental scans, which run independently up to several hours.

The control program runs on an ordinary IBM-PC under Windows XP. The interface to the experiment is given by one digital PCI card[20] and two analog PCI cards[21]. All in all we have 64 TTL-channels and eight analog channels with 12 bit resolution and eight further analog channels with 16 bit resolution. The digital channels are isolated by opto-couplers and a transistor circuit for each channel allows us to drive devices with 200 mA at 50 Ω. The analog signals are all piped through a discriminator to vary the amplification or the offset of the output voltage. There exists a bunch of electronic circuits for further processing of the signals, like basic logical operations (AND, OR, XOR, NOT), multiplexers to generate with one TTL signal two arbitrary voltages and pulse generators. The latter is necessary since the time resolution of the control program is limited to 100 μs. The pulse generators can create TTL pulses down to 20 ns. To generate even shorter pulses we use specialized signal generators.

The control software not only takes care of the progression during the experiment, but also saves any desired parameter and the sequence itself to a file and takes care of the paths, where the pictures have to be recorded. This records also serves as additional documentation of the conducted experiments. The control of the cameras is also done by home-made LabView (National Instruments) programs. On a second computer the analysis of all accumulated data can be done simultaneously to the experiments. A large library[22] of self written MatLab (MathWorks) routines allows us to combine the recorded pictures (or any other signal) with the data exported from the control program and to do any wished analysis in real time.

3.5 An intense Rubidium source

There exists a wide range of atomic sources to load efficiently magneto-optical traps (MOT). Most common in present Bose-Einstein condensation setups are double-MOT systems [203, 204], two-dimensional MOTs [205, 206], dispensers [189, 207] and effusive cells in combination with a Zeeman-slower [208]. The latter delivers compared to all other sources the highest flux of cold atoms and is also used in our setup. Another advantage of the Zeeman slowing technique is the little amount of cooling light needed and the rather simple adjustment of just one optical axis. Disadvantageous is the necessity of elaborate magnetic field distributions, which have to be manufactured very carefully, and its rather bulky layout. However, the elongated tubing of the Zeeman-slower serves as an additional differential pumping stage between the oven and the main chamber and improves by this the quality of the ultra-high vacuum.

The oven in our experiment is usually heated up to 160 °C which corresponds to a vapor pressure of $8 \cdot 10^{-3}$ mbar. The nozzle of the oven is simply a circular aperture with 4 mm in diameter. To speak of an effusive oven it is necessary that the mean free path of the particles is larger than the wall thickness of the orifice. One can estimate the cross section of any atom with the Massey-Mohr formula [209] (given in atomic units)

$$\sigma = 8.083 \left(\frac{C_6}{\hbar v_r} \right)^{2/5}, \tag{3.15}$$

[20] DIO-64, Viewpoint Systems
[21] PCI NI 6733 and PCI NI 6713, National Instruments
[22] Most of the procedures for data analysis were written by Piet Schmidt [166].

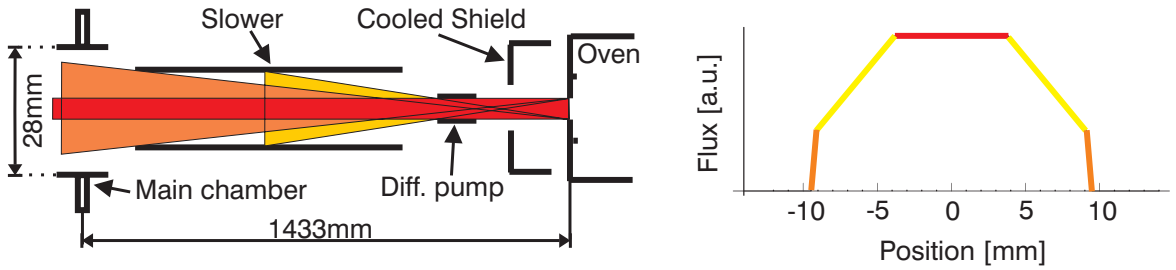

Figure 3.11: Flux distribution of the effusive beam. The figure on the left side depicts a horizontally compressed view of the vacuum chamber including all apertures. The color coding reflects the flux per unit area and time. The red area is the fraction of the unperturbed flux as given in equation (3.16). The orange part is already diminished by the end aperture of the Zeeman-slower and the yellow by the end of the differential pumping tube. The graph on the right side shows the truncated intensity distribution in radial direction at the center of the main chamber.

where $C_6 = 4426$ [$a.u.$] is the C_6-coefficient for Rubidium [210, 211] also given in atomic units and v_r the relative velocity of the two colliding particles in the center of mass frame. With an oven temperature of 160 °C the mean free path is about 300 μm and therefore comparable with the wall thickness of 1 mm, hence we assume our source to be effusive [212].

The flux $d\Phi_0$ of atoms per second emitted into a solid angle $d\Omega$ is given by [213]

$$d\Phi_0 = \sqrt{\frac{2}{\pi m k_b T}} \frac{\oslash_{oven}^2}{8} p(T) \cos\theta \, d\Omega, \tag{3.16}$$

where $\oslash$=4 mm is the diameter of the nozzle, $p(T)$ the vapor pressure of Rubidium (see equation A.1) and θ the angle with respect to the normal of the aperture area.

To obtain the total flux Φ_0 leaving the oven within the full cosine distribution, one has to integrate over $d\Omega$

$$\Phi_0 = \sqrt{\frac{2\pi}{m k_B T}} \frac{\oslash_{oven}^2}{8} p(T). \tag{3.17}$$

.

At 160 °C the total flux of atoms leaving the orifice is $1.4 \cdot 10^{17}$ atoms/s. But a small fraction the integrated flux reaches the center of the main vacuum chamber, where the magneto-optical trap is located. Figure 3.11 depicts the geometric situation. The atomic beam is trimmed by two apertures, the exit area of the differential pumping tube and the end of the Zeeman-slower. Atoms which hit any part of the vacuum chamber stick to the wall and are therefore lost from the beam. Without any apertures the intensity distribution is constant over the small orientational changes of $d\Omega$. To obtain the real intensity distribution (flux per unit area) one has to weight equation (3.16) with a weight function as depicted in figure 3.11. This function was determined straight forward by a geometric treatment [213]. The central part of the beam is not affected by the apertures and stays unaltered. There exists an area which cannot be reached geometrically by any atom and the intensity is set to zero. The region in between is a penumbra in which the intensity decreases linearly. The integration of the differential flux including the weight function at an oven temperature of 160 °C gives a total flux into the MOT-area of $2.7 \cdot 10^{12}$ atoms/s. This includes both Rubidium isotopes.

The longitudinal velocity distribution of the emitted atoms follows a modified Maxwell-Boltzmann distribution [213]

$$f(v) = \frac{2}{\alpha} v^3 e^{-\frac{v^2}{\alpha^2}}, \tag{3.18}$$

with $\alpha = \sqrt{2k_B T/m}$. The mean velocity is given by $\overline{v} = \sqrt{8k_B T/(\pi m)}$ and is at 160 °C 325 m/s. The radial velocity is limited by the apertures for a particle with a mean velocity of 325 m/s to a maximum value of 2.6 m/s.

3.6 The Zeeman slower

A magneto-optical trap (MOT) is unfortunately not able to catch most of the atoms of a thermal beam emitted by an effusive oven. The capture range of a MOT of about 30 m/s is ten times smaller than the mean velocity of the atomic beam leaving an effusive oven at 160 °C. However, the thermal atoms can be slowed down by scattering resonant photons from a counter-propagating laser beam. With each photon absorbed, the momentum of the atom is reduced in average by $\hbar k$. The recoil velocity per absorption is 5.88 mm/s and assuming an initial velocity of 300 m/s an atom has to scatter roughly $5 \cdot 10^4$ photons to bring it to a halt. Including the maximum scattering rate $\Gamma/2$ (see table A.2) the atoms come to rest within 3 ms. The maximum acceleration $a_{\text{max}} = 1.1 \cdot 10^5$ m/s^2 reduces the minimum length of the slower to less than half a meter. The downside of the longitudinal slowing is a radial increase of momentum by spontaneously emitted photons. Although the center of mass of all emitted photons add up to zero, remains a contribution of the mean square deviation, which scales with the square root of number of scattered photons. For the parameters given above the increase of the radial velocity is about 1.3 m/s.

The technical implementation of such a slowing method is the Zeeman-slowing technique [214]. The altering Doppler shift of the atoms during deceleration is compensated by suitable magnetic fields to keep them in resonance by the Zeeman shift. A much more detailed description of the Zeeman-slowing technique than given here, can be found in [215].

The necessary slower length to stop Rubidium atoms with an initial velocity of 305 m/s is 0.422 m. In our actual slower design this length was doubled to be 0.850 m to ensure robust operation. By this, irregularities in the magnetic field and scattering rates below $\Gamma/2$ can be corrected.

As the atoms are slowed down, the reduced Doppler shift has to be compensated with a spatial dependent magnetic field appropriate to the velocities of the atoms. There are two ways to compensate the Doppler shift, first using the $|F = 2, m_F = -2\rangle \rightarrow |F' = 3, m'_F = -3\rangle$ cycling transition with a decreasing magnetic field for slower atoms or the $|F = 2, m_F = 2\rangle \rightarrow |F' = 3, m'_F = 3\rangle$ with an increasing magnetic field. The latter has the advantage that the large magnetic field at the end of the slower for the stopped atoms results in a large detuning of the σ^+ polarized cooling light and is not disturbing the MOT when it passes through it. One can take advantage of this effect by even enlarging this detuning with an additional magnetic offset field. The disadvantage of this method is an additional magnetic field at the position of the MOT, which has to be compensated by some extra coils.

To determine the geometry of the actual slower design and the required magnetic field distributions we start with the maximum acceleration acting on the atoms

$$a = \frac{\hbar k \Gamma}{2m}, \tag{3.19}$$

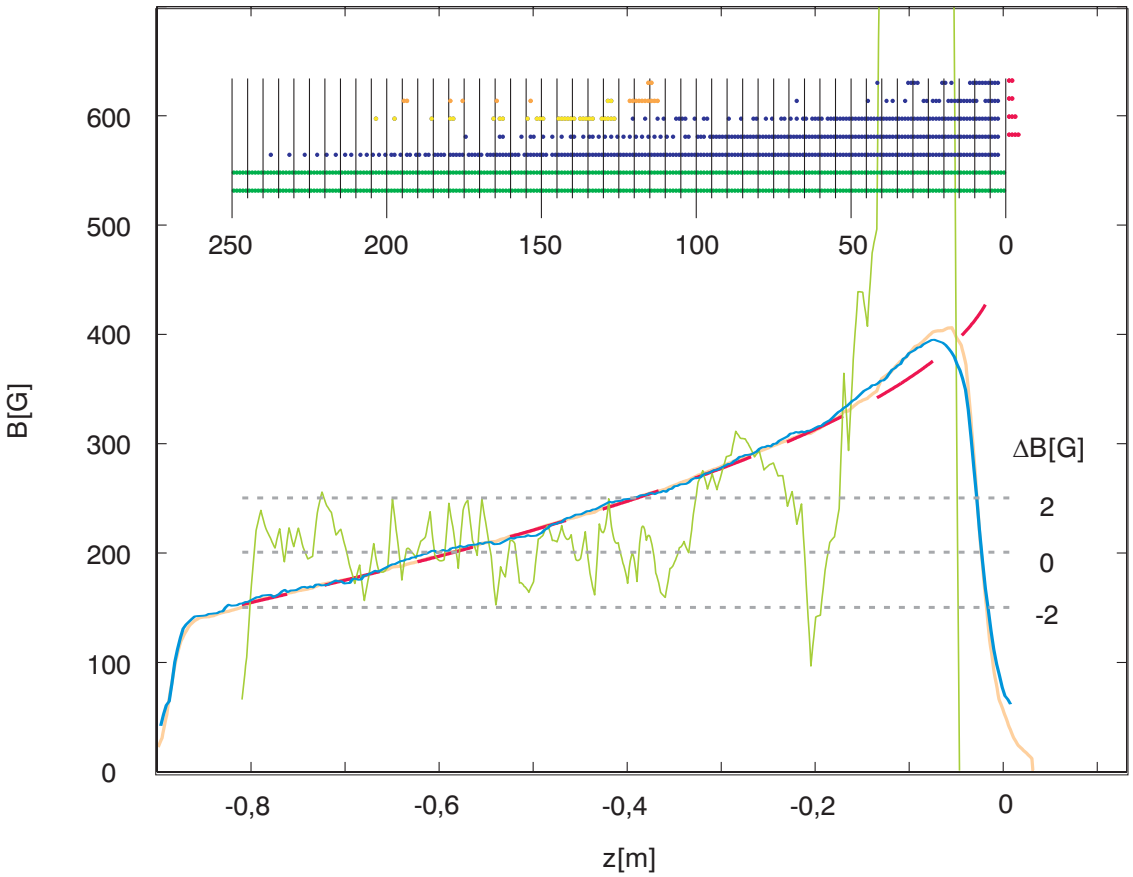

Figure 3.12: Winding plan of the Zeeman-slower and the resulting magnetic field. In the upper part of the figure the windings are displayed by the filled circles. The vertical lines give the number of rows where a winding has to be located. The colors indicate the applied currents. Green 20 A, blue 15 A, red 100 A, yellow -5.7 A and orange 5.7 A. The red curve in the lower graph is the desired course of the magnetic field. The brown curve is calculated with the winding plan and the given currents. The blue curve is a measurement of the actual slower and the green curve gives the deviation from the theoretical (brown) result.

which is valid for large intensities. An atom starting from the oven with a velocity v_0 will be decelerated as

$$v(z) = \sqrt{v_0^2 - 2az}. \tag{3.20}$$

The length of the slower is therefore $L = (v_0^2 - v_{\text{end}}^2)/2a$. The magnetic field shifts the atomic transition as

$$\delta = (m_F' g_F' - m_F g_F)\mu_B B_z/\hbar, \tag{3.21}$$

assuming that there is only a magnetic field along the z-direction present. For any stretched transition, as we use it here, becomes the detuning $\delta = \mu_B B_z/\hbar$. Putting everything together the progression of the magnetic field has to be

$$B(z) = \frac{\hbar}{\mu_B}\left(-k v_0 + k\sqrt{v_0^2 - 2az}\right) + B_0, \tag{3.22}$$

where B_0 is the additional constant magnetic field along the z-direction.

Of interest is finally only the loading rate of Zeeman slowed atoms into the MOT. For this the atoms have to be at first slow enough to be in the capture range of the MOT. But they also have to be spatially inside the capture radius of the MOT which is on the order of a few centimeters. There are in principal three spatial broadening mechanisms which have to be taken into account. First of all we have seen in chapter 3.1.1 that there is a principal broadening of the hot atom beam due to the geometrical constraints of the apertures (see figure 3.11). This radial distribution is additionally broadened by the increased time of flight time of the slowed atoms. The radial heating by the spontaneous emitted photons has to be added to the radial temperature by geometrical constraints. The transversal velocity due to heating at the end of the slower is given by

$$v_\rho = \frac{\hbar k}{m}\sqrt{n}. \tag{3.23}$$

The number n of scattered photons is $n = m(v_i - v_f)/\hbar k$ with v_i the initial velocity and v_f the final velocity. For an atom starting with 300 m/s and decelerating it down to standstill, the transversal velocity calculates $v_\rho = 1.3$ m/s. Adding the radial velocity of 2.6 m/s from geometrical constraints with the radial heating in quadrature, the transversal velocity is approximately 2.9 m/s. More details of this additional broadening effects can be found in [215].

There are two laser frequencies required to operate the Zeeman-slower. Besides the cooling laser one has to include a repumping laser, which transfers atoms from the $F = 1$ state into the $F = 2$ ground state. The repumper is tuned to the $F = 1 \rightarrow F' = 2$ transition from which the atoms can decay into the F=2 state. Since the Landé factor for $F = 1$ ($g_{F=1} = -1/2$) differs from $F = 2$ ($g_{F=1} = 1/2$) it is not possible to keep the repumping laser in resonance over the full length of the slower. So it is best to tune the repumper such, that the atoms leaving the oven are as soon as possible transferred into the $F = 2$ state. It is also advantageous to have the same polarization for the repumping laser and the cooling laser, because this transfers the equally occupied m_F states towards the desired $m_F = 2$ state. Inside the slower the atoms stay most likely within the cycling transition, even with an imperfect circular polarization of the cooling beam. The differing Zeeman-shifts for π-transitions (or even larger shifts for σ^-) reduces the pumping into wrong states. Table 3.2 summarizes the experimental specifications of our Zeeman-slower.

Length	0.850m
Maximum capture velocity	305m/s
Offset field	150 G
Field at slower end	428 G
Total detuning of cooling laser	599 MHz
Detuning due to Doppler shift	389 MHz
Detuning due to offset field	210 MHz

Table 3.2: *Properties of the Zeeman-slower.*

Finally the loading rate R of the magneto-optical trap shall be estimated.

$$R = \xi_1\xi_2\xi_3\Phi. \tag{3.24}$$

The initial flux Φ reaching the region of the magneto optical trap (MOT) is reduced by several constraints. First of all $\xi_1 = 0.28$ (see chapter A.1) takes care of the natural abundance of ^{87}Rb. The next factor accounts for the capture range of the Zeeman-slower which was designed to be at 305 m/s. For an oven temperature of 160 °C one can calculate the reduced flux with equation (3.18) to $\xi_2 = 0.309$. The last factor ξ_3 is the contribution of the finite spatial capture range of the MOT. Since this last factor depends on the size of the laser beams, the magnetic field gradients of the MOT and the detailed radial flux distribution of the Zeeman-slowed atoms, is it difficult to give an exact value. A reasonable elaborate estimation following [192] gives $\xi_3 = 0.2$. With an initial flux of $\Phi = 2.7 \cdot 10^{12}$ atoms/s at 160 °C is the expected loading rate of the MOT $R = 4.7 \cdot 10^{10}$ atoms/s.

3.7 Magneto-optical trap and molasses cooling

This chapter presents the experimental results of the different laser cooling steps. Since the first realization of a magneto-optical trap (MOT) in 1987 [132] several hundred articles dealing with all kind of aspects of laser cooling have been published till today. The physics of MOTs with not a too large atom number is understood very well [81, 82, 83, 216]. But with an increasing atom number the complexity of interactions raises and only phenomenological models [217, 136] are available. For even larger numbers of trapped atoms, as we realized it in our setup, no theoretical description is available at all.

3.7.1 Magneto-optical trap

The cold atomic beam, described in the chapter before, is now used to load a MOT. The MOT operates with three orthogonal pairs of counter-propagating circular polarized laser beams and a magnetic quadrupole field (see chapter 2.1.2). The laser beams enter radially the vacuum chamber at the ports 2, 5, 8 and 11 and axially through ports 18 as defined in figure 3.2. There is a total power of 300 mW cooling light available, which is detuned to the red by about 2.5 Γ from the $F = 2$ to $F' = 3$ transition. The beam size of the radial beams is roughly ($1/e^2$ radius) 2.5 cm and axially, limited by the size of the viewport, about 1.2 cm. The measured intensities in the center of each radial beam are about 8 saturation intensities (I_{sat}=1.6W/m^2) and axially 23 saturation intensities.

In addition to the cooling light the repumping light is overlapped in two axes of the radial ports. The repumper returns the atoms via the $F = 1$ to $F' = 2$ transition, from which they decay with a 50 % probability into the $F = 2$ ground state, back into the cooling cycle. The total available repumping power for the MOT is 40 mW.

The magnetic quadrupole field is generated by two coils in anti-Helmholtz configuration (see section 3.9). A current of 17.5 A in each coil results in an axial gradient of 17 G/cm and radially of 8.5 G/cm.

It is preferable to have a large atom number in the MOT because it eases the succeeding evaporative cooling. In figure 3.13 some properties of the MOT are depicted. The oven temperature was set to 160 °C. We are able to load the MOT with well more than 10^{10} atoms, which is on the large side of all reported MOTs. The largest reported atom number of $6 \cdot 10^{10}$ atoms in a MOT has been achieved by [179]. The loading curve was fitted to the solution of simple rate equation $\dot{N} = R - \Gamma_{MOT} N$ with an atom number N in the MOT. The measured loading rate into the MOT

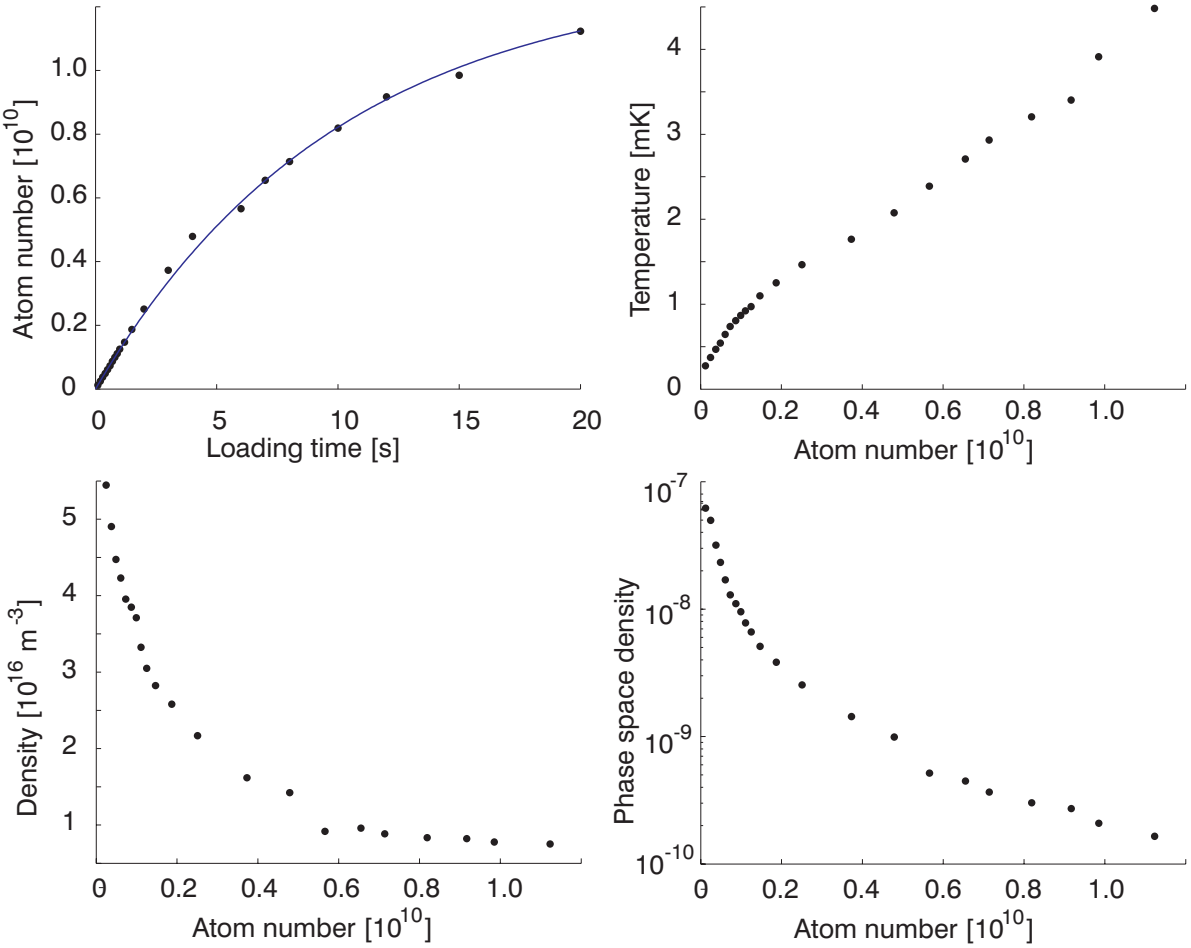

Figure 3.13: Meausered properties of the magneto-optical trap. Upper left: Loading of the MOT. The solid line is a simple model discussed in the text. Upper right: Temperature of the MOT versus atom number in the MOT. Lower left: Peak density in the MOT verus atom number. Lower left: Peak phase space density versus atom number.

is $R = 1.3 \cdot 10^9$ atoms/s and the loss rate is $\Gamma_{\mathrm{MOT}} = 0.1$ 1/s. The appendant curve is plotted in the upper left of figure 3.13. The measured loading rate is by more than an order of magnitude lower than the expected $R = 4.7 \cdot 10^{10}$ atoms/s given in chapter 3.6. The major forfeit of flux is probably due to a slight misalignment of the oven nozzle, the differential pumping tube and the Zeeman-slowing tube, which clips a part of the thermal beam leaving the oven.

The advantage of a large atom number in the MOT comes along with a temperature increase up to several milli-Kelvin and a distinct loss in density. Both reduces the phase space density by nearly three orders of magnitude. The reason for this is the large optical density of the cloud, such that the cooling light cannot reach anymore the inner lying atoms. This also leads to multiple scattering of light inside the cloud (radiation trapping) and by this to heating. The high temperature is not a problem, as the sample can be shock-frosted by molasses cooling as shown in the next section. The density could also be increased, by compressing the MOT via rising the current for the magnetic quadrupole field quickly at the end of the loading step [122, 218]. However we are hindered to do so right now, since the currently used power supplies feature not enough current.

After the mechanical shutter in the oven part is closed, disrupting the atomic flux, the MOT starts

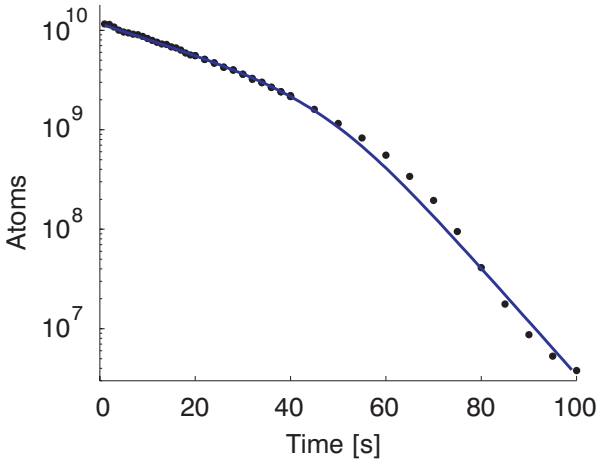

Figure 3.14: Non-exponential decay of the atom number in a magneto-optical trap.

to decay. Looking at the semi-log representation of the decay in figure 3.14, it exhibits a clear nonlinear behavior. At high enough densities two-body losses by light assisted collisions [219] have to be added in the rate equation

$$\frac{dN}{dt} = -\Gamma_{\mathrm{MOT}} N - \beta N \langle n \rangle. \tag{3.25}$$

The two-body loss is proportional to the mean density $\langle n \rangle$ which is itself a function of the atom number N (see figure 3.13). To solve this differential equation I extracted from the data an interpolating function $\langle n \rangle(N)$ and integrated the differential equation numerically. The best agreement was reached for $\beta = 4.6 \cdot 10^{-18}$ m^3/s and $\Gamma_{MOT} = 0.023$ s^{-1}. A previous measurement gave $\beta = 3.4 \cdot 10^{-18}$ m^3/s [219]. The lifetime of the MOT is about $\Gamma_{MOT}^{-1} = 43$ s which is much shorter than the sole lifetime due to background pressure of about 163 s. But atoms are also lost from the MOT by imbalance of the intensities of the laser beams or by regions with a speckled patterns contribution.

3.7.2 Molasses cooling

The temperature of the MOT is way too large to be caught in a pure magnetic trap and a further cooling step is inevitable. The so called molasses cooling [141] is such a method and can be implemented with the same arrangement of the lasers as used for the MOT. The polarization is the same, but one has to set the frequency of the cooling light by some linewidths into the red and switch of all magnetic fields. To be sure that there is not any magnetic field present, we added three pairs of Helmoltz coils, one for each axes, to tune the magnetic field to zero. By this the earth magnetic field and stray fields from the ion pumps can easily be compensated.

After the MOT is loaded, all magnetic fields are switched off and the compensation fields are switched on. Simultaneously the detuning of the laser is switched to -15.5 Γ. The intensity drops due to the reduced efficiency of the accusto-optical modulator by 30 %. The molasses is kept on for 10 ms, after which the atoms have reached their equilibrium temperature. There is an initial atom loss of more than 50 % compared to the MOT, but the atom number stays nearly constant if the molasses time is extended to 50 ms. Figure 3.15 shows the temperatures after 10 ms of

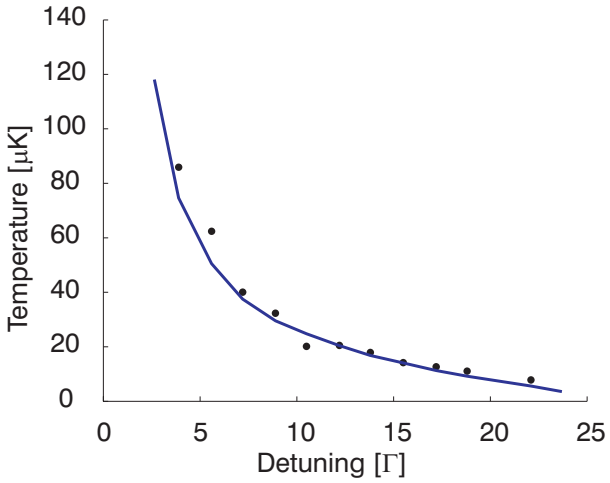

Figure 3.15: Molasses temperature versus detuning from resonance. The light for molasses cooling was applied for 10 ms. The solid line is proportional to I/δ to guide the eye.

molasses cooling time for different detunings. The solid line follows the expected course of the temperature as $T \sim I/\delta$ [217, 137]. The loss in density after the molasses cooling stage can be attributed to the loss of atoms.

The cold atomic cloud after the molasses cooling step is typically quite large with an 1/e width of $\sigma = 3$ mm. It is very hard to catch such a large cloud in a magnetic trap without loss of phase space densitity, since the trapping frequencies for a mode matched trap have to be very small (see chapter 3.9). One possibility to avoid this problem is to introduce a compression step at the end of the loading of the MOT [220].

3.8 Optical pumping

After the molasses cooling step the atoms are equally distributed over all m_F levels and have to be transferred into the trapable $F = 2$, $m_F = 2$ state. This is done by an axial circular polarized pumping beam. We apply this beam for 1 ms while the magnetic trapping fields are switched on. Doing so, we end up with about three times more atoms caught in the magnetic trap. Without pumping we would expect to catch only 2/5 of the atoms, which gives a maximum gain of trapped atoms by a factor of 2.5. The explanation for this even better gain in trapped atom numbers is most likely given by an unequal distribution over the five magnetic sub-levels of the $F = 2$ state after the molasses cooling step. Finally it should be mentioned that the cloud is not noticeable heated by the pumping light.

3.9 Magnetic trapping

In our setup we use a magnetic trap in the so called cloverleaf configuration [154, 155]. The design of the actual trap is limited by the geometric boundary conditions given by the physical dimensions of the vacuum chamber (see appendix F) and the resistance of the copper wires.

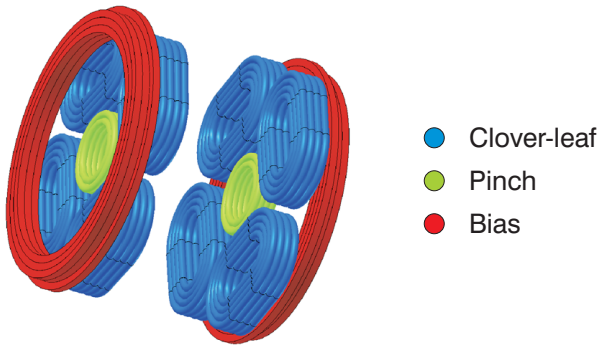

Figure 3.16: The winding scheme of the cloverleaf magnetic trap. The functionality is explained in chapter 2.2. A single leaf (blue) consists of 16 loops arranged in four windings in four layers. In the middle of the four leafs, consisting of four windings and two layers, are the pinch coils (green) located. The offset field produced by the pinch coils is compensated by the bias coils (red). They are made of four layers of the first windings and three layers for the remaining three windings. The inner open diameter of the pinch coils is 29 mm and the outer diameter of the bias coils is 155 mm.

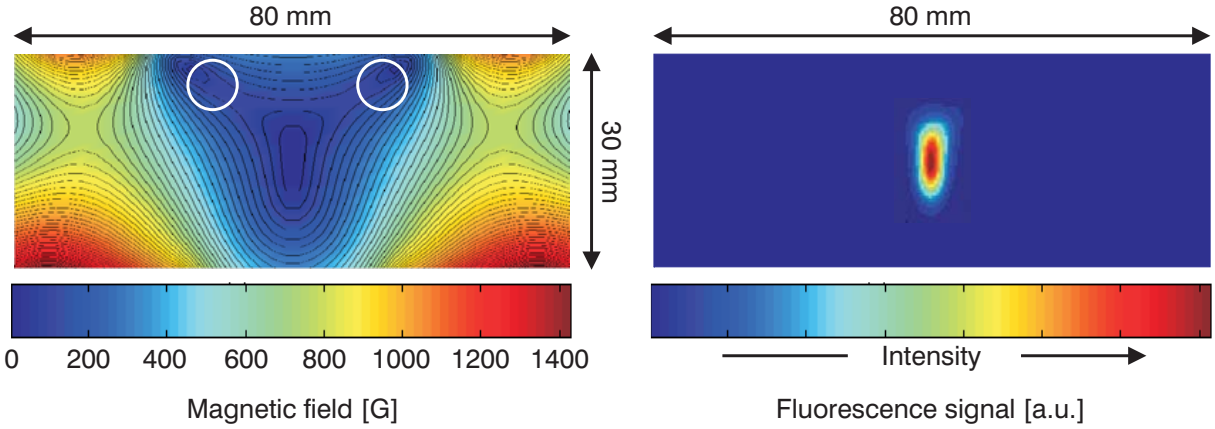

Figure 3.17: Magnetic field distribution and magnetically trapped atoms. The left figure shows the calculated absolute value of the magnetic field for 400 A in all coils with the given geometry as defined in figure 3.9. The offset field in the center (dark blue) is about one Gauss. The white circles indicate the instability points of the trap, which are potential saddle points at which the atoms can leave the trap (see equation 2.24). On the right a fluorescence picture of $2 \cdot 10^9$ trapped atoms at 500 μK is shown. The trapped atoms exhibit the shape as expected from the magnetic field distribution with an additional slightly triangular contribution.

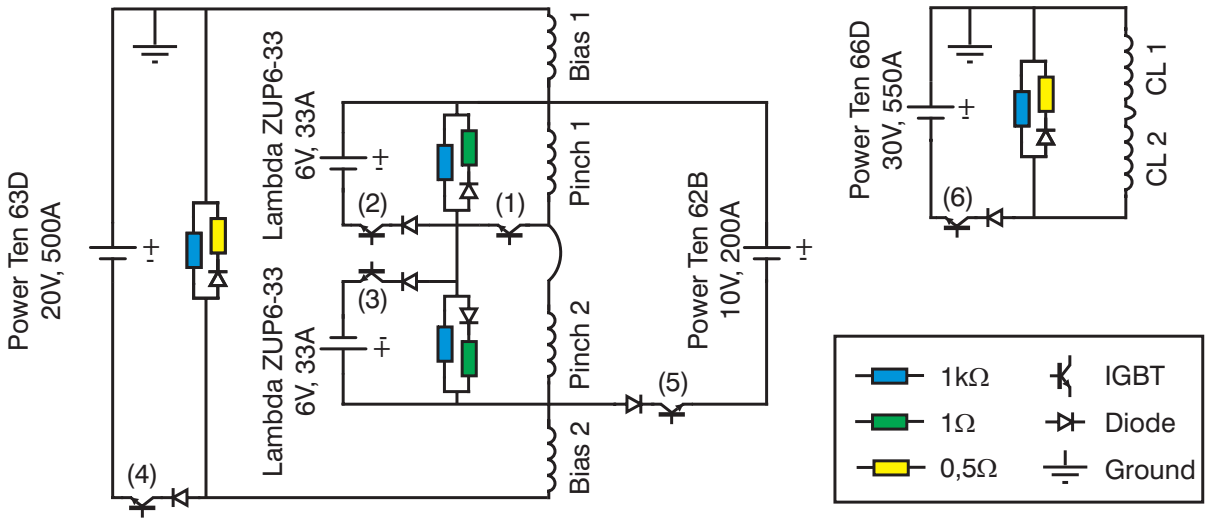

Figure 3.18: Circuits for magnetic field generation. The elementary circuit consists of a power supply, an IGBT switch (insulated-gate bipolar transistor), a diode to avoid opposite currents and a ring-down assembly. The coils exhibit an ohmic resistance as well an inductive load. When switching off the current with the IGBT switch, the stored inductive energy is transferred via an ultra fast rectifier diode into the ring down circuity, where it is dissipated in a small ohmic resistor (0.5 Ω or 1 Ω). A parallel resistor (1 kΩ) discharges remanent voltages on the ring down diode. To protect the power supplies, IGBTs and diodes against high voltage pulses we inserted on several places varistors and transient voltage suppressors. Additionally the power supplies are protected against opposite currents with bypassing diodes.
The field gradients for the MOT are generated by the two ZUP6-33 power supplies and closing the switches (1), (2) and (3). Pinch 1 and pinch 2 refer to the pinch coils on each side of the vacuum chamber. The catch trap is operated with the three Power Ten supplies and the IGBTs (4), (5) and (6). The opened IGBT (1) takes care, that no current is bypassed via the ring down of the upper ZUP6-33. During compression of the trap, the current of the Power Ten 62B supply is ramped down and finally switched off with IGBT (5). The full compressed trap is operated at 400 A in the pinch coils, the bias coils and the electronically separated cloverleaf coils (CL).

To achieve adequate field strengths it turns out that the needed current densities are to large for simple copper wires. Therefore we use hollow copper tubings through which cooling water is pumped. The used tubing has an outer diameter of 4 mm and an inner diameter of 2 mm. One leaf of the cloverleafs is made of about 20 m of copper tubing. At a pressure of 12 bar is the cooling water flux through one leaf about 2 l/min, which allows us to apply currents up to 500 A continuously. The temperature of the coils increases then only by a few degree Celsius. The detailed geometry of the coils is shown in figure 3.9.

To obtain the actual absolute value of the magnetic field distributions we either gave the atoms a kick by an magnetic field pulse and measured the oscillation of the center of mass or we recorded directly the density distribution inside the trap. We did so for different temperatures of the clouds and combinations of currents. The axial curvature is given by $B'' = 0.5$ G/cm^2 per Ampere and a radial gradient of $B' = 0.607$ G/cm per Ampere. The offset field is about 1 G, when 400 A are running through the cloverleaf coils and as well through the pinch and bias coils. With additional axial coils in Helmholtz configuration one can fine tune the offset by a few Gauss.

By applying 400 Amperes in all coils the trapping frequencies are measured to be 18 Hz axially and 310 Hz radially. Figure 3.9 shows the distribution of the absolute value of the magnetic field and the shape of a trapped atomic cloud. The simulation of the magnetic field is done by decomposing

the windings into small linear sections and calculating the field of each piece with Biot-Savarts law [221].

The requirements on the high current power supplies are very demanding. Any current noise of the source leads to parametric heating of the trapped atoms [222, 223]. We estimated that the noise level has to be lower than 10^{-5} to be on the save side. This specifications are fulfilled by the power supply units used in our setup[23]. It is also necessary to switch the currents very fast on and off. The detailed electronic circuits are explained in figure 3.18. The switch on time is on the order of a few 100 μs, which is achieved by biasing the supplies to a certain voltage. The switch off time has to be short compared to the trapping frequency to avoid any adiabatic effects for the time of flight expansion. This is accomplished by special ring-down circuits, which pick up the currents and dissipate them within 50 μs in a specialized low-ohmic resistor. However, there remain some magnetic fields due to eddy currents in the copper gaskets of the CF250 flanges (see figure F.1). These fields do not significantly alter the expansion of the cloud but make it impractical to do absorption imaging within the the first milliseconds after releasing the cloud from the magnetic trap.

After the molasses cooling step and the optical pumping the atoms are initially transferred into a mode matched magnetic trap. This catching trap ideally exhibits the same temperature and density distribution for the trapped atoms as it does for the molasses cooled cloud. This would allow to transfer all atoms without loss in phase space density from the molasses cooled cloud to the magnetic trap. In our case we have to deal with rather large sized magneto-optical traps, which demand small curvatures and leads to a too large gravitational sag. To optimize the transfer we shifted the magneto-optical trap by an additional constant field downwards to the equilibrium position of the catch trap. Since the trap is too shallow for the desired parameters, we have to use a steeper confinement than desired. This leads to an loss in phase space density by more than one order of magnitude (see figure 3.1).

The catch trap is only kept on for one millisecond during which the polarizing light is applied. In a last step the trap is compressed to the final setting within 600 ms. The peak phase space density increases by such a compression from a harmonic trap to a linear one by an factor of $e = 2.718\ldots$, which is due to the altered geometry [224].

3.10 Evaporative cooling

About $2 \cdot 10^9$ atoms at 600-700 μK are initially trapped in a magnetic trap in the $F = 2, m_F = 2$ state. The trap has an offset B_0 of 1.5 G, a radial gradient B′ of 243 G/cm and an axial curvature of 200 G/cm^2. The initial scattering rate $n \cdot \sigma \cdot v$ is about ten per second. Contrary to this stands the trap loss collision rate of 1/163 per second (see figure 3.6). This gives a ratio of good (elastic) to bad (trap loss) collisions of 1600.

The forced evaporation cooling scheme for our experimental situation is shown in figure 3.19. The magnetic trap creates a space dependent Zeeman shift for the trapped atoms. A radio frequency field is tuned to the difference of the Zeeman shift between two magnetic sublevels. In our case we only address states within one hyperfine manifold, but with the usage of the microwave setup (see chapter 5.2) we also demonstrated evaporative cooling by transferring the atoms form $F = 2, m_F = 2$ state into the untrapped $F = 1, m_F = 0$ state.

[23] P63D 20330, P63D 20500 and P66D 30550, PowerTen

Figure 3.20 shows the geometry of the radio frequency antenna used for evaporative cooling. The coils had to be placed beyond the recessed buckets, since the center of the trap is already reserved for the field plates (see chapter 5.3). The consequence is, that the atoms are not located in the near field of the antenna, since the distance to the antenna is larger than the extensions of the coil. It is also disadvantageous that parts of the antenna are hidden (from the atom perspective) behind the recessed buckets and that the distance of the buckets is much smaller than the wavelength. The measurement of the evanescent field at the position of the trapped atoms, shows that the magnetic field strength is still sufficient for evaporative cooling.

The efficiency ξ of the evaporative cooling can be expressed in the gain of phase space density versus atom loss.

$$\xi = \left| \frac{d\,\mathrm{psd}/\mathrm{psd}}{dN/N} \right|. \tag{3.26}$$

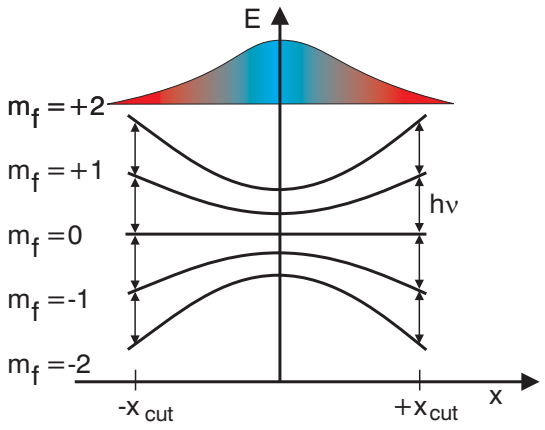

Figure 3.19: Evaporation of magnetically trapped atoms by radio frequency fields. Depicted are the Zeeman energies of the magnetic sub-states. The top shows a schematic distribution of a thermal atomic cloud. The atoms are trapped in the $F = 2, m_F = 2$ state. Atoms with more than average energy extend to regions of larger magnetic field, where they undergo a Landau-Zener transition into lower lying states due to a radio frequency field with energy $h\nu$. After two transitions the atoms are in a $m_F = 0$ state and are not anymore trapped. With this technique it is possible to extract only the most energetic atoms out of the trap as demanded in chapter 2.3

In our experiment we reach a value of ξ=2.6 by drawing a line connecting the initial cloud before evaporation and the point of the phase transition as shown in figure 3.21. Other groups [159, 225, 226, 147] reported values of about three.

Figure 3.22 shows the same set of data as in figure 3.21 but now as a function of temperature. In this figure are the truncation energies E_{cut} of the radio-frequency field included (horizontal lines), which are defined by

$$E_{\mathrm{cut}} = 2h\nu - m_F g_F \mu_B B_0. \tag{3.27}$$

Every atom with an energy larger than E_{cut} will be removed from the trap. The truncation energy has to be corrected by the offset of the magnetic trap. The horizontal lines on figure 3.22 represent

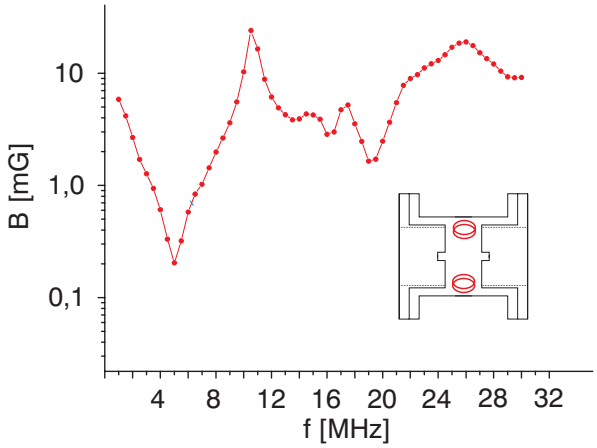

Figure 3.20: Magnetic field generated by the antennas inside the chamber versus applied frequency. The antenna (red) consists of a pair of two windings in Helmholtz configuration (see F.1). The field was measured with a single pick-up loop. The loop was aligned such, that the measured magnetic field component was perpendicular to the quantization field of the magnetic trap. The applied power was 500 mW. In the final setup we used a homebuild frequency generator which is capable to generate arbitrary frequencies up to 45 MHz. The synthesizer has also an analog input to adjust the power. The rf signal from the frequency generator is subsequent amplified (AP5500-2, FPA) to a maximum power of 2 W. This is a factor of 2 in the magnetic field as depicted above.

the truncation temperature, which is simply $T_{\mathrm{cut}} = E_{\mathrm{cut}}/k_B$. Finally one can define a truncation parameter η as

$$\eta = \frac{E_{\mathrm{cut}}}{k_B T}. \tag{3.28}$$

The optimum truncation parameter should be between 4 and 8 [158] to reach the regime of the so-called runaway evaporation [158]. In our experiment the initial truncation parameter is 6.8 and increases during evaporation continuously to about 30 close to the phase transition. The accuracy of the position of the truncation parameter decreases with lower temperatures. Although one can obtain reliable values for the temperatures of the cloud and the frequency of the rf field, it is much harder to get an exact value for the offset field. If the measured offset field of 1.5 G is only lower by 10 % changes the final truncation parameter from 30 to 20. Nevertheless it still seems that the truncation parameter is too large at very cold temperatures. This could have its reason in a too strong coupling of the radio-frequency field to the magnetic transition which is equivalent to a undesired broadening of the rf knife.

One can also define an efficiency for the evaporative cooling process in the temperature versus atom number representation

$$\alpha = \frac{dT/T}{dN/N}. \tag{3.29}$$

In our measurement we reached a value of $\alpha = 0.99$ by again connecting linearly the data point of the initial atomic cloud and the point of the phase transition. In [159] a value of $\alpha = 1.1$ was reached.

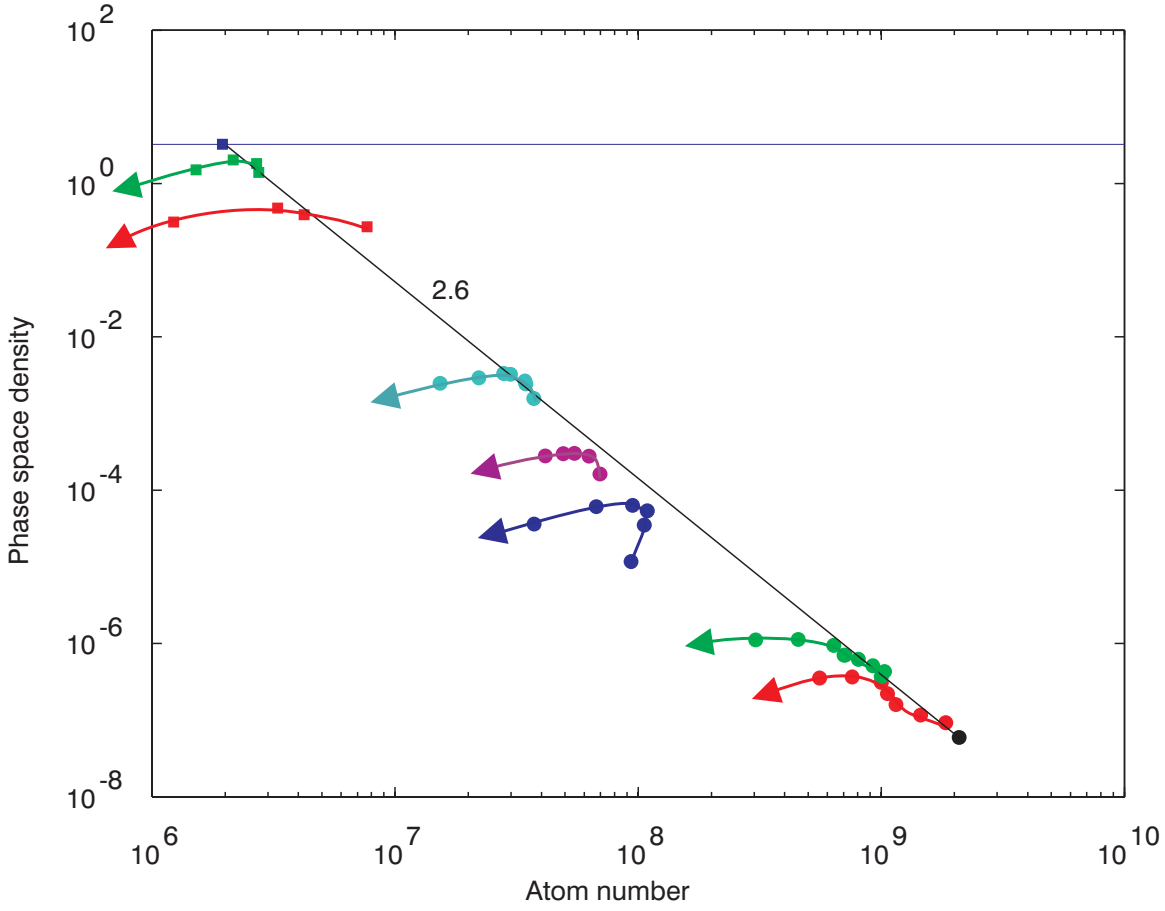

Figure 3.21: Phase space density versus atom number. The dots are acquired with fluorescence imaging and the squares with absorption imaging. The black dot on the lower right represents the initial situation in the magnetic trap. As a first evaporative step (red dots) a constant radio frequency of 36 MHz is applied for different times. The arrow indicates the direction of increasing time from 1 s to 60 s. The best value of 15 s is taken and the next step, a linear ramp (green dots) from 36 MHz down to 18 MHz is added. The time steps were altered again from 1 s to 60 s with 3 s being the best value. The blue dots represent a linear ramp from 18 Mhz to 5.625 Mhz within 1 s up to 60 s and the best result at 6s. The magenta colored dots are a ramp from 5.625 MHz to 3.94 MHz from 1 s to 15 s and 3 s best. This is followed by the cyan ramp from 3.94 MHz to 2.25 MHz, lasting 1 s to 30 s, and optimal at 3 s. The red squares are ramped from 2.25 MHz down to 1.4 MHz from 1 s to 9 s. The green squares are ramped from 2.25 MHz to 1.35 MHz within 1 s to 12 s. Additionally a constant rf field at 1.35 MHz was added for 100 ms. The final ramp which reaches the critical phase space density of 2.612 (blue line) starts also at 2.25 MHz and stops at 1.32 MHz within 3 s plus 100 ms at 1.32 MHz. The total evaporation takes 33.1 s. The bottom of the trap is 1.51 G which corresponds to a frequency of 1.06 MHz. The slope of 2.6 of the solid black line is the efficiency ξ of the evaporation as defined in equation (3.10).

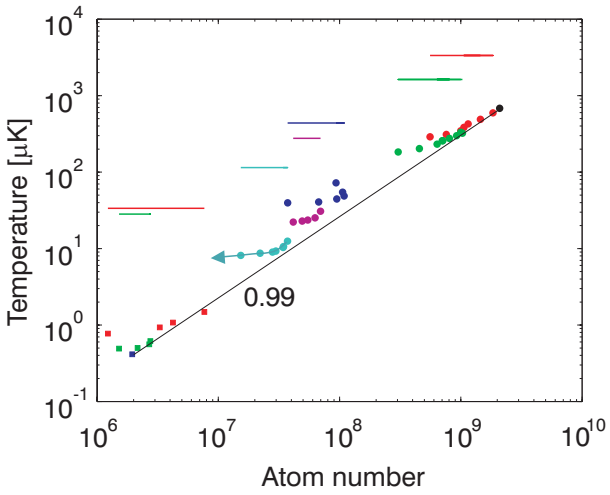

Figure 3.22: Temperature versus atom number. The color coding is identical to figure 3.21. The arrow within the cyan dots shows the direction of increasing time as explained in the caption of figure 3.21. The horizontal solid lines indicate the truncation energy for each step in the same color according to equation (3.10). For all linear ramps the final value of the the rf-sweep is taken. The slope 0.99 of the solid black line is the efficiency α as defined in equation (3.29) .

The measured phase transition occurs approximately at 400 nK with $1.5{\cdot}10^6$ atoms. The trapping frequencies for the given offset field of 1.5 G are radially 250 Hz and axially 18 Hz. The theoretically expected temperature of the phase transition is for this parameters 537 nK (see equation 2.39) and is in good agreement with the measured value.

3.11 Bose-Einstein condensation

When the evaporative cooling proceeds towards the critical temperature for the phase transition the density distribution undergoes an alteration from a pure Gaussian shape via a thermal Bose distribution to the parabolic shape of a pure Bose-Einstein condensate at T=0 K. Figure 3.23 shows the condensate fraction of the cold cloud as a function of temperature. The solid line refers to equation (2.40) with a critical temperature of 375 nK. The expected critical temperature (see equation 2.39) should be at 537 nK for the measured atom number and trap parameters. The temperatures for each data point in figure 3.23 have been extracted from a single absorption picture after 21 ms time of flight by fitting a Gaussian to the wings of the density distribution and is correct within 10 %. The deviation of the measured transition temperature can be caused by the finite number of particles as well by the interaction among the atoms. This effects are discussed in detail at the end of this chapter.

Figure 3.24 illustrates the analysis of the absorption images carried out on clouds after 21 ms time of flight. This analysis yields the temperature, the number of thermal atoms, the number of condensed atoms and the fraction of condensed atoms. Well above T_c the density distribution follows a simple Boltzmann distribution which has a Gaussian shape in real space as well in momentum space for a harmonic trapping potential. The widths σ of the cloud after a time of flight t can be converted into a temperature by assuming that the initial widths are negligible small by $k_b T = m(\sigma/t)^2$.

At temperatures close to T_c one has to take the enhanced occupation probability of lower lying states into account. This is caused by the Bose-distribution, which favors the lower lying states

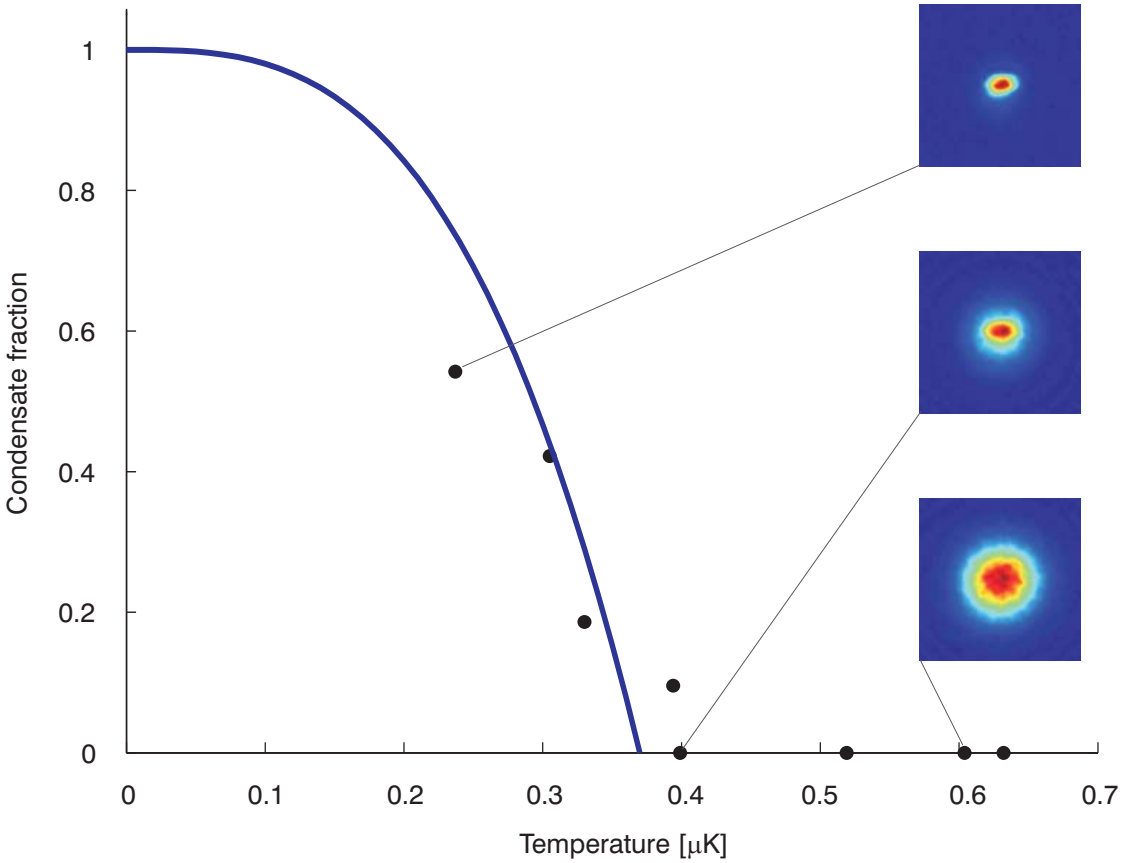

Figure 3.23: Fraction of Bose condensed atoms versus temperature. At the critical temperature T_c a macroscopic fraction of the atoms populates the ground state as described in chapter 2.4. The three absorption pictures are taken after 21 ms time of flight. The cloud well above T_c has a Gaussian distribution and is isotropic as expected for a thermal cloud. At $T = T_c$ the atomic cloud in the absorption picture is already anisotropic as one expects to see for a Bose-Einstein condensate. But the fitted cloud (right picture in figure 3.24) shows that there exists no condensate fraction. The anisotropy is caused by the distinct increase of the peak density due to the Bose enhancement. Finally the last absorption picture shows a clear Bose-Einstein condensate with about 55 % of the atoms in the condensate phase.

compared to the Boltzmann distribution. It has been shown [227, 228] that there exists a semiclassical description of the density distribution. This is valid in the ideal gas limit when the temperature is much higher than the level spacings of the confining potential $U(\vec{r})$. The density distribution is then given by

$$n(\vec{r}) = \frac{1}{\lambda_{\mathrm{dB}}^3} \sum_{j=1}^{\infty} \frac{e^{j(\mu - U(\vec{r}))/k_B T}}{j^{3/2}} = \frac{1}{\lambda_{\mathrm{dB}}^3} g_{3/2}\left(e^{(\mu - U(\vec{r}))/k_B T}\right). \tag{3.30}$$

To compare the theoretical density distribution with the two dimensional absorption pictures we have to integrate equation (3.30) along the y-axis.

$$\overline{n}_{\mathrm{Bose}}(x, z) = \overline{n}_{\mathrm{Bose},0} \sqrt{\pi} y_0 g_2\left(e^{-(x/x_0)^2 - (z/z_0)^2}\right) \tag{3.31}$$

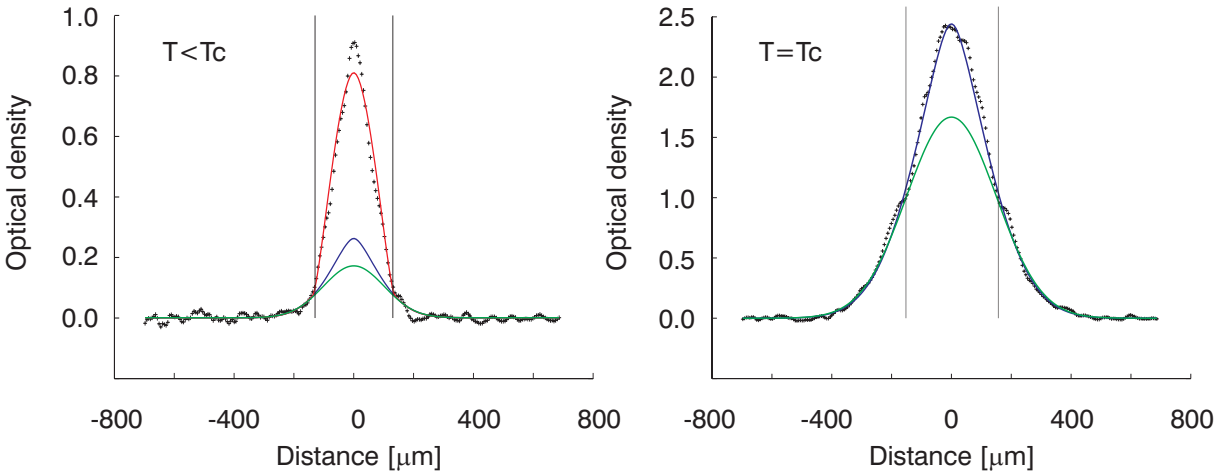

Figure 3.24: Density distribution at different temperatures. The picture show a central slice of two absorption images taken after 21 ms time of flight. The figure on the right is a thermal cloud just at the critical temperature as shown in figure 3.23. On the left an atomic cloud well below T_c is shown, which correspond to the data point with a condensate fraction of 55 % in figure 3.23. The vertical black lines indicate the part of the cloud which was taken for fitting the thermal contribution. The green curve is a Gaussian fit on the wings beyond the black lines. The blue line is the Bose enhanced distribution which shows, that there is actually no condensate present in the right figure. Finally the red line is the condensate in Thomas-Fermi approximation. The condensate fraction is reduced by the enhancement of the Bose distribution compared to the Gaussian distribution.

The trap is radially symmetric along z and one can set $x_0 = y_0$. The free parameters for a full two-dimensional fit are the peak column density and the widths x_0 and z_0. The fugacity[24] was set to one which corresponds to a chemical potential of $\mu = 0$. By this one neglects the effect of interactions in the non-condensed part of the atomic clouds. In order to use the density distribution (3.31) as a fitting function one has to expand the poly-logarithmic function according to $g_2(x) = \sum_{j=1}^{\infty} x^j/j^2$. In our case we included the first twenty terms.

The fraction of atoms, which is not fitted by the Bose distribution can be assigned to the Bose-Einstein condensate. For the degenerate part of the cloud we include again the interaction among the atoms and use also the Thomas-Fermi approximation. In a parabolic trap the density distribution has also a parabolic shape. Integration along the y-axis gives

$$\overline{n}_{\mathrm{BEC}}(x,z) = \max\left(\frac{4}{3}\overline{n}_{\mathrm{BEC},0} r_{\mathrm{TF},y}\left(1 - \frac{x^2}{r_{\mathrm{TF},x}^2} - \frac{x^2}{r_{\mathrm{TF},z}^2}\right)^{(3/2)}, 0\right), \tag{3.32}$$

with the Thomas-Fermi radii r_{TF} as defined in chapter 2.4. Also the condensed fraction of the cloud is radially symmetric along z and one can set $r_{\mathrm{TF},y} = r_{\mathrm{TF},x}$. The free parameters for fitting the measured distributions in the absorption pictures are, similar to the case of the Bose-distribution, the column peak densities $\overline{n}_{\mathrm{BEC},0}$ and the two Thomas-Fermi radii $r_{\mathrm{TF},y}$ and $r_{\mathrm{TF},x}$.

The sequence of fitting the data includes three steps. First a rectangular region in the center of the cold cloud is removed from the data and the remaining wings are fitted with a Gaussian

[24] The fugacity is defined as $z = e^{\beta\mu}$, with $\beta = k_B T$

to extract the temperature from their widths. The same wings are then fitted with the Bose-distribution to obtain the thermal fraction of the atomic ensemble. In the third step the fitted Bose distribution is subtracted from the complete cloud and the remaining data is fitted with the parabolic Bose-Einstein distribution.

The Bose-Einstein condensates contain about $3 \cdot 10^5$ atoms in a trap with a radial frequency of 250 Hz and axially of 18 Hz. This gives a peak density of $3.5 \cdot 10^{14}$ cm^{-3} and an interaction energy (chemical potential) of $\mu = 3$ kHz. The radial size is $r_{\mathrm{TF},x} = r_{\mathrm{TF},y} = 3.3\mu$m and axially $r_{\mathrm{TF},z} = 46\mu$m.

With the knowledge of the density it is possible to estimate the lifetime of the condensate due to three body recombination. The coefficient for this inelastic process is $\beta = 1.8 \cdot 10^{29}$ cm^6/s. The total scattering rate in the center of the cloud is then 2.2 s^{-1}, which corresponds to a lifetime of about 450 ms.

Now the effect of a finite particle number and the interaction among the atoms on the transition temperature shall be discussed. The finite size effect of a finite atom number shifts the transition point to lower temperatures and can be approximated by [164]

$$T_c(N) = \left(1 - \frac{\zeta(2)\zeta(3)^{-2/3}}{2}\frac{1}{N^{1/3}}\right) T_c^0 \approx \left(1 - 0.7275\frac{1}{N^{1/3}}\right) T_c^0, \tag{3.33}$$

where T_c^0 is the critical transition temperature in the thermodynamic limes, N the atom number and $\zeta(x)$ Riemann's zeta-function [163]. For atom numbers above one million, close to the critical temperature, this shift is less than 1 % and can be neglected in our case.

For a trapped gas in a harmonic oscillator potential is the shift due interactions given to the lowest order in the coupling constant $4\pi\hbar^2 a/m$ given by [229, 230]

$$T_c(a, N) = \left(1 - 1.33\frac{a}{\bar{a}_{ho}}N^{1/6}\right) T_c, \tag{3.34}$$

where a is the scattering length and $\bar{a}_{ho}$ the mean harmonic oscillator length of the trap. For our parameters the evaluated correction is well beyond the validity of the expansion and one can state that the critical temperature is shifted by more than 10 % due to interactions. A more detailed treatment of the real critical temperature has to be done numerically and is beyond the scope of this thesis.

In conclusion this chapter on the experimental methods shows that the performance of the setup is as desired and BECs can be produced reliably. The functionalities of the individual steps are well understood and quantitative specifications have been produced. With the full characterization of the BEC is the system now ready for exploring novel physics.

4 Theoretical results

4.1 The light induced dipole-dipole interaction

In this chapter, I investigate new physical aspects that arise in dense cold atomic samples irradiated by a near resonant laser beam. Atoms exposed to an electromagnetic wave respond as damped harmonic oscillators and exhibit an alternating electric dipole moment. The interaction energy of such dipoles can exceed the one of magnetic dipoles in atomic ground states by several orders of magnitude.

The idea of the proposed experiment described here is to study the coherent interaction of laser induced electric dipoles by transferring the interaction energy among the dipoles into kinetic energy, which can be probed with standard time of flight techniques. Initially, the dipoles are generated for a certain flash time by a laser beam with linear polarization in a spin polarized sample of cold atoms. During the flash time, the dipole moments reach a steady state and the light-induced dipole-dipole interaction potential is build up. As a first step, I calculate these potentials for a certain density distribution including the retardation effects of the dipolar fields and the driving electromagnetic wave. The flash time is chosen long enough that the atoms can evolve in the induced potential, namely to gain momentum, but short enough not to change the initial density distribution. As a next step I discuss the change of the initial momentum distribution for different geometries of the atomic cloud and as a function of the angle with respect to the linear polarization of the laser light.

The results of this chapter were published in [231] and are discussed in more detail in [232].

4.1.1 Light-induced dipole moments

In the following I assume a two level atom with an excited state lifetime Γ and an energy separation ω_0. The dynamics of an atom irradiated by coherent light with frequency ω can be treated with the optical Bloch equations as introduced in chapter 2.1. The operator of the dipole moment can be written as

$$\hat{d} = d_{ge}\left(|g\rangle\langle e| + |e\rangle\langle g|\right), \tag{4.1}$$

where d_{ge} is the dipole matrix element .

$$d_{ge} = \sqrt{\frac{3\varepsilon_0 h c^3}{2\omega_0^3}\Gamma}. \tag{4.2}$$

The expectation value $\langle\hat{d}\rangle$ of the dipole moment is

$$\langle\hat{d}\rangle = 2d_{ge}\left(u\cos(\omega t) - v\sin(\omega t)\right). \tag{4.3}$$

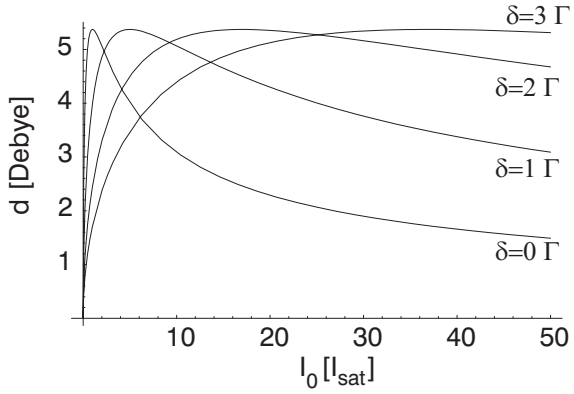

Figure 4.1: Expectation value of the amplitude of the dipole moment as given in equation (4.5).

The steady state expectation value d_{st} of this dipole moment is then, by inserting the steady state solutions for u and v

$$d_{st} = \frac{2d_{ge}}{\omega_R}\frac{s}{s+1}\left(\delta\cos(\omega t) - \frac{\Gamma}{2}\sin(\omega t)\right), \tag{4.4}$$

where $\delta = \omega - \omega_0$ is the detuning of the driving field. The dipole moment oscillates with the laser frequency with a phase shift depending on the detuning. The amplitude d of this oscillating dipole moment is

$$d = \sqrt{\frac{3\Gamma\varepsilon_0 hc^3}{\omega^3}}\frac{\sqrt{\frac{I_0}{I_{sat}}\left(1+\frac{4\delta^2}{\Gamma^2}\right)}}{1+\frac{4\delta^2}{\Gamma^2}+\frac{I_0}{I_{sat}}}. \tag{4.5}$$

As can be seen in figure 4.1 there exists for any detuning δ an intensity I_0 which maximizes the amplitude of the dipole moment to $d_{max} = \sqrt{3\Gamma\varepsilon_0 hc^3/4\omega^3}$. This happens if the intensity is set to

$$I_0 = I_{sat}\left(1+\frac{4\delta^2}{\Gamma^2}\right). \tag{4.6}$$

4.1.2 Potentials of interacting dipoles

In the following, I am dealing with oscillating dipoles driven by an electromagnetic wave with linear polarization and wave vector k. I assume that all dipole moments are of equal strength, oriented parallel and oscillate with the same frequency ω. The phase between two dipoles depends on the position of the atoms with respect to the electromagnetic wave phase fronts and the interatomic distance. The retarded interaction potential for two interacting dipoles with one dipole located at the origin and the other at $\vec{r_0}$ reads [233]

$$\tilde{V}_{\mathrm{dd}}(\vec{r_0},0) = \frac{d^2\cos(\vec{k}\cdot\vec{r_0})}{4\pi\varepsilon_0 r_0^3}\cdot \tag{4.7}$$
$$\cdot\sum_{i,j}[(\delta_{ij}-3\tfrac{r_{0,i}\,r_{0,j}}{r_0^2})(\cos(kr_0)+kr_0\sin(kr_0)) - (\delta_{ij}-\tfrac{r_{0,i}\,r_{0,j}}{r_0^2})(k^2r_0^2\cos(kr_0))], \qquad i,j = x,y,z,$$

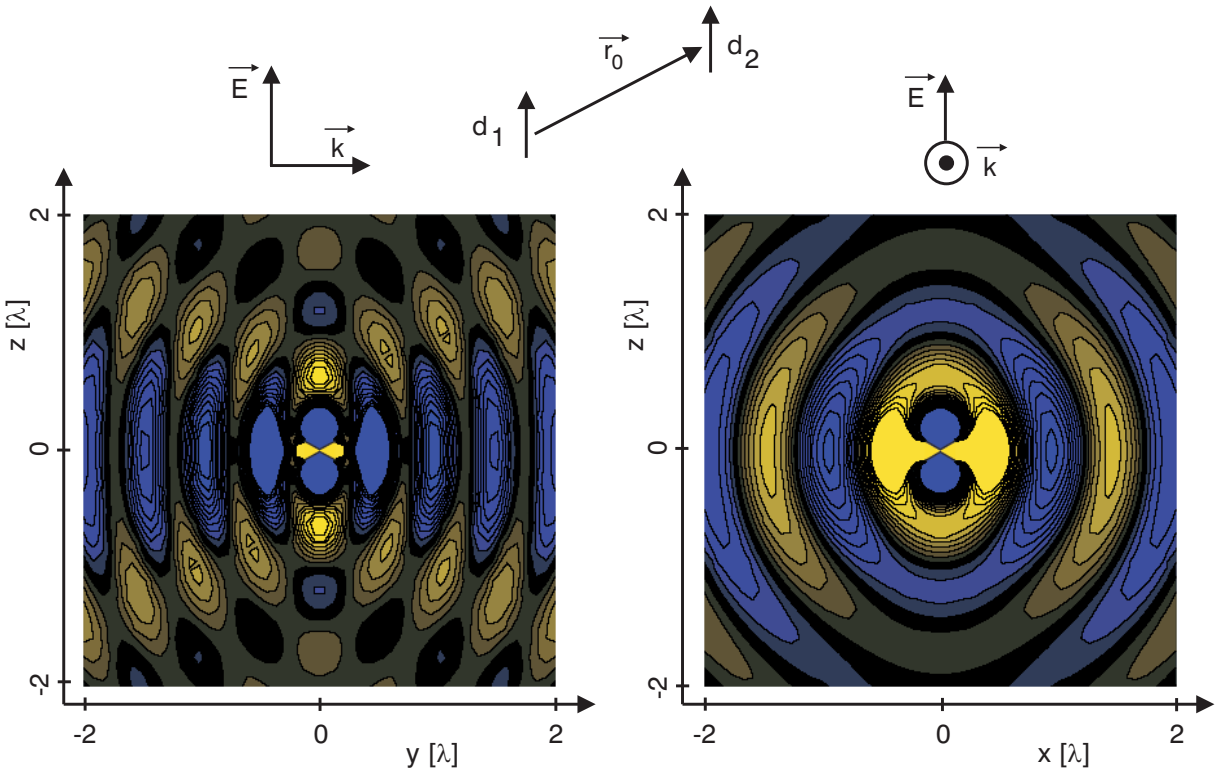

Figure 4.2: Retarded interaction potentials of two oscillating dipoles driven by an electromagnetic wave according to equation (4.7). The laser field is in both figures linearly polarized along the z-direction and the wave vector k of the traveling wave points in the y-direction. The two dipoles are separated by $\vec{r}$, where one is placed at the origin. The yellow regions correspond to a repulsive, the blue to an attractive potential. In the left figure the two dipoles lie in the yz-plane and in the right figure in the xz-plane.

where d is the absolute value of the dipole moment and $\vec{k}$ the wave vector of the driving field. The potentials generated by equation (4.7) are illustrated in figure 4.2. The retardation generates a potential pattern, where the potential is depending on the position either attractive or repulsive.

In a Bose-condensed sample we are typically dealing with many atoms. So I want to extend the description to a system of N pairwise interacting dipoles with a density distribution $n(\vec{r})$. The superposed potential $V_{\mathrm{dd}}(\vec{r_0})$ for a dipole at position $\vec{r_0}$ is given by

$$V_{\mathrm{dd}}(\vec{r_0}) = \int \tilde{V}_{\mathrm{dd}}(\vec{r_0}, \vec{r}) n(\vec{r}) d^3 r. \tag{4.8}$$

Replacing $\tilde{V}_{\mathrm{dd}}(\vec{r_0}, \vec{r})$ by $d^2 \cos(\vec{k} \cdot (\vec{r_0} - \vec{r})) \mathrm{V}'_{\mathrm{dd}}(\vec{r_0} - \vec{r})$, it is possible to rewrite the integral as a convolution

$$V_{\mathrm{dd}}(\vec{r_0}) = \int d^2 \cos(\vec{k} \cdot (\vec{r_0} - \vec{r})) \mathrm{V}'_{\mathrm{dd}}(\vec{r_0} - \vec{r}) n(\vec{r}) d^3 r, \tag{4.9}$$

to which the convolution theorem can be applied.

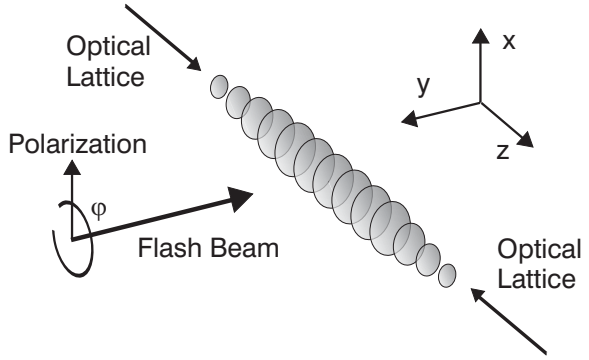

Figure 4.3: A Bose-Einstein condensate within an one-dimensional optical lattice. The resulting density distribution is a stack of pancake-shaped condensates. A laser along the y-direction induces the dipole-dipole interaction. The linear polarization of the flash beam can be altered from x-polarization (φ=0°) to z-polarization (φ=90°). The altered momentum distribution is either projected onto the x-z plane or the y-z plane.

4.1.3 The experimental situation

The underlying geometries of the proposed experiment are shown in figure 4.3. The desired parameters are realistic in a typical Bose-Einstein condensate experiment with ^{87}Rb atoms in the F=2, m_F=2 ground state. The atomic cloud is confined in a cigar-shaped magnetic trap with the long axes along z as depicted in figure 4.3. In addition, I adiabatically switch on a retro-reflected laser beam with a wavelnegth of 785 nm to create an optical lattice along the z-axis to increase the density. The depth of the lattice is set to 100 recoil energies, which results in an axial trapping frequency of 105 kHz. The additional axial confinement due to the magnetic trap is neglected in the following. Radially, the trapping frequency is set to 1 kHz which can either be generated by the magnetic trapping potential or the dipole potential of the optical lattice. Due to the strong axial confinement, the density distribution of the ground state can not be calculated in the Thomas-Fermi approximation. I solved the full Gross-Pitaevskii equation [22] numerically with an imaginary time Schrödinger equation for 250 atoms in a single lattice site for the given trapping frequencies. The resulting pancake-shaped density distribution can be approximated in radial direction by a parabola with a Thomas-Fermi radius of 1.15 μm and axially by an Gaussian distribution with a $1/e^2$ radius of 34.2 nm. The resulting peak density is $9.7 \cdot 10^{20}$ m^{-3} and the chemical potential is 5.8 kHz. In the following, I assume an infinite stack of equal pancakes separated by $\lambda/2$=785/2 nm.

The intensity of the flash beam is set to 1120 I_{sat} and its frequency is blue-detuned by 100 MHz from the F=2 to F=3 transition (D_2 multiplet of Rubidium) at 780.249 nm, which corresponds to a detuning of 16.7 Γ. Using such a large detuning, one can neglect an inhomogeneous illumination of the atomic cloud since only a small fraction of the light is absorbed. The induced dipole potentials alters the effective detuning to the flash beam which results in an altering phase and magnitude of the oscillating dipoles within the cloud. This effect can also be neglected, since the detuning of the flash beam is much larger than the induced dipole potential. Also nonlinear effects as lensing by the inhomogeneous density distribution [199] and radiation trapping [234] are strongly suppressed. The flash beam propagates along the y-direction and its polarization angle φ can be altered from 0° (polarization along the x-axis) to 90° (polarization along the z-axis). The steady state dipole moment with this parameters is 5.26 Debye. The flash beam is applied for 300 ns with constant intensity, which is long compared to $1/\Gamma$ and allows all atoms to reach the steady state. The

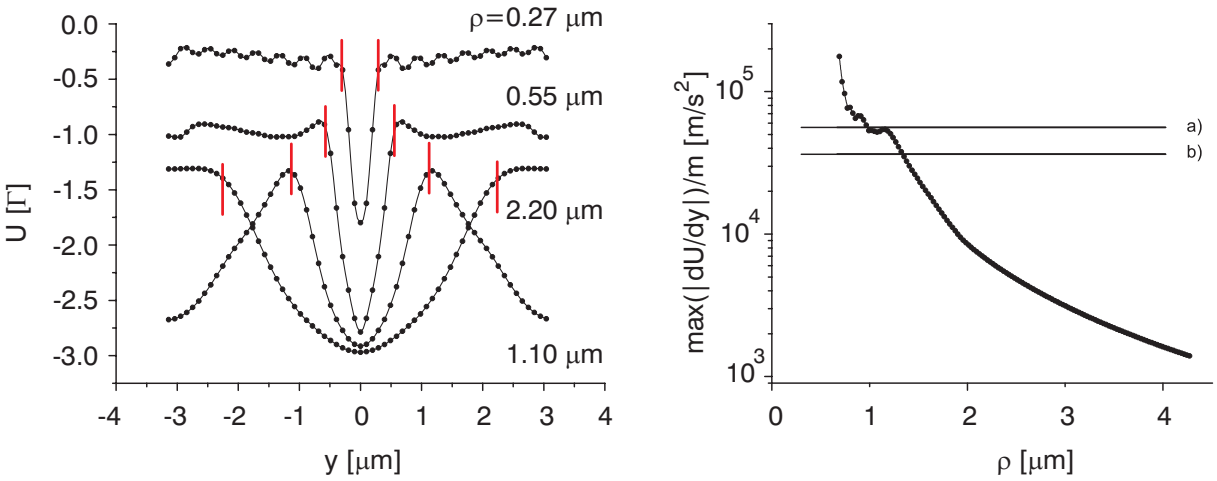

Figure 4.4: The left figure shows the induced potentials along the y-axes at x=z=0 for different radial widths ρ of the atomic clouds. The vertical red bars at each plot indicate the radial Thomas-Fermi radius. The peak atomic density was kept constant at $9.7 \cdot 10^{20}\mathrm{m}^{-3}$ for all widths. The polarization of the flash beam points always along the x-axis. On the right side, the maximum acceleration as dependence of the radial Thomas-Fermi radius ρ is depicted. The data shows the maximum gradient of the potentials divided by the mass of a Rubidium atom (m=1.44 $\cdot 10^{-25}$kg). The horizontal line a) gives an upper limit for the unidirectional acceleration ($\frac{d\langle p\rangle}{dt}/m = \hbar k\Gamma/4m$) due to radiation pressure. The horizontal line b) marks the maximum acceleration due to momentum diffusion caused by spontaneous emission processes ($\frac{d\sqrt{\langle p^2\rangle}}{dt}/m$). The flashing laser has a detuning of 100 MHz and an intensity of 1120 I_{sat}.

switching time of the light can be reduced to several tenth of nano-seconds with an accusto-optical modulator and is therefore short compared to the 300ns flashing time.

4.1.4 Outline of the calculation and results

For a given density distribution and with the knowledge of the retarded dipole potentials one can calculate the potential within a single pancake. Since there exists no analytical solution to equation (4.9), the integral is discreticized on a simple cubic lattice for a numerical calculation. The grid for the numerical calculation is chosen to be $64 \times 64 \times 128 = 65.536$ lattice points and the grid lattice spacing is $\lambda_l/32 = 24.5$ nm where λ_l is the wavelength of the laser generating the optical lattice. By using the convolution theorem one can straightforward use a common FFT algorithm for evaluation. The full potential, including all lattice sites, is simply obtained by superposing the calculated single pancake potential in an infinite one dimensional chain. The result of such a calculation is shown in figure 4.4

The induced dipole potential V_{dd} changes the momentum distribution of the atomic cloud. In the following, I assume a density distribution of a Bose-Einstein condensate with all atoms having the same phase. The undisturbed wave function can be written as $\psi_0(\vec{r}) = e^{i\varphi(t)}\sqrt{n_0(\vec{r})}$. The wave function is an eigen-state of the unperturbed situation and therefore the time evolution operator of the system, after the interaction is switched on, writes $\hat{U}(\vec{r},t) = \exp(-iV_{\mathrm{dd}}(\vec{r})t/\hbar)$ and with this $\psi(\vec{r},t) = \hat{U}(\vec{r},t)\psi_0(\vec{r})$. Here I demand that the density distribution does not change during the interaction time, which is legitimate in the so called Raman Nath regime [235]. The Raman-Nath approximation is valid as long the gained kinetic energy is much smaller than the interaction

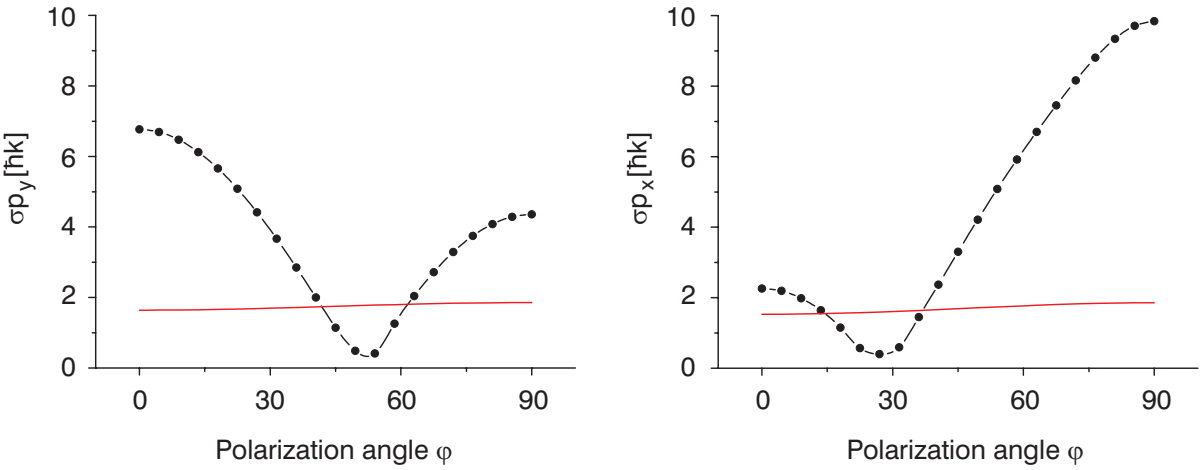

Figure 4.5: The two graphs depict the width of the momentum distribution of the atomic cloud after the light-induced dipole-dipole potential was applied for 300ns. The Thomas Fermi radius was set to 1.15 μm. The graph on the left shows the broadening in momentum space projected onto the y-axes as a function of the polarization angle and the right the projection onto the x-axes. The slash-dotted line includes the effect of the light-induced potentials and the chemical potential. The solid line is the incoherent background of the spontaneous scattered photons as a function of the polarization angle φ. To receive the full width in momentum space one has to add the two curves in quadrature.

potential. The momentum distribution after the interaction time t is given by

$$\tilde{n}(\vec{k},t) = \frac{1}{8\pi^3}\left|\int e^{i\vec{k}\vec{r}}\hat{U}(\vec{r},t)\psi_0(\vec{r},0)d^3r\right|^2 . \tag{4.10}$$

During the interaction time of 300ns the atoms experience a maximum acceleration of about $5\times10^4\,\mathrm{m/s^2}$ (see figure 4.4) which results in a spatial displacement of less than 1% of the wavelength of the driving field. The kinetic energy after such an acceleration is about 1% of the calculated interaction energy. Therefore it is a fair approximation to carry out the simulation in the Raman-Nath regime. This means also that superradiant effects can be neglected [236].

To account for additional broadening effects of the momentum distribution by spontaneous scattering events, the time evolution of the full atomic density matrix was carried out see appendix D. This includes the different polarizations of the driving field, the pumping of the atoms into other m_F states and the angular distribution of the acquired recoil. For given parameters, about three photons are scattered per atom. The amount of scattered photons can be experimentally checked for consistency purposes by the shift of the center of mass position after some time of flight of the atom cloud.

The final momentum distribution is then given by the convolution of the momentum gain due to the induced dipole potential, the mean field of the Bose-Einstein condensate and the spontaneously scattered photons. To extract a mean momentum broadening, the convoluted distribution was fitted with very good agreement by a Gaussian distribution.

In figure 4.4 the distribution of the light-induced dipole-dipole interaction potential through the center of a pancake along the y-axis is shown. The contribution of the neighboring pancakes is included by periodic boundary conditions. The different curves represent pancakes with different radial sizes but at fixed axial size and constant density and show the dependence of the induced

potentials on the geometry of the atomic cloud. In the limit of an infinite cloud with a constant density distribution, the potential would be just a constant and its mechanical effect on the atoms vanishes. The increase of the induced potentials in the center of the cloud with larger radii arises form the greater atom number within the cloud, since the density is kept constant. The interaction potential is on the order of several MHz, which is large compared to all other energy scales in the system like the trapping frequencies and the chemical potential due to the interaction via s-wave scattering.

The right hand side of figure 4.4 shows the maximum acceleration extracted from the potentials. For sufficiently small radial sizes of the atomic cloud, the maximum acceleration prevails the unidirectional acceleration $\frac{\hbar k \Gamma}{4}$ due to the spontaneous light force. This allows to clearly distinguish the effects emerging from the dipole-dipole interaction from spontaneous scattering events.

Finally the slash-dotted curves in figure 4.5 show the calculated widths of the momentum distribution for the previous parameters along the x and y direction as a function of the polarization angle. Not included in the slash-dotted curves is the contribution of the spontaneous scattering events represented by the solid lines. The broadening in momentum space can be up to 10 recoils, which is fairly larger than the contribution of the chemical potential. Noticeable is the existence of a strong dependence of the broadening on the polarization angle φ. In both directions exists an angle at which the effect of the dipole-dipole interaction nearly vanishes and the momentum distribution is dominated by the released chemical potential. The plot on the left side shows a minimum close to the so-called magic angle at 54.74° where the interaction of two dipoles vanishes. Such a minimum broadening is a clear signature of the dipolar character of the potentials since it can not be explained by other light-atom interaction mechanisms.

This theoretical treatment of the light induced dipole-dipole interaction identifies a new regime of coherent atom-light interaction. The mechanical effect of this interaction can be detected in a standard BEC-setup as we use. The smoking gun of the dipolar character is the angular dependence of the momentum distribution, which can not be explained by spontaneous scattering events.

5 Experimental results

In this chapter I review the results of three distinct experimental projects, which were accomplished during the last year. Each of them involved an additional setup, which will be presented in detail. The projects were realized with the help of three diploma students and more details on the conducted experiments can be found in [180, 237, 238]. The outcome of these experiments are important cornerstones towards the two main research routes of this project, namely Rydberg matter and the Spin-Boson model (for more details on these see chapter 6.2).

5.1 Bose-Einstein condensates in an optical lattice

The first result is the observation of diffraction of a Bose-Einstein condensate in a one-dimensional electromagnetic standing wave. The comparison of the experimental data with the theoretical predictions derived in chapter 2.5.1 allows the assignation of the experimental conditions needed for future experiments involving optical lattices. The focus hereby is on the experimental investigation of the Spin-Boson model which is addressed in chapter 6.2. A more detailed discussion of the accomplished experiments with optical lattices and the technical background of the experimental setup, as well the theoretical treatment, can be found in [180]. The general status of research involving cold atoms and optical lattices is reviewed in chapter 1.1.

5.1.1 Experimental setup

To test the performance of the laser setup shown in figure 5.1 we implemented as a first step a one-dimensional optical lattice with a wavelength of 820 nm. By monitoring the diffraction orders in dependence of the interaction time of the BEC with the optical lattice, we can draw conclusions about the geometry of the lattice, the achieved potential depths and its reproducibility.

The two laser beams generating the optical lattice were aligned through the viewport ⑱ (see figure 3.5) along the long axis (z-axis) of the cigar shaped BEC. The signal of an external reference cavity was used to stabilize the frequency of the Titanium:Sapphire laser. The light was brought to the vacuum chamber by a polarization maintaining fiber. This increases the pointing stability of the laser beams with respect to the atoms, since the free propagation in air is reduced to about half a meter. The polarization of the light is cleaned after the fiber additionally by a polarizing beam splitting cube. To avoid additional optics for beam expansion we use a collimation package[1] which delivers right away a parallel beam with an $1/e^2$ waist of 600 μm. This collimated beam is then focused onto the atoms with a f=300 mm lens, which yields at the position of the atoms a beam waist of 130 μm with the corresponding Rayleigh-range of 7.1 mm. The Thomas-Fermi radii 3.3 μm $\times$ 3.3 μm $\times$ 46 μm of the magnetically trapped BEC are in both directions well smaller than the extension of the focused laser beam. By this one can assume the intensity distribution to be constant over the condensate. For retro-reflecting the laser beam we mounted another f=300 mm

[1] 60FC-4-A6.2S, Schäfter-Kirchhoff

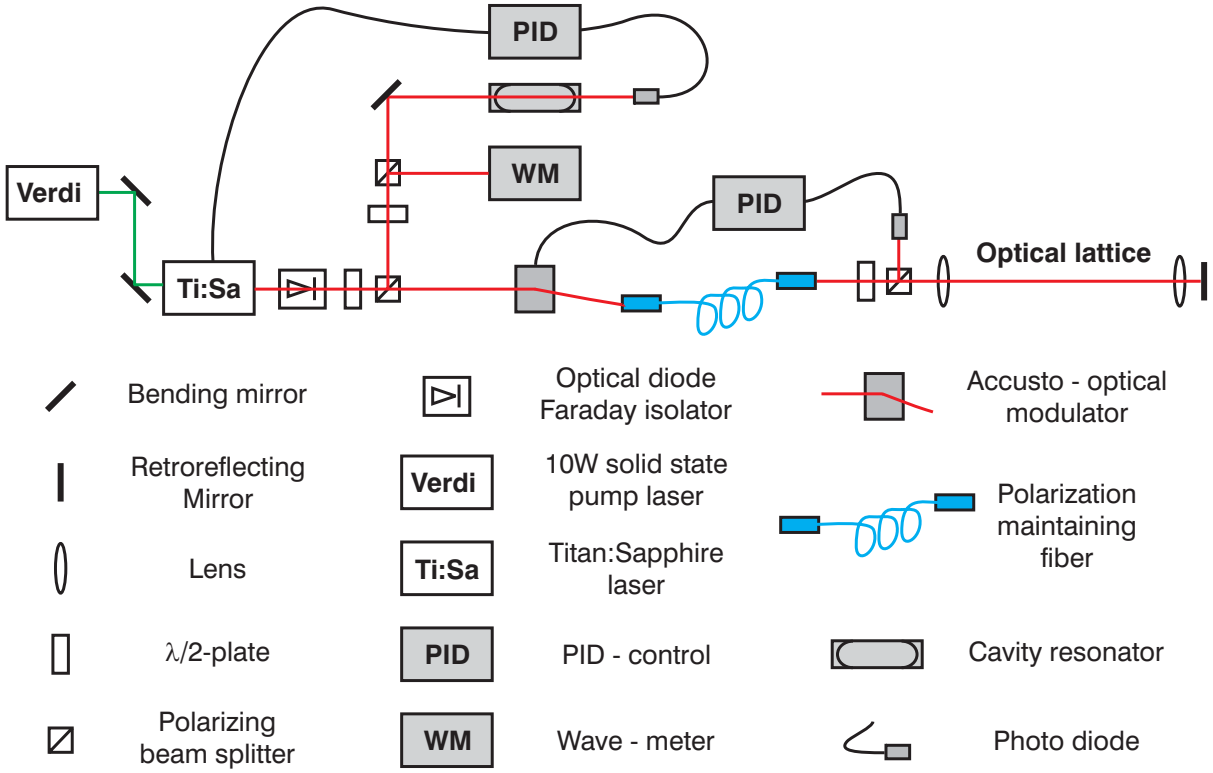

Figure 5.1: Laser-system for experiments with optical dipole traps and optical lattices. A Titanium:Sapphire laser (TIS-SF07, Tekhno-Scan), pumped by a solid-state laser (Verdi-10, Coherent), delivers about 1 Watt of laser power at a wavelength of 820 nm. The signal of an external cavity resonator is used to control the resonator length of the Ti:Sa laser, which is equivalent to stabilize the laser frequency. An accusto optical modulator (AOM) is used to adjust the depth of the dipole potentials. By implementing a photo diode after the optical fiber we can control the intensity by regulating the rf power entering the AOM with a PID loop. The response time of the loop circuitry is sufficient for adiabatic ramping of the dipole potentials but not for the short time scales required in diffraction experiments. For such experiments only the passive stability of the intensity is used.

lens in a 2f-setup behind the vacuum chamber. To ensure a good overlap between the two beams, we installed a photo-diode in front of the fiber and aligned the retro-reflected beam with a 0° mirror again through the fiber.

5.1.2 Results

To optimize the alignment of the lattice we transferred in a first step thermal atoms with a temperature of a few μK into the focus of a single laser beam (without the retro-reflected beam). The position of the dipole trap was then optimized on the transfer efficiency of the atoms. By increasing linearly the power of the light trap to a maximum value of about 200 mW and then switching off suddenly the magnetic trap, we achieved a transfer efficiency of almost 100 %. As a next step we added the retro-reflected laser beam to generate an optical lattice. To transfer the atoms into the optical lattice potential we proceeded in the same manner as for the single beam trap. Also in this case we transferred almost all atoms into a pure dipole potential. We tested the adiabaticity of the transfer by first ramping up the laser power within 100 ms, holding the atoms for

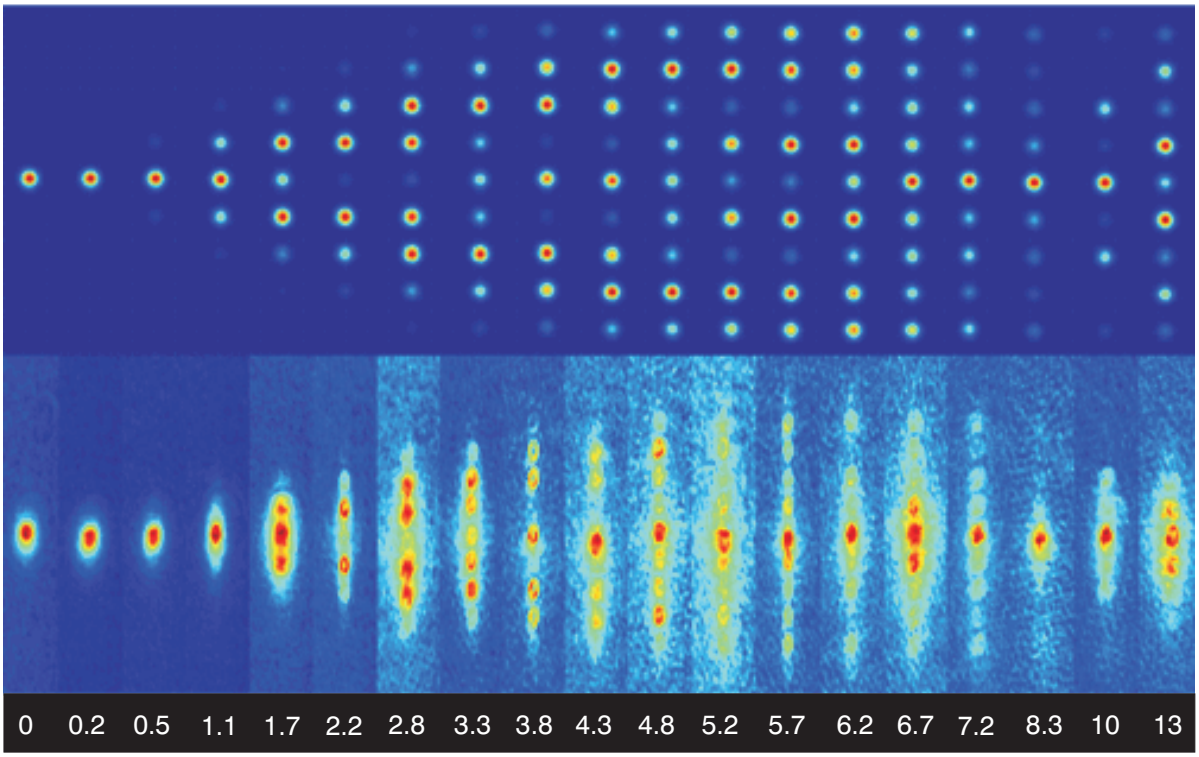

Figure 5.2: Absorption images of a Bose-Einstein condensate diffracted in an optical lattice. The lower part of the figure shows absorption images of the diffracted atoms for different interaction times. The numbers below indicate the exposure in μs. The color coding reflects the number of detected atoms (from little atom number colored blue to high ones in red). Above the experimental result is a theoretical simulation for a potential depth of 91 E_{rec} depicted. With the great agreement between experiment and theory, we can specify the depth of the lattice potential within 5% accuracy.

several ms in the combined potential of the magnetic trap and the optical trap and then decreased the power again within 100 ms. For thermal clouds at a temperature of a few μK we measured almost no heating of the cloud. But when transferring a Bose-Einstein condensate into the lattice the atoms were severely heated. Since we monitored also a loss in the atom number, we identified this heating with inelastic three body collisions (see chapter 2.4.3).

To determine the depth of the optical lattice potential we conducted a standard diffraction experiment [179]. After the generation of a BEC with about $2 \cdot 10^5$ atoms (as described in chapter 3.11) the lattice laser light was switched on for a chosen time with constant power of about 200 mW, while the condensate was still confined in the magnetic trap. The flashing time was varied from 200 ns to 12.6 μs by switching on and off the radio-frequency power of the accusto-optical modulator and with this the laser light. The rise and fall times of the intensity was on the order of 25 ns. This switching time is of 25 ns was included in a numerical simulation of the experiment and it turned out that it is not changing the time evolution of the diffraction patterns severely. 100 μs after the lattice light pulse was switched on, we released the atoms from the magnetic trap for a time of flight measurement. The momentum distribution of the atoms was detected after 17 ms of free evolution by absorption images (see chapter 3.3.2).

In figure 5.2 absorption images for increasing interaction times are shown. The upper part of the figure shows a theoretical calculation following chapter 2.5.1 for a lattice depth of 91 E_{rec}.

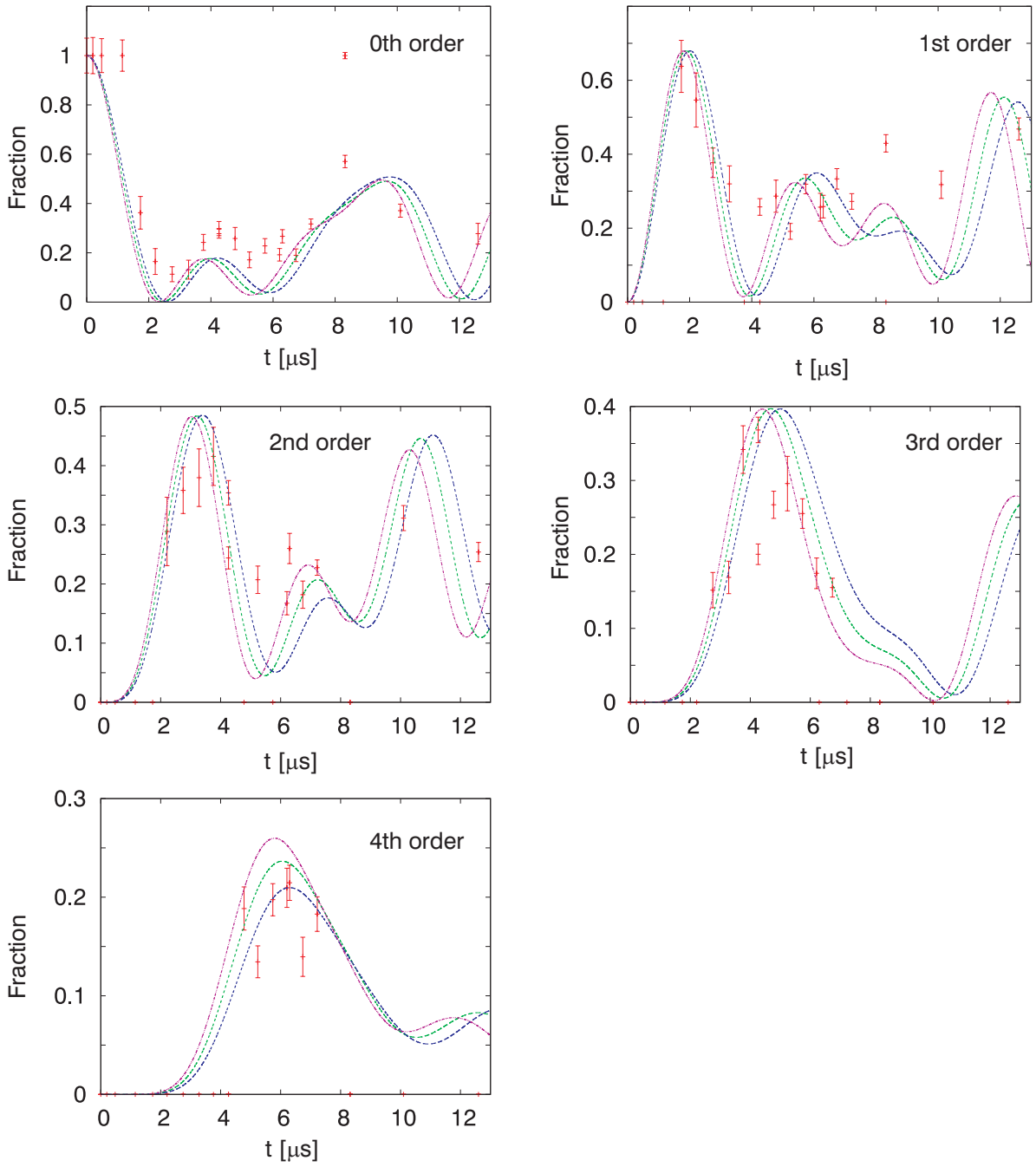

Figure 5.3: Occupation fraction of the different diffraction orders. Each plot shows the normalized atom number for each order as function of the interaction time with the optical lattice potential. The atom number per order is the sum of the two symmetric diffraction peaks. The solid lines are theoretical calculation for three different potential depths, namely 86 E_{rec} (blue), 91 E_{rec} (green) and 96 E_{rec} (magenta).

Diffraction peaks up to the fourth order are clearly visible. A more detailed analysis of the data is shown in figure 5.3. The five plots show the time dependent occupation of the individual diffraction order from 0th to 4th order. The fraction of each order was determined by summing the number of atoms for the two symmetric diffraction orders and normalizing it to the total atom number. The intensity fluctuation of the laser was about of 5% from shot to shot, since the PID-loop for the intensity stabilization could not be used for such short pulses. The variation of the intensity is most likely due to the pointing instability of the Ti:Sa laser, which leads to a reduced injection efficiency into the optical fiber. The differing intensities are reflected in figure 5.3 by three theoretical curves for potential depths at 86 E_{rec} (blue), 91 E_{rec} (green) and 96 E_{rec} (magenta).

The available laser power of about 200 mW leads at the position of the atoms to a peak intensity of I_{max}=980 W/m^2. The expected potential depth (see Appendix E) is then about 130 E_{rec}. The observed potential depth of about 91 E_{rec} is 30% below the expected value, which can be explained by several circumstances. The two viewports (made of fused silica) through which the laser beams enter the vacuum chamber feature no antireflection coating, which reduces the potential depth of the optical lattice already by 15%. A further effect for a decreased potential depth is the slight change of the linear polarization by the optical viewports which exhibit some birefringence. Because of the large detuning are single beam dipole traps almost immune to this effect, but the optical lattice depends on the interference of the electric field components. If the direction of the electric field component of the linear polarization is tilted by an angle θ with respect to the initial beam and the retro-reflected on changes the potential depth as $\cos^2\theta$. Finally remains a uncertainty in the overlap of the two foci, since the focus of the retro-reflected beam can not be adjusted independently as it is done for the primary beam. However is this effect rather negligible at such large Rayleigh ranges as used in our case.

The observation of the diffraction peaks gives not only information about the depth of the optical potential, but can also be used to calibrate the imaging system. Each diffraction order n corresponds to a recoil mode of $\pm 2n\hbar k$. With the well known recoil velocity at 820 nm and the knowledge of the time of flight duration it is possible to calibrate the magnification very accurately.

The absorption pictures in figure 5.2 show not only distinct diffraction peaks but also a cloud of scattered atoms. To estimate the number of scattered atoms one has to include the time dependence of the density distribution. The total number of scattering events is given by the integrated scattering rate $\int n(t)\cdot\sigma v dt$. The evolution of the density distribution consists of three steps. In the first step the lattice potential is applied to the magnetically trapped atoms from a few ns up to to 13 μs. The density of the cloud does almost not change during this pulse and can be set to be constant. The velocity of the diffracted atoms for the nth order is n times the recoil velocity ·11.2 mm/s. For a mean density of 10^{14} cm^{-3} only a few percent of the atoms are scattered. The atoms reside after the pulse for 100 μs in the magnetic trap. The center of mass of the first diffraction order moves in this time about 1 μm, which is much less than the Thomas-Fermi radius of about 50 μm along the z-axis. Also here one can assume the density to be constant, and about 10 % of the atoms moving with two recoil velocities get scattered during this time. Finally the atoms are released from the magnetic trap and undergo a free expansion as described in chapter 3.3.3. During the expansion the scattering rate drops accordingly to the reduction of the density. In the case of cigar shaped condensates, as given in our case, the density drops roughly quadratically in time. If one takes for example a situation where about half of the atoms are diffracted into the first diffraction order (see absorption figure at 1.7 μs) the integration of the scattering rate results in a total scattering probability of about 50%, which is in good agreement with the observed fraction.

To obtain a better visibility of the diffraction peaks, one has to reduce in future experiments the

density of the initial cloud either by reducing the strength of the confining magnetic trap or by applying the lattice potential after some time of flight. If for example the radial trapping frequency of the magnetic trap is reduced by a factor of ten, one limits the scattering events already to only a few percent.

This realization of a one-dimensional lattice is an important step towards the investigation of the Spin-Boson model (see chapter 6.2.1). The next step is the extension of the setup to a two-dimensional lattice in the same manner as described above. With a lattice depth of 30 E_{rec} for each axis one reaches the regime of one-dimensional gases as required for the implementation of the Spin-Boson model.

5.2 Rabi oscillations between the two hyperfine ground states

To transfer atoms coherently between the two hyperfine ground states of ^{87}Rb one needs either a microwave field at 6.8 GHz or two phase locked lasers for Raman transitions. The latter is already available in our institute [239] and will be implemented in our setup for experiments 6.2.1 in the framework of the Spin-Boson model. The combination of the rf-fields used for evaporative cooling (see chapter 3.10) and this microwave assembly will be used to transfer the atoms in any desired magnetic sublevel of the $F = 1$ or $F = 2$ ground state manifold. The availability of a flexible microwave assembly is a powerful tool for many experimental situations. The major aim is on the ability to transfer atoms into arbitrary magnetic sub-level of both hyperfine ground states or mixtures of different states, also called spinor condensates [55]. But it can also be used for evaporative cooling, driving clock transitions or for sensitive spectroscopy with a resolution well below 1 kHz [240].

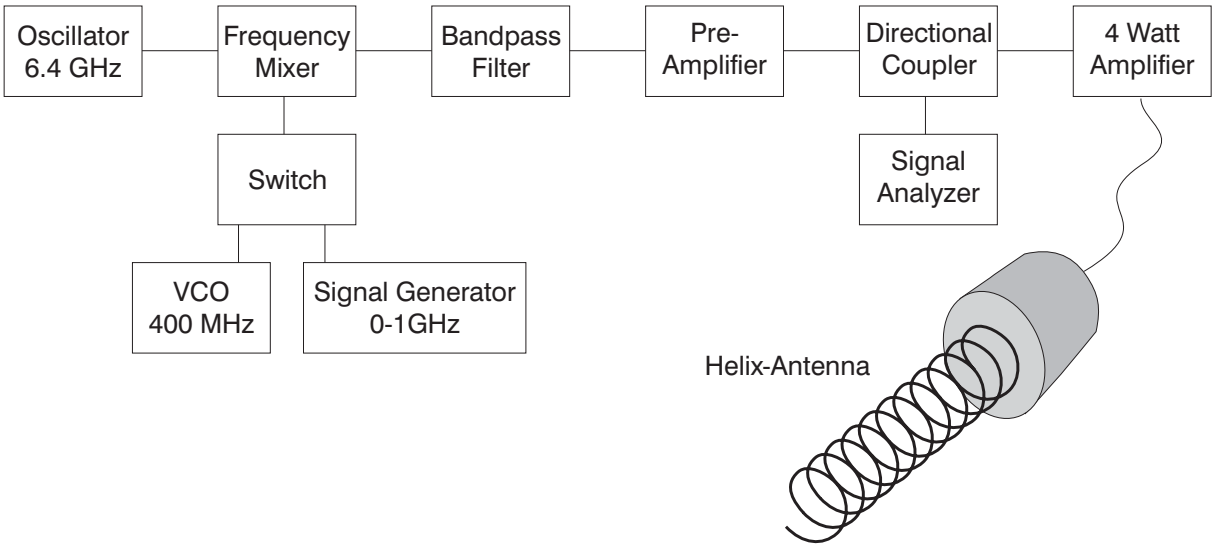

Figure 5.4: Schematic setup for microwave generation. A detailed description is given in the text.

The setup for generating microwave radiation at 6.8 GHz is shown in figure 5.4. The key design criteria were excellent frequency stability, with a frequency drift better than 1 kHz per hour, a

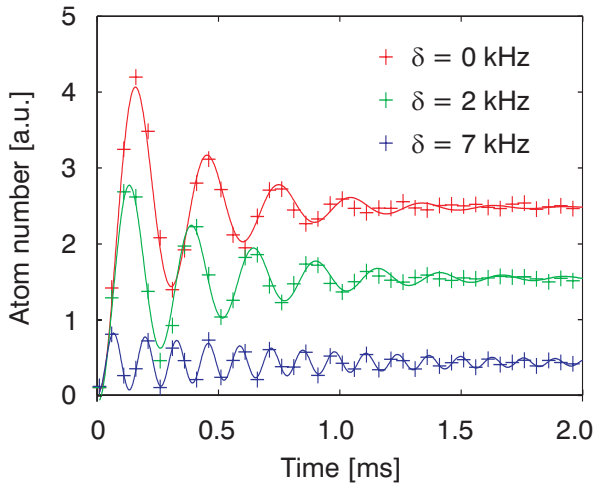

Figure 5.5: Damped Rabi oscillations in the time domain. The three data sets show Rabi oscillations between the $F = 1, m_F = 0$ and $F = 2, m_F = 0$ state for three different detunings δ=0 kHz (red), δ=2 kHz (green) and δ=7 kHz (blue). By fitting the data (crosses) with an exponentially damped cosine (solid line) one can extract the effective Rabi frequency Ω_{eff} and the damping Γ. On resonance (δ=0 kHz) is the fitted effective Rabi frequency Ω_{eff}=1.10 kHz, for 2 kHz detuning 1.24 kHz and for 7 kHz detuning 2.45 kHz. The effective Rabi frequency is plotted in figure 5.6 as a function of the detuning. The damping Γ is on resonance 900 Hz, at 2 kHz detuning 702 Hz and for 7 kHz detuning 356 Hz.

phase noise below -100 dBc/Hz and high power of several Watts in the radiation field. The heart of the system is a YIG-oscillator[2] at 6.4 GHz, which is subsequently frequency mixed[3] with a signal generator[4] to obtain the desired 6.8 GHz. By controlling the signal generator either by GPIB or TTL signals one can generate almost arbitrary frequency ramps (between 5.4 GHz and 7.4 GHz) and pulse sequences respectively. The mixed signal is cleaned by a bandpass filter[5] and amplified in two steps[6] [7] up to 4 Watt. The monitoring of the signal is either done via a directional coupler[8] or directly inline by a zero-biased Schottky-diode[9].

The hole setup is terminated with a homebuild impedance matched helical antenna [241]. Its special winding pattern produces a directional radiation pattern of circularly polarized microwaves. The antenna itself consists of a helical wire wound on a rod made of plexiglass[10]. The dimensions of the antenna can be reduced by the value of the refractive index (ε_r=2.475) of the plexiglas used. One side of the antenna is terminated by a baseplate, which acts as an reflector for the microwave. There are eight windings on a rod of 77.6 mm length and 11 mm diameter, which gives a forward gain of 17 dBm compared to an ordinary dipole antenna. The baseplate has a diameter of 21 mm and is furnished with a SMA connector on the backside. More details about the antenna design and its radiation performance can be found in [237].

Microwave radiation at 6.8 GHz has a vacuum wavelength of 44.1 mm. The open aperture between

[2] Agate Series Crystal Oscillator, Wenzel Associates, Inc.
[3] Double balanced mixer J-4080 M, Eclipse Microwave, Inc.
[4] SSG MG3641A, Anritsu
[5] AAMCS-BPF-250M-3dB-Sf, AA-MCS, Inc.
[6] ZX60-8008E, Mini-Circuits
[7] AM53-6.3-73-35-35, MA-LTD, Inc.
[8] 780-30-6.000, Meca Electronics
[9] DZR124AA, Herotek
[10] PMMA, Degussa

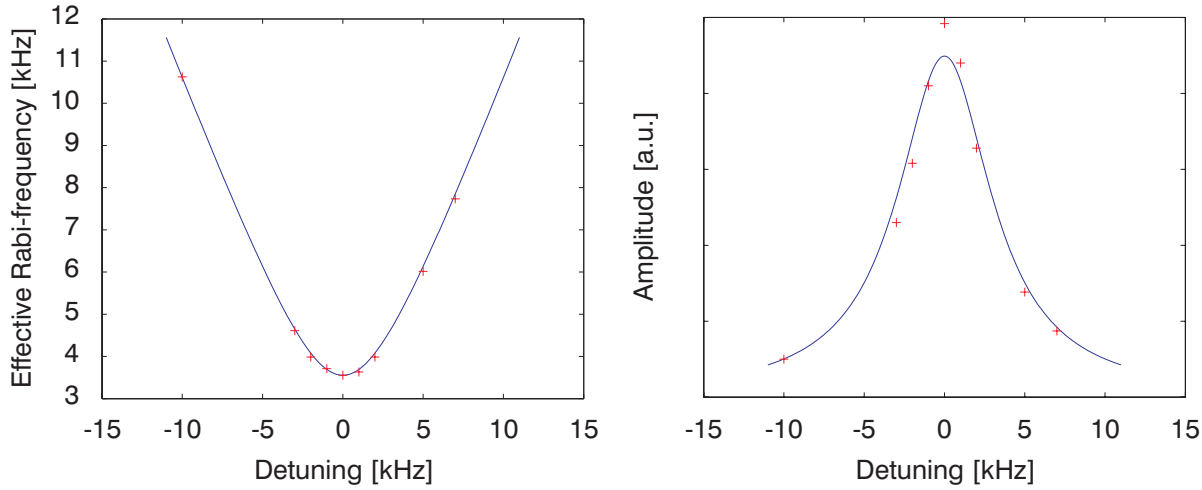

Figure 5.6: Analysis of the Rabi oscillations between the $F = 1, m_F = 0$ and $F = 2, m_F = 0$ state as shown in figure 5.5. On the left side is the dependence of the effective Rabi-frequency on the detuning shown. The blue line is a plot of the effective Rabi frequency $\Omega_{eff} = \sqrt{\omega_R^2 + \delta^2}$ (see equation 5.1) with a coupling strength of $\omega_R = 3.55$ kHz. To the right is the dependence of the amplitude versus detuning depicted. The blue line is proportional to the expected amplitude $\frac{\omega_R^2}{\omega_R^2+\delta^2}$ and plotted again for a coupling strength of $\omega_R = 3.55$ kHz.

the two resessed buckets of 28 mm is larger than half the microwave wavelength, which allows a traveling wave inside the buckets. The antenna is placed in front of the viewport ⑪ (see figure 3.5), which is no handicap for the radiation because of its large diameter. The actual radiation pattern at the position of the atoms is probably quite complicated due to the complex geometry of the vacuum chamber. To gain more insight about the intensity distribution inside the chamber one has to use advanced numerical methods, which has not been done yet. Nevertheless is the field distribution more or less independent over the typically used frequency range of a few MHz, which was not the case for the radio-frequency fields used for evaporative cooling (see chapter 3.10).

We tested the performance of the setup by observing Rabi oscillations between the two hyperfine ground states of ^{87}Rb. For this we prepared initially a laser cooled cloud in the $F = 1$ state with a temperature of about 20 μK. In order to achieve a two-level system, we applied a small magnetic field of 200 mG in z-direction and tuned the microwave frequency to the $F = 1, m_F = 0 \rightarrow F = 2, m_F = 0$ transition. This so called clock transition exhibits only a quadratic Zeeman shift with the magnetic field strength and is by this comparatively insensitive to magnetic fields (see appendix B).

The driven two level system can be described by optical Bloch equations (see chapter 2.1) and has for a constant driving field following solution

$$p_2 = \frac{\omega_R^2}{\omega_R^2 + \delta^2} \frac{1}{2} \left(1 - \cos \sqrt{\omega_R^2 + \delta^2} \right), \tag{5.1}$$

where p_2 is the population fraction of atoms in state $F = 2, m_F = 0$. The fraction p_1 in $F = 1, m_F = 0$ is then $1 - p2$. The effective Rabi-frequency is given by $\Omega_{\text{eff}} = \sqrt{\omega_R^2 + \delta^2}$ with the ordinary Rabi frequency ω_R and the detuning δ. The coupling strength for the given transition is given by

$$\omega_R = \frac{\mu_B}{\hbar}|\vec{B}_{rf} \cdot \vec{e}_z|, \tag{5.2}$$

where the direction of the magnetic field $\vec{B}_{rf}$ has to be parallel to the quantization axis $\vec{e}_z$. For a measured coupling strength of 3.55 kHz gives this a perpendicular magnetic field component of 3 mG.

The experimental results on coherent Rabi oscillations are combined in figure 5.6. The radio frequency was applied to the atoms in the $F = 1$ state for a certain time, after which the atoms in the $F = 2$ state were selectively detected. The collected data (up to 10 ms) exhibited damped oscillations shown in figure 5.5, which were analyzed in time- and frequency-space. On resonance a clear damping with corresponding line width of 900 Hz was apparent, which is most likely due inhomogeneities of the microwave field within the vacuum chamber. By this inhomogeneities exhibit the atoms a differing effective Rabi frequency depending on their position. In the case of large detuning this effect does contribute less and for δ=10 kHz was the damping already reduced to 76 Hz. More details to the microwave-setup, its performance and experimental implications can be found in [237].

As mentioned above this system will be used to manufacture the initial state for investigating the Spin-Boson model (see chapter 6.2.1) but has also many other applications. It can be used to generate mixtures of different spin states for studying Spinor condensates [55] or to measure the interaction energy among the atoms [240]. But it has also manifold implementations for investigating Rydberg matter (see chapter 6.2.2). By applying Landau-Zener sweeps [242] on the magnetically trapped atoms one can remove a certain fraction of atoms and adjust by this the atomic density at constant temperature. This method is ideal to study the density dependence of blockade effects of the Rydberg excitation due to van-der-Waals or dipole-dipole interaction. A further application is given by the Stark effect of Rydberg states as depicted in figure C.1. At certain electric fields the level splittings are on the same order as the available microwave frequencies. With this one can transfer the atoms within one L-manifold to any angular momentum state. Of special interest are here the stretched states with maximum L which exhibit extremely long lifetimes [78].

5.3 Experiments with Rydberg atoms

The focus of the experiments presented subsequently was mainly put on the characterization of the multi-channel plates and the electric field configurations. We tested the field plates by measuring the quadratic Stark-effect of Rydberg atoms in the $43S_{1/2}$ state. The laser system and the data acquisition has been already examined carefully on a different setup [189]. One step beyond testing the setup is the measurement of the excited state lifetime of the $43S_{1/2}$ state at a temperature of 20 μK and a density of $5 \cdot 10^{12}$ cm^{-3}. Samples at such low temperatures and high densities were until now not available in any experiment on Rydberg atoms.

5.3.1 Laser system for a two photon excitation into Rydberg-states

The excitation into Rydberg states with main quantum numbers ranging from n=20 up to the ionization threshold is accomplished by a two-photon excitation scheme as introduced in appendix G. For this transition two wavelengths at 780 nm and 480 nm are needed, whereas the latter one is generated by frequency doubling of light at 960 nm. Figure 5.3.1 depicts the schematic setup of the laser system. The two diode lasers systems for the red (780 nm) and the infrared (960 nm)

light, as well all elements for frequency stabilization are located in a separate room to increase the stability. By this we reached an overall line-width of the two laser frequencies well below one MHz. The infrared light is brought to the laboratory by an optical fiber, passes a tapered amplifier, a frequency doubling cavity[11] and is finally delivered by another fiber to the experiment. A third fiber takes the red light (780 nm) directly from the secluded room to the experiment.

Our setup shown in figure 5.3.1 allows us to choose easily different laser frequencies for manifold experimental situations. The red light at 780 nm can be locked to any line of the polarization spectroscopy. Before it enters the vacuum chamber, it passes an accusto-optical modulator[12] in a double-pass configuration. With this AOM we can tune the frequency of the light by 100 MHz with almost constant intensity. In combination with the locking scheme we can tune the light right on a resonance, or detune it at most by 400 MHz to any transition with respect to the $5S_{1/2}(F = 2) \rightarrow 5P_{3/2}(F' = 3)$ transition. The transfer cavity is used to stabilize the infrared light (960nm) with respect to the already stabilized red light (780 nm). The 30 cm long cavity is made of stainless steel and has a mode spacing of 125 MHz. The length of the cavity can be altered by a piezo actuator, which are also used to stabilize the length of the cavity onto the red light (780 nm). Additionally we evacuate the cavity to avoid changes in the refractive index of the air due to atmospheric pressure and humidity. The master laser at 960 nm can now be stabilized to any mode of the cavity in steps of 125 MHz. A subsequent AOM in double pass configuration, allows us to scan the infrared light by 250 MHz, which corresponds to 500 MHz of the frequency doubled blue light at 480 nm. To scan a larger frequency region than available by the AOMs, we control the grating of the infrared diode laser directly and scan by this the frequency without mode-jumps for more than 6 GHz. To calibrate the frequency of the scanned array we simultaneously record the signal from the Fabry Perot resonator.

The two laser beams for the two-photon excitation have been overlapped before entering the vacuum chamber at an dichroic mirror. The overlapped beams were aligned parallel to the long z-axis, which is also the quantization axis of the magnetic trap. The polarization of the red and blue light was set to σ^+ respectively σ^-. At the position of the atoms the $1/e^2$ radius of the red light (780 nm) was set to 550 μm and the blue (480 nm) to 40 μm which yields roughly a constant intensity distribution across the atoms.

5.3.2 Electric field configurations and ion detection

The high sensitivity of Rydberg atoms to electric fields is a beneficial tool to do experiments with them. To produce electric field shapes as versatile as possible, we installed eight field plates close to the atoms. The spatial arrangement can be seen in figure 5.8 and figure 3.5. Each of these plates can be addressed individually, which allows us to generate nearly any field configuration starting from constant fields in arbitrary directions, to one dimensional gradients, two dimensional quadrupoles, hyperbolic concave saddles or hyperbolic convex fields with a positive curvature in all three dimensions. Some realizations are shown in figure 5.9 and discussed in more detail in H.

The eight field plates are made of stainless steel with a thickness of 0.5 mm. They are glued with 1 mm thick ceramic spacers onto the resessed buckets. The dimensions of the spacers have to be small enough, that they are completely hidden behind the field plates from the viewpoint of the atoms. Any insulating surface can accumulate charge and falsify the desired field configuration. To charge the field plates they are spot welded to a stainless steel wire, which are radially led outwards

[11] TA-SHG 110 1V0-00025, Toptica
[12] 3200-121, Crystal Technology

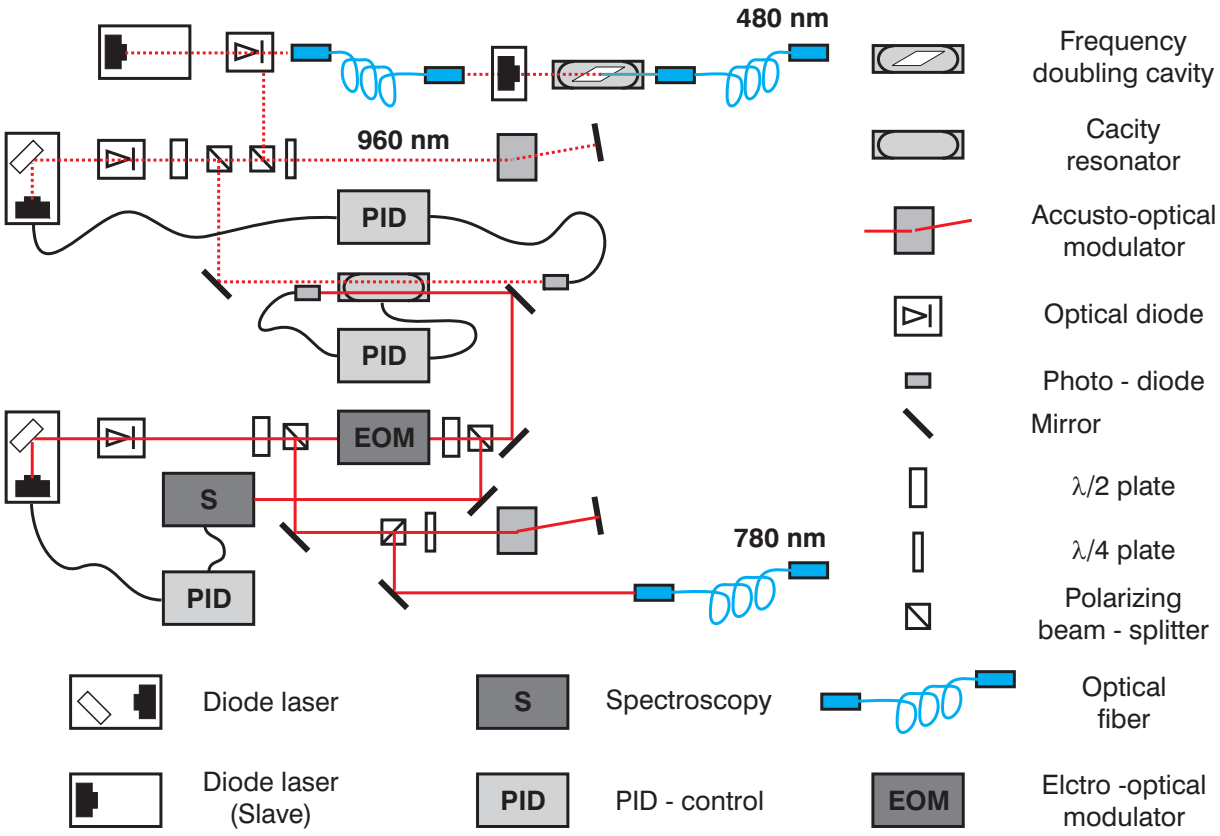

Figure 5.7: Laser-system for two photon excitation of ^{87}Rb into Rydberg states. The red light at 780 nm is generated by a standard diode laser system identical to the repumping system discussed in chapter 3.2. The production of blue light in the range of 475 nm to 483 nm is more involved. For this purpose we use a master slave setup, where a standard diode laser setup delivers infrared light at 960 nm which is amplified by a tapered amplifier. A subsequent frequency doubling cavity delivers the desired wavelength. The two laser frequencies are stabilized against each other by a transfer cavity, which is itself stabilized with the red laser system to a spectroscopy signal in a Rubidium gas cell.

as can be seen best in figure 3.5. At the edge of the resessed bucket the wires are fixed in position by short ceramic tubings, which are also glued to the buckets and are subsequently connected to capton-insulated copper wires. These copper wires are then finally connected to one of the fourfold high voltage feed-throughs. To avert breakthroughs inside the chamber induced by sharp edges we rounded off all four edges of each plate with a radius of 1.5 mm. Finally we etched and electro-polished all field plates including the spot welded wires to burnish also small spikes. The polishing was done in a acid bath consisting of one part of 96% sulfuric acid, two parts of 85% phosphoric acid and six parts of distilled water [243]. After two minutes at a current of 5 Amperes about 70 μm of stainless steel from the plates was removed and they exhibited a semi gloss surface. After installation of the field plates and evacuating the chamber we measured no current leakage up to 3000 Volts for all plates.

During the experimental course it is necessary to switch the applied voltages within short times. To do so we use bipolar high voltage switches[13] which have an intrinsic rise-time of 60 ns. The

[13] HTS-6103 GSM, Behlke

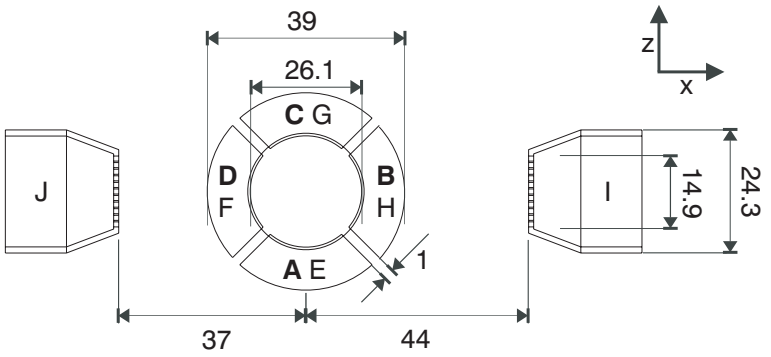

Figure 5.8: Electric field plates (A-H) and Faraday cages (*I* and *J*) for the multi-channel plates. Four field plates are glued onto each of the resessed buckets (see appendix F), such that plate *A*, *B*, *C*, and *D* lie vis-a-vis to the plates *E*, *F*, *G* and *H*. The inner distance between the plates is 25 mm. All dimensions given in the figure are in millimeters. The MCPs were located as close as possible to the center of the vacuum chamber without loosing any optical access, which resulted in the two different distances.

push-pull circuit of the switch has to be adjusted to match the capacitive load of 50 pF of each field plate as well the 300 pF load of the high voltage coax cable, which connects the switch to the high voltage feedthroughs.

Three different field distributions are shown in figure 5.9. The calculations have been done with a finite element method[14], which included the most relevant (grounded) parts of the vacuum chamber as well the eight field plates and the two Faraday-cages of the MCPs [238]. The results show, that we are able to generate fields, which are almost constant, linear or quadratic. This examples do not include the cages of the MCPs, which can be added to generate even more complex field distributions. With the help of the analytical expressions for a generalized octopole given in appendix H) one can design all kind of desired field configurations.

For a high detection sensitivity of Rydberg atoms, we installed two MCPs[15] inside the vacuum chamber. After field ionization of the Rydberg atom, we use already one of the MCPs to detect the ions. The second one is planned to detect simultaneously the electrons. An MCP consists mainly of a thin (500 μm) glass-plate with about one million holes (10 μm) in it. Between the front and the back side of the plate one applies several thousand volts. If now a charged particle hits one of the channels, it produces secondary electrons, which produce by striking the walls further electrons. This electron avalanche is then detected by an anode, which sits behind the glass plate that collects the electrons. To improve the amplification even further, we use MCPs in a Chevron configuration, which consists of two successive glass plates with a small spacing in-between. The electron current arriving at the anode is converted by a large resistor to a voltage and then amplified by a homebuild circuit [189]. The whole MCP Chevron-assembly is boxed into a Faraday cage, which shields the atoms in the center of the chamber from the biased front side, typically with -2000 V. The Faraday cage is closed in the front by a grid with an diameter of 12 mm and a transmissibility of 85%. The active area of the MCP front side has an diameter of 8.5 mm. It is not possible to switch any voltage of the MCP very fast because of the large capacitance of the stacked plates. On the other hand the anode is also shielded by the Faraday cage from capacitive cross-talking to the field plates, when their voltages are switched during the experiment.

[14] Comsol, Femlab
[15] Type B012VA, Tectra

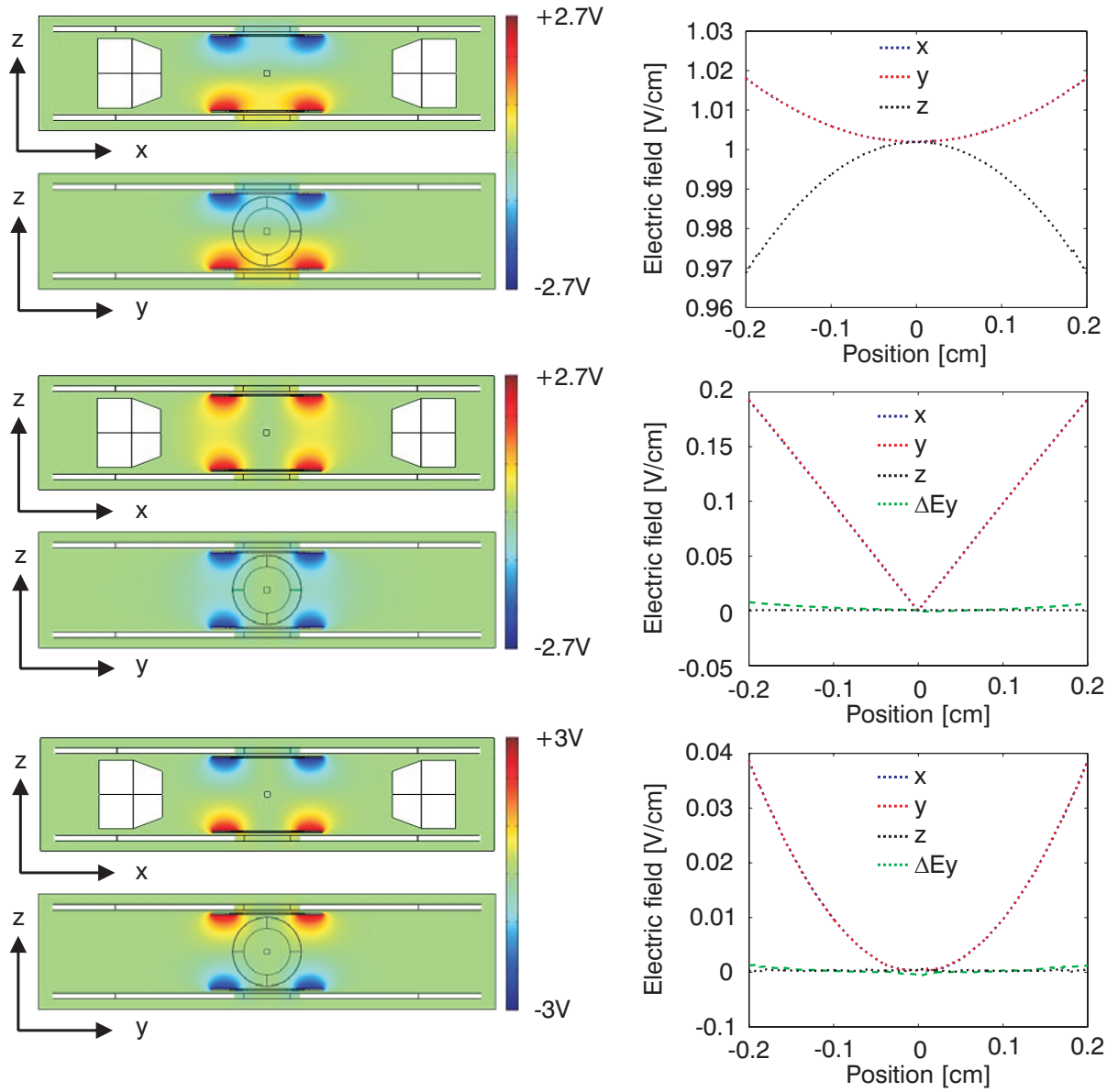

Figure 5.9: Simulated electric field configurations. The three figures show the realization of a constant electric field distribution (top), a gradient field (middle) and a field with constant curvature (bottom). On the left are the potentials in the x-z plane as well in the y-z plane shown. The small squares in the center of each potential plot indicates the plotting range for the absolute value of the electric field components depicted on the right. The green curve ΔE_y displays the derivation of the desired gradient field $E_y = 1\ \mathrm{V/cm^2} \cdot y$, respectively curvature field $E_y = 1\ \mathrm{V/cm^3} \cdot y^2$. To obtain a constant electric field of 1 V/cm the plates *A*, *B*, *C* and *D* have to be charged to +2.6 V and *E*, *F*, *G* and *H* to -2.6 V. In the case of the gradient field the plates *A*, *C*, *E* and *G* were set to +2.7 V and *B*, *D*, *F* and *H* respectively to -2.7 V. For the third configuration for a field with a constant curvature the plates *A*, *C*, *F* and *H* are set to -3 V and *B*, *D*, *E* and *G* to +3 V.

To detect the Rydberg atoms with an MCP, one has at first to field ionize the excited atoms. This can be done by a large enough electric field as described in appendix C, which is in the case of an $43S_{1/2}$ state about 160 V/cm. In our case we want to detect the ions and and one has to provide a suitable electric field distribution which guides the ions into the MCP J.

Usually the magnetic fields of the trapping potential are still switched on, when the ions fly towards the MCP. The combination of electric and magnetic fields provoke a drift on the ions according to the force $F = q(\vec{E} + \vec{v} \times \vec{B})$. A numerical simulation for the given experimental situation, shows that the drift is in our case in the order of 1 mm and by this well below the aperture of the MCP of 8.5 mm.

We calibrated the MCP ion signal by monitoring the losses in a cold atomic cloud due to Rydberg excitation and the corresponding voltage signal on the anode. After amplification, which is the same for the subsequent experiments, we acquire 1 Vs per $3.65 \cdot 10^{10}$ atoms. In principal one could distinguish between single ion events, but the noise level of the signal limits our minimum sensitivity to about a few hundred ions.

5.3.3 Stark effect in a magnetically trapped cloud

To examine the electric fields generated by the field plates, we make use of the quadratic Stark effect exhibited by the $43S_{1/2}$ state. The energy shift ΔW of this state located in an electric field E is given by [189]

$$\Delta W = \frac{1}{2}\alpha E^2 \tag{5.3}$$

with $\alpha/2 = 8.06$ MHz/(V/cm)^2.

The electric field for the Stark shift was provided by the field plates B and H, which was tuned from -15 V to +15 V. All other field plates as well the cage of the MCP I was set to ground. The simulation of the emerging field gives in the geometric center a field of 0.14 V/cm per applied unit of voltage on field plate B and H. The orientation of the field is parallel to the x-axis. The intrinsic asysmmteric configuration of the field exhibits additionally an gradient along the x-axis of 0.1 V/cm^2 per applied unit of voltage. This field is superposed with a remanent field of the faraday cage of the MCP J, which was set to -15 V. The calculated field remaining from the cage at the center is 0.2 V/cm plus a gradient of 2 V/cm^2. For detection of the Rydberg atoms we switch after excitation the voltage on plate B and H to +1000 V, which is sufficient for field ionization. The field configuration with the plates B and H at a positive voltage and the Faraday cage at -15 V drags the positive ions towards the MCP for detection.

As an atomic cloud for excitation we used a evaporative cooled sample confined in the magnetic trap as described in chapter 3.10. At a temperature of 40 μK the cloud is in the harmonic regime of the magnetic trap with an radial width of about 40 μm. For such small clouds one can neglect the broadening of the spectroscopic lines due to inhomogeneties of the electric field. For the given parameters above, the broadening is less than one percent of the magnitude of the Stark shift energy.

Figure 5.10 shows the result on the measured Stark shift. The parabolic fit (blue line) is shifted by 1.337 V with respect to 0 V, which is caused by the additional offset field of the Faraday cage. At 0 V one gets an Stark shift of 0.58 MHz which corresponds to an offset field of 0.27 V/cm (calculated 0.2 V/cm). The curvature of the fitted parabola can be used to calibrate the electric

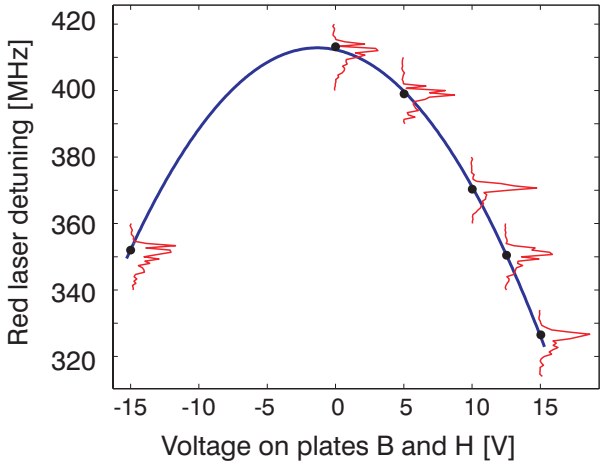

Figure 5.10: Stark shift of the $43S_{1/2}$ state. The black dots represent the maxima of the measured Rydberg signals (red). The field was applied to the atoms by charging the field plates B and H with a certain voltage. The blue line is a parabolic fit to the data: Detuning(MHz)=$-0.3252(U_{B,H} - 1.337V)^2$ MHz/V^2 + 412.8 MHz

field for the applied voltages at field plate B and H. To achieve 1 V/cm at the position of the atoms one has to apply 5 V at both field plates. The expected value from the theoretical calculation has been 7.2 V. Both deviations from the theoretical can be explained if the atomic cloud is shifted along the x-axis by a few millimeters away from the geometric center. More likely are imprecisions of the numerical calculations, since the parametrization of the full vacuum chamber geometry is not feasible.

The spectroscopic lines (plotted in red) exhibit a broadening which is not independent on the applied electric field. There are two possible paths for the two photon transition $5S_{1/2} \rightarrow 5P_{3/2} \rightarrow 43S_{1/2}$. The desired transition ends in the $j = +1/2$ state of the $43S_{1/2}$ manifold, which is the only one allowed by the chosen polarizations. Nevertheless is the direction of the magnetic field adjacent to the trapping center not anymore parallel to the z-axis and atoms can also be transferred to the $j = -1/2$ which is not anymore insensitive to the magnetic field. The g_j factor of the Rydberg state is 2 and the total change in magnetic momentum is 2 μ_B. For the given width of the of atomic cloud this results in a broadening of about 3 MHz, which explains the observed widths very well. The magnetic field offset of the magnetic trap of about 1 G leads to an line shift of 2.8 MHz which is barely resolved in the available data.

5.3.4 Lifetime of the 43S$_{1/2}$ state

The measurement of the lifetime has been carried out on a magnetically trapped cloud at 20 μK and a density of about $5 \cdot 10^{12}$ cm^{-3} of ground state atoms. The mean distance between the magnetically trapped atoms of only 600 nm becomes comparable to the diameter of 250 nm of a Rydberg atom in the 43S$_{1/2}$ state (see table 2.3). The question is wether the excited state lifetime is altered by the nearby ground state atoms or not. The configuration of the laser beams is the same as before. The power of the laser beams was set to 200 μW (780 nm) and to 45 mW (480nm). We excited about $3 \cdot 10^7$ trapped atoms for 20 μs and field ionized the remaining

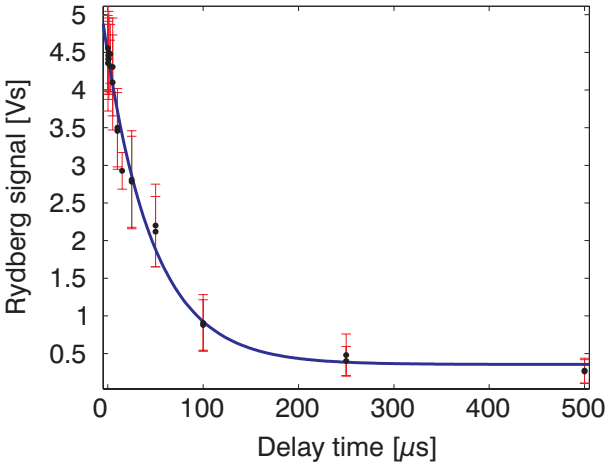

Figure 5.11: Measurement of the $43S_{1/2}$ state lifetime. The blue line is an exponential fit to the red data points with a time constant of $\tau = 98.8\mu$s. The offset of the MCP signal is 0.36 Vs.

Rydberg atoms after a certain delay time Δt and detected the ions on the MCP.

The results are shown in figure 5.11. Each data point is an average of 200 measurements. The loss of Rydberg atoms follows very well a simple exponential decay with a time constant of 99 μs $\pm$15 μs. This corresponds exactly to the expected theoretical value of 99 μs given by equation (2.76). On the other hand a reduction of the lifetime by an factor of two due to black body radiation is expected. A more detailed treatment of the influence of black body radiation in a finite size cavity in appendix I shows, that the reduction of the lifetime is only about 5% which is consistent with the measurement. This shows on the other side, that for the given density of $5 \cdot 10^{12}$ cm^{-3} the lifetime is not influenced noticeable by nearby ground state atoms or by the interaction among the Rydberg atoms.

In conclusion these results on the measurement of the Stark effect and the excited state lifetime show that all components for experiments with Rydberg atoms are running properly and are calibrated carefully. This system establishes a completely new regime for research of Rydberg matter and some future projects are illustrated in chapter 6.2.2.

6 Summary and Outlook

The goal of this thesis was to set up a Bose-Einstein condensation experiment, which can be used to address many novel questions connected to quantum degenerate systems, atomic physics and solid state theory. During the course of the last three years I designed the experimental setup from scratch and planned its realization. The successful conversion of the blueprints into a real experimental setup was realized within a year with the help of an enduring diploma student [192]. At the end of this process we can produce quantum degenerate samples on demand and use them as a launching pad for physical investigations. These require suitable tools, of which several were developed alongside and are summarized in the milestones below.

6.1 Milestones

All in all we set up an ultra-high vacuum system, three complex laser systems, elaborate high current and high voltage electronics, specialized magnetic coils, field plates for manifold electric field configurations, sensitive ion detectors, a complex control- and analysis software and many small gadgets alongside.

6.1.1 A running Bose-Einstein condensation machine

The precondition for experiments with Bose-condensed atoms is a reliable, efficient, calibrated and flexible setup. With the setup presented in this thesis, we are able to produce on a daily basis every 45 seconds a Bose-Einstein condensate consisting of half a million atoms. The maintenance of the whole system requires every other week an alignment of the laser systems and the adjustment of the orientation of the laser beams for laser cooling. The vacuum system needs no attendance, besides a new layer of Titanium in the sublimation pump once per year and the exchange of the Rubidium vial in the oven every second year. All other components, as e.g. the imaging system, the high current electronics, the control program, the analysis software, etc. are debugged and ready set.

The combination of a Zeeman-slower with a clover-leaf trap is up to date the most efficient way to produce large Bose-Einstein condensates with long lifetimes. The repetition rate of 45 seconds can still be improved, but will be ultimately limited to about 20-30 seconds [122].

The reliability of the system also includes the calibration of its detection methods and its tools for manipulation, which allow the deduction of quantitative information. For detection we use the imaging systems and the multi-channel plates. The two imaging setups, fluorescence and absorption, are both calibrated in their magnification scaling and detection efficiency to an absolute accuracy of about 90 %. The detection efficiency of the field ionized Rydberg atoms is accurate to roughly 75 %.

The major tools tested in this thesis are the magnetic fields produced by the clover-leaf trap, the electric field configurations for experiments with Rydberg atoms, the far-off resonant light potentials generating optical lattices and the properties of the microwave generation at 6.8 GHz.

The versatility of this setup is innately given by the extremely good optical access of the vacuum chamber to the atomic samples. Almost all experiments conducted so far with quantum degenerate gases require more or less complex combinations of several laser beams. What distinguishes the present setup from all other existing assemblies worldwide is its specific layout for experiments with Rydberg atoms.

6.1.2 Experimental realization of an optical lattice

With the observation of the time dependent diffraction of a Bose-Einstein condensate in an optical lattice and its agreement with the theoretical treatment, we could determine all relevant parameters. The theoretical tools developed to describe the observed diffraction peaks are also capable to simulate time dependent lattice potentials or varying interactions among the atoms, which leads to new physical insights [180]. Optical lattices are going to be a major ingredient for future experiments dealing with the spin-Boson model, but are also relevant for experiments with Rydberg atoms.

6.1.3 Coherent coupling of two hyperfine ground states

We have set up a high-class system for microwave generation and tested its performance by driving a two level system coherently [237]. The observation of Rabi flopping and its excellent agreement with the theoretical predictions, endows us a calibrated tool for manifold applications. In combination with the radio-frequency setup for evaporative cooling, we are now able to transfer atomic populations coherently in any magnetic sub-level in both hyperfine state. This will be either used in the context of the spin-Boson model, but can also be used to manipulate the atomic samples for Rydberg experiments.

6.1.4 Investigation of ultra-cold Rydberg atoms

To connect the physics of quantum degenerate gases with the field of Rydberg atoms, we successfully installed and tested several novel technologies into our setup. Novel has to be read in the context of traditional trapping and cooling setups. The excitation of Rubidium atoms is done by a laser system, which was previously built and tested on a separate setup [189]. To make use of the sensitivity of Rydberg atoms we installed eight field plates inside the vacuum chamber to generate complex field configurations [238]. The functionality of the plates was tested and calibrated by measuring the Stark shift for different electric fields. The detection of Rydberg atoms is only made possible by the field plates, which are used to field ionize the Rydberg atoms and to guide the remaining ions into a multi-channel plate. We installed two MCPs inside the vacuum chamber, one for electron detection and the other one for ion detection. Both of them are working, but we used in the experiments, presented in this thesis, only one for ion detection. The calibration of the detection efficiency allows us, together with the knowledge of the atom numbers deduced from the imaging systems, to extract quantitative excited state fractions. Finally we measured the lifetime of the $43S_{1/2}$ state, which is in accordance with the theoretical predictions. We conclude from this, that the influence of nearby ground state atoms onto the Rydberg atoms is small enough, which actually permits one to conduct experiments at such densities.

6.1.5 Theoretical treatment of light induced dipole-dipole interactions

The proposed experiment [231, 232] on measuring the light induced dipole-dipole interaction illustrates how coherent, long-range and anisotropic interactions can be brought together with quantum degenerate gases. Beyond this effect exists up to date only one experimental system, which exhibits such natured interactions. The confirmation of the dipolar character in a Chromium condensate [165] has triggered a huge amount of theoretical proposals to investigate such systems in more detail.

6.2 What's next?

The experimental setup presented in this thesis has a disposition for many different scientific fields, but in the end one has to focus on a few distinct topics. The investigation of Rydberg excitations from a BEC was already the motivation for the experimental layout of the whole experiment and is one of the key enterprises. As a second goal is the experimental realization of the spin-Boson model with the help of a BEC.

6.2.1 The spin-Boson model

Quantum impurity systems have been studied extensively by many theoretical groups [75, 244, 245] but only little experimental insight is available [246, 247]. The key idea of the so called spin-Boson model which describes the decoherence of a generalized spin **S**, which couples to a bosonic environment **E**. Degenerate quantum gases can be used to realize such models with the possibility to adjust the fundamental parameters over a wide range [77, 76].

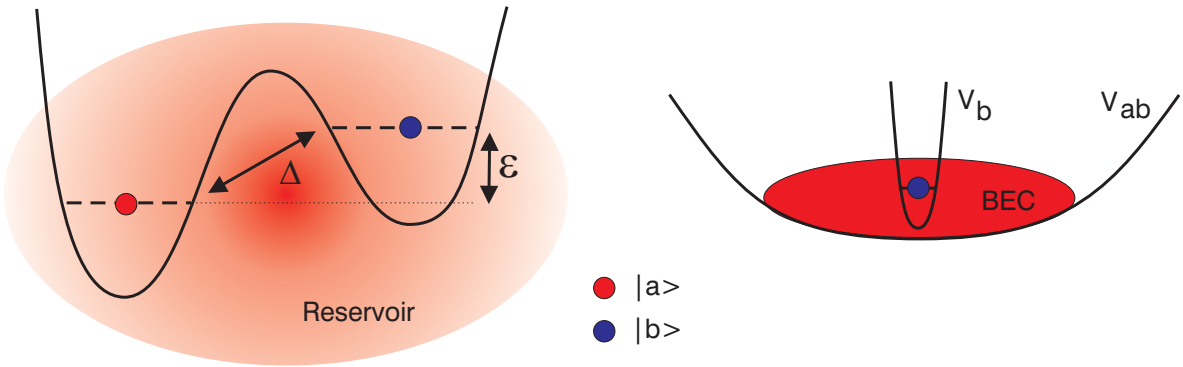

Figure 6.1: The spin-Boson model. The left part of the figure shoes the two states $|a\rangle$ and $|b\rangle$ of a generalized spin **S** embedded in a bath **E** of bosonic excitations. The two spin states are separated by an bias energy ϵ and are coupled by a tunneling coupling Δ. On the right side is an experimental implementation of the spin-Boson model shown. The two spin states are now represented by the two different hyperfine ground states of ^{87}Rb and the bath by the excitations in a Bose-Einstein condensate. The atoms of the condensate in state $|a\rangle$ are confined in potential V_{ab} which acts on both spin states. An additional potential V_b only acts on the spin state $|b\rangle$. The tunneling coupling is obtained by coherent Raman transitions between the two hyperfine states.

A schematic illustration of the underlying physical system is given in figure 6.1. It consists of a two level system with states $|a\rangle$ and $|b\rangle$, also referred to as a quasi-spin, which is embedded in an environment. The spin is coupled to the bosonic excitations, described as harmonic oscillator states, of the environment. The large degrees of freedom of the bath causes a decoherence of the coherent evolution of the spin state. Such a coherent evolution is for example given by a tunnel coupling as shown in the right part of figure 6.1 or by an external driving field as is it planned in our realization (see right part of figure 6.1). The spin-Boson Hamiltonian H_{sB} is then [76] given by

$$H_{sB} = -\frac{\hbar\Delta}{2}\sigma_x + \sum_q \hbar\omega_q b_q^\dagger b_q + \frac{\hbar}{2}\sigma_z\left(\frac{\epsilon}{\hbar} + \sum_q \lambda_q(b_q + b_q^\dagger)\right). \tag{6.1}$$

The spin states are now given by $|a\rangle = (1,0)$ and $|b\rangle = (0,1)$ and σ_x and σ_z are the ordinary Pauli spin matrices. The first term describes the coherent coupling between the two spin states and the second term the bosonic bath in second quantization description, where b_q and $b_q^\dagger$ are the annihilation and and creation operators of the phonon modes. They are characterized by a momentum q and the dispersion relation $\omega_q = u \cdot q$, where u is the speed of sound. With the last term the spins are coupled to the bath. The bosonic bath can be reduced to an effective density of states for sufficient low frequencies as

$$J(\omega) = \lambda_q^2\delta(\omega - \omega_q) = 2\alpha\omega^s. \tag{6.2}$$

One can distinguish between different physical cases depending on the exponent s and the dissipation parameter α. The most interesting case is the so called ohmic one with $s = 1$, which is our goal. For a damping $\alpha > 1$ one expects at $T = 0$ a localization in one spin state, which is not feasible with Bose-Einstein condensates. The interesting regime is for α ranging between 0 and 1/2, which results in undamped Rabi oscillations at $\alpha = 0$, damped oscillations for $0 < \alpha < 1/2$ and a purely exponential decay at $\alpha = 1/2$. Experimentally we will be able to vary α from 0 to 0.08 as will be discussed below with all the other required preconditions.

Preparation of the environment E Ohmic damping with $s = 1$ is given in the case of a one dimensional Tonks-Girardeau gas, also known as Luttinger liquid [58, 59]. This regime can be realized with the help of a two dimensional optical lattice (see chapter 5.1), which delivers into the bargain up to 100 identical and independent reservoirs. The condensate is initially prepared in the $F = 2, m_F = +2$ state and then transferred adiabatically into the optical dipole trap. With the help of a microwave field (see chapter 5.2) the atoms are then transferred into the $F = 1, m_F = +1$ which is equivalent to the state $|a\rangle$.

Preparation of the quasi-spin S and the coupling Δ The other spin state $|b\rangle$ is equivalent to the $F = 2, m_F = -1$ state. The coupling Δ between the two spin states is then done by driving coherent Raman transitions with laser light [19]. Such a laser system is already available and was tested extensively by observing electromagnetically induced transparencies in a vapor cell [239]. It is important that only one atom per reservoir undergoes Rabi oscillations. To assure that an additional potential V_b is superposed, which only acts on state $|b\rangle$ but not on state $|a\rangle$. The selectivity is achieved by tuning the Raman transition such, that it is in resonance with the ground state energy of the potential V_b. On the other hand has the on-site interaction to be large enough that it shifts the niveau out of resonance, if more than one atom is confined in the potential V_b. This requires a quite steep potential, which involves a sharp focused laser beam. The state selectivity of the dipole potential is given for linear polarized light at 787 nm, as described in appendix E. With an

available laser power of 300 mW and a width of 5 μm of the focused Gaussian beam one achieves, in combination with the two-dimensional lattice, in all three dimensions a confinement with more than 200 kHz.

Variation of the coupling strength to the bath To distinguish between the desired decoherence due to the coupling to the bath and other unwished disturbances, is one possibility to alter the coupling α to the reservoir. This can be achieved in two ways. There exists an interstate Feshbach resonance between the two states $F = 1, m_F = +1$ and $F = 2, m_F = -1$ at 9.1 G [42] by which α can be altered continuously from 0 to 0.03. Another possibility is to change the one dimensional density by a factor of two, which extends the range of α up to 0.08.

Detection Finally one has to detect the atoms state dependent to acquire the damped Rabi-oscillations. The experiment will be executed on about 100 identical systems, with each containing only one driven spin state. This demands a detection sensitivity of better than 100 atoms. The detection efficiency of field ionized Rydberg atoms is already on the order of a few hundred ions 5.3 and is presently limited by the quality if the detection circuitry. An improvement of the detection efficiency by a factor of ten should be sufficient. The state selective excitation into a Rydberg state has been shown in [189] for our laser system and is adequate for our scope.

6.2.2 Rydberg matter

In most quantum optical systems the interactions among the particles are the key to novel phenomena. These are in the field of quantum gases the short range contact interaction and in experiments dealing with ion taps the long-range Coulomb repulsion. One exception to this restriction is the first realization of a dipolar quantum fluid, in which the magnetic dipole-dipole interaction becomes comparable to the contact interaction and thus visible.

Rydberg atoms can exhibit large permanent electric dipole moments, which lead to anisotropic and long-range interactions among the atoms. The investigation of the coherence properties and the possibilities to control this dipolar interactions in a many particle system will be a major task. This is also interesting with a vision of realizing quantum logical elements with the help of Rydberg states. The interaction of the dipoles with electric fields can also be used to exert forces on the Rydberg atoms or even to store them in an conservative potential. Finally we are interested in the generation of molecules consisting of Rydberg atoms and ground state atoms.

Dipole blockade The energy levels among two neighboring Rydberg atoms are shifted by either the van der Waals interaction or their dipolar moment. For large enough shifts, or to small interatomic distances, leads this to a blockade effect, which was already observed for the van der Waals interaction [87, 86]. The goal is the measurement of a dipole blockade effect, which will be a first step towards quantum information processing with Rydberg atoms [91]. The strength of the dipolar interaction can be controlled by the induced dipole-moments of a state exhibiting a quadratic Stark effect via the strength of the electric field.

Trapping Rydberg atoms With the help of the eight field plates we are able to generate an electric field distribution with a field minimum in the center. In this geometry we are able to catch weak field seeking states. The strongest confinement is achieved with the most extremal hydrogen-like state exhibiting the largest dipole moments. For atoms in $n = 40$ state and voltages up to 3000 V at the field plates result in trapping frequencies of 1 MHz. This is compared to the excited state lifetime large enough, that one can clearly talk about trapped Rydberg atoms. The evidence will be a measurement of the trapping frequency of a kicked Rydberg atom. With the control over

the position of Rydberg atoms one can manipulate and examine the interactions of Rydberg states with a independently trapped (magnetically or optically) Bose-Einstein condensate.

Molecules The existence of polar molecules consisting of one Rydberg atom and one ground state atom has been postulated in [92]. The vibrational states of such a molecule would have a level spacing ranging from MHz to GHz. This could be resolved spectroscopically with our laser system.

Quantum Information Processing (QIP)

The realization of QIP [248, 249] requires several conditions, which have to be accomplished simultaneously:

- A scalable physical system with well-characterized qubits
- The ability to initialize the qubit state
- Decoherence times much longer than the quantum gate operation
- A universal set of quantum gates
- The ability to measure specific qubits

A regular pattern of N ^{87}Rb atoms confined in an optical lattice can be the starting point for QIP with N qubits. The two states of the qubit are the two hyperfine ground states $F = 1$ and $F = 2$ of ^{87}Rb. Initially all atoms are prepared in identical quantum state, which is made possible by a Mott-insulating phase [72]. Now all atoms exhibit the same internal (e.g. $|F = 1\rangle$) and external quantum state. The next step is the generation of a quantum input register by transferring specific qubits into the other spin state $|F = 2\rangle$ by a 1-qubit operation. This can be done by combining the narrow line width of microwave transitions with a space dependent Zeeman shift. This requires a spatial resolution of the different lattice sites by suitable magnetic field gradients.

Now is the application of 2-qubit operations with the help of the dipole-blockade effect among Rydberg-atoms [91] possible. The dipole-dipole interaction among the Rydberg atoms suppresses the excitation of an atom into a Rydberg-state, if a neighboring atom is already in a Rydberg state. A more detailed discussion how to realize a c-NOT quantum gate is given in [189]. A implementation of this gate, requires that only two nearby lattice sites are involved. The selection of two specific lattice positions can be achieved with the help of the Stark-shift and the narrow line widths of Rydberg excitations. Unfortunately it is not possible in our setup to generate electric fields, which have only at two distinct positions the same field strength. To get around this problem, one can use two laser beams, with each being in resonance at one lattice site. As a last step one has to readout the result, which is stored in the spin states. To do so, one addresses again a specific lattice site with an electric field and excites the atom state selectively into a Rydberg state. Subsequently the Rydberg atom is field ionized and detected with a multi-channel plate.

A The element Rubidium

The element Rubidium is since almost 20 years the standard atom for cold atom physics. Although the first trapping and cooling experiments were done with Sodium [132], the development of cheaper diode laser systems made Rubidium more and more attractive [250]. Its simple electronic level scheme, common to all alkali elements, gives experimentalists almost a two-level system at hand.

In nature Rubidium is found in two stable isotopes, namely ^{85}Rb and ^{87}Rb [251]. The latter is used in our experiments due to its well behaved scattering properties at low temperatures. ^{85}Rb exhibits a negative scattering length at small magnetic fields which makes Bose-Einstein condensation difficult [8]. The natural ratio between this two isotopes is 72 to 28, with ^{87}Rb holding the smaller fraction. ^{87}Rb is radioactive and decays with a rate of 4.9 10^{10} years into ^{87}Sr [252]. The other isotopes, ^{82}Rb, ^{83}Rb and ^{84}Rb, can be created artificially but are not found in nature.

A.1 Physical properties of ^{87}Rb

The vapor pressure of ^{87}Rb in torr in the liquid phase can be modeled by

$$\log_{10} P_v = 15.88253 - \frac{4529.635}{T} + 0.0058663T - 2.99138 \log_{10} T, \tag{A.1}$$

with T being the temperature in Kelvin [131]. All further important properties are listed in table A.1.

Atomic number	37
Total nucleons	87
Relative natural abundance	27.83
Atomic mass (SI)	1.443 160 60(11) $\times 10^{-25}$ kg
Atomic mass (a.u.)	86.909 180 520(15) u
Melting point	39.31°C
Boiling point	608°C
Vapor pressure at 25°C	3.0 $\times 10^{-7}$ torr

Table A.1: *Physical properties of ^{87}Rb*

A.2 Optical properties of ^{87}Rb

For a more detailed description of the optical properties of Rubidium than given here see [131, 125]. The electronic ground state configuration of Rubidium is $1s^2 2s^2 2p^6 3s^2 3p^6 3d^{10} 4s^2 4p^6 5s^1$, with

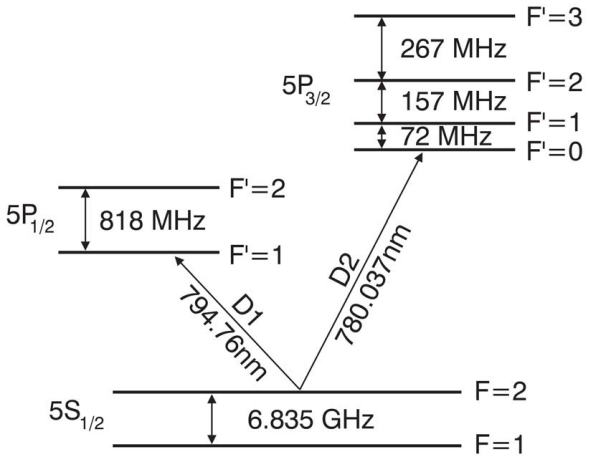

Figure A.1: Level scheme of the D-line doublet with its hyperfine structure of ^{87}Rb.

one solely electron in the 5s shell. The energetically next excited state is a doublet due to the fine structure splitting, which are commonly known as the D_1 line $5\,^2S_{1/2} \rightarrow 5\,^2P_{1/2}$ and the D_2 line $5\,^2S_{1/2} \rightarrow 5\,^2P_{3/2}$. The nucleus has a spin of I=3/2, which gives an hyperfine structure on top of the fine structure doublet.

The calculation for each transition strength within in the manifolds can be simplified by extracting the angular dependence of the transition dipole moments [125]. To calculate the dynamics of the multilevel system irradiated by a laser of a certain polarization, intensity and detuning, one needs to know the Rabi frequency for each transition $\Omega = -\mu_{eg}E_0/\hbar$ and the spontaneous decay rates for each decay channel $\Gamma = \omega^3\mu_{eg}^2/(3\pi\varepsilon_0\hbar c)$. E_0 is the amplitude of the electric field of the driving light field and $\hbar\omega$ the energy difference between the ground and excited state. The dipole matrix element is given by

$$\mu_{eg} = e\langle e|\hat{\varepsilon}\cdot\vec{r}|g\rangle = e\langle n'L'm_L'|\hat{\varepsilon}\cdot\vec{r}|nLm_L\rangle, \tag{A.2}$$

with elementary charge e and the unity vector of the polarization $\hat{\varepsilon}$ of the electric field. The primes indicate the excited state. The atomic eigen-states are given in the F, m_F-basis of the hyperfine manifold. To calculate (A.2) one can make use of the Wigner-Eckhardt theorem [253, 254] to decompose the couplings of the angular momenta

$$\begin{aligned}\mu_{eg} = (-1)^{1+L'+S+J+J'+I-m_F'}\sqrt{(2J+1)(2J'+1)(2F+1)(2F'+1)}\\ \times\begin{Bmatrix} L' & J' & S \\ J & L & 1\end{Bmatrix}\begin{Bmatrix} J' & F' & I \\ F & J & 1\end{Bmatrix}\begin{pmatrix} F & 1 & F' \\ m_F & q & -m_F'\end{pmatrix} e\langle n'L'||r||nL\rangle.\end{aligned} \tag{A.3}$$

The reduced matrix element $\langle n'L'||r||nL\rangle$ depends only on the radial distribution of the atomic wave function. For transitions within the D2 manifold is $J = 1/2$, $J' = 3/2$, $L = 0$, $L' = 1$ and $I = 3/2$. The polarization of the light is given by $q = 0$ for linear polarized light and $q = \pm 1$ for σ^+ respectively σ^- polarized light. The expression in curly brackets are 6j-symbols and in round brackets 3j-symbols. The reduced matrix element can be derived indirectly from the measured life time of the excited state or by straight forward by integration of the dipole matrix element. The

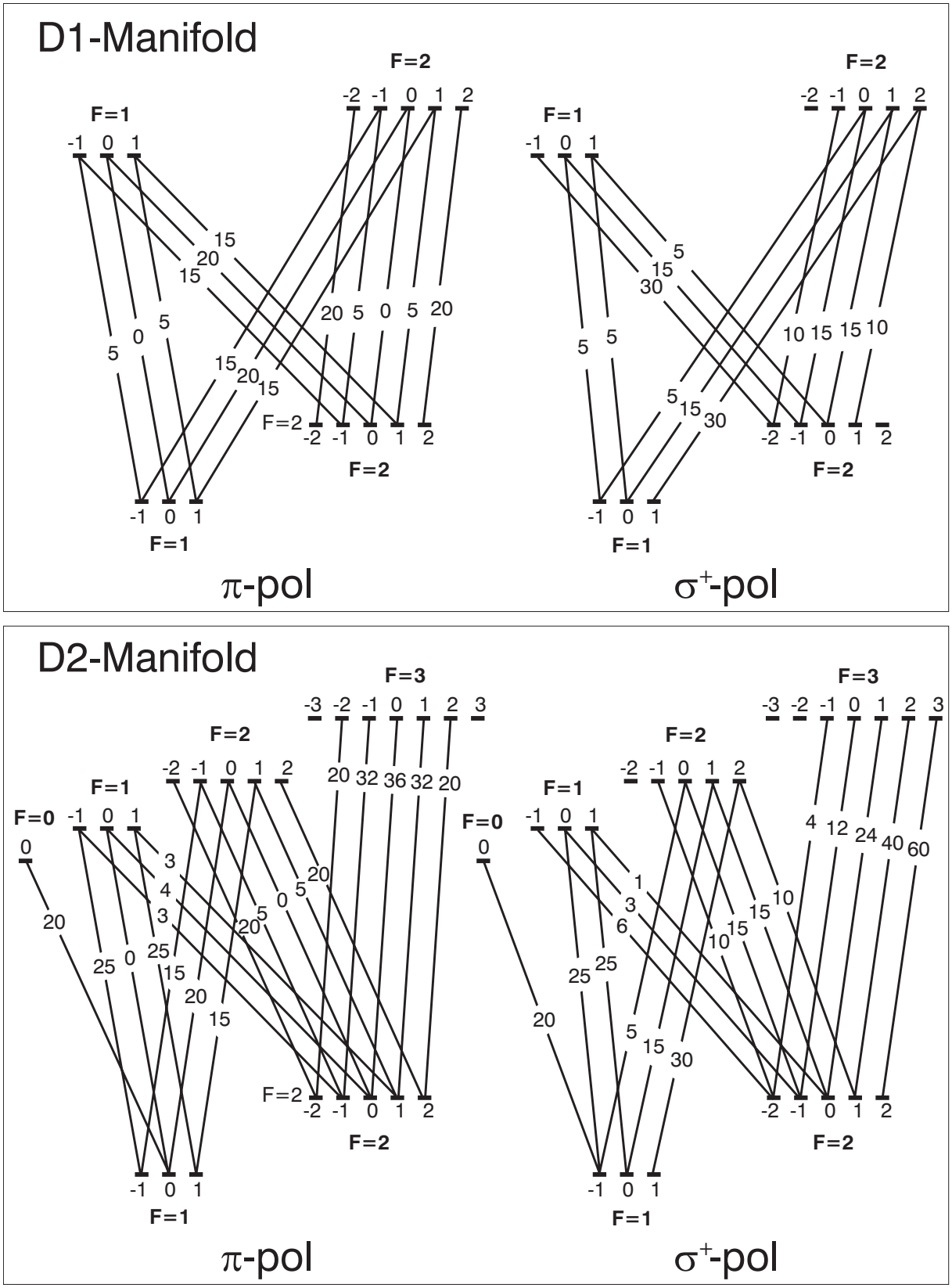

Figure A.2: Transitions strengths within in the D2 manifold for linear and circular polarized light. The strengths are normalized to the weakest transition to obtain only integers.

latter method requires a very good knowledge of the radial wave function and is therefore not trivial [189]. The optical properties of the D1 and D2 manifold are given in the table A.2.

Property	**Value**
D2-line ($5S_{1/2} \rightarrow 5P_{3/2}$)	
Frequency	2π 384.227 981 877 3(55) THz
Wave length (vacuum)	780.246 291 629(11) nm
Lifetime $5P_{3/2}$	26.24(4) ns
Line width $5P_{3/2}$	2π 6.065(9)MHz
Saturation intensity	16.7 W/m^2
Recoil velocity	5.8845 mm/s
Recoil energy	2π 3.7710 kHz
Recoil temperature	361.96 nK
Doppler shift with v_{atom}=v_{recoil}	2π 7.5419 kHz
Doppler temperature	146 μK
Hyperfine splitting F=1, F=2 (ground state)	6.834 682 610 904 29(9) GHz
Hyperfine splitting F′=0, F′=1 (excited state)	72.218(4) MHz
Hyperfine splitting F′=1, F′=2 (excited state)	156.947(7) MHz
Hyperfine splitting F′=0, F′=1 (excited state)	266.650(9) MHz
D1-line ($5S_{1/2} \rightarrow 5P_{1/2}$)	
Frequency	2π 377.107 463 5(4) THz
Wave length (vacuum)	794.978 850 9(8) nm
Lifetime $5P_{3/2}$	27.70(4) ns
Line width $5P_{3/2}$	2π 5.746(8) MHz
Saturation intensity	14.9 W/m^2
Recoil velocity	5.7754 mm/s
Recoil energy	2π 3.6325 kHz
Recoil temperature	348.66 nK
Hyperfine splitting F′=1, F′=2 (excited state)	816.656(30) MHz

Table A.2: *Optical properties of the ^{87}Rb D1 and D2 manifold*

B Rubidium atoms in magnetic fields

The Zeeman energy of the different hyperfine ground states in Rubidium can be calculated by using the Breit-Rabi formula [143, 213]. For the case of zero angular momentum second order perturbation theory gives

$$E_{F,m_F}(B) = (-1)^F \frac{\hbar\omega_{hf}}{2}\sqrt{1+\frac{4m_F}{2I+1}x+x^2}+\text{const} \tag{B.1}$$

with

$$x = \frac{(g_I+g_s)\mu_B B}{\hbar\omega_{hf}} \tag{B.2}$$

The spin of the nucleus is $I = 3/2$, the g-Factor of the nucleus $g_I = 0.995\,10^{-3}$ and the g-Factor of the electron $g_s = 2.0023$. The hyperfine splitting of the two ground states is $\omega_{hf} = 2\pi\,6.8346826128(5)$ Hz.

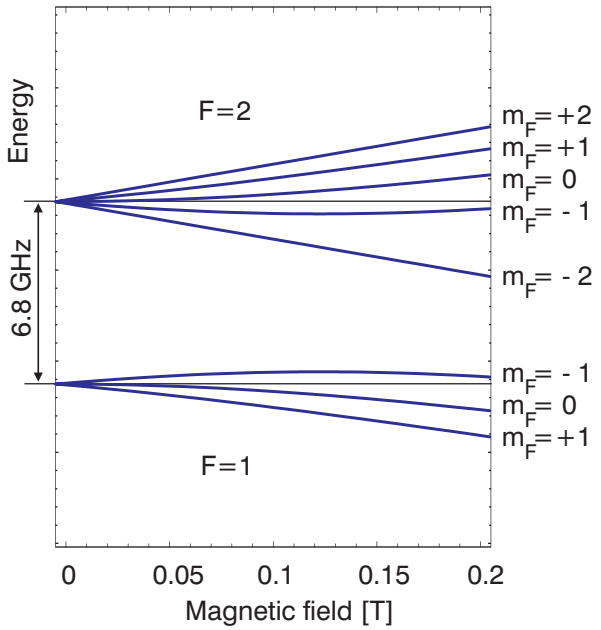

Figure B.1: Zeeman shift of magnetic sub-levels of ^{87}Rb in the presence of a magnetic field.

For not to large magnetic fields the Zeeman splitting can be approximated to second order as long the Zeeman splitting $E_{F,m_F}(B) \ll \omega_{hf}$.

$$E_{F,m_F}(B) = (-1)^F\left(\frac{\hbar\omega_{hf}}{2}+m_F g_F \mu_B B+\frac{(4-m_F^2)}{16}\frac{(g_s\mu_B B)^2}{\hbar\omega_{hf}}\right)+\text{const} \tag{B.3}$$

with

$$g_F = (-1)^F \frac{1}{2I+2} g_s \tag{B.4}$$

For this approximation also $g_I \ll g_s$ was assumed. For large magnetic fields the hyperfine coupling of the nucleus spin I and the angular momentum J breaks down and the lines group into two pairs $J = \pm 1/2$ (orbital momentum L=0) and the four projections of the nucleus $I = \pm 3/2, \pm 1/2$.

From special interest are the so called clock-transitions between two $m_F = 0$ magnetic sub-levels, since they are least sensitive to magnetic fields. The energy shift for a clock transition from $F = 1, m_F = 0 \rightarrow F = 2, m_F = 0$ depends only quadratically on the magnetic fields as

$$\Delta_E = \frac{(g_s \mu_B)^2}{2\hbar\omega_{hf}} B^2. \tag{B.5}$$

This gives a frequency shift of 575.15 Hz/G^2.

C Rubidium Rydberg atoms in electric fields

Since the highly excited electron is only weakly bound to the core, the Rydberg atoms exhibit strong interactions with electric fields. The energies of the new eigen-states of a Rydberg atom in an constant electric field are shown in the Stark map in figure C.1. The denotation of the states is only valid for zero electric field. With increasing electric field the unperturbed states acquire more and more admixtures by other states. The calculation of the eigen-energies for Rubidium was done carefully in [189] including the fine-structure and the hyperfine structure. The contribution of the latter is on the order of a few kHz and shall be omitted here.

The Hamiltonian of an atom in an constant electric field E along z is given by

$$H = H_0 + H_{fs} + Ez \tag{C.1}$$

where H_0 is the unperturbed atom and H_{fs} the fine structure energy due to the coupling of the orbital momentum to the electron spin. To calculate the Stark map by diagonalization the full Hamiltonian H one has to know the unperturbed Rubidium eigen-states and the matrix elements due to the electric field.

$$\left\langle n, l, m \left| Ez \right| n', l', m' \right\rangle = \delta_{m,m'} \delta_{l,l'\pm 1} E \left\langle l, m \left| \cos\theta \right| l', m' \right\rangle \cdot \left\langle n, l \left|\left| r \right|\right| n', l' \right\rangle \tag{C.2}$$

The contribution of the orbital part $\langle l, m | \cos\theta | l', m' \rangle$ can be calculated algebraically [255]. The reduced matrix elements $\langle n, l || r || n', l' \rangle$ are overlap integrals of the radial part and have to integrated numerically.

Now we have to include the fine structure which couples the orbital momentum l with the spin $s = \pm 1/2$ to a new angular momentum $j = l \pm 1/2$. The coupling matrix elements are now

$$\begin{aligned} \left\langle n, l, j, m_j \left| Ez \right| n', l', j', m_j' \right\rangle &= \delta_{m_j, m_j'} \delta_{l,l'\pm 1} \left\langle n, l, j \left|\left| r \right|\right| n', l', j' \right\rangle E \\ &\times \sum_{m_l = m_j \pm \frac{1}{2}} \left\langle l, \frac{1}{2}, m_l, m_j - m_l | j, m_j \right\rangle \left\langle l', \frac{1}{2}, m_l, m_j - m_l | j', m_j \right\rangle \\ &\times \left\langle l, m_l \left| \cos\theta \right| l', m_l \right\rangle, \end{aligned} \tag{C.3}$$

The first line in equation (C.3) are again the reduced matric elements of the radial part. The second line is a sum over Clebsch-Gordan coefficients which can be looked up in [253, 254] and the last line are the angular overlap integrals as introduced in equation (C.2).

The $43S_{1/2}$ state is of special interest, which was also used throughout in our experiments (see chapter 5.3), since it only exhibits a quadratic Stark effect. The calculated Stark shift $\Delta\nu = pE^2$ gives a value of -8.06 MHz/(V/cm)^2 for p.

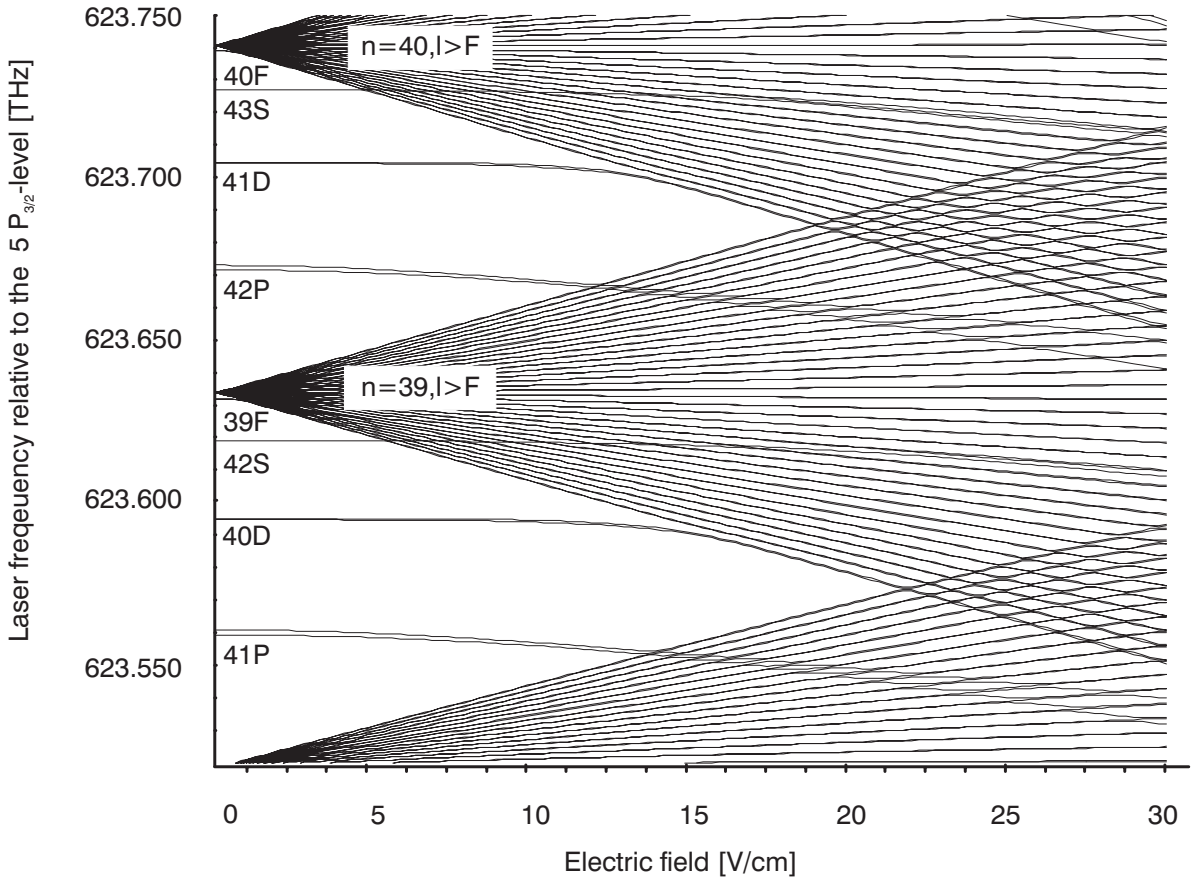

Figure C.1: Calculated Stark map including the LS-coupling [189]. The angular momentum states with $l \leq 3$ exhibit a quadratic dependence on the electric field and the states with l>3 are linear.

By increasing the electric field more and more it is possible to detach the weakly bound electron from the core. This process is called field ionization. The two emerging charged fragments, a solely electron and a Rn^+ ion, can be detected with multi-channel plates with a high efficiency. Let us assume classically the Coulomb potential of Hydrogen atom in an constant electric field E.

$$V = -\frac{e^2}{4\pi\varepsilon_0 r} + eEr \tag{C.4}$$

Figure C.2 shows the unperturbed (blue) and the perturbed (red) Coulomb potential. The new local maximum of the combined potential is given by

$$V_{max} = -2\sqrt{\frac{Ee^3}{4\pi\varepsilon_0}} \tag{C.5}$$

The ionization field can be calculated [189] to be

$$E = \frac{E_0}{16n^4} \tag{C.6}$$

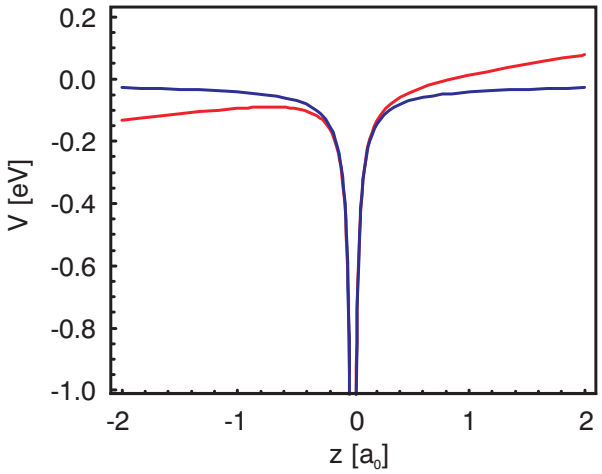

Figure C.2: Coulomb potential of a charge $+e$ perturbed by a constant electric field along z with a field strength of 10^6 V/m.

where $E_0 = \frac{e^5 m_e^2}{64\pi^3 \varepsilon_0^3 \hbar^4}$. The Rydberg states can ionize even at lower fields by tunneling through the barrier.

The field ionization can be used in an experiment to gain detailed information about the physical situation. Since the ionization energy depends on the Rydberg state one can detect the population of the states by slowly increasing the electric field. By this method one detects first the higher excited states followed by the lower ones. Beyond this, the arrival time of the ions on the multi-channel plates gives valuable information about time-dependent processes in an frozen Rydberg gas. A detailed experimental investigation of the Stark map close by the $43S_{1/2}$ state can be found in [189, 256].

D Optical Bloch equations in a multi-level atom

The master equation (2.5) for a two-level system irradiated by an light field was given in chapter 2.1. This system of coupled equations can be expanded to a multi-level as exhibited by ^{87}Rb [131].

$$\begin{array}{rcl} \rho_{ee} & = & \frac{i}{2}\sum_g \Omega_{eg}(\rho_{eg}-\rho_{ge}) - \Gamma\rho_{ee} \\ \rho_{gg} & = & \frac{i}{2}\sum_e \Omega_{eg}(\rho_{ge}-\rho_{eg}) + \sum_e \Gamma_{eg}\rho_{ee} \\ \rho_{eg} & = & \frac{i}{2}\Omega_{eg}(\rho_{ee}-\rho_{gg}) - \frac{\Gamma}{2}\rho_{eg} - i\delta_{eg}\rho_{eg} \\ \rho_{ge} & = & \frac{i}{2}\Omega_{eg}(\rho_{gg}-\rho_{ee}) - \frac{\Gamma}{2}\rho_{ge} - i\delta_{eg}\rho_{ge} \end{array} \tag{D.1}$$

The excited states are labeled with e and the ground states with g. The coupled equations (D.1) only include density matrix elements which are coupled by a driving field or a spontaneous decay channel. The Rabi-frequencies between the magnetic sub-levels are given by

$$\Omega_{eg} = -\frac{2\langle F_e||er||F_g\rangle E_{-q}}{\hbar} = \Gamma\sqrt{\frac{I}{2\,I_{\text{sat}}}} \begin{pmatrix} F & 1 & F' \\ m_F & q & -m_F' \end{pmatrix} \tag{D.2}$$

which is valid for transitions within in the D2 manifold of ^{87}Rb. The excited states are labeled with a prime. The lifetime of any excited state is Γ which was given in table A.2. An excited state can decay in different magnetic levels of the ground state with following rates

$$\Gamma_{eg} = \begin{pmatrix} F & 1 & F' \\ m_F & q & -m_F' \end{pmatrix}^2 \Gamma \tag{D.3}$$

The polarization of the light is taken into account by setting $q = 0$ for linear polarized light and $q = \pm 1$ for $\sigma^{\pm}$ light. If a magnetic field B is present the detuning $\delta_e g$ has to be corrected according to the Zeeman-shift of the magnetic sub-levels.

$$\delta_{eg} = \delta_0 + (m_F\prime g_F' - m_F g_F)\mu_B B \tag{D.4}$$

By solving the coupled equations (D.1) numerically one can extract from this the time dependent population of the magnetic sublevels and the heating of the cloud due to the number of scattered photons. The radiation patterns for circular and linear polarization are anisotropic and so is also the momentum transfer to the atoms anisotropic. The probability to find a scattered photon in a solid angle $d\Omega$ is given by

$$\begin{array}{rcl} P_\pi(\theta) & = & \frac{3}{8\pi}\sin^2\theta \\ P_\sigma(\theta) & = & \frac{3}{16\pi}(1+\cos^2\theta) \end{array} \tag{D.5}$$

D.1 Spontaneous scattering and the light induced dipole-dipole interaction

In chapter 4.1 I presented a proposal to measure the effect of a light induced dipole-dipole potential in momentum space. Beyond the desired momentum gain of the atoms due to the induced potential one acquires also momentum by the recoils of spontaneous scattering events. To calculate this contribution one has to solve the time evolution of the density matrix. For intensities well below the saturation intensity, which is not the case here, one could also use a rate model, which neglects the coherences of the off-diagonal density matrix elements.

The linear polarized laser light couples the atoms from the $5S_{1/2}$, F=2 ground state to the excited $5P_{3/2}$, F=3 state. Due to momentum conservation spontaneous decay can only happen back into F=2. The frequency of light is shifted by $\delta = 16.7\Gamma$ to higher energies with respect to resonance, which reduces off-resonant excitation into other F-states. If the direction of the polarization is parallel to the quantization axes of the atoms, one can write down the coupled equations of motion:

$$
\begin{aligned}
\dot{\rho}_{(-2',-2')} &= i\cdot\tfrac{\omega_r}{2\sqrt{3}}\cdot(\rho_{(-2',-2)}-\rho_{(-2,-2')}) - \Gamma\cdot\rho_{(-2',-2')}\\
\dot{\rho}_{(-2,-2)} &= i\cdot\tfrac{\omega_r}{2\sqrt{3}}\cdot(\rho_{(-2,-2')}-\rho_{(-2',-2)}) + \tfrac{\Gamma}{3}\cdot\rho_{(-2',-2')}+\tfrac{\Gamma}{15}\cdot\rho_{(-1',-1')}\\
\dot{\rho}_{(-2,-2')} &= i\cdot\tfrac{\omega_r}{2\sqrt{3}}\cdot(\rho_{(-2,-2)}-\rho_{(-2',-2')}) - i\cdot\delta\cdot\rho_{(-2,-2')}-\tfrac{\Gamma}{2}\cdot\rho_{(-2,-2')}\\
\dot{\rho}_{(-2',-2)} &= i\cdot\tfrac{\omega_r}{2\sqrt{3}}\cdot(\rho_{(-2',-2')}-\rho_{(-2,-2)}) - i\cdot\delta\cdot\rho_{(-2',-2)}-\tfrac{\Gamma}{2}\cdot\rho_{(-2',-2)}\\
\\
\dot{\rho}_{(-1',-1')} &= i\cdot\tfrac{\omega_r\sqrt{8}}{2\sqrt{15}}\cdot(\rho_{(-1',-1)}-\rho_{(-1,-1')}) - \Gamma\cdot\rho_{(-1',-1')}\\
\dot{\rho}_{(-1,-1)} &= i\cdot\tfrac{\omega_r\sqrt{8}}{2\sqrt{15}}\cdot(\rho_{(-1,-1')}-\rho_{(-1',-1)}) + \tfrac{2\Gamma}{3}\cdot\rho_{(-2',-2')}+\tfrac{8\Gamma}{15}\cdot\rho_{(-1',-1')}+\tfrac{\Gamma}{5}\cdot\rho_{(0',0')}\\
\dot{\rho}_{(-1,-1')} &= i\cdot\tfrac{\omega_r\sqrt{8}}{2\sqrt{15}}\cdot(\rho_{(-1,-1)}-\rho_{(-1',-1')}) - i\cdot\delta\cdot\rho_{(-1,-1')}-\tfrac{\Gamma}{2}\cdot\rho_{(-1,-1')}\\
\dot{\rho}_{(-1',-1)} &= i\cdot\tfrac{\omega_r\sqrt{8}}{2\sqrt{15}}\cdot(\rho_{(-1',-1')}-\rho_{(-1,-1)}) - i\cdot\delta\cdot\rho_{(-1',-1)}-\tfrac{\Gamma}{2}\cdot\rho_{(-1',-1)}\\
\\
\dot{\rho}_{(0',0')} &= i\cdot\tfrac{\omega_r\sqrt{3}}{2\sqrt{5}}\cdot(\rho_{(0',0)}-\rho_{(0,0')}) - \Gamma\cdot\rho_{(0',0')}\\
\dot{\rho}_{(0,0)} &= i\cdot\tfrac{\omega_r\sqrt{3}}{2\sqrt{5}}\cdot(\rho_{(0,0')}-\rho_{(0',0)}) + \tfrac{2\Gamma}{5}\cdot\rho_{(-1',-1')}+\tfrac{3\Gamma}{5}\cdot\rho_{(0',0')}+\tfrac{2\Gamma}{5}\cdot\rho_{(1',1')}\\
\dot{\rho}_{(0,0')} &= i\cdot\tfrac{\omega_r\sqrt{3}}{2\sqrt{5}}\cdot(\rho_{(0,0)}-\rho_{(0',0')}) - i\cdot\delta\cdot\rho_{(0,0')}-\tfrac{\Gamma}{2}\cdot\rho_{(0,0')}\\
\dot{\rho}_{(0',0)} &= i\cdot\tfrac{\omega_r\sqrt{3}}{2\sqrt{5}}\cdot(\rho_{(0',0')}-\rho_{(0,0)}) - i\cdot\delta\cdot\rho_{(0',0)}-\tfrac{\Gamma}{2}\cdot\rho_{(0',0)}\\
\\
\dot{\rho}_{(1',1')} &= i\cdot\tfrac{\omega_r\sqrt{8}}{2\sqrt{15}}\cdot(\rho_{(1',1)}-\rho_{(1,1')}) - \Gamma\cdot\rho_{(1',1')}\\
\dot{\rho}_{(1,1)} &= i\cdot\tfrac{\omega_r\sqrt{8}}{2\sqrt{15}}\cdot(\rho_{(1,1')}-\rho_{(1',1)}) + \tfrac{\Gamma}{5}\cdot\rho_{(0',0')}+\tfrac{8\Gamma}{15}\cdot\rho_{(1',1')}+\tfrac{2\Gamma}{3}\cdot\rho_{(2',2')}\\
\dot{\rho}_{(1,1')} &= i\cdot\tfrac{\omega_r\sqrt{8}}{2\sqrt{15}}\cdot(\rho_{(1,1)}-\rho_{(1',1')}) - i\cdot\delta\cdot\rho_{(1,1')}-\tfrac{\Gamma}{2}\cdot\rho_{(1,1')}\\
\dot{\rho}_{(1',1)} &= i\cdot\tfrac{\omega_r\sqrt{8}}{2\sqrt{15}}\cdot(\rho_{(1',1')}-\rho_{(1,1)}) - i\cdot\delta\cdot\rho_{(1',1)}-\tfrac{\Gamma}{2}\cdot\rho_{(1',1)}\\
\\
\dot{\rho}_{(2',2')} &= i\cdot\tfrac{\omega_r}{2\sqrt{3}}\cdot(\rho_{(2',2)}-\rho_{(2,2')}) - \Gamma\cdot\rho_{(2',2')}\\
\dot{\rho}_{(2,2)} &= i\cdot\tfrac{\omega_r}{2\sqrt{3}}\cdot(\rho_{(2,2')}-\rho_{(2',2)}) + \tfrac{\Gamma}{15}\cdot\rho_{(1',1')}+\tfrac{\Gamma}{3}\cdot\rho_{(2',2')}\\
\dot{\rho}_{(2,2')} &= i\cdot\tfrac{\omega_r}{2\sqrt{3}}\cdot(\rho_{(2,2)}-\rho_{(2',2')}) - i\cdot\delta\cdot\rho_{(2,2')}-\tfrac{\Gamma}{2}\cdot\rho_{(2,2')}\\
\dot{\rho}_{(2',2)} &= i\cdot\tfrac{\omega_r}{2\sqrt{3}}\cdot(\rho_{(2',2')}-\rho_{(2,2)}) - i\cdot\delta\cdot\rho_{(2',2)}-\tfrac{\Gamma}{2}\cdot\rho_{(2',2)}
\end{aligned}
\tag{D.6}
$$

The notation is an abbreviated form for e.g $\rho_{(2',2)} = \rho_{|F'=2,m'_F=2\rangle\langle F=2,m_F=2|}$, where the primes denote the excited state. The coupling between the states is established by the Rabi-frequency

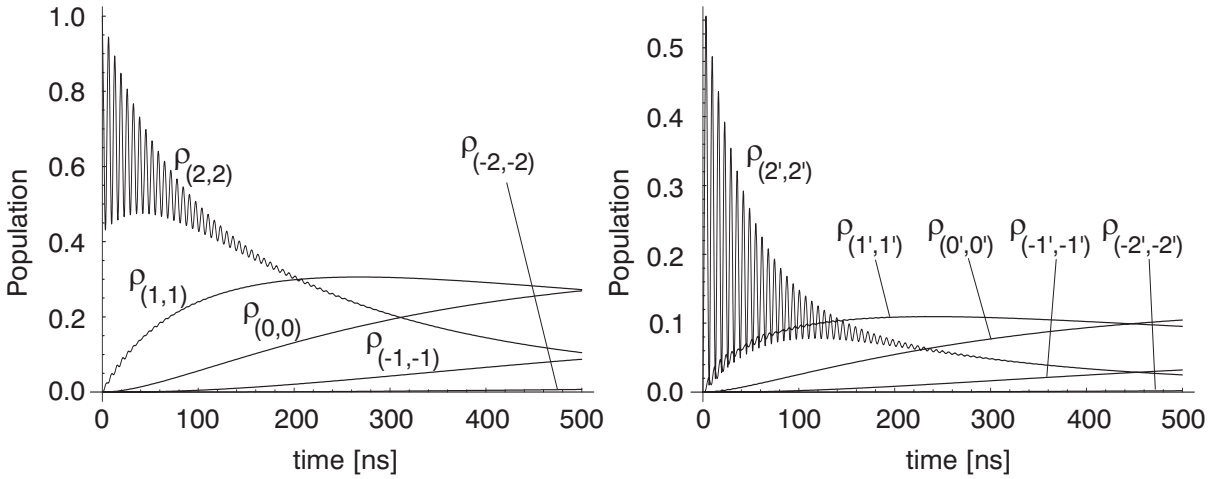

Figure D.1: Time evolution of the diagonal matrix elements. The numerical simulation was done for atoms initially in the $F = 2, m_F = 2$ state irradiated by a linear polarized beam with 1120 I_{sat} and 16.7 Γ detuning. The polarization is parallel to the quantization axis of the atoms. In this configuration are the matrix elements $\tilde{\rho}$ equivalent to ρ The left figure shows the population of the different magnetic sublevels of the ground state and the right figure the excited states.

$\omega_R = \Gamma\sqrt{I/2I_{sat}}$. The Rabi-frequency for each transition has to by weighted with the according Clebsch-Gordan coefficients taken from appendix A. The intensity I was set to 1120 saturation intensities I_{sat}.

The twenty equations (D.6) are not the complete set of coupled equations. The full system consists of 100 coupled equations, which can be sorted to be in a Jordan form (diagonal block matrix), with a 20x20 and 80x80 sub-matrix. The 80x80 matrix sub-matrix contains no explicit coupling to the light-field and the corresponding density matrix elements (for example $\rho_{(2,0)}$) decay to zero within $\Gamma/2$.

To solve the coupled equations numerically (with e.g. Mathematica, Wolfram Research) one has to define the starting conditions at t=0. If the Bose-condensed atoms are initially in the $F = 2, m_F = 2$ ground state and the quantization axis (here the direction of the magnetic field) is parallel to the electric field of the linear polarization, one hast to set $\rho_{(2,2)}(t = 0) = 1$ and all other elements to zero. This is only one special situation of the proposed experiments and usually the polarization and the magnetic field are not parallel. This problem can be solved either by transforming the light field into the reference frame of the atoms [166] or vice versa. The first method introduces new polarization components, which leads to more coupled equations and is avoided here. It is easier to rotate the $J = 2$ spinor of the atoms into the reference frame of the light field [254]. If the angle between the magnetic field and the electric field is θ and the trapped atoms are in the $F = 2, m_F = 2$, they can be represented in the reference frame of the light field as

$$\begin{aligned}
\tilde{\rho}_{(2,2)} &= \cos^4(\tfrac{\theta}{2})\rho_{(2,2)} \\
\tilde{\rho}_{(1,1)} &= -\tfrac{1}{2}\sin\theta(1+\cos\theta)\rho_{(2,2)} \\
\tilde{\rho}_{(0,0)} &= \sqrt{\tfrac{3}{8}}\sin^2\theta\rho_{(2,2)} \\
\tilde{\rho}_{(-1,-1)} &= \tfrac{1}{2}sin\theta(cos\theta-1)\rho_{(2,2)} \\
\tilde{\rho}_{(-2,-2)} &= \sin^4(\tfrac{\theta}{2})\rho_{(2,2)}
\end{aligned} \tag{D.7}$$

Figure D.1 shows a numerical integration of the differential equations (D.6) for the parameters given above and in the caption. The saturation parameter for the given intensity and detuning is $s = 1$, which gives in steady state an excited state fraction of 1/4 (see equation 2.8). With the full knowledge of the time evolution one can directly calculate the number of spontaneous scattering events. Every excited state decays with Γ into one of the allowed ground states, whereas each decay channel has to be weighted by its Clebsch-Gordan coefficient. By this one can distinguish between the emission of σ- and π-polarized light. The number N of scattered photons is then

$$\begin{array}{l} N_\pi = \Gamma \int \left(\frac{1}{3}\tilde{\rho}_{(-2',-2')} + \frac{8}{15}\tilde{\rho}_{(-1',-1')} + \frac{3}{5}\tilde{\rho}_{(0',0')} + \frac{8}{15}\tilde{\rho}_{(1',1')} + \frac{1}{3}\tilde{\rho}_{(2',2')} \right) dt \\ N_\sigma = \Gamma \int \left(\frac{2}{3}\tilde{\rho}_{(-2',-2')} + \frac{7}{15}\tilde{\rho}_{(-1',-1')} + \frac{2}{5}\tilde{\rho}_{(0',0')} + \frac{7}{15}\tilde{\rho}_{(1',1')} + \frac{2}{3}\tilde{\rho}_{(2',2')} \right) dt \end{array} \tag{D.8}$$

The spontaneous emissions of the photons follow the radiation patterns given in equations (D.5). The reference frame for these distributions is given by the polarization of the light field. For the parameters given above, each atom scatters on average during the first 300ns 1.52 circular polarized and 1.28 linear polarized photons.

Of interest is the projection of the emission patterns on the x- respectively the y-axes as the proposed measurement in chapter 4.1 requires. The definition of the coordinates and of the angle ϕ, which determines the direction of the polarization, are also taken from chapter 4.1. The projections of the probability distribution (D.5) on the y-axis, which is independent of the orientation of the polarization, and the x axis are:

$$\begin{array}{lcl} P_\pi(\kappa)|_y &=& -\frac{3}{8}(1+\kappa^2) \\ P_\sigma(\kappa)|_y &=& -\frac{3}{16}(3-\kappa^2) \\ P_\pi(\kappa)|_x &=& -\frac{3}{8}\left((1-\kappa^2)\cos^2\phi + 2\kappa^2\sin^2\phi + (1-\kappa^2)\right) \\ P_\sigma(\kappa)|_x &=& -\frac{3}{16}\left(2 + 2\kappa^2\cos^2\phi + (1-\kappa^2)\sin^2\phi\right). \end{array} \tag{D.9}$$

The projected distributions are spanned for $\kappa = [-1, 1]$. As a last step one has to calculate the standard derivatives for each distribution $\sqrt{\int_{-1}^{1} P(\kappa) d\kappa}$, which gives

$$\begin{array}{lcl} \sigma_\pi|_x &=& \sqrt{\frac{2}{5}} \\ \sigma_\sigma|_x &=& \sqrt{\frac{3}{10}} \\ \sigma_\pi|_y &=& \sqrt{\frac{1}{10}(3-\cos(2\phi))} \\ \sigma_\sigma|_y &=& \sqrt{\frac{1}{20}(7+\cos(2\phi))} \end{array} \tag{D.10}$$

The width in momentum space is then simply given by the product of the standard derivative, the number of scattered linear or circular polarized photons and the recoil momentum. The results for all angles ϕ are shown in figure 4.5.

E Optical dipole potentials in a multi-level atom

The approximation of a two level system coupled to a light field (see chapter 2.1 is in many cases not valid and one has to expand the theory for multilevel atoms by including all allowed transitions. In our case we can restrict the allowed transitions to the D1 and D2 manifold which were specified in appendix A. For small saturation parameters or adequate detuning one can derive explicit expressions for the dipole potentials and the scattering rates for multilevel atoms [172]. The approximative expressions (E.1) and (E.2) are valid, as long the excited state fraction is still small compared to the ground state one. The energy shift of an atom situated in a light field with frequency ω is

$$U_{\mathrm{dip}} = \sum_j -\frac{3\pi c^2}{2\omega_{ij}^3}\left(\frac{\Gamma_{ij}}{\omega_{ij}-\omega}+\frac{\Gamma_{ij}}{\omega_{ij}+\omega}\right) I(\vec{r}) \tag{E.1}$$

The atom in state $|i\rangle$ is coupled by the light field $I(\vec{r})$ with frequency ω to all allowed states $|j\rangle$ with a transition strength Γ_{ij}. Also the scattering rate can be calculated and is given by

$$\Gamma_{\mathrm{sc}} = \sum_j -\frac{3\pi c^2}{2\hbar\omega_{ij}^3}\left(\frac{\omega}{\omega_{ij}}\right)^3\left(\frac{\Gamma_{ij}}{\omega_{ij}-\omega}+\frac{\Gamma_{ij}}{\omega_{ij}+\omega}\right)^2 I(\vec{r}) \tag{E.2}$$

With this two equations it is possible to calculate state dependent potentials as required for the Spin-Boson model (see chapter 6.2.1), the potential depth of the optical lattice used in our experiments (see chapter 5.1) and the corresponding scattering rates.

In most cases laser light is applied to atoms in the $F = 2, m_F = 2$ state which is the case for our Bose-Einstein condensates. For this situation are the expected potentials and scattering rates explicitly carried out and the results are plotted in figure E.1 as a function of the wavelength. The color coding in the two graphs represents the three different polarizations of the light field. They are valid as long the k-vector of the circular polarized light, or the electric field vector of the linear polarized light, is parallel to the quantization axis of the atoms.

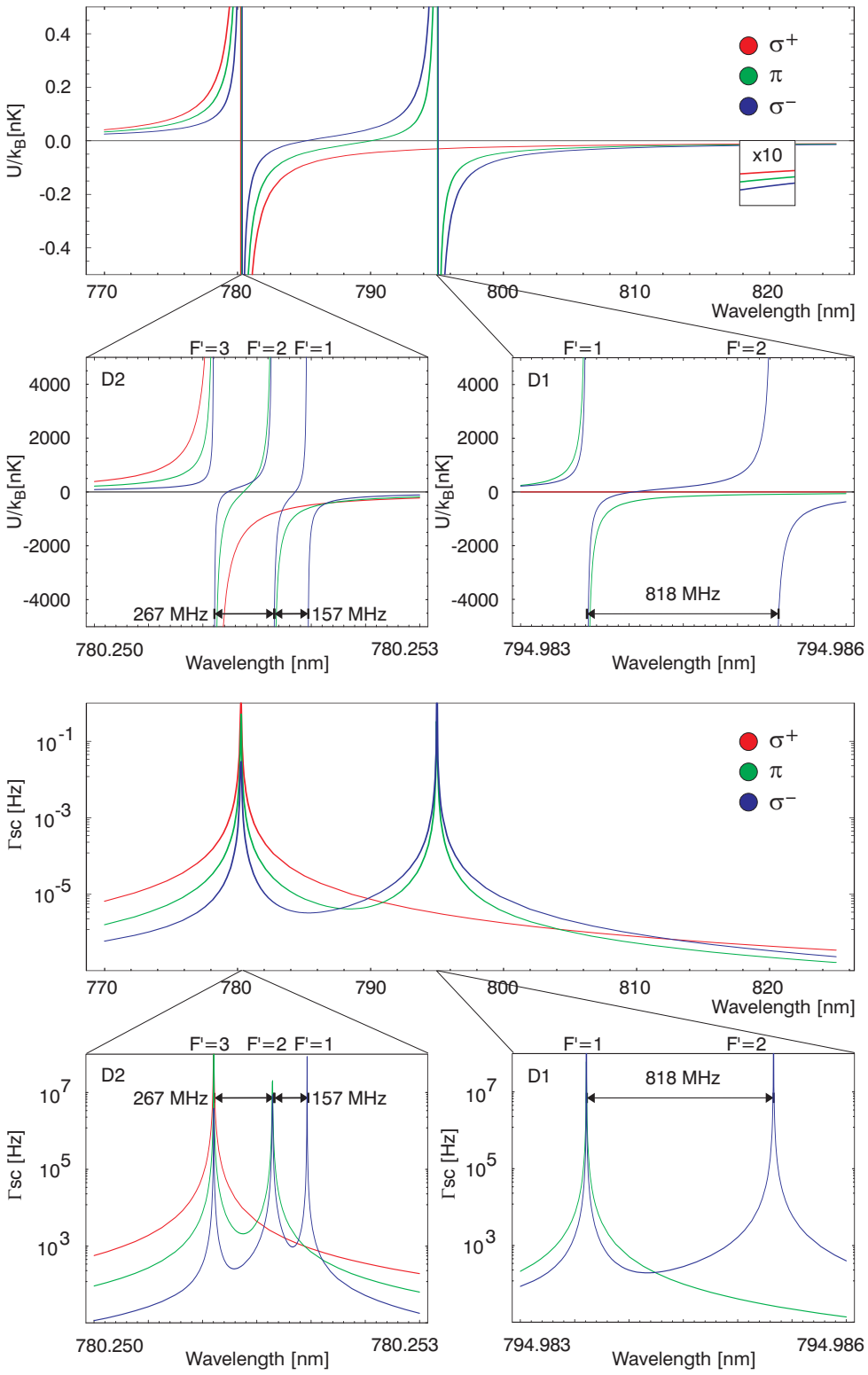

Figure E.1: Dipole potentials and spontaneous scattering rate for an ^{87}Rb-atom in a $F = 2, m_F = 2$ state for σ^+, σ^- and π polarized light. The intensity of the light field was set to 16 W/m^2.

F Physical dimensions of the main vacuum chamber

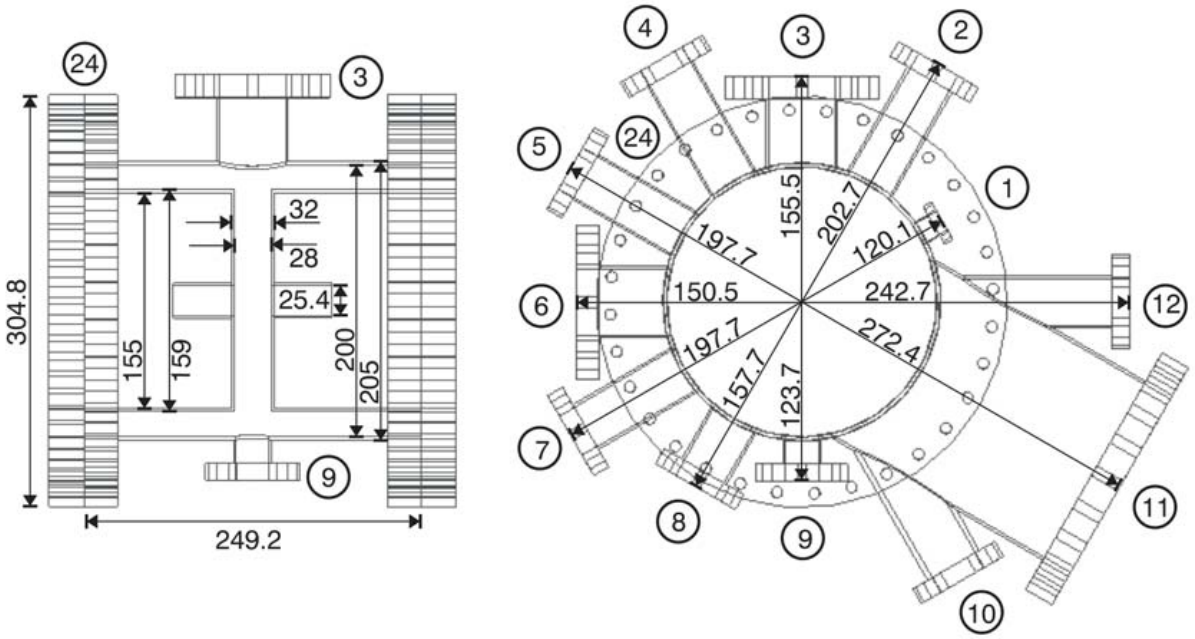

Figure F.1: Sheer plan of the main chamber.
① CF16 flange for Zeeman-slower
② CF35 optical port for the magneto-optical trap (MOT)
③ CF63 optical port for absorption imaging, alternative optical lattice
④ CF35 Multi-channel plate attached to a fourfold high voltage feed-through (ion detection)
⑤ CF35 optical port for the MOT
⑥ CF63 optical port for fluorescence imaging, alternative absorption imaging or optical lattice
⑦ CF35 optical port for the Zeeman-slowing light
⑧ CF35 optical port for the MOT
⑨ CF35 optical port for absorption imaging, alternative optical lattice
⑩ CF35 Multi-channel plate attached to a fourfold high voltage feed-through (electron detection)
⑪ CF150 flange towards pumping cross and optical port for the MOT
⑫ CF35 optical port for optical lattice, alternative absorption imaging
㉔ CF250 main flange, on which the buckets are mounted

G Three level systems

The excitation of Rydberg states was done in our experiments (see chapter 5.3) with a two photon excitation scheme. The underlying theory of this technique is similar to the treatment of the two-level systems introduced in chapter 2.1. A more detailed of three level systems can be found in [257] Figure G.1 shows schematically the three level system with an ground state $|1\rangle$, an intermediate state $|2\rangle$ and the Rydberg state $|3\rangle$. The laser frequencies for excitation may be detuned to the energy difference between the electronic states by δ_1 relative to $\hbar\omega 1$ (blue arraow) and δ_2 relative to the total energy difference $\hbar\omega 1 + \hbar\omega 2$ (red + blue arraow).

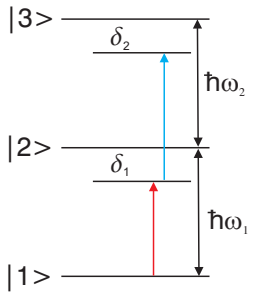

Figure G.1: Two photon excitation scheme. The population of state $|1\rangle$ is transferred by two photons, here labeled as the red and blue arrows, into an excited state $|3\rangle$.

The Hamilton operator for this system in the basis set $|1\rangle = (1,0,0)$, $|2\rangle = (0,1,0)$, $|3\rangle = (0,0,1)$ and after applying the rotating wave approximation [258] is

$$H = \begin{pmatrix} 0 & \frac{1}{2}\omega_{R1} & 0 \\ \frac{1}{2}\omega_{R1} & \delta_1 & \frac{1}{2}\omega_{R2} \\ 0 & \frac{1}{2}\omega_{R2} & \delta_2 \end{pmatrix}. \tag{G.1}$$

The Rabi-frequencies ω_{Ri} are analogous to the definition in chapter 2.1. The time evolution of the populations is given by the Liouville equation

$$\dot{\rho} = \frac{i}{\hbar}[H,\rho] + \left(\Gamma_2\hat{D}_2 + \Gamma_3\hat{D}_3\right)\rho + \hat{\Gamma}\rho. \tag{G.2}$$

The decay rates Γ_2 and Γ_3 are as usual the lifetimes of state $|2\rangle$ respectively state $|3\rangle$. The damping of the off-diagonal density matrix elements is determined by the reduced Lindblad operators $\hat{D}_i$ [127], analogous to the two-level systems ontroduced in chapter 2.1.

$$\hat{D}_i\rho = -\left(\sigma_i^-\sigma_i^+\rho + \rho\sigma_i^-\sigma_i^+\right) \tag{G.3}$$

Here we introduced the raising and lowering operators $\sigma_i^{\pm}$ defined as

$$\sigma_2^- = \begin{pmatrix} 0 & 0 & 0 \\ 1 & 0 & 0 \\ 0 & 0 & 0 \end{pmatrix} \quad \sigma_2^+ = \begin{pmatrix} 0 & 1 & 0 \\ 0 & 0 & 0 \\ 0 & 0 & 0 \end{pmatrix} \tag{G.4}$$

$$\sigma_3^- = \begin{pmatrix} 0 & 0 & 0 \\ 0 & 0 & 0 \\ 0 & 1 & 0 \end{pmatrix} \quad \sigma_3^+ = \begin{pmatrix} 0 & 0 & 0 \\ 0 & 0 & 1 \\ 0 & 0 & 0 \end{pmatrix} \tag{G.5}$$

The diagonal damping terms have to be included by a separate operator $\hat{\Gamma}$. The atoms in state $|3\rangle$ decay with a rate $a\Gamma_3$ into state $|1\rangle$ and with rate $b\Gamma_3$ into state $|2\rangle$. Further all atoms in state $|2\rangle$ decay with a rate Γ_2 into state $|1\rangle$. If other decay channels are excluded then holds $a + b = 1$ and the trace of the density matrix is conserved. The diagonal damping is then

$$\hat{\Gamma}\rho = \begin{pmatrix} \Gamma_2\rho_{22} + a\Gamma_3\rho_{33} & 0 & 0 \\ 0 & b\Gamma_3\rho_{33} - \Gamma_2\rho_{22} & 0 \\ 0 & 0 & -\Gamma_3\rho_{33} \end{pmatrix}. \tag{G.6}$$

If one chooses a large detuning δ_2 with $|\delta_2| \gg \omega_{R1}, \omega_{R2}$, the population of the intermediate state $|2\rangle$ goes to zero and can be neglected. By this one reaches again a two-level system with an effective 1-Photon coupling

$$\Omega_{\text{eff}} = \sqrt{\frac{\omega_{R1}^2\omega_{R2}^2}{4\delta_2^2} + \delta_3^2} \tag{G.7}$$

which can be treated with the optical Bloch-equations (2.6).

H Taylor expansion of a generalized octopole

If the eight field plates (see chapter 5.3) are treated as point charges located at the corners of a cuboid, it is possible to give analytical expressions for the electric field distributions. The potentials and the electric fields can be expanded into a Taylor series in cartesian coordinates. This is done to obtain analytical expressions in an polynomial form and by this a better approach to desired field configurations. The model potential consists of eight point charges q_i located at the positions $\vec{r}_{ci}$ as shown in figure H.1.

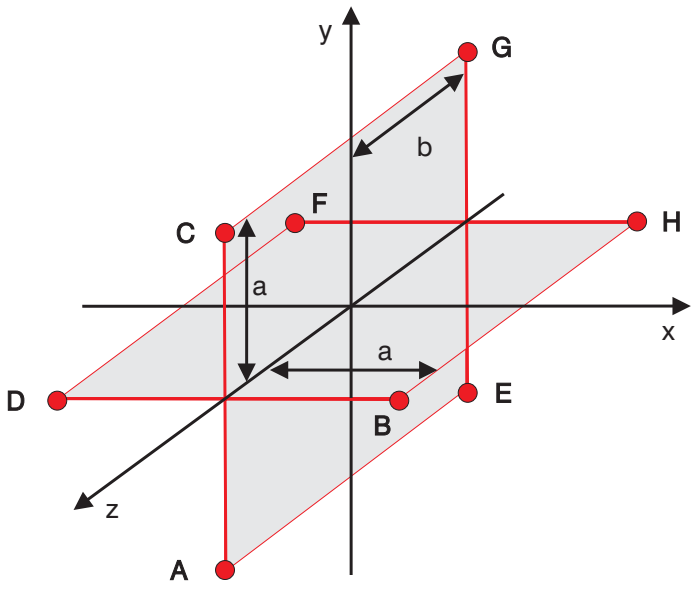

Figure H.1: Generalized Octopole. The eight charges of the octopole are located at the corners of a cuboid with length b, height a and width a, which reflects the symmetry of the actual field plates inside the vacuum chamber. The labeling $A - H$ of the charges as well the orientation of the coordinate system is equivalent to that in chapter 5.3.

Each point charge can be set independently to any value, such as in reality also each field plate. The total potential U_{tot} is then simply obtained by superposing the individual potentials U_i as $U_{\text{tot}} = \sum_{i=1}^{8} U_i$. Actually there are also the two Faraday cages of the multi-channel plates available for field generation, but they will be excluded in the following discussion.

The expansion of the potential of a single point charge at position $\vec{r}_{ci}$ is carried out around $\vec{r} = 0$ up to fifth order and yields

$$
\begin{aligned}
&U_i = \tfrac{1}{4\pi\varepsilon_0}\tfrac{q_i}{|\vec{r}-\vec{r}_{ci}|} = \tfrac{q_i}{4\pi\varepsilon_0}\textstyle\sum_{n=0}^{\infty}\tfrac{1}{n!}\left(-\vec{r}\cdot\nabla_{\vec{r}_{ci}}\right)^n\tfrac{1}{|\vec{r}_{ci}|} = \tfrac{q_i}{4\pi\varepsilon_0}\times \\
&\tfrac{1}{|\vec{r}_{ci}|} + && \text{0th order} \\
&\tfrac{\vec{r}\cdot\vec{r}_{ci}}{|\vec{r}_{ci}|^3} + && \text{1st order} \\
&\tfrac{1}{2}\left(\tfrac{3(\vec{r}\cdot\vec{r}_{ci})^2}{|\vec{r}_{ci}|^5} - \tfrac{|\vec{r}|^2}{|\vec{r}_{ci}|^3}\right) + && \text{2nd order} \\
&\tfrac{1}{6}\left(\tfrac{15(\vec{r}\cdot\vec{r}_{ci})^3}{|\vec{r}_{ci}|^7} - \tfrac{9(\vec{r}\cdot\vec{r}_{ci})|\vec{r}|^2}{|\vec{r}_{ci}|^5}\right) + && \text{3rd order} \\
&\tfrac{1}{24}\left(\tfrac{105(\vec{r}\cdot\vec{r}_{ci})^4}{|\vec{r}_{ci}|^9} - \tfrac{90(\vec{r}\cdot\vec{r}_{ci})^2|\vec{r}|^2}{|\vec{r}_{ci}|^7} + \tfrac{9|\vec{r}|^4}{|\vec{r}_{ci}|^5}\right) + && \text{4th order} \\
&\tfrac{1}{120}\left(\tfrac{945(\vec{r}\cdot\vec{r}_{ci})^5}{|\vec{r}_{ci}|^{11}} - \tfrac{1050(\vec{r}\cdot\vec{r}_{ci})^3|\vec{r}|^2}{|\vec{r}_{ci}|^9} + \tfrac{225(\vec{r}\cdot\vec{r}_{ci})|\vec{r}|^4}{|\vec{r}_{ci}|^7}\right) + \ldots && \text{5th order.}
\end{aligned}
\tag{H.1}
$$

From interest is the electric field distribution which is determined by $\vec{E}_{\text{tot}} = -\nabla U_{\text{tot}}$. Again this is done for a single charge at position $\vec{r}_{ci}$

$$
\begin{aligned}
&\vec{E}_i = -\nabla U_i = \tfrac{q_i}{4\pi\varepsilon_0}\times \\
&\tfrac{\vec{r}_{ci}}{|\vec{r}_{ci}|} + && \text{0th order} \\
&\tfrac{1}{2}\left(\tfrac{6(\vec{r}\cdot\vec{r}_{ci})\vec{r}_{ci}}{|\vec{r}_{ci}|^5} - \tfrac{2\vec{r}}{|\vec{r}_{ci}|^3}\right) + && \text{1st order} \\
&\tfrac{1}{6}\left(\tfrac{45(\vec{r}\cdot\vec{r}_{ci})^2\vec{r}_{ci}}{|\vec{r}_{ci}|^7} - \tfrac{9|\vec{r}|^2\vec{r}_{ci}+18(\vec{r}\cdot\vec{r}_{ci})\vec{r}}{|\vec{r}_{ci}|^5}\right) + && \text{2nd order} \\
&\tfrac{1}{24}\left(\tfrac{420(\vec{r}\cdot\vec{r}_{ci})^3\vec{r}_{ci}}{|\vec{r}_{ci}|^9} - \tfrac{180|\vec{r}|^2(\vec{r}\cdot\vec{r}_{ci})\vec{r}_{ci}+180(\vec{r}\cdot\vec{r}_{ci})^2\vec{r}}{|\vec{r}_{ci}|^7} + \tfrac{36|\vec{r}|^2\vec{r}}{|\vec{r}_{ci}|^5}\right) + && \text{3rd order} \\
&\tfrac{1}{120}\left(\tfrac{4725(\vec{r}\cdot\vec{r}_{ci})^4\vec{r}_{ci}}{|\vec{r}_{ci}|^{11}} - \tfrac{3150|\vec{r}|^2(\vec{r}\cdot\vec{r}_{ci})^2\vec{r}_{ci}+210(\vec{r}\cdot\vec{r}_{ci})^3\vec{r}}{|\vec{r}_{ci}|^9} + \tfrac{225|\vec{r}|^4\vec{r}_{ci}+900|\vec{r}|^2(\vec{r}\cdot\vec{r}_{ci})\vec{r}}{|\vec{r}_{ci}|^7}\right) + \ldots && \text{4th order.}
\end{aligned}
\tag{H.2}
$$

The combined electric field $\vec{E}_{\text{tot}}$ of all eight charges is also given by summation of the individual fields as $\vec{E}_{\text{tot}} = \sum_{i=1}^{8}\vec{E}_i$.

The distance between the facings of the field plates is 28 mm and by this is b set to 14 mm. The effective distance a between the four field plates remains to be determined. In figure 5.9 are electric field distributions shown, which were calculated with a finite element method[1] for the real geometries of the field plates including the surrounding vacuum chamber. By expanding the simulated field configurations also into a Taylor series and comparing the individual orders with equation (H.1) and (H.2) one obtains a good agreement if a is set to about 15 mm in all orders. The error in the electric field norm at the origin is then below 10 % compared to the full simulation shown in figure 5.9. To do even better one can assign a distance a for each expansion order.

When a is altered from 14 mm to 16 mm the basic geometry of the potential and the electric field does not change. To discuss some basic configurations it is set for now to $a = b$. For this cubical octopole are now four different configurations of the electric fields explicitly written out according to the expansion (H.2). This four configurations are also depicted in figure H.

[1] Comsol, Femlab

Constant electric field For this situation are the charges A, B, C and D set to $-q$ and E, F, G, H to $+q$. The electric fields along the three coordinate axes are then

$$\begin{aligned}
\vec{E}_{\text{tot}}(y, z=0) &\sim \begin{pmatrix} 0 \\ 0 \\ 1+\frac{3}{16}x^2+\frac{15}{256}x^4 \end{pmatrix} \\
\vec{E}_{\text{tot}}(x, z=0) &\sim \begin{pmatrix} 0 \\ 0 \\ 1+\frac{3}{16}y^2+\frac{15}{256}y^4 \end{pmatrix} \\
\vec{E}_{\text{tot}}(x, y=0) &\sim \begin{pmatrix} 0 \\ 0 \\ 1-\frac{3}{8}z^2-\frac{85}{128}z^4 \end{pmatrix}.
\end{aligned} \tag{H.3}$$

A constant electric field along z can also be generated by only charging the plates B and D to $-q$ and the opposite plates F and H to $+q$. This increases the curvatures roughly by an factor of two. In the experimental investigation of the Stark shift of the 43S state (see chapter 5.3) we actually used an even simpler configuration by just charging only two plates, B and H to $+q$.

$$\begin{aligned}
\vec{E}_{\text{tot}}(y, z=0) &\sim \begin{pmatrix} -1-2x+\frac{3}{8}x^2+\frac{13}{16}x^3+\frac{85}{128}x^4 \\ 0 \\ 0 \end{pmatrix} \\
\vec{E}_{\text{tot}}(x, z=0) &\sim \begin{pmatrix} -1+\frac{3}{4}y^2-\frac{15}{32}y^4 \\ y-\frac{3}{4}y^3 \\ 0 \end{pmatrix} \\
\vec{E}_{\text{tot}}(x, y=0) &\sim \begin{pmatrix} -1-\frac{9}{8}z^2+\frac{45}{128}z^4 \\ 0 \\ -\frac{1}{2}z+\frac{13}{16}z^3 \end{pmatrix}.
\end{aligned} \tag{H.4}$$

This produces already a gradient field along the x-axis, which guides the field ionized ions towards the multi-channel plate. On the other hand is the gradient small enough, that for small atomic samples it does not contribute to the linewidth as it is the case for the spectroscopic results shown in figure 5.10.

Linear gradient field A field which exhibits a linear gradient in all directions is simply fabricated by setting all charges to $+q$:

$$\begin{aligned}
\vec{E}_{\text{tot}}(y, z=0) &\sim \begin{pmatrix} x+\frac{1}{8}x^3 \\ 0 \\ 0 \end{pmatrix} \\
\vec{E}_{\text{tot}}(x, z=0) &\sim \begin{pmatrix} 0 \\ y+\frac{1}{8}y^3 \\ 0 \end{pmatrix} \\
\vec{E}_{\text{tot}}(x, y=0) &\sim \begin{pmatrix} 0 \\ 0 \\ -2z+\frac{13}{14}z^3 \end{pmatrix}.
\end{aligned} \tag{H.5}$$

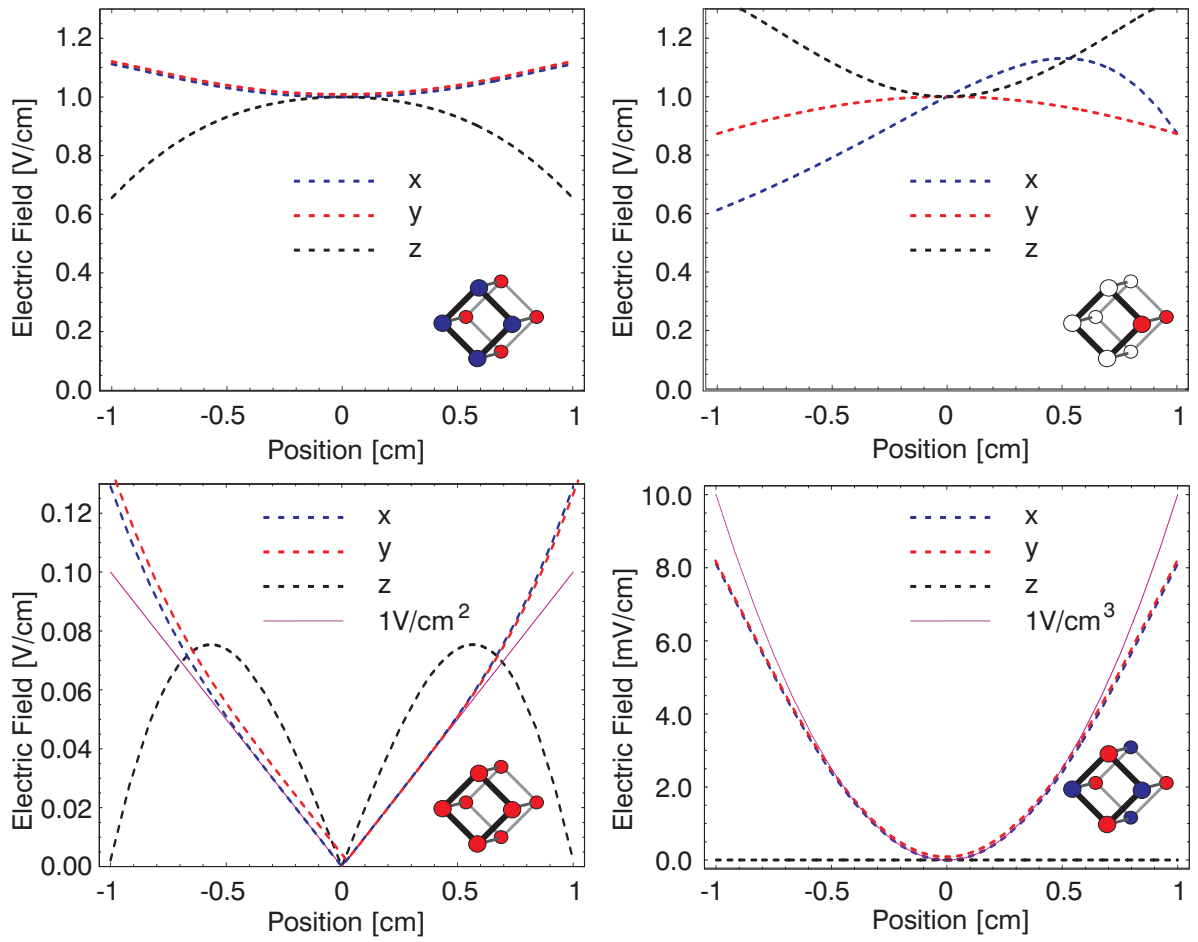

Figure H.2: Four different field configurations. For all four cases was a set to 15 mm and b to 14mm. The individual graphs show the absolute value of the electric field along the three coordinate axes. On top are the two configurations (H.3) and (H.4) for constant field generation shown. The charges were chosen such, that the field norm at the origin is 1 V/cm. For the upper left case the charges A, B, C and D were set to $-q$ and E, F, G, H to $+q$. The realization of electric fields as used in the experiments with Rydberg atoms (see chapter 5.3) uses only the plates B and H at positive values and is shown on the upper right. A quadrupolar field with constant gradients along all three coordinate axes (see equation H.5) is realized by setting all all charges to the same value and is depicted on the lower left. The magenta colored line represents a constant gradient field with 1 V/cm^2. Finally is on the lower right the situation for a field with constant curvatures shown as stated by equation (H.6). In this case the plates A, C, F and H are charged to $+q$ and B, D, E and G respectively to $-q$. The magenta colored line is a field with a constant curvature of 1 V/cm^3.

Quadratic fields The last configuration can be used to generate a quadratic field dependence in two directions and zero field along z. To do so one can charge the plates for example alternately with $+q$ (A, C, F and H) and $-q$ (B, D, E and G) to obtain

$$\begin{aligned} \vec{E}_{\text{tot}}(y, z=0) &\sim \begin{pmatrix} 0 \\ 0 \\ x^2 - \frac{7}{16}x^4 \end{pmatrix} \\ \vec{E}_{\text{tot}}(x, z=0) &\sim \begin{pmatrix} 0 \\ 0 \\ -y^2 + \frac{7}{16}y^4 \end{pmatrix} \\ \vec{E}_{\text{tot}}(x, y=0) &\sim \begin{pmatrix} 0 \\ 0 \\ 0 \end{pmatrix}. \end{aligned} \tag{H.6}$$

In figure H is the absolute value of the electric field for this four configurations shown. The plotted fields show the Taylor series (H.3) to (H.6) up to the fourth order. At this order there is almost no difference of this approximation to the real electric field distribution.

The Taylor series of the electric field can also be seen as a set of linear equations in q_i. By setting boundary conditions on the shape of the electric field, one can solve the equations for each expansion order to obtain the required charges. All in all there are three field components for each expansion order, which are well-defined by the eight charges. For a given electric field is the system over-determined and no solution for the charges may be available. Easier to handle are the potentials, which reduces the number of equations by a factor of three. Now one starts with a conservative potential U_{tot} and proceeds as before.

I Reduction of the lifetime of Rydberg states due to black body radiation

The lifetime of Rydberg states can be calculated with the help of equation (2.75) and yields for an atom in the $43S_{1/2}$ state a lifetime of $\tau = 99\ \mu$s. In [78] is a correction for the lifetime due to black body radiation given (see equation 2.76), which reduces it at a temperature of 300 K to $\tau = 47\ \mu$s. For this correction it was assumed that the atoms change their internal state by induced emissions or absorptions of photons given by an ordinary black body radiation spectral density:

$$\rho(\nu)d\nu = \frac{8\pi h\nu^3}{c^3(e^{h\nu/k_BT}-1)}. \tag{I.1}$$

This equation is valid in free space, but gets altered for the mode distribution in a finite size cavity [259, 260]. For a parallelepiped with sides L_x, L_y and L_z with conducting walls the eigenfrequencies are given by

$$\nu_{n_x,n_y,n_z} = \frac{c}{2}\sqrt{\frac{n_x^2}{L_x^2}+\frac{n_y^2}{L_y^2}+\frac{n_z^2}{L_z^2}} \quad \text{with} \quad n_i = 0,1,2,... \tag{I.2}$$

With the inner dimensions of the vacuum chamber of 28 mm x 200 mm x 200 mm (see appendix F) has the lowest lying mode a frequency of about 5 GHz and is well below the lowest possible transition frequency at 50 GHz of the $43S_{1/2}$ state. By this it is a fair approximation to express equation (I.2) with an effective length $\bar{L} = (L_xL_yL_z)^{1/3}$ as

$$\nu_n = \frac{c}{2\bar{L}}(2n)^{1/3} \quad \text{with} \quad n = 0,1,2,... \tag{I.3}$$

which depends now only on one index n. The frequency distance between two successive modes $\Delta\nu$ calculates then to

$$\Delta\nu = \frac{c^3}{12\nu^2\bar{L}^3}, \tag{I.4}$$

which is plotted in figure I.1. To calculate actual transition rates it is convenient to express the radiation field in terms of number of photons $\bar{N}$ per mode [261]

$$\bar{N} = \frac{1}{e^{h\nu/k_BT}-1}, \tag{I.5}$$

which is also plotted in figure I.1 for $T = 300$ K. What is left to calculate the lifetime of any state are the Einstein A coefficients for all possible transitions, which are given by [121]

$$A_{n',l',nl} = \frac{2}{3}\frac{e^2\omega^3_{n',l',n,l}}{\varepsilon_0 c^3 h}|\langle n',l'|r|n,l\rangle|^2 \tag{I.6}$$

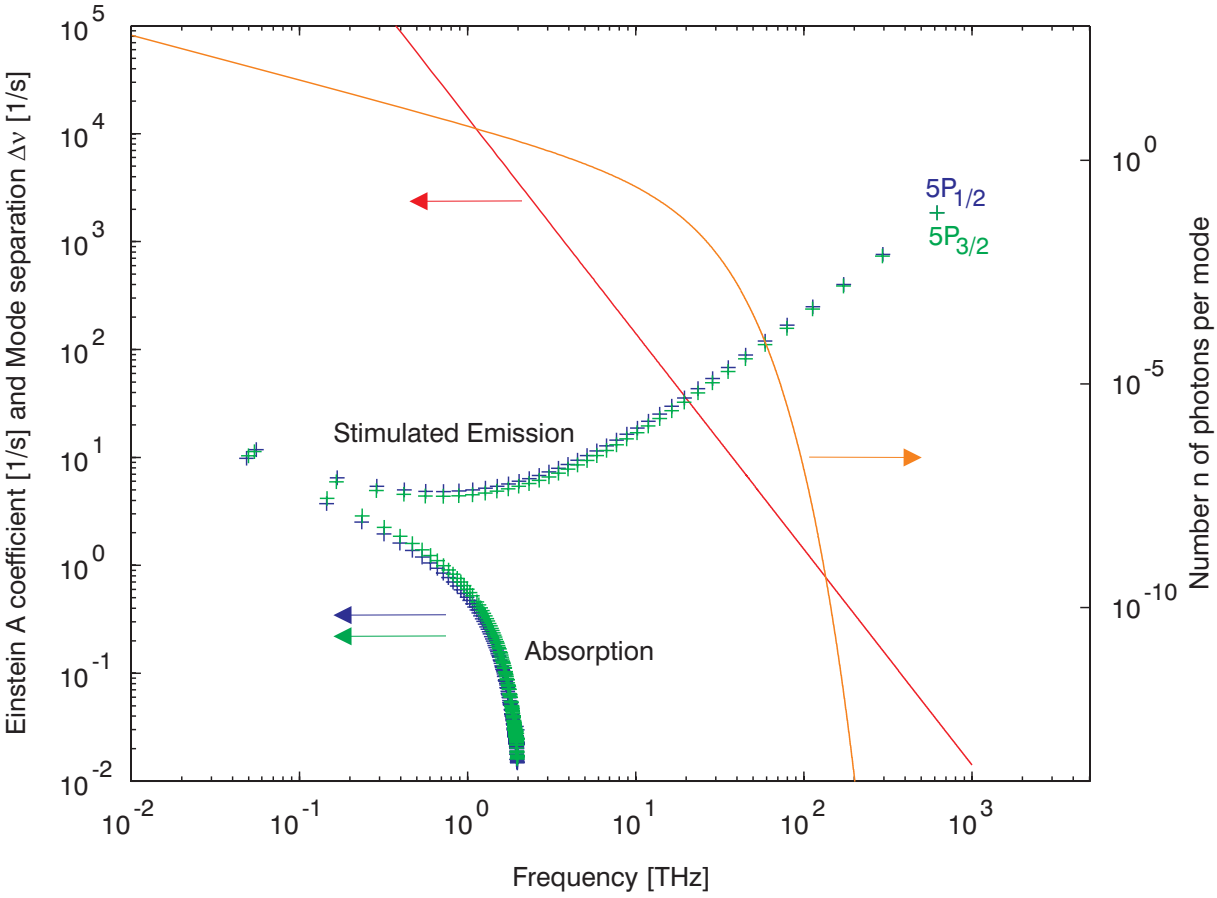

Figure I.1: Einstein A coefficients and properties of the black body radiation in a finite size cavity. Each cross represents the Einstein A coefficient for transitions from the $43S_{1/2}$ state to a $nP_{1/2}$ state (blue) and $nP_{3/2}$ state (green). The coefficients are plotted again the energy difference $\hbar\omega_{n',l',n,l}$ in THz from $n = 5$ (ground state) to $n = 200$. The orange line depicts the average photon number per mode with frequency ν as given by equation (I.5). The graph also includes the mode spacing (red line) at a certain frequency ν for a finite size cavity with the dimensions of the vacuum chamber according to equation (I.4).

The initial state is denoted with $|n', l'\rangle$ and is separated by an energy $\hbar\omega_{n',l',n,l}$ to a state $|n, l\rangle$. The energy differences can be calculated with equation (2.73). To calculate the dipole matrix elements $\langle n', l'|r|n, l\rangle$ one has to solve the time-independent Schrödinger equation, including the quantum defect for Rubidium, to obtain the necessary wave-functions. With the knowledge of the wave-functions one can simply calculate the overlap integral of the $43S_{1/2}$ with all states allowed by a dipole transition, here $nP_{1/2}$ and $nP_{3/2}$. This was carried out up to $n = 200$ and the result is depicted in figure I.1.

As a first step shall the lifetime τ of the $43S_{1/2}$ without the influence of the black body radiation be calculated [78]

$$\tau^{-1} = \sum_{n=5}^{42} \sum_{j=1/2}^{3/2} A. \tag{I.7}$$

This gives an value of $\tau = 123\ \mu$s which is in good agreement with the 99 μs calculated previous with equation (2.75). The deviation is most likely due to the quality of the calculated wave-functions for small quantum numbers at which the quantum defect model is less accurate. With the knowledge of the Einstein A coefficients is it now possible to calculate explicitly the influence of the ordinary black body radiation. The stimulated emission rate is simple $\bar{N}$ times as large as the spontaneous rate, where $\bar{N}$ is the average photon number given by equation (I.5). This statement also holds for absorption processes to states with a higher energy. The correction to the lifetime is then

$$\tau_{bb}^{-1} = \sum_{n=5}^{42} \sum_{j=1/2}^{3/2} \bar{N}(\nu) A + \sum_{n=43}^{\infty} \sum_{j=1/2}^{3/2} \bar{N}(\nu) A. \tag{I.8}$$

The first term corresponds to stimulated emission and the second to absorption processes and the evaluation yields $\tau_{bb} = (4099\,1/s + 3460\,1/s)^{-1} = 132\ \mu$s. The effective lifetime is then reduced to

$$\frac{1}{\tau_{\text{eff}}} = \frac{1}{\tau} + \frac{1}{\tau_{bb}} \tag{I.9}$$

and evaluates to $\tau_{\text{eff}} = 64\ \mu$s which is about 50% of the undisturbed lifetime of 123 μs. This reduction of the lifetime is almost identical to the one calculated with the help of equations (2.75) and (2.76). The sum was carried out to n=200 for which it already converged. There exists also absorption of photons to continuum states, which was neglected since the corresponding Einstein coefficients are very small.

To include the discrete spectrum of a finite size cavity the Einstein coefficients are additionally weighted by the ratio of the Einstein coefficient and the mode spacing $\Delta\nu$. This reflects the probability that a cavity mode is in resonance with a possible transition. The correction of the lifetime is now

$$\tau_{cbb}^{-1} = \sum_{n=5}^{42} \sum_{j=1/2}^{3/2} \bar{N}(\nu) \frac{A^2}{2\pi\Delta\nu(\nu)} + \sum_{n=43}^{\infty} \sum_{j=1/2}^{3/2} \bar{N}(\nu) \frac{A^2}{2\pi\Delta\nu(\nu)}. \tag{I.10}$$

Carrying out this evaluation one receives for $\tau_{cbb}^{-1} = (1093.3\,1/s + 1.4\,1/s)^{-1} = 1/9.1\ \mu\text{s}^{-1}$ which gives an effective lifetime of $\tau_{\text{eff}} = 118\ \mu$s and corresponds to a reduction of roughly 5% of to the undisturbed lifetime of 123 μs.

Bibliography

[1] D. G. Fried, T. Killian, L. Willmann, D. Landhuis, S. Moss, D. Kleppner, and T. Greytak, *Bose-Einstein Condensation of Atomic Hydrogen*, Phys. Rev. Lett. **81**, 3811 (1998).

[2] A. Robert, O. Sirjean, A. Browaeys, J. Poupard, S. Nowak, D. Boiron, C. Westbrook, and A. Aspect, *A Bose-Einstein Condensate of Metastable Atoms*, Science **292** (2001).

[3] A. Griesmaier, J. Werner, S. Hensler, J. Stuhler, and T. Pfau, *Bose-Einstein Condensation of Chromium*, Phys. Rev. Lett. **94**, 160401 (2005).

[4] T. Weber, J. Herbig, M. Mark, H.-C. Nägerl, and R. Grimm, *Bose-Einstein Condensation of Cesiums*, Science **299**, 232 (2003).

[5] G. Modugno, G. Ferrari, G. Roati, R. J. Brecha, A. Simoni, and M. Inguscio, *Bose-Einstein Condensation of Potassium Atoms by Sympathetic Cooling*, Science **194**, 1320 (2001).

[6] C. C. Bradley, C. A. Sackett, J. J. Tollett, and R. G. Hulet, *Evidence of Bose-Einstein Condensation in an Atomic Gas with Attractive Interactions*, 75 p. 1687 (1995).

[7] K. Davis, M. Mewes, M. Andrews, N. van Druten, D. Durfee, D. Kurn, and W. Ketterle, *Bose-Einstein Condensation in a Gas of Sodium Atoms*, Phys. Rev. Lett. **75**, 3969 (1995).

[8] S. Cornish, N. Claussen, J. Roberts, E. Cornell, and C. Wieman, *Stable ^{85}Rb Bose-Einstein Condensates with Widely Tunable Interactions*, Phys. Rev. Lett. **85**, 1795 (2000).

[9] M. H. Anderson, J. R. Ensher, M. R. Matthews, C. E. Wieman, and E. A. Cornell, *Observation of Bose-Einstein-Condensation in a Dilute Atomic Vapor*, Science **269**, 198–201 (1995).

[10] Y. Takasu, K. Maki, K. Komori, T. Takano, K. Honda, M. Kumakura, T. Yabuzaki, and Y. Takahashi, *Spin-Singlet Bose-Einstein Condensation of Two-Electron Atoms*, Phys. Rev. Lett. **91**, 040404 (2003).

[11] J. Kasprzak, M. Richard, S. Kundermann, A. Baas, P. Jeambrun, J. Keeling, F. Marchetti, M. Szymanacuteska, R. Andre, J. Staehli, V. Savona, P. Littlewood, B. Devaud, and L. Dang, *Bose-Einstein Condensation of Exciton Polaritons*, Nature **443**, 409 (2006).

[12] S. Demokritov, V. Demidov, O. Dzyapko, G. Melkov, A. Serga, B. Hillebrands, and A. Slavin, *Bose-Einstein Condensation of Quasi-Equillibrium Magnons at Room Temperature Under Pumping*, Nature **443**, 430 (2006).

[13] M. Mewes, M. Andrews, N. van Druten, D. Kurn, D. Durfee, C. Townsend, and W. Ketterle, *Collective Excitations of a Bose-Einstein Condensate in a Magnetic Trap*, Phys. Rev. Lett. **77**, 988 (1996).

[14] D. Stamper-Kurn, H.-J. Miesner, S. Inouye, M. Andrews, and W. Ketterle, *Collisionless and Hydrodynamic Excitations of a Bose-Einstein Condensate*, Phys. Rev. Lett. p. 500 (1998).

[15] D. Jin, J. Ensher, M. Matthews, C. Wieman, and E. Cornell, *Collective Excitations of a Bose-Einstein Condensate in a Dilute Gas*, Phys. Rev. Lett. **77**, 420.

[16] O. Marago, S. Hopkins, J. Arlt, E. Hodby, G. Hechenblaikner, and C. Foot, *Observation of the Scissors Mode and Evidence for Superfluidity of a Trapped Bose-Einstein Condensed Gas*, Phys. Rev. Lett. **84**, 2056.

[17] F. Chevy, V. Bretin, P. Rosenbusch, K. Madison, and J. Dalibard, *Transverse Breathing Mode of an Elongated Bose-Einstein Condensate*, Phys. Rev. Lett. **88**, 250402 (2002).

[18] M. Andrews, D. Kurn, H.-J. Miesner, D. Durfee, C. Townsend, S. Inouye, and W. Ketterle, *Propagation of Sound in a Bose-Einstein Condensate*, Phys. Rev. Lett. **79**, 549 (1997).

[19] D. Stamper-Kurn, A. Chikkatur, A. Görlitz, S. Inouye, S. Gupta, D. Pritchard, and W. Ketterle, *Excitation of Phonons in a Bose-Einstein Condensate by Light Scattering*, Phys. Rev. Lett. p. 2876 (1999).

[20] R. Ozeri, J. Steinhauer, N. Katz, and N. Davidson, *Direct Observation of the Phonon Energy in a Bose-Einstein Condensate by Tomographic Imaging*, Phys. Rev. Lett. **88**, 220401 (2002).

[21] F. London, *The λ-Phenomenon of Liquid Helium and the Bose-Einstein Degeneracy*, Nature **141**, 643 (1938).

[22] F. Dalfovo, S. Giorini, P. Pitaevskii, and S. Stringari, *Theory of Bose-Einstein condensation in trapped gases*, Rev. Mod. Phys. **71**, 463 (1999).

[23] C. Raman, M. Köhl, R. Onofrio, D. Durfee, C. Kuklewicz, Z. Hadzibabic, and W. Ketterle, *Evidence for a Critical Velocity in a Bose-Einstein Condensed Gas*, Phys. Rev. Lett. **83**, 2502 (1999).

[24] A. Chikkatur, A. Görlitz, D. Stamper-Kurn, S. Inouye, S. Gupta, and W. Ketterle, *Suppression and Enhancement of Impurity Scattering in a Bose-Einstein Condensate*, Phys. Rev. Lett. **85**, 483 (2000).

[25] S. Burger, F. Cataliotti, C. Fort, F. Minardi, M. Inguscio, M. Chiofalo, and M. Tosi, *Superfluid and Dissipative Dynamics of a Bose-Einstein Condensate in a Periodic Optical Potential*, Phys. Rev. Lett. **86**, 4447.

[26] M. Matthews, B. Anderson, P. Haljan, D. Hall, C. Wieman, and E. Cornell, *Vortices in a Bose-Einstein Condensate*, Phys. Rev. Lett. **83**, 2498.

[27] K. Madison, F. Chevy, W. Wohlleben, and J. Dalibard, *Vortex Formation in a Stirred Bose-Einstein Condensate*, Phys. Rev. Lett. **84**, 806.

[28] J. Abo-Shaeer, C. Raman, J. Vogels, and W. Ketterle, *Observation of Vortex Lattices in Bose-Einstein Condensates*, Science **476**, 292 (2001).

[29] S. Inouye, S. Gupta, T. Rosenband, A. Chikkatur, A. Görlitz, T. Gustavson, A. Leanhardt, D. Pritchard, and W. Ketterle, *Observation of Vortex Phase Singularities in Bose-Einstein Condensates*, Phys. Rev. Lett. **87**, 080402 (2001).

[30] M. Andrews, C. Townsend, H.-J. Miesner, D. Durfee, D. Kurn, and W. Ketterle, *Observation of Interference Between two Bose Condensates*, Science **275**, 637 (1997).

[31] D. Hall, M. Matthews, C. Wieman, and E. Cornell, *Measurements of Relative Phase in Two-Component Bose-Einstein Condensates*, Phys. Rev. Lett. **81**, 1543 (1998).

[32] Y. Shin, M. Saba, T. A. Pasquini, W. Ketterle, D. E. Pritchard, and A. E. Leanhardt, *Atom Interferometry with Bose-Einstein Condensates in a Double-Well Potential*, Phys. Rev. Lett. **92**, 050405 (2004).

[33] S. Gupta, K. Dieckmann, Z. Hadzibabic, and D. Pritchard, *Contrast Interferometry using Bose-Einstein Condensates to Measure h/m and α*, Phys. Rev. Lett. **89**, 140401.

[34] S. Burger, K. Bongs, S. Dettmer, W. Ertmer, K. Sengstock, A. Sanpera, G. Shlyapnikov, and M. Lewenstein, *Dark Solitons in Bose-Einstein Condensates*, Phys. Rev. Lett. **83**, 5198.

[35] B. Anderson, P. Haljan, C. Regal, D. Feder, L. Collins, C. Clark, and E. Cornell, *Watching Dark Solitons Decay into Vortex Rings in a Bose-Einstein Condensate*, Phys. Rev. Lett. **86**, 2926.

[36] B. Eiermann, T. Anker, M. Albiez, M. Taglieber, P. Treutlein, K.-P. Marzlin, and M. K. Oberthaler, *Bright Bose-Einstein Gap Solitons of Atoms with Repulsive Interaction*, Phys. Rev. Lett. **92** (2004).

[37] L. Deng, E. Hagley, J. Wen, M. Trippenbach, Y. Band, P. Julienne, J. Simsarian, K. Helmerson, S. Rolston, and W. Phillips, *Four-Wave Mixing with Matter Waves*, Science **398**, 218 (1999).

[38] S. Inouye, M. Andrews, J. Stenger, H.-J. Miesner, D. Stamper-Kurn, and W. Ketterle, *Observation of Feshbach Resonances in a Bose-Einstein Condensate*, Nature **392**, 151 (1998).

[39] P. Courteille, R. Freeland, D. Heinzen, F. van Abeelen, and B. Verhaar, *Observation of a Feshbach Resonance in Cold Atom Scattering*, Phys. Rev. Lett. **81**.

[40] J. Werner, A. Griesmaier, S. Hensler, J. Stuhler, T. Pfau, A. Simoni, and E. Tiesinga, *Observation of Feshbach Resonances in an Ultracold Gas of ^{52}Cr*, Phys. Rev. Lett. **94**, 183201 (2005).

[41] A. Marte, T. Volz, J. Schuster, S. Dürr, G. Rempe, E. van Kempen, and B. Verhaar, *Feshbach Resonances in Rubidium 87: Precision Measurement and Analysis*, Phys. Rev. Lett. **89**, 283202 (2002).

[42] M. Erhard, H. Schmaljohann, J. Kronjager, K. Bongs, and K. Sengstock, *Measurement of a mixed-spin-channel Feshbach resonance in ^{87}Rb*, Phys. Rev. A **69**, 032705 (2004).

[43] E. Donley, N. Claussen, S. Thompson, and C. Wieman, *Atom-Molecule Coherence in a Bose-Einstein Condensate*, Nature **417**, 529 (2002).

[44] J. Herbig, T. Kraemer, M. Mark, T. Weber, C. Chin, H.-C. Nägerl, and R. Grimm, *Preparation of a Pure Molecular Quantum Gas*, Science **301**, 1510 (2003).

[45] M. Greiner, C. Regal, and D. Jin, *Emergence of a Molecular Bose-Einstein Condensate from a Fermi Gas*, Nature **426**, 537 (2003).

[46] M. Bartenstein, A. Altmeyer, S. Riedl, S. Jochim, C. Chin, J. H. Denschlag, and R. Grimm, *Crossover from a Molecular Bose-Einstein Condensate to a Degenerate Fermi Gas*, Phys. Rev. Lett. **92**, 120401 (2004).

[47] M. Zwierlein, C. Stan, C. Schunck, S. Raupach, A. Kerman, and W. Ketterle, *Condensation of Pairs of Fermionic Atoms Near a Feshbach Resonance*, Phys. Rev. Lett. **92**, 120403 (2004).

[48] M. Mewes, M. Andrews, D. Kurn, D. Durfee, C. Townsend, and W. Ketterle, *Output Coupler for Bose-Einstein Condensed Atoms*, Phys. Rev. Lett. **78**, 582 (1997).

[49] E. Hagley, L. Deng, M. Kozuma, J. Wen, K. Helmerson, S. Rolston, and W. Phillips, *A Well-Collimated Quasi-Continuous Atom Laser*, Science **283**, 1706 (1999).

[50] I. Bloch, T. Hänsch, and T. Esslinger, *Atom Laser With a Cw Output Coupler*, Phys. Rev. Lett. **82**, 3008 (1999).

[51] S. Inouye, T. Pfau, S. Gupta, A. Chikkatur, A. Görlitz, D. Pritchard, and W. Ketterle, *Observation of Phase-Coherent Amplification of Atomic Matter Waves*, Nature **402**, 641 (1999).

[52] M. Kozuma, Y. Suzuki, Y. Torii, T. Sugiura, T. Kuga, E. Hagley, and L. Deng, *Phase-Coherent Amplification of Matter Waves*, Science **286**, 5448 (1999).

[53] L. Hau, S. Harris, Z. Dutton, and C. Behroozi, *Light Speed Reduction to 17 Metres per Second in an Ultracold Atomic Gas*, Nature **397**, 594 (1999).

[54] S. Inouye, R. Löw, S. Gupta, T. Pfau, A. Görlitz, T. Gustavson, D. Pritchard, and W. Ketterle, *Amplification of Light and Atoms in a Bose-Einstein Condensate*, Phys. Rev. Lett. **85**, 4225.

[55] J. Stenger, S. Inouye, D. Stamper-Kurn, H.-J. Miesner, A. Chikkatur, and W. Ketterle, *Spin Domains in Ground State Spinor Bose-Einstein Condensates*, Nature **74**, 345 (1995).

[56] H. Schmaljohann, M. Erhard, J. Kronjager, M. Kottke, S. van Staa, L. Cacciapuoti, J. J. Arlt, K. Bongs, and K. Sengstock, *Dynamics of F = 2 Spinor Bose-Einstein Condensates*, Phys. Rev. Lett. **92**, 040402 (2004).

[57] L. Sadler, J. Higbie, S. Leslie, M. Vengalattore, and D. Stamper-Kurn, *Spontaneous Symmetry Breaking in a Quenched Ferromagnetic Spinor Bose-Einstein Condensate*, Nature **443**, 312 (2006).

[58] B. Peredes, A. Widera, V. Murg, O. Mandel, S. Fölling, I. Cirac, G. Shlyapnikov, T. Hänsch, and I. Bloch, *Tonks-Girardeau Gas of Ultracold Atoms in an Optical Lattice*, Nature **429**, 277 (2004).

[59] T. Kinoshita, T. Wenger, and D. Weiss, *Observation of a One-Dimensional Tonks-Girardeau Gas*, Science **305**, 1125 (2004).

[60] T. Kraemer, M. Mark, P. Waldburger, J. Danzl, C. Chin, B. Engeser, A. Lange, K. Pilch, A. Jaakkola, H.-C. Nägerl, and R. Grimm, *Evidence for Efimov Quantum States in an Ultracold Gas of Caesium Atoms*, Nature **440**, 315 (2006).

[61] O. Mandel, M. Greiner, A. Widera, T. Rom, T. W. Hänsch, and I. Bloch, *Controlled Collisions for Multi-Particle Entanglement of Optically Trapped Atoms*, Nature **425**, 937 (2003).

[62] M. Weidemüller and C. Zimmermann, *Interactions in Ultracold Gases* (Wiley-VCH, 2005), 1st edition.

[63] M. Kasevich, *Coherence with Atoms*, Science **298**, 1363 (2002).

[64] J. Hudson, B. Sauer, M. Tarbutt, and E. Hinds, *Measurement of the Electron Electric Dipole Moment Using YbF Molecules*, Phys. Rev. Lett. **89**, 023003 (2002).

[65] M. Oberthaler and T. Pfau, *One-, Two- and Three-Dimensional Nanostructures With Atom Lithography*, J. Phys.: Condens. Matter **15**, R233 (2003).

[66] See Project Area C in the Sonderforschungsbereich/Transregio 21, Control of quantum correlations in tailored matter: Common perspectives of mesoscopic systems and quantum gases in Stuttgart, Ulm, Tübingen,.

[67] B. Anderson and M. Kasevich, *Macroscopic Quantum Interference from Atomic Tunnel Arrays*, Science **273**, 1686 (1998).

[68] C. Waschke, H. Roskos, R. Schwedler, K. Leo, H. Kurz, and K. Köhler, *Coherent Submillimeter-Wave Emission From Bloch Oscillations in a Semiconductor Superlattice*, Phys. Rev. Lett. **70**, 3319 (1993).

[69] S. Wilkinson, C. Bharucha, K. Madison, Q. Niu, and M. Raizen, *Observation of Atomic Wannier-Stark Ladders in an Accelerating Optical Potential*, Phys. Rev. Lett. **76**, 4512 (1996).

[70] M. Jona-Lasinio, O. Morsch, M. Cristiani, N. Malossi, J. H. Muller, E. Courtade, M. Anderlini, and E. Arimondo, *Asymmetric Landau-Zener Tunneling in a Periodic Potential*, Phys. Rev. Lett. **91**, 230406 (2003).

[71] N. MOTT, *Metal-Insulator Transition*, Rev. Mod. Phys. **40**, 677 (1968).

[72] M. Greiner, O. Mandel, T. Esslinger, T. Hänsch, and I. Bloch, *Quantum Phase Transition from a Superfluid to a Mott Insulator in a Gas of Ultracold Atoms*, Nature **415**, 39 (2002).

[73] D. Jaksch, C. Bruder, J. Cirac, C. Gardiner, and P. Zoller, *Cold Bosonic Atoms in Optical Lattices*, Phys. Rev. Lett. **81**, 3108 (1998).

[74] D. Jaksch and P. Zoller, *The Cold Atom Hubbard Toolbox*, Ann. Phys. **1**, 37 (2005).

[75] U. Weiss, *Quantum Dissipative Systems* (World Scientific, Singapore, 1999), 2nd edition.

[76] A. Recati, P. Fedichev, W. Zwerger, J. von Delft, and P. Zoller, *Dissipative Spin-Boson Model and Kondo Effect in Low Dimensional Quantum Gases*, arXiv pp. cond–mat/0212413 (2002).

[77] A. Recati, P. Fedichev, W. Zwerger, J. von Delft, and P. Zoller, *Atomic Quantum Dots Coupled to a Reservoir of a Superfluid Bose-Einstein Condensate*, Phys. Rev. Lett. **94**, 040404 (2005).

[78] T. F. Gallagher, *Rydberg Atoms* (Cambrige University Press, Cambridge, 1994).

[79] A. Dalgarno, *Rydberg atoms in astrophysics*, in *Rydberg states of atoms and molecules*, edited by R. F. Stebbings and F. B. Dunning (Cambridge University Press, 1983).

[80] P. Koch, *Rydberg studies using fast beams*, in *Rydberg states of atoms and molecules*, edited by R. F. Stebbings and F. B. Dunning (Cambridge University Press, 1983).

[81] S. Chu, *Nobel Lecture: The manipulation of neutral particles*, Rev. Mod. Phys. **70**, 685 (1998).

[82] C. N. Cohen-Tannoudji, *Nobel Lecture: Manipulating atoms with photons*, Rev. Mod. Phys. **70**, 707 (1998).

[83] W. D. Phillips, *Nobel Lecture: Laser cooling and trapping of neutral atoms*, Rev. Mod. Phys. **70**, 721 (1998).

[84] W. Anderson, J. Veale, and T. Gallagher, *Resonant Dipole-Dipole Energy Transfer in a Nearly Frozen Rydberg Gas*, Phys. Rev. Lett. **80**, 249 (1998).

[85] I. Mourachko, D. Comparat, F. de Tomasi, A. Fioretti, P. Nosbaum, V. Akulinm, and P. Pillet, *Many-Body Effects in a Frozen Rydberg Gas*, Phys. Rev. Lett. **80**, 253 (1998).

[86] K. Singer, M. Reetz-Lamour, T. Amthor, L. G. Marcassa, and M. Weidemüller, *Suppression of Excitation and Spectral Broadening Induced by Interactions in a Cold Gas of Rydberg Atoms*, Phys. Rev. Lett. **93**, 163001 (2004).

[87] D.Tong, S. Farooqi, J. Stanojevic, S. Krishnan, Y. Zhang, R. Côté, E. Eyler, and P. Gould, *Local Blockade of Rydberg Excitation in an Ultracold Gas*, Phys. Rev. Lett. **93**, 063001 (2004).

[88] T. Carroll, K. Claringbould, A. Goodsell, M. Lim, and M. W. Noel, *Angular Dependence of the Dipole-Dipole Interaction in a Nearly One-Dimensional Sample of Rydberg Atoms*, Phys. Rev. Lett. **93**, 153001 (2004).

[89] K. Afrousheh, P. Bohlouli-Zanjani, D. Vagale, A. Mugford, M. Fedorov, and J. Martin, *Spectroscopic Observation of Resonant Electric Dipole-Dipole Interactions between Cold Rydberg Atoms*, Phys. Rev. Lett. **93**, 233001 (2004).

[90] W. Li, P. J. Tanner, and T. Gallagher, *Dipole-Dipole Excitation and Ionization in an Ultracold Gas of Rydberg Atoms*, Phys. Rev. Lett. **94**, 173001 (2005).

[91] D. Jaksch, J. I. Cirac, P. Zoller, S. L. Rolston, R. Cote, and M. D. Lukin, *Fast Quantum Gates for Neutral Atoms*, Phys. Rev. Lett. **85**, 2208 (2000).

[92] C. Greene, A. Dickinson, and H. Sadeghpour, *Creation of Polar and Non-polar Ultra-Long Range Rydberg Molecules*, Phys. Rev. Lett. **85**, 2458 (2000).

[93] The Nobel Prize in Physics 2001 at www.nobelprize.org.

[94] W. Ketterle, *Nobel lecture: When atoms behave as waves: Bose-Einstein condensation and the atom laser*, Rev. Mod. Phys. **74**, 1131 (2002).

[95] E. A. Cornell and C. E. Wieman, *Nobel Lecture: Bose-Einstein condensation in a dilute gas, the first 70 years and some recent experiments*, Rev. Mod. Phys. **74**, 875 (2002).

[96] R. Löw, *Dressing and Trapping Bose-Einstein Condensates with Light*, Diploma thesis, Massachusetts Institute of Technology (2000).

[97] N. S. Bose, *Plancks Gesetz und Lichtquantenhypothese*, 26 p. 178 (1924).

[98] A. Einstein, *Quantentheorie des idealen einatomigen Gases*, Sitzber. Kgl. Preuss. Akad. Wiss. p. 261 (1924).

[99] A. Einstein, *Quantentheorie des idealen einatomigen Gases. Zweite Abhandlung*, Sitzber. Kgl. Preuss. Akad. Wiss. p. 3 (1925).

[100] L. de Broglie, *Recherches sur la théorie des Quanta*, Phd thesis, Faculte des Sciences de Paris (1924).

[101] The Nobel Prize in Physics 1924 at www.nobelprize.org.

[102] L. Tisza, *Transport phenomena in He II*, Nature **141**, 913 (1938).

[103] C. Hecht, *The Possible Superfluid Behaviour of Hydrogen Atom Gases and Liquids*, Physica **25**, 1195 (1959).

[104] W. Stwalley and L. Nosanow, *Possible "New" Quantum Systems*, Phys. Rev. Lett. **36**, 910 (1976).

[105] The Nobel Prize in Physics 1997 at www.nobelprize.org.

[106] F. Zambelli, L. Pitaevskii, D. Stamper-Kurn, and S. Stringari, *Dynamic Structure Factor and Momentum Distribution of a Trapped Bose Gas*, Phys. Rev. A **61**, 063608 (2000).

[107] W. Hänsel, P. Hommelhoff, T. Hänsch, and J. Reichel, *Bose-Einstein Condensation on a Microelectronic Chip*, Nature **498**, 498 (2001).

[108] H. Ott, J. Fortagh, G. Schlotterbeck, A. Grossmann, and C. Zimmermann, *Bose-Einstein Condensation in a Surface Microtrap*, Phys. Rev. Lett. **87**, 230401 (2001).

[109] J. Stuhler, A. Griesmaier, T. Koch, M. Fattori, T. Pfau, S. Giovanazzi, P. Pedri, and L. Santos, *Observation of Dipole-Dipole Interaction in a Degenerate Quantum Gas*, Physical Review Letters **95**, 150406 (2005).

[110] F. Bloch, *Über die Quantenmechanik der Elektronen in Kristallen*, Z. Physik **52**, 555 (1928).

[111] C. Zener, *A Theory of the Electrical Breakdown of Solid Dielectrics*, Proc. Roy. Soc. London Ser. A **145**, 523 (1934).

[112] B. Josephson, *Possible New Effects in Superconductive Tunneling*, Phys. Lett. **1**, 251 (1962).

[113] F. Cataliotti, S. Burger, C. Fort, P. Maddaloni, F. Minardi, M. Inguscio, A. Trombettoni, and A. Smerzi, *Josephson Junction Arrays With Bose-Einstein Condensates*, Science **293**, 843 (2001).

[114] A. Truscott, K. Strecker, W. McAlexander, G. Patridge, and R. Hulet, *Observation of Fermi Pressure in a Gas of Trapped Atoms*, Science **291**, 2570 (2001).

[115] F. Schreck, L. Khaykovich, K. Corwin, G. Ferrari, T. Bourdel, J. Cubizolles, and C. Salomon, *Quasipure Bose-Einstein Condensate Immersed in a Fermi Sea*, Phys. Rev. Lett. **87**, 080403 (2001).

[116] Z. Hadzibabic, C. Stan, K. Dieckmann, S. Gupta, M. Zwierlein, A. Görlitz, and W. Ketterle, *Two-Species Mixture of Quantum Degenerate Bose and Fermi Gases*, Phys. Rev. Lett. **88**, 160401 (2002).

[117] M. Zwierlein, J. Abo-Shaeer, A. Schirotzek, C. Schunck, and W. Ketterle, *Vortices and Superfluidity in a Strongly Interacting Fermi Gas*, Nature **435**, 1047 (2005).

[118] J. Fraunhofer, *Joseph von Fraunhofer's gesammelte Schriften, hrsg. von E. Lommel* (Königlich Bayerische Akademie der Wissenschaften, 1888), 1. Auflage.

[119] G. Kirchhoff, *Gesammelte Abhandlungen* (Vdm Verlag Dr. Müller, 2006), 1. Auflage.

[120] J. Rydberg, *Untersuchungen über die Beschaffenheit der Emissionsspektren der chemischen Elemente (Recherches sur la constitution des spectres d'émission des elements chimiques)* (Akademische Verlagsgesellschaft Leipzig, 1889), ostwald's Klassiker der exakten Wissenschaften, 1. Auflage, Erscheinungsjahr 1922.

[121] H. Bethe and E. Salpeter, *Quantum mechanics of one-and two-electron atoms* (Plenum, New York, 1957).

[122] E. Streed, A. Chikkatur, T. Gustavson, M. Boyd, Y. Torii, D. Schneble, G. Campbell, D. Pritchard, and W. Ketterle, *Experimental Setup for BEC Experiment*, Rev. Sci. Instrum. **77**, 023106 (2006).

[123] Cohen-Tannoudji, C., Dupont-Roc, J., and G. Grynberg, *Atom-photon interactions* (John Wiley & Sons, 1992).

[124] T. Pfau, *Bergmann, Schäfer, Band 3, Optik, Optik mit Materiewellen: Atomoptik* (de Gruyter & Co, Berlin, 1991), 10. Auflage.

[125] H. J. Metcalf and P. van der Straten, *Laser Cooling and Trapping* (Springer Verlag, New York, 1999).

[126] P. Meystre, *Atom Optics* (Springer Verlag, New York, 2001).

[127] G. Lindblad, *On the Generators of Quantum Dynamical Semigroups*, Comm. Math. Phys **48**, 199 (1976).

[128] P. Jessen and I. Deutsch, *Optical lattices*, Adv. At. Mol. Opt. Phys **37**, 1 (1996).

[129] T. Hänsch and A. Schawlow, *Cooling of Gases by Laser Radiation*, Opt. Com. **13**, 68 (1975).

[130] P. Lett, W. Phillips, S. Rolston, C. Tanner, R. Watts, and C. Westbrook, *Optical molasses*, J. Opt. Soc. Am. B **6**, 2084 (1989).

[131] D. Steck, *Rubidium 87 D Line Data*, http://steck.us/alkalidata.

[132] E. Raab, M. Prentiss, A. Cablev, S. Chu, and D. Pritchard, *Trapping of Neutral Sodium Atoms with Radiation Pressure*, Phys. Rev. Lett. **59**, 2631 (1987).

[133] D. Pritchard, E. Raab, V. Bagnato, C. Wieman, and R. Watts, *Light Traps Using Spontaneous Forces*, Phys. Rev. Lett. **57**, 310 (1986).

[134] T. Walker, D. Sesko, and C. Wieman, *Collective behavior of optically trapped neutral atoms*, Phys. Rev. Lett. **64**, 408 (1990).

[135] D. Sesko, T. Walker, and C. Wieman, *Behavior of Neutral Atoms in a Spontaneous Force Trap*, J. Opt. Soc. Am. B **8**, 946 (1991).

[136] A. Steane, M. Chowdhury, and C. J. Foot, *Radiation Force in the Magneto-optical trap*, J. Opt. Soc. Am. B **9**, 2142 (1992).

[137] C. Wallace, T. Dinneen, K. Tan, A. Kumarakrishnan, P. Gould, and J. Javanainen, *Measurements of Temperature and Spring Constant in a Magneto-optical Trap*, J. Opt. Soc. Am. B **11**, 703 (1994).

[138] C. Cooper, G. Hillenbrand, J. Rink, C. Townsend, K. Zetie, and C. Foot, *The Temperature of Atoms in a Magneto-optical Trap*, Europhys. Lett. **28**, 397 (1994).

[139] K. Kim, H. Noh, and W. Jhe, *Measurement of Trap Parameters of a Magneto-optical trap by Parametic Resonance*, Phys. Rev. A **71**, 033413 (2005).

[140] J. Dalibard and C. N. Cohen-Tannoudji, *Laser cooling below the Doppler limit by polarization gradients: simple theoretical models*, J. Opt. Soc. Am. B **6**, 2023 (1989).

[141] D. Boiron, A. Michaud, P. Lemonde, Y. Castin, C. Salomon, S. Weyers, K. Szymaniec, L. Cognet, and A. Clairon, *Laser Cooling of Cesium Atoms in Gray Optical Molasses Down to 1.1 μK*, Phys. Rev. A **53**, R3734 (1996).

[142] W. Wing, *On Neutral Particle Trapping in Quasistatic Electromagnetic Fields*, Prog. Quant. Elect. **81**, 181 (1984).

[143] G. Breit and I. Rabi, *Measurement of Nuclear Spin*, Phys. Rev. **38**, 2082 (1931).

[144] E. Majorana, *Atomi Orientata in Compo Magnetico Veriabile*, Nuovo Cimento **9**, 43 (1932).

[145] D. M. Brink and C. V. Sukumar, *Majorana spin-flip transitions in a magnetic trap*, Phys. Rev. A **74**, 035401 (2006).

[146] A. Migdall, J. Prodan, W. Phillips, T. Bergeman, and H. Metcalf, *First Observation of Magnetically Trapped Neutral Atoms*, Phys. Rev. Lett. **54**, 2596 (1985).

[147] U. Ernst, A. Marte, F. Schreck, J. Schuster, and G. Rempe, *Bose-Einstein Condensation in a Pure Ioffe Pritchard Field Configuration*, Euro. Phys. Lett. **41**, 1 (1998).

[148] D. Pritchard, *Cooling Neutral Atoms in a Magnetic Trap for Precision Spectroscopy*, Phys. Rev. Lett. **51**, 1336 (1983).

[149] W. Petrich, M. Anderson, J. Ensher, and E. Cornell, *Stable, Tightly Confining Magnetic Trap for Evaporative Cooling of Neutral Atoms*, Phys. Rev. Lett. **74**, 3352 (1995).

[150] T. Bergemann, G. Erez, and H. Metcalf, *Magnetostatic Trapping Fields for Neutral Atoms*, Phys. Rev. A **35**, 1429 (1987).

[151] T. Esslinger, I. Bloch, and T. Hänsch, *Bose-Einstein condensation in a quadrupole-Ioffe-configuration trap*, Phys. Rev. A **58**, R2664 (1998).

[152] S. Gupta, K. Murch, K. Moore, T. Purdy, and D. Stamper-Kurn, *Bose-Einstein condensation in a circular waveguide*, Phys. Rev. Lett. **95**, 143201 (2005).

[153] J. Reichel, W. Hänsel, and T. Hänsch, *Atomic Micromanipulation with Magnetic Surface Traps*, Physical Review Letters **83**, 3398 (1999).

[154] M. Mewes, M. Andrews, N. van Druten, D. Kurn, D. Durfee, and W. Ketterle, *Bose-Einstein Condensation in a Tightly Confining dc Magnetic Trap*, Phys. Rev. Lett. **77**, 416 (1996).

[155] D. Stamper-Kurn, *Peeking and Poking at a New Quantum Fluid: Studies of Gaseous Bose-Einstein Condensates in Magnetic and Optical Traps*, Phd thesis, Massachusetts Institute of Technology (2000).

[156] M. Barrett, J. Sauer, and M. Chapman, *All-optical formation of an atomic Bose-Einstein condensate*, Phys. Rev. Lett. **87**, 010404 (2001).

[157] K. Davis, M. Mewes, M. Joffe, M. Andrews, and W. Ketterle, *Evaporative Cooling of Sodium Atoms*, Phys. Rev. Lett. **74**, 5202 (1995).

[158] W. Ketterle and N. van Druten, *Evaporative Cooling of Trapped Atoms*, Adv. At. Mol. Opt. Phys. **37**, 181 (1996).

[159] K. Dieckmann, *Bose-Einstein Condensation with High Atom Number in a Deep Magnetic Trap*, Phd thesis, University Amsterdam (2001).

[160] P. Valkering, *Optimazition of Evaporative Cooling of Rubidium Atoms in a Magnetic Trap*, Master thesis, University of Utrecht (1999).

[161] K. Huang, *Statistical Mechanics* (Wiley, 1988), 2nd edition.

[162] C. Pethich and H. Smith, *Bose-Einstein Condensation in Dilute Gases* (Cambridge Press, 2002), 1st edition.

[163] M. Abramowitz and I. Stegun, *Handbook of Mathematical Functions* (Dover Publications, New York, 1968), 5. edn.

[164] W. Ketterle and N. van Druten, *Bose-Einstein Condensation of a Finite Number of Particles Trapped in One or Three Dimensions*, Phys. Rev. A **54**, 656 (1996).

[165] A. Griesmeier, *Dipole-Dipole Interaction in a Degenerate Quantum Gas: Bose-Einstein Condensation of Chrmium Atoms*, Phd thesis, Universität Stuttgart (2006).

[166] P. O. Schmidt, *Scattering properties of Ultra-Cold Chromium Atoms*, Phd thesis, Universität Stuttgart (2003).

[167] S. Hensler, *Wechselwirkungen in ultrakalten dipolaren Gasen*, Phd thesis, Universität Stuttgart (2004).

[168] E. Burt, R. Ghirst, C. Myatt, M. Holland, E. Cornell, and C. Wieman, *Cohernece, Correlations and Collsions: What One Learns about Bose-Einstein Condensates from their Decay*, Phys. Rev. Lett. **79**, 337 (1997).

[169] J. Söding, D. Guery-Odelin, P. Desbiolles, F. Chevy, H. Inamori, and J. Dalibard, *Three-Body Decay of a Rubidium Bose-Einstein Condensate*, Appl. Phys. B **69**, 257 (1999).

[170] P. Meystre and S. Stenholm, *The Mechanical Effects of Light*, Opt. Soc. Am. B **6**, 1705 (1985).

[171] S. Chu and C. Wieman, *Laser Cooling and Trapping of Atoms*, Opt. Soc. Am. B **6**, 1961 (1989).

[172] R. Grimm, M. Weidemüller, and Y. Ovchinnikov, *Optical dipole traps for neutral atoms*, Adv. At. Mol. Opt. Phys **42**, 95 (2000).

[173] S. Chu, J. Bjorkholm, A. Ashkin, and A. Cable, *Experimental Observation of Optically Trapped Atoms*, Phys. Rev. Lett. **57**, 314 (1986).

[174] D. Stamper-Kurn, M. Andrews, A. Chikkatur, S. Inouye, H. Miesner, J. Stenger, and W. Ketterle, *Optical Confinement of a Bose-Einstein Condensate*, Phys. Rev. Lett. p. 2027 (1998).

[175] O. Morsch and M. Oberthaler, *Dynamics of Bose-Einstein Condensates in Optical Lattices*, Rev. Mod. Phys. **78**, 179 (2006).

[176] N. Ashcroft and M. David, *Solid State Physics* (Saunders College, Philadelphia, 1976).

[177] P. Kapitza and P. Dirac, *Diffraction of an Electron Beam off a Standing Light Wave*, Proc. Cambridge Philos. Soc. **29**, 297 (1933).

[178] D. Freimund, K. Aflatooni, and H. Batelaan, *Observation of the Kapitza-Dirac Effect*, Nature **413**, 142 (2001).

[179] J. Schoser, *Erzeugung eines Bose-Einstein-Kondensats in einer stark anisotropen Magnetfalle*, Phd thesis, Universität Stuttgart (2003).

[180] J. Nold, *Ultrakalte Quantengase in optischen Gittern*, Diploma thesis, Universität Stuttgart (2006).

[181] W. Hartley, J. Chem. Soc. **43**, 390 (1883).

[182] J. Rydberg, Phil. Mag. 5^{th}series **29**, 331 (1890).

[183] W. Li, I. Mourachko, M. Noel, and T. Gallagher, *Millimeter-wave spectroscopy of cold Rb Rydberg atoms in a magneto-optical trap: Quantum defects of the ns, np, and nd series*, Phys. Rev. A **67**, 052502 (2003).

[184] S. A. Lee, J. Helmcke, J. L. Hall, and B. P. Stoicheff, *Doppler-free two-photon transitions to Rydberg levels: convenient, useful, and precise reference wavelengths for dye lasers*, Optics Lett. **3**, 141 (1978).

[185] C.-J. Lorenzen and K. Niemax, *Quantum Defects of the* $n^2P_{1/2,3/2}$ *Levels in* ^{39}K *I and* ^{85}Rb *I*, Phys. Scr. **27**, 300 (1983).

[186] B. Stoicheff and E. Weinberger, Can. J. Phys. **57**, 2143 (1979).

[187] I. Johannson, Ark. f. Fysik **20**, 135 (1961).

[188] M. Seaton, *Quantum defect theory*, Rep. Prog. Phys. **46**, 167 (1983).

[189] A. Grabowski, *Aufbau einer Messaperatur zur Laserkühlung und hochauflösenden Rydberg-Spektroskopie an* ^{87}Rb*-Atomen*, Phd thesis, Universität Stuttgart (2006).

[190] A. de Oliveira, M. Mancini, V. Bagnato, and L. Marcassa, *Measurement of Rydberg-state lifetimes using cold trapped atoms*, Phys. Rev. A **65**, 031401 (2002).

[191] C. E. Theodosiou, *Lifetimes of alkali-metal atom Rydberg states*, Phys. Rev. A **30**, 2881 (1984).

[192] U. Raitzsch, *Aufbau einer UHV-Kammer zur Durchführung von Experimenten mit Bose-Einstein-Kondensaten in optischen Gittern*, Diploma thesis, Universität Stuttgart (2004).

[193] BEC III setup, Center for Ultra-Cold Atoms (CUA), Massachusetts Institute of Technology, Cambridge, USA, http://cua.mit.edu/ketterlegroup.

[194] T. Mukai and M. Yamashita, *Efficient Rapid Production of a Bose-Einstein Condensate by Overcoming sSrious Three-Body Loss*, Phys. Rev. A **70**, 013615 (2004).

[195] K. Bongs, S. Burger, G. Birkl, K. Sengstock, W. Ertmer, K. Rzazewski, A. Sanpera, and M. Lewenstein, *Coherent Evolution of Bouncing Bose-Einstein Condensates*, Phys. Rev. Lett. **83**, 3577 (1999).

[196] Y. Torii, Y. Suzuki, M. Kozuma, T. Sugiura, and T. Kuga, *Mach-Zehnder Bragg Interferometer for a Bose-Einstein Condensate*, Phys. Rev. A **61**, 041602 (2000).

[197] W. Demtröder, *Experimentalphysik 2: Elektrizität und Optik* (Springer Verlag, 1991), 2. Auflage.

[198] L. Ricci, M. Weidemüller, T. Esslinger, A. Hemmerich, C. Zimmermann, V.Vuletic, W.Knig, and T. Hänsch, *A compact grating-stabilized diode laser system for atomic physics*, Opt. Commun. **117** (1995).

[199] A. Marte, *Feshbach-Resonanzen bei Stßen ultrakalter Rubidiumatome*, Phd thesis, Technische Universität München (2003).

[200] M. Andrews, M. Mewes, N. van Druten, D. Durfee, D. Kurn, and W. Ketterle, *Direct, Non-Destructive Imaging of a Bose Condensate*, Science **273**, 84 (1996).

[201] Y. Castin and R. Dum, *Bose-Einstein Condensation in Time-Dependent Trap*, Phys. Rev. Lett. **77**, 5315 (1996).

[202] J. Werner, *Observation of Feshbach Resonances in an Ultracold Gas of ^{52}Cr*, Phd thesis, Universät Stuttgart (2006).

[203] A. Steane, P. Szriftgiser, P. Desbiolles, and J. Dalibard, *Phase Modulation of Atomic de Broglie Waves*, Phys. Rev. Lett. **74** (1995).

[204] T. B. Swanson, D. Asgeirsson, J. A. Behr, A. Gorelov, and D. Melconian, *Efficient transfer in a double magneto-optical trap system*, J. Opt. B:Quantum Semiclass. Opt. **15**, 2641 (1998).

[205] J.Schoser, A.Batär, R.Löw, V.Schweikhard, A.Grabowski, Y.B.Ovchinnikov, and T.Pfau, *Intense Source of Cold Rb Atoms From a Pure Two-dimensional Magneto-optical Trap*, Phys. Rev. A **66**, 023410 (2002).

[206] K. Dieckmann, R. J. C. Spreeuw, M. Weidemüller, and J. T. M. Walraven, *Two-dimensional magneto-optical trap as a source of slow atoms*, Phys. Rev. A **58**, 3891–3895 (1998).

[207] J. Fortagh, A. Grossmann, T. W. Hänsch, and C. Zimmermann, *Fast loading of a magneto-optical trap from a pulsed thermal source*, J. Appl. Phys. **84**, 6499 (1998).

[208] C. A. Stan and W. Ketterle, *Multiple species atom source for laser-cooling experiments*, Rev. Sci. Instrum. p. 063113 (2005).

[209] H. Massey and C. Mohr, *Free Paths and Transport Phenomena in GAses and the Quantum Theory of Collisions. II. The Determination of the Laws of Force Between Atoms and Molecules*, Proc. R. Soc. London **A144**, 188 (1932).

[210] M. Marinescu, H. R. Sadeghpour, , and A. Dalgarno, *Dispersion Coefficients for Alkali-Metal Dimers*, Phys. Rev. A **49**, 982 (1994).

[211] H. Boesten, C. Tsai, J. Gardner, D. Heinzen, and B. Verhaar, *Observation of a Shape Resonance in the Collision of Two Cold ^{87}Rb Atoms*, Phys. Rev. A **55**, 636 (1997).

[212] Priv. comm. with Dr. Wieland Schöllkopf, Fritz-Haber-Institut der Max-Planck-Gesellschaft.

[213] N. F. Ramsey, *Molecular Beams* (Claredon Press, Oxford, 1956), 2nd edition.

[214] W. Phillips and H. Metcalf, *Laser Deceleration of an Atomic Beam*, Phys. Rev. Lett **48**, 596 (1982).

[215] S. Kroboth, *Laserkühlung von Ytterbiumatomen*, Diploma thesis, Universität Stuttgart (2002).

[216] M. Drewsen, P. Laurent, A. Nadir, G. Santarelli, A. Clairon, Y. Castin, D. Grison, and C. Salomon, *Investigation of sub-Doppler cooling effects in a caesium magneto-optical trap*, Appl. Phys. B **59**, 283 (1994).

[217] C. G. Townsend, N. H. Edwards, C. J. Cooper, K. P. Zetie, C. J. Foot, A. M. Steane, P. Szriftgiser, H. Perrin, and J. Dalibard, *Phase-space density in the magneto-optical trap*, Phys. Rev. A **52**, 1423 (1995).

[218] W. Petrich, M. Anderson, J. Ensher, and E. Cornell, *Behavior of Atoms in a Compressed Magneto-Optical Trap*, J. Opt. Soc. Am. B p. 1332 (1994).

[219] C. D. Wallace, T. P. Dinneen, K.-Y. N. Tan, T. T. Grove, and P. L. Gould, *Isotopic Difference in Trap Loss Collisions of Laser Cooled Rubidium Atoms*, Phys. Rev. Lett. **69**, 897 (1992).

[220] W. Petrich, M. Anderson, J. Ensher, and E. Cornell, *Compressing an Atom Cloud in a Magneto-Optical Trap*, PROC INT QUANTUM ELECTRON CONF, IEEE, PISCATAWAY, NJ, (USA) p. 236 (1994).

[221] J. Jackson, *Classical Electrodynamics* (Wiley, 1998), 3rd edition.

[222] M. Gehm, K. O. Hara, T. Savard, and J. Thomas, *Dynamics of Noise-Induced Heating in Atom Traps*, Phys. Rev. A **58**, 3914 (1998).

[223] V. Schweikhard, *Ultracold Atoms in Far-Detuned Optical Lattices*, Diploma thesis, Universität Stuttgart (2001).

[224] P. W. H. Pinske, A. Mosk, M. Weidemüller, M. Reynolds, T. Hijmans, and T. Walraven, *Adiabtically Changing the Phase Space Density of a Trapped Bose Gas*, Phys. Rev. Lett. **78**, 990 (1997).

[225] The Bose-Einstein condensate experiment (2001) in Amsterdam in the group of J.T.M. Walraven.

[226] The Bose-Einstein condensate experiment (1998) in Konstanz in the group of G. Rempe.

[227] J. Robinson, *Note on the Bose-Einstein Integral Functions*, Phys. Rev. **678** (1951).

[228] V. Bagnato, D. Pritchard, and D. Kleppner, *Bose-Einstein Condensation in an External Potential*, Phys. Rev. A **85**, 4354 (1987).

[229] S. Giorgini, L. P. Pitaevskii, and S. Stringari, *Condensate Fraction and Critical Temperature of a Trapped Interacting Bose Gas*, Phys. Rev. A **54**, R4633 (1996).

[230] A. Albus, S. Giorgini, F. Illuminati, and L. Viverit, *Critical Temperature of Bose-Einstein Condensation in Trapped Atomic Bose-Fermi Mixtures*, J. Phys. B At. Mol. Opt. Phys. **23**, 35 (2002).

[231] R. Löw, R. Gati, J. Stuhler, and T. Pfau, *Probing the Light-Induced Dipole-Dipole Interaction in Momentum Space*, Europhys. Lett. **71**, 214 (2005).

[232] R. Gati, *Interaction of Ultracold Atoms in Periodical Potentials*, Diploma thesis, Universität Stuttgart (2004).

[233] D. P. CRAIG and T.THIRUNAMACHANDRAN, *Molecular Quantum Electrodynamics* (Dover Publications, Inc., 1998).

[234] A. Molisch and B. Oehry, *Radiation Trapping in Atomic Vapors* (Clarendon Press, Oxford, 1998).

[235] U. Janicke and M. Wilkens, *Atomic Motion in a Magneto-Optical Field*, Phys. Rev. A **50**, 3265 (1994).

[236] D. Schneble, Y. Torii, M. Boyd, E. W. Streed, D. E. Pritchard, and W. Ketterle, *Intense source of cold Rb atoms from a pure two-dimensional magneto-optical trap*, Science **300**, 475 (2003).

[237] H. Bender, *Mikrowellenanregung von ultrakalten Atomen*, Diploma thesis, Universität Stuttgart (2006).

[238] E. Kuhnle, *Rydberg Exciatation of a Bose-Einstein Condensate*, Diploma thesis, Universität Stuttgart (2006).

[239] H. Kübler, *Elektromagnetisch Induzierte Transparenz in einer Rubidium Dampfzelle*, Diploma thesis, Universität Stuttgart (2005).

[240] A. Görlitz, T. Gustavson, A. Leanhardt, R. Löw, A. Chikkatur, S. Gupta, S. Inouye, D. Pritchard, and W. Ketterle, *Sodium Bose-Einstein Condensates in the F=2 State in a Large-volume Optical Trap*, Phys. Rev. Lett. **90**, 090401 (2003).

[241] J. Kraus and R. Marhefka, *Antennas* (McGraw-Hill, 2002), 3rd edition.

[242] J. Rubbmark, M. Kash, M. Littman, and D. Kleppner, *Dynamical effects at avoided level crossings: A study of the Landau-Zener effect using Rydberg atoms*, Phys. Rev. A **23**, 3107 (1981).

[243] M. Buhlert, *Elektropolieren und Elektrostrukturieren von Edelstahl, Messing und Aluminium. Untersuchung des transpassiven Abtragprozesses einschließlich unerwünschter Nebeneffekte* (Fortschritt-Berichte VDI, VDI-Verlag, Düsseldorf, 2000), reihe 2, Nr. 553.

[244] A. Leggett, S. Chakravarty, A. Dorsey, M. Fisher, A. Garg, and W. Zwerger, *Dynamics of the Dissipative Two-State System*, Rev. Mod. Phys. **59**, 1 (1987).

[245] H. Grabert and A. N. (editors), *The Spin-Bose Problem: From Electron Transfer to Quantum Computing*, Special Issue: Chem. Phys. **296**, 121–356 (2004).

[246] C. Myatt, B. King, Q. Turchette, C. Sackett, D. Kielpinski, W. Itano, C. Monroe, and D. Wineland, *Decoherence of Quantum Superpositions Through Coupling to Engineered Reservoirs*, Nature **403**, 269 (2000).

[247] M. Brune, E. Hagley, J. Dreyer, X. Maitre, A. Maali, C. Wunderlich, J. Raimond, and S. Haroche, *Observing the Progressive Decoherence of the Meter in a Quantum Measurement*, Phys. Rev. Lett. **77**, 4887 (1996).

[248] A. Steane, *Quantum computing*, Rep. Prog. Phys. **61**, 117 (1998).

[249] D. DiVincenzo, *The Physical Implementation of Quantum Computing*, Fortschr. Phys. **48**, 771 (2000).

[250] B. Sheehy, S. Shang, R. Watts, S. Hatamian, and H. Metcalf, *Diode-Laser Deceleration and Collimation of a Rubidium Beam*, J. Opt. Soc. Am. B **6**, 2165 (1989).

[251] A. Radzig and B. Smirnov, *Reference Data on Atoms, Molecules and Ions* (Springer Verlag, Berlin, 1985).

[252] D. Lide, *CRC Handbook of Chemsitry and Physics* (CRC Press, Taylor and Francis Group LCC, 2006), 87th edition.

[253] I. Sobelmann, *Atomic spectra and radiative transitions* (Springer Verlag, New York, 1992).

[254] R. Zare, *Angular Momentum* (John Wiley & Sons, 1988).

[255] M. L. Zimmermann, M. Littman, M. Kash, and D. Kleppner, *Stark structure for the Rydberg states of alkali-metal atoms*, Phys. Rev. A **20**, 2251 (1979).

[256] A. Grabowski, R. Heidemann, R. Löw, J. Stuhler, and T. Pfau, *High Resolution Rydberg Spectroscopy of ultracold Rubidium Atoms*, Fortschr. Phys. **54**, 765 (2006).

[257] D. Suter, *The Physics of Laser-Atom Interactionss* (Cambridge Studies in Modern Optics (No. 19), 2005).

[258] B. Shore, *The Theory of coherent atomic excitation* (Wiley, New York, 1990).

[259] K. Case and S. Chiu, *Electromganetic Fluctuations in a Cavity*, Phys. Rev. A **1**, 1170 (1970).

[260] A. Kolokolov and G. Skrotskii, *Equillibrium Radiation in a Finite-Size Cavity*, Opt. Spectrosc. **36**, 127 (1974).

[261] R. Loudon, *The Quantum Theory of Light* (Oxford University Press, London, 1973), 1st edition.

Danksagung

An dieser Stelle sei noch allen ein Dank ausgesprochen, die durch ihre direkte und indirekte Unterstützung während der letzten Jahre zur Entstehung und zum Gelingen meiner Doktorarbeit beigetragen haben.

Tilman Pfau möchte ich dafür danken, dass er mich von der Geburtsstunde des PI5 an aktiv teilhaben ließ und mir die Aufgabe übertrug dieses Projekt zu planen und aufzubauen. Dabei ist es ihm hoch anzurechnen, dass er trotz der selbstzerstörerischen Kreativität der Apparatur nie das Vertrauen in sein Rubidium-Team und dessen tollkühne Kiste verlor. Ohne seine visionären Ideen, die dem Experiment immer ein paar Schritte vorraus sind, wäre der derzeitige Erfolg dieses Projektes nie so möglich gewesen.

Damit eine Apparatur, die aus so unglaublich vielen Einzelteilen besteht, überhaupt mal funktionieren kann, ist die Mitarbeit und Unterstützung vieler Menschen nötig, und denen möchte ich hier danken:

- Ulrich Raitzsch, der sich durch nichts abschrecken ließ und wirklich von der Stunde Null an mit dabei war. Meine kreative zeitsparende Arbeitsweise mit dem Klebeband ergänzte er durch akkurate Sorgfalt, und die erreichte Stabilität des Experiments ist sicher sein Verdienst. Und wenn an allem mal wieder die Fourierebene schuld war, blieb er doch immer ruhig und gelassen. Dafür: Gib Bussi.

- Rolf Heidemann, der das ganze türkisfarbene Lasersystem aufgebaut hat und sich auch, wahrlich heldenhaft, geopfert hat die Steuersoftware umzuprogrammieren (studiert ist studiert). Durch seine vorausschauende Art im Labor (Ich hab das schon mal vorbereitet) wurde er zurecht der Namenspatron des "Ehren-Rolf-Awards" des PI5. Außerdem danke ich ihm für viele angenehme Messnächte, die wir zusammen halb schlafend durchwacht haben.

- Axel Grabowski, der wirklich vor keinem Problem zurückschreckte und alles immer sofort in Angriff nahm, dabei immer seinem Leitspruch folgend: Das kann doch gar nicht so schwer sein. Unvergessen werden mir die ersten, höchst kriminellen, Testläufe unserer Hochspannungelektronik sein, bei denen sich Rolf als Sicherheitsbeauftragter mit Grausen abwandte. Selbst wenn 10 Watt Laserstrahlen kreuz und quer durchs Labor schossen, konnte ihn das nicht aus der Ruhe bringen.

- Jürgen Schoser, mit dem ich unendlich viele Meßnächte an der alten Apparatur (it's a bug, not a feature) verbrachte und dabei alle Höhen und Tiefen eines Physikerlebens durchlebte.

Aber mit unglaublicher Zähigkeit konnten wir der Maschine doch noch ein paar Ergebnisse abringen. Von all diesen durchwachten Nächten werden mir vor allem die kulturhistorischen Ausflüge weit nach Mitternacht, während die Kiste hinter uns mal wieder machte was sie wollte, immer in Erinnerung bleiben.

- Vera Bendkowsky, die nun seit einem Jahr im Rubidium-Team ist und dem reinen Männerhaufen durch Ihre ausgegelichene Art etwas Zivilisation näher brachte. Als Hüterin des türkisfarbenen Lichtes ist sie unentbehrlich geworden.

- Jürgen Stuhler und Axel Görlitz, die für meine Fragen und Probleme stets ein offenes Ohr hatten und zu vielen Lösungen beitrugen.

- Mir waren viele motivierte Nachwuchskräfte als Diplomand bzw. Diplomandin ganz oder zumindest teilweise ausgeliefert. Jeder von Ihnen hat einen wichtigen Teil zum Aufbau oder zum Gelingen der Experimente beigetragen. Das sind im einzelnen Alexander Batär, Rolf Heidemann, Volker Schweikhard, Jochen Steinmann, Rudolf Gati, Ulrich Raitzsch, Johannes Nold, Helmar Bender, Eva Kuhnle und Björn Butscher, die bislang alle nach Ihrer Diplomarbeit als Doktoranden dem Foschungsgebiet treu geblieben sind.

- Weiterhin möchte ich allen ehemaligen und gegenwärtigen Kollegen von den anderen Arbeitsgruppen für die freundschaftliche Zusammenarbeit sowie dem regen Austausch von Know-How (und Equipment) danken. Vor allem mit Piet Schmidt, Sven Hensler, Bernd Kaltenhäuser und Axel Griesmeier hatte ich viele interessante physikalische und auch nichtphysikalische Diskussionen.

- Axel Grabowski, Rolf Heidemann und Ulrich Raitzsch danke ich für die sorgfältige Korrektur dieser Arbeit und Sylvia Tassy für die vielen Kommata.

- Einen wesentlichen Beitrag haben die einzelnen Werkstätten geleistet. Allen voran die Feinmechanik um Herrn Kamella. Herrn Kube sei für die Herstellung der Vakuumkammer gedankt und Herrn Dietrich, der jedes noch so komplizierte Teil herstellen konnte, sowie all den anderen Mitarbeitern die eine Vielzahl von Komponenten hergestellt haben. Bei den Elektro-nikern muss ich mich bei Herrn Möhrle, Herrn Henning und Herrn Braun für die Realisierung all meiner, manchmal etwas ausgefallenen, Ideen bedanken. Die Elektrik um Herrn Kern hat mir stets gute Dienste geleistet, wenn es mal wieder um Komponenten für viel Strom ging. Sehr dankbar bin ich Herrn Maurer von der Tieftemperaturabteilung, der immer schnell und unkompliziert mit seinem Heliumschnüffler angerückt ist. Zuletzt sei noch der Glaswerkstatt um Herrn Quack und der Schreinerei um Herrn Hauke gedankt.

- Den Mitarbeitern im Sekretariat, Sylvia Tassy und Nadine Prellwitz, die stets die erste Front für Rechnungen und Administratives hielten.

- Eine wichtige Rolle spielte Karin Otter, die die gute Seele des PI5 war und in mir die Leidenschaft zum Exponatebau weckte. Der große Erfolg der Experimenta und der Highlights wäre ohne sie nie möglich gewesen.

- Herrn Prof. Stroth danke ich für die unkomplizierte und zügige Mitberichterstattung dieser Arbeit.

- Herrn Prof. Mahler danke ich dafür, dass er kurzfristig den Prüfungsvorsitz übernommen hat, und dass ich ihn oft mit meinen theoretischen Problemen behelligen durfte.

- Der Studienstiftung des deutschen Volkes danke ich für die finanzielle Unterstützung.

- Ich danke außerdem all den Menschen, die mich außerhalb des Labors unterstützt haben. Das sind meine Eltern, die mir das Physikstudium ermöglicht haben, meine Schwester Iris, die immer an mich geglaubt hat und unter allen Freunden und Bekannten vor allem Tobias Seidl, der dafür sorgte, dass ich den Anschluss an das reale Leben nicht verlor.

Mein größter Dank geht an Pati für die moralische Unterstützung, wenn es mal mit den Atomen nicht so klappte, und ihre Freude, wenn dann doch mal was gelang. Dabei musste sie viel auf mich verzichten, da ich auch daheim noch oft mit dem Kopf im Labor war. Für das alles und noch vieles mehr: Danke!